

IBRAHIM ISSAH

Multilayer Structures for Enhanced Light-matter Interactions

Classical Applications and Quantum Extensions

IBRAHIM ISSAH

Multilayer Structures for
Enhanced Light-matter Interactions
Classical Applications and Quantum Extensions

ACADEMIC DISSERTATION

To be presented, with the permission of
the Faculty of Engineering and Natural Sciences
of Tampere University,
for an online public discussion
on 26th of January 2024, at 16 o'clock

ACADEMIC DISSERTATION

Tampere University, Faculty of Engineering and Natural Sciences
Finland

*Responsible
supervisor
and Custos*

Associate Professor
Marco Ornigotti
Tampere University
Finland

Supervisors

Associate Professor
Marco Ornigotti
Tampere University
Finland

University Instructor
Mikko Huttunen
Tampere University
Finland

Pre-examiners

Associate Professor
Michele Celebrano
Politecnico di Milano
Italy

Senior Lecturer
Sebastian A. Schulz
University of St Andrews
United Kingdom

Opponent

Professor
Nathaniel Kinsey
Virginia Commonwealth
University
United States of America

The originality of this thesis has been checked using the Turnitin OriginalityCheck service.

Copyright ©2024 Ibrahim Issah

Cover design: Roihu Inc.

ISBN 978-952-03-3287-7 (print)

ISBN 978-952-03-3288-4 (pdf)

ISSN 2489-9860 (print)

ISSN 2490-0028 (pdf)

<http://urn.fi/URN:ISBN:978-952-03-3288-4>



Carbon dioxide emissions from printing Tampere University dissertations have been compensated.

PunaMusta Oy – Yliopistopaino
Joensuu 2024

Dedicated to the Almighty God, Liana Burns, and my family.

ACKNOWLEDGMENTS

I would like to express my sincere gratitude to the Almighty God for helping me throughout my work. I humbly acknowledge the early supervision by Prof. Humeyra Caglayan and the resources provided through her research group. These resources enabled me to perform the work done in this thesis. I also thank Prof. A. Priimägi and the faculty of engineering sciences for the experimental and facility support in my academic journey. I would also like to thank Prof. Marco Ornigotti and Dr. Mikko Huttunen for their supervision and help during the final stages of my thesis.

I also thank the members of my thesis committee, Prof. Mika Valden, Prof. Michele Celebrano, and Dr. Sebastian A. Schulz as my pre-examiners, for their valuable insights, constructive feedback, and helpful suggestions during the last development of my thesis and my opponent Prof. Nathaniel Kinsey.

I am grateful as well to my colleagues and friends in the engineering and science department at Tampere University for creating a supportive and collaborative environment in which to conduct my research. In particular, I would like to thank S. Chervinskii, M. Mekhael, D. Briukhanova M. Habib, Lucero C. Razo, N. Zia, and the nonlinear optics group members for their helpful discussions and for always being willing to lend a helping hand. Much thanks to S. Lehtimäki and M. Koskinen for their help and guidance in the lab and cleanroom activities.

Finally, I want to express my love and appreciation to my family for their unwavering support and encouragement. Without their love and encouragement, I would not have been able to complete this journey.

Thank you!

Tampere, 10.10.2023

Ibrahim Issah

ABSTRACT

The study of metamaterials, materials engineered with specific subwavelength nanostructures, has led to a significant advancement in light-matter interactions, with numerous applications in optics and photonics. These materials have fascinating optical properties that can be tailored to achieve desired values, making them useful in energy harvesting, sensing, and quantum computing. This thesis explores some of these interesting applications in both classical and quantum regimes, focusing on the resonance and epsilon-near-zero (ENZ) properties of these metamaterials and their coupling capabilities with emitters. The study begins with a discussion of a lithography-free metal-insulator-metal structure, its resonance properties, and its coupling capabilities with emitters. This simple structure led to the discussion of more complex polymer-based hyperbolic metamaterials with hyperbolic dispersion relations, high- k modes, ENZ properties, and coupling mechanisms with emitters. The study also covers cylindrical metamaterials fabricated using a self-rolling technique to obtain a 3D rolled-up multilayered waveguide. This cylindrical medium served as the basis to extend the study into the quantum regime, where the interaction of light with a single quantum system is weak and difficult to control. The thesis investigates the concept of such a cylindrical medium that can sustain the quantum properties of distantly spaced qubits, which is essential for practical implementations. It also introduces the fabrication of a rolled-up zero-index waveguide with ENZ properties, which illustrates the existence of unique extended modes that can be integrated with emitters to exhibit interesting light-matter interactions. The thesis concludes by investigating the ENZ properties of spherical nanoparticles using the effective medium approach to model the optical response of a multilayered sphere as an effective bulk spherical medium. The results of this study demonstrate the potential of planar multilayered structures, spherical nanoparticles, and cylindrical rolled-up waveguides for various classical and quantum applications, including optical filtering, radiative engineering, quantum communication, and superradiance.

CONTENTS

1	Introduction	1
1.1	General overview	1
1.2	Research objectives and the scope of this work	2
2	Multilayered metamaterials	5
2.1	Background and optical properties of metamaterials	5
2.1.1	Asymmetric Fabry–Pérot-like cavity	7
2.1.2	Spectral changes via temperature and humidity control	11
2.1.3	Enhancing spontaneous emission in metamaterials	14
3	Planar metamaterial	17
3.1	Hyperbolic media	17
3.1.1	Building blocks of hyperbolic media	20
3.1.2	Hyperbolic media optical response	22
3.1.3	High- k modes origin in a hyperbolic media	25
3.1.4	Photonic density of states	27
3.2	Epsilon-near-zero features of hyperbolic media	29
3.2.1	Structure design and modeling	30
3.2.2	Sample fabrication and characterization	31
3.2.3	Results and discussion	33
3.2.3.1	Spectral response of the polymer-based hyperbolic metamaterial	34
3.2.3.2	Luminescence and lifetime measurement	36
3.2.4	Summary	38

4	Cylindrical metamaterial	39
4.1	Rolling mechanism	39
4.1.1	Strain engineering techniques	41
4.1.2	Release mechanism	43
4.1.3	Two-step lithography technique	44
4.2	Applications	46
4.2.1	High-resolution imaging	46
4.2.2	Enhanced scattering properties	48
4.3	Near-zero-index feature of a cylindrical media	53
4.3.1	Quantum extension	56
5	Spherical metamaterial	67
5.1	Spherical nanoparticle	67
5.2	Epsilon-near-zero properties	69
5.2.1	Results and discussion	71
5.2.2	Summary	75
6	Summary and future work	77
	References	81
	Appendix A Appendix	101
	A.1 Transfer matrix method	101
	A.2 List of other publications	104
	Publication I	109
	Publication II	121
	Publication III	135
	Publication IV	149
	Publication V	159

List of Figures

- 2.1 Multilayered structures (planar, spherical, and cylindrical) for enhanced light-matter interactions. The planar unstructured patterns are shown on the left side which illustrates the three-layered metal-insulator-metal (MIM) structure and its hyperbolic metamaterial (HMM) counterpart. The middle part depicts the cylindrical rolled-up structures counterparts where classical and quantum formulations were utilized to comprehend their optical and quantum properties and the right far-end shows the multilayered metamaterial in the spherical regime. 7
- 2.2 Top: schematic of the hydrogel MIM structure in a) *dry* and b) *wet* states. The inset graph illustrates the corresponding changes in the reflectance spectra between these two states. Bottom: images of the NIR and VIS samples in c) *dry* and d) *wet* states. Adapted from [P1]. 10
- 2.3 a) Calculated reflectance of MIM structure for different thicknesses of the hydrogel insulator layer. Note the presence and tunability of the several resonant orders. b,c) Electric field amplitudes for an MIM with a 300-nm thick hydrogel layer at 1082 nm (b) and 568 nm (c). Adapted from [P1]. 11
- 2.4 Reflectance spectra at varied environmental conditions: a,b) VIS sample, c,d) NIR sample. a,c) Time dependencies of the reflectance spectra, time steps II - VI are 3 hours (a) and 6 hours (c). The sample temperature and relative humidity of the environment at different times are shown in the bars at top of the graph. b,d) Reflectance spectra at the end of each time step. Adapted from [P1]. 12

2.5	Dependence of the resonant wavelengths on a,c) humidity (at ambient temperature) and b,d) temperature (at 80% rel. humidity) for a,b) VIS and c,d) NIR samples. Note the different vertical scales in c, and d before and after the break. Lines are for eye-guiding only. Adapted from [P1].	13
3.1	Isofrequency contour for (a) isotropic and (b) anisotropic media. . . .	19
3.2	Hyperboloid isofrequency surface for a uniaxial medium with an extremely anisotropic dielectric response for (a) Type I and (b) Type II medium. They both can support waves with infinitely large wavevectors in the effective medium limit. However, such waves in a vacuum are evanescent and decay exponentially.	20
3.3	Uniaxial media schematic depicting alternating layers with permittivities ϵ_1 (dielectric) and ϵ_2 (metal) with thicknesses t_1 (t_d) and t_2 (t_m) and permittivity components $\epsilon_{ }$ and ϵ_{\perp} . (a) 3D schematic and (b) 2D representation with refractive index n	21
3.4	The error plot between TMM calculations (red solid lines) and the comparison between the local (blue dotted lines) and non-local EMT (star symbol) predictions versus the number of periods (N) and the $\theta_{in} = 59.98^\circ$ incident angle for TE polarized waves. Adapted from [73].	24

- 3.5 (a) TMM approach transmission (log scale) heatmap of a 30 nm low loss Ag layer sandwiched between two dielectric half-spaces with its schematic presented as an inset. Even (short-range SPP) and odd (long-range SPP) modes are realized through mode hybridization due to near-field interaction between the SPP at the top and bottom metal surfaces presented as the yellow-colored curve in the inset. Roman numbers I and II represents the core layer with thickness d and the claddings, respectively. (b) Similar heatmap for a 200 nm homogenized Ag-TiO₂ hyperbolic media. The high- k modes, which are the structure's Bloch waveguide modes, are shown by the bright bands in the Type I and Type II HMM areas. 26
- 3.6 (a) Schematic of the Au-PMMA structure consisting of 9 nm thick Au and 29 nm thick PMMA layers. Three polymeric PMMA samples were incorporated with three different dyes each [HMM + 3L dye]. I-M represents the insulator-metal interface. M-I-M represents the metal-insulator-metal interface. (b) similar HMM structure with dye-doped PMMA on the top layer [HMM + 1L dye]. (c) schematic of the MIM structure. (d) similar representation of dye-doped PMMA on top of the 9 nm Au layer [IL Au + 1L dye]. Adapted from [P2]. 31
- 3.7 Experimental setup schematic for spectral response measurement by altering the left-hand configuration with a broadband optical source and removal of filters as they are required for the case of PL and fluorescence lifetime measurement. M, mirror, BS, beam splitter, L, lens, DM, dichroic mirror, and the rotating sign below the sample stage signifies a motorized scanning stage. 32

3.8 Dispersion relation of the polymer-based structure exhibiting high- k modes and the associated photonic density of states (PDOS). (a) Transmission of evanescent waves in logarithmic scale through the three bilayers of Au (9 nm)-PMMA (29 nm) multilayered structure using the local EMT approach. In the local effective medium limit, there are infinite high- k waves in a Type-II HMM due to the existence of strong spatial dispersion effects which can be corrected using the non-local EMT approach presented in (b). (c) Similar dispersion relation using the TMM approach. In this realistic case, the size of the unit cell imposes a cut-off to the tunneling of the high- k modes in the structure. (d) The corresponding PDOS of the polymer-based HMM composite using the TMM approach. Adapted from [P2]. 33

3.9 (a) P-polarized field (E_p) distribution through the HMM composite as a function of spectral wavelength. I-M corresponds to the insulator (PMMA) and metal (Au) interface. (b) Real [$\text{Re}(\varepsilon_{\parallel})$, $\text{Re}(\varepsilon_{\perp})$] and imaginary $\text{Im}(\varepsilon_{\parallel})$ permittivities from local EMT, experimentally retrieved effective permittivity $\text{Ext}(\varepsilon_{\parallel})$ [dashed lines] and the figure of merit (FOM) of the polymer-based HMM composite. ENZ wavelength is defined as the spectral wavelength where the structure permittivity crosses zero. (c) Spectral response of the polymer-based HMM material. Reflectance R and transmittance T acquired both numerically (using TMM) and experimentally (R_{Exp} , T_{Exp}). The inset depicts the experimentally measured transmission in the presence of a pump source T_{pump} and without a pump source T . Adapted from [P2]. 35

4.1	(a) Bending schematic of a thick substrate owing to tensile strained (top) and compressed (bottom) thin film. (b) Bent bilayer film schematic with a radius of curvature R and a strain gradient. (c). Numerically predicted diameters of a rolled-up structure composed of a metal (Au) and dielectric (SiO_2)	40
4.2	(a) Upward self-rolling process schematic based on the non-epitaxial technique. (b) A rolled-up and ready cylindrical metamaterial schematic.	42
4.3	(a) Microscope and scanning-electron microscope image (b) of the full rolled-up nanostructure from the top and from the side (c) showing also the cross-section with a diameter of 700 nm. The green scale bar is 9 and $10\mu\text{m}$ for the microscope and scanning-electron microscope, respectively. Adapted from [P3].	45
4.4	(a) Cylindrical wave basis expansion of a plane wave scattered by an object (in green). Low electric field intensity areas are depicted in light blue, whereas high electric field intensity areas are displayed in deep blue. (b) High angular momentum modes in an isotropic cylindrical medium and (c) in an anisotropic cylinder made of an effective hyperbolic medium with dielectric permittivities having different signs in the tangential and radial directions ($\varepsilon_\theta > 0$, $\varepsilon_r < 0$). (d) Front-view cross-section of a possible practical realization of a hyperlens, consisting of alternating concentric metal and dielectric layers. Adapted (a), (b), (c) from [145].	47
4.5	(a). NSCS spectra for cylinder-shaped silver, TiO_2 and CHMM, with a similar outer diameter. (b). A density map of NSCS as a function of wavelength and the dielectric permittivity for CHMMd. (c) and (d). Resonance modes overlap for CHMMd and TiO_2 . Adapted from [150].	50

- 4.6 (a). The dispersion relation of a cylindrical hollow waveguide with different core diameters D . The black circular inset represents the schematic of the homogeneous circular waveguide. (b). The dispersion relation of the rolled-up zero-index waveguide (solid lines) [grey circular inset]. The dotted lines in (b) show similar dispersion calculated for the cylindrical hollow metallic waveguide [yellow circular inset]. The cutoff wavelength varies as a function of D in both figures (top panel). (c). The different electric $|E|$ field mode profiles excited in the rolled-up zero-index waveguide for different effective indices (n_{eff}) with $n_{\text{eff}} \simeq 0$ depicting the fundamental TE_{11} mode. Adapted from [P3]. 55
- 4.7 Schematics depicting (a) the mode propagation trends in a conventional and epsilon-near-zero (ENZ) medium. The inset in (a) depicts the quantum emitters. (b) qubit-qubit interactions in free space and (c) show similar interactions in a rolled-up ENZ waveguide. 56
- 4.8 Schematics of (a) rolled-up ENZ, and (b) rectangular ENZ waveguide with their corresponding cross-section in the x-y plane. E_1 and E_2 represent the two quantum emitters interacting with the corresponding ENZ waveguides. (c) The electric $|E|$ and magnetic $|H|$ fields of the fundamental TE_{11} mode (zero-index mode) of the rolled-up ENZ waveguide, and (d) the fundamental TE_{10} mode (zero-index mode) of the rectangular ENZ waveguide. Reproduced from [P4], with the permission of AIP Publishing. 57

4.9	Normalized decay rate enhancement γ_{12}/γ and dipole–dipole interaction g_{12}/γ as a function of normalized interatomic emitter distance r_{12}/λ_0 of (a) rolled-up ENZ waveguide and (b) rectangular waveguide. The measure of entanglement as a function of concurrence C for (c) rolled-up ENZ tube and (d) rectangular ENZ waveguide. Adapted from [P4].	61
4.10	Dynamics of the density matrix elements for qubits under external pumping. (a), (c), and (e) Population dynamics of qubits inside the rolled-up ENZ waveguide. (b), (d), and (f) Similar dynamics of qubits inside the plasmonic rectangular waveguide at different pump intensities. Adapted from [P4].	63
4.11	Two pumps steady-state entanglement at different inter-atomic distance r_{12}/λ_0 for (top panel) rolled-up ENZ waveguide and (bottom panel) rectangular waveguide. Adapted from [P4].	65
4.12	(a) Rolled-up nanomembranes embedded with quantum emitters labeled as [A, B, C, D] (b) Photoluminescence (PL) spectra of the NV-centers at label C on the rolled-up tube inset. (c) PL heatmap of the rolled-up tubes with bright spots depicting the location of the NV centers embedded.	66
5.1	Metallic nanoparticles polarization depicting the classical interpretation of the excitation of plasmons.	68
5.2	Schematic representation of the bi-layer spherical NP. a_2 and a_1 denote the inner and outer radius of the sphere. The inner, dark blue, sphere represents the dielectric core (SiO_2) of the NP, while the outer, light blue, shell represents the Ag coating. Adapted from [P5].	69

5.3	Effective permittivities of different bilayer spheres and their characteristic ENZ wavelengths, (a) $a_{2,1} = \{38, 40\}$, (b) $a_{2,1} = \{68, 70\}$, and (c) $a_{2,1} = \{98, 100\}$ nm. (Re) and (Im) denote the real and imaginary parts of effective permittivity. The ENZ wavelengths are marked with red dashed lines. Adapted from [P5].	71
5.4	The electric field distribution for the bilayer structure, $a_{2,1} = \{98, 100\}$ nm at the ENZ wavelength. (a) The actual bilayer structure, and (b) the bulk effective medium structure. (c) The difference in the near-field distribution between (b) and (a). Adapted from [P5].	72
5.5	(a) Absorption and (b) Scattering cross-sections for the bilayered spherical NP with full permittivity (solid lines) and effective permittivity (dashed lines) for radii $a_{2,1} = \{38, 40\}$ nm, $a_{2,1} = \{68, 70\}$ nm, and $a_{2,1} = \{98, 100\}$ nm. The values in the legend denote the radius values of the inner and outer spherical layers. Adapted from [P5].	73
5.6	ENZ wavelengths calculated for three different structures of a set of SiO ₂ layers, with varying thicknesses (d). The SiO ₂ inner core and the Ag layers in between are fixed with a radius of $a_2 = \{98\}$ nm and a thickness of 2 nm. The compositions of the multilayer nanospheres are schematically presented with red (SiO ₂) and gray (Ag) circular layers, next to the relevant λ_{ENZ} plots, corresponding to 2 (blue), 4 (red), and 6 layers (green), respectively with thickness d values ranging from $\{10 - 60\}$ nm. Adapted from [P5].	74

List of Tables

- 3.1 Lifetime measurements of the three dyes on a fused silica substrate, on 9 nm gold (Au) layer and, on top of the HMM structure and embedded within the polymer-based HMM structure. Adapted from [P2]. 37
- 5.1 The ENZ NP with their characteristic ENZ wavelengths as well as their corresponding resonance wavelengths. Adapted from [P5]. . . 73

ABBREVIATIONS

AIBN	Azobisisobutyronitrile
C	Concurrence (measure of entanglement)
CHMM	Cylindrical multilayered metamaterial
CL	Cathodoluminescence
DI	Di-ionized
EMT	Effective medium theory
ENP	Epsilon-near-pole
ENZ	Epsilon-near-zero
FDTD	Finite-difference time-domain
FEEM	Finite-element eigenmode
FEM	Finite-element method
FOM	Figure of merit
FP	Fabry–Pérot
FWHM	Full width at half maximum
HBT	Hanbury Brown and Twiss
HF	Hydrogen fluoride
HMDS	Hexamethyldisilazane
HMM	Hyperbolic metamaterial
IFC	Isofrequency contours
IPA	Isopropanol
LCST	Lower critical solution temperature

LDOS	Local density of state
LH	Left handed
LSPR	Localized-surface plasmon resonance
MBE	Molecular beam epitaxy
MIM	Metal-insulator-metal
MIMS	Metal-insulator-metasurface
NA	Numerical aperture
NSCS	Normalized scattering cross section
NV	Nitrogen vacancy
OEMA	Operator approach to effective-medium approximation
PDOS	Photonic density of state
PL	Photoluminescence
PMMA	Polymethyl methacrylate
PMMs	Periodic multilayered metamaterials
PNIPAm-BP	N-isopropylacrylamide - acrylamidobenzophenone copolymer
PRR	Two-photon detection probability
PYR	Pyromethene
QD	Quantum dots
QED	Quantum electrodynamics
RhB	Rhodamine B
rpm	Revolutions per minute
RTMM	Recursive transfer matrix method
SE	Spontaneous emission
SEM	Scanning electron microscopy
SPAD	Single-photon avalanche diode
SPP	Propagating surface plasmon
TCSPC	Time-correlated single-photon counting

TE	Transverse electric
THz	Terahertz
TM	Transverse magnetic
TMDs	Transition metal dichalcogenides
TMM	Transfer matrix method
UV	Ultraviolet
VPTT	Volume phase-transition temperature
WG	Waveguide
XeF ₂	Xenon Difluoride
XOI	Compound materials on insulator

ORIGINAL PUBLICATIONS

- Publication I S. Chervinskii, I. **Issah**, M. Lahikainen, A. R. Rashed, K. Kuntze, A. Priimagi and H. Caglayan. Humidity- and Temperature-Tunable Metal-Hydrogel-Metal Reflective Filters. *ACS Applied Materials & Interfaces* **13**, 42 (2021), 50564–50572. DOI: 10.1021/acsami.1c15616.
- Publication II I. **Issah**, T. Pihlava, A. R. Rashed and H. Caglayan. Mechanism of emitters coupled with a polymer-based hyperbolic metamaterial. *Opt. Express* **30**, 6 (2022), 8723–8733. DOI: 10.1364/OE.451960.
- Publication III I. **Issah**, M. Habib and H. Caglayan. Long-range qubit entanglement via rolled-up zero-index waveguide. *Nanophotonics* **10**, 18 (2021), 4579–4589. DOI: 10.1515/nanoph-2021-0453.
- Publication IV I. **Issah** and H. Caglayan. Qubit-qubit entanglement mediated by epsilon-near-zero waveguide reservoirs. *Applied Physics Letters* **119**, 22 (2021), 221103. DOI: 10.1063/5.0073134.
- Publication V I. **Issah**, J. Pietila, T. Kujala, M. Koivurova, H. Caglayan and M. Ornigotti. Epsilon-near-zero nanoparticles. *Phys. Rev. A* **107** (2023), 023501. DOI: 10.1103/PhysRevA.107.023501.

Author's contribution

- Publication I The author contributed as a co-author in performing the numerical modeling, fitting of the experimental data and helped in writing of the manuscript. S.Ch. fabricated the samples, performed environmentally controlled measurements, analyzed the data, and wrote the main manuscript. M.L. and K.K. prepared the PNIPAm-BP material. A.R.R. performed spectral measurements. A.P. and H.C. supervised the project.
- Publication II The author contributed as a lead author in performing the numerical modeling, fabrication, characterization, analyses of the experimental data, and the writing of the manuscript. T.P. helped in the fabrication and characterization of the samples. A.R. R. contributed to the design of the sample. H.C. steered the project.
- Publication III The author contributed as a lead author in performing the numerical modeling and writing of the manuscript. M.H. helped in the fabrication of the samples. H.C. steered the project.
- Publication IV The author contributed as a lead author in performing the numerical modeling and writing of the manuscript. H.C. steered the project.
- Publication V The author contributed as a lead author in performing the numerical modeling and the analyses of the numerical data as well as writing of the manuscript. J. P. and T.K. helped in the numerical modeling. M.K. and M.O. contributed in developing the mathematical formulations. All authors contributed in the writing of the manuscript. H.C. and M. O. supervised the project.

1 INTRODUCTION

1.1 General overview

The ability to shape and process materials to achieve desired properties has played a prominent role in modern civilization and development. The interaction of these materials with electromagnetic radiation has led to a better understanding of their chemical (atomic) compositions. Based on these compositions, different materials are enriched with different electromagnetic properties, such as unique electric permittivity and magnetic permeability. However, conventional electromagnetic structures face limitations in their design and production, depending on the accessibility of materials [1]. These limitations may make certain desired properties unattainable.

For some time now, a new class of engineered materials has come to the forefront of photonics research, where the artificial nanostructuring of such materials determines the fundamental properties governing their interactions with electromagnetic radiation, rather than their atomic compositions. These engineered materials coined as metamaterials (from the Greek word: *meta*, meaning *beyond*, i.e., beyond conventional material properties) exhibit well-arranged functional nanostructuring with a pitch size smaller than its corresponding incident radiation wavelength [2]. Metamaterials derive their interesting properties from their subwavelength nanosized orientations and their resonant properties when interacting with electromagnetic radiation. The field of metamaterials has quickly developed, involving researchers from different disciplines, and has enabled the consistent development of artificially engineered materials with atomic-level precision and accuracy.

Among these metamaterials, thin film synthesis and its applications, as well as their assembly to form multilayered structures, have attracted a lot of attention due to their interesting optical properties and dispersion relations. Their interactions with electromagnetic fields could play a prominent role in spectroscopy, sensing, and quantum information processing, as these artificially engineered material patterns

can manipulate how light is confined, focused, reflected, or transported.

1.2 Research objectives and the scope of this work

This thesis is a self-contained and comprehensive work that reviews the publications (P1–P5) to comprehend the interaction of electromagnetic radiation and engineered multilayered structures from planar through to spherical nanoparticles, to three-dimensional (3D) cylindrical structures, as well as clarify and expand upon their interesting classical applications and quantum extensions. The research questions addressed include the mechanisms that enhance these interactions, and how the unusual properties of these engineered materials and their coupling capabilities can be used for novel light-based technologies such as communications, energy harvesting, spectral filtering, and sensing, as well as the possibility of using the effective-medium approach to model the optical responses of a multilayered structure in the spherical domain. The text is divided into six (6) chapters which detail different concepts but are intimately connected to one another. Each chapter will be introduced and concluded independently.

Chapter 2 provides an overview of the fundamental concepts of photonics-based multilayered metamaterials. This includes a discussion of planar asymmetric Fabry–Pérot-like cavity structures and their relationship with emitters for spontaneous emission mechanisms, as presented in Publication 1 (P1). The section begins by reviewing a class of metamaterials with few-layered planar stacks that offer functionality similar to bulk metamaterials but in a more compact, lighter, and loss-efficient manner (i.e., with lower Q-factors). Specifically, a simple polymer-based metal–insulator–metal structure is discussed, which is responsive to environmental changes and has various optical applications. This structure is further explored in Ref. [3], one of our recent works, where its fluorescence modulations when coupled with emitters are detailed. This simple metal–insulator–metal structure paved the way to extend the discussion towards multilayered structures in chapter 3. As such, the discussion then shifts towards multilayered structures, forming the so-called polymer-based hyperbolic metamaterials (HMM) in P2. The chapter explores the epsilon-near-zero (ENZ) features of these structures and provides a detailed explanation of the fundamental equations and their sequential formulations required to determine the interesting features of the multilayered structures. Furthermore, chapter 3 reports on the

schemes used to experimentally characterize the different optical features of the multilayered structures, as well as the numerical methods implemented to attain results in **P2**. Overall, this section provides a comprehensive overview of the fundamental concepts and properties of planar multilayered metamaterials, including both their theoretical foundations and practical applications.

After identifying the distinctive properties of the planar multilayered thin films and some of their unique photonic applications, the thesis is extended to cylindrical multilayered structures in chapter 4, where their unique photonic properties and quantum extension are exploited in **P3** and compared with other plasmonic waveguides in **P4**. In this chapter, the different strain engineering technique utilized to attain a more robust 3D fabrication of this structural morphology is introduced and compared to the multilayer-planar part which is quite strenuous due to its fabrication procedure. Also, some interesting classical applications and their extension into the quantum regimes are discussed by utilizing the cylinder-shaped structure as waveguide reservoirs for quantum emitters.

From the discussions on the planar and cylindrical geometries, the work is further extended towards the spherical nanoparticles domain to look at some of its potential applications and ENZ features in **P5**. Chapter 6 details the concluding remarks with a summary of the main results. Some possibilities for future works are also discussed. Overall, the research detailed in this thesis will have a far-reaching relevant impact on the photonics industry in both classical and quantum regimes. The results redefine the range of light-matter interactions and elucidate the potential photonic applications of multilayered metamaterials.

2 MULTILAYERED METAMATERIALS

2.1 Background and optical properties of metamaterials

Over the past decades, the design, synthesis, characterization, and applications of materials at the nanoscale, have been a major area of research focus. This is because materials at the atomic scale, possess interesting physical and chemical properties as stated earlier. By engineering these nanoscale features of a material, one can create distinctive electromagnetic properties, leading to an increased interest in metamaterials, which are man-made materials with structural units known as meta-atoms or meta-molecules, significantly smaller in size and periodicity than the incident wavelength being considered. These meta-atoms possess inhomogeneities, but the whole material is seen as macroscopically uniform. The response of metamaterials to electromagnetic radiation is then mainly determined by diffraction and interference effects. However, larger inhomogeneity scale responses of such materials are typically described using geometric optics.

To date, different metamaterials with remarkably-tailored optical functionalities across the electromagnetic spectrum have been developed. However, the surge of interest in this research field can not be mentioned without appreciating some seminal papers that laid down their foundation of the modern metamaterials era. To start with, is the theoretical prediction of the possibility of left-handed (LH) metamaterials or negative refractive index metamaterials reported by Veselago [4, 5]. His paper detailed an unusual phenomenon, where the electric, \mathbf{E} , magnetic, \mathbf{H} , and the wave, \mathbf{k} vectors form a LH system. His work showed that, the required material parameters to help in achieving such an unusual phenomenon, is when a material simultaneously exhibits both negative values of permittivity ϵ and permeability μ . Smith et al. [6] then made a huge leap by experimentally validating the theoretical formulations of Veselago. Pendry's work [7] on the perfect lens also elucidated an exciting application of novel metamaterials. Notably, all the pioneering works on

metamaterials were based on negative refraction; however, the research focus has expanded beyond this limit in recent times. Various engineered metamaterials are now demonstrating uncommon electromagnetic properties that are not seen in naturally occurring materials and cannot be obtained by conventional synthesis techniques.

These unique electromagnetic properties of metamaterials are classically bound by Maxwell's equations. The equations describe the relationship between material properties, their considered fields, and optical sources. The material properties, in particular, are mainly determined by their permittivity ϵ and permeability μ . These properties describe the interactions of a material with the electromagnetic components of a classical wave and could be utilized to classify materials into metal, doped semiconductors, transparent dielectrics, metamaterials, and ferromagnetic materials.

Conventional materials such as dielectrics typically possess positive values of ϵ and μ , whereas, noble metals at optical frequencies exhibit negative values of ϵ [$\epsilon < 0$, $\mu > 0$]. In addition, ferromagnetic media near resonance exhibit negative μ [$\epsilon > 0$, $\mu < 0$]. These variations in material property values determine the orientation of field quantities when propagated in these electromagnetic media [8]. Also, as the index of refraction n , is dependent on these material parameters $n = \sqrt{\epsilon\mu}$, one negative parameter leads to an imaginary index n , and as such, no propagating wave is supported in such mediums. However, when both material parameters are negative [$\epsilon < 0$, $\mu < 0$], the index exhibits a negative sign, which does not occur in conventional materials. This novel feature can exist in engineered materials and thereby exhibit interesting optical phenomena such as inverse Doppler effect [9], reversed Cherenkov radiation [10], perfect lens [7], and backward wave propagation, to mention a few.

Among the many relevances of engineered metamaterial stem planar, cylindrical, and spherical multilayered structures. This is in the pursuit of enhancing the weak interaction between light and matter and allowing for a richer design space for photon control and manipulations which is the focus of this work. As such, we artificially designed various metamaterials, shown in Fig. 2.1, from planar thin-films to their spherical regime to uncover their electromagnetic responses and distinctive ENZ properties. We also utilized some of these engineered planar structures as sub-wavelength cavities to elucidate the mechanisms of emitters when coupled to them. This pursuit of enhancing light-matter interactions in multilayered structures is then extended into the quantum regime by developing and engineering unique cylindri-

cal multilayered structures to help sustain the quantum properties of qubits coupled to them. After elucidating the distinctive properties of the planar and cylindrical structures, we geared towards a multilayered spherical configuration to explore their interesting optical responses.

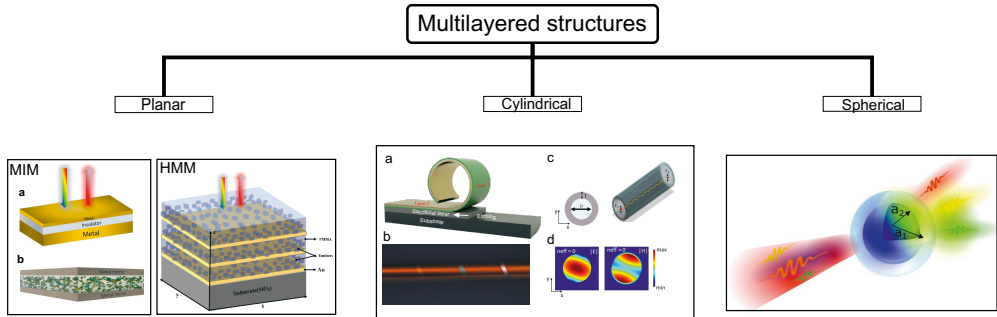


Figure 2.1 Multilayered structures (planar, spherical, and cylindrical) for enhanced light–matter interactions. The planar unstructured patterns are shown on the left side which illustrates the three-layered metal–insulator–metal (MIM) structure and its hyperbolic metamaterial (HMM) counterpart. The middle part depicts the cylindrical rolled-up structures counterparts where classical and quantum formulations were utilized to comprehend their optical and quantum properties and the right far-end shows the multilayered metamaterial in the spherical regime.

2.1.1 Asymmetric Fabry–Pérot-like cavity

To unravel some of the interesting capabilities of planar multilayer structures and their response to electromagnetic radiation, we begin the thesis discussions by examining a three-layer-based metal–insulator–metal (MIM) structure. These structures are lithography-free nanostructures that rely on thin film depositions and/or bottom-up self-assembly. They are worth exploring as an alternative candidate for spectral engineering of optical properties controlled by layer thicknesses instead of an in-plane nanostructure size in plasmonic nanomaterials or optical metasurfaces which requires lithography techniques. As such, the effort to fabricate continuous, unstructured thin films involving planar surfaces are relatively promising and paves way toward low-cost large-area fabrication of photonic devices.

Figure 2.1 (a) under the planar structure of the multilayer hierarchy block list (MHBL) shows a typical MIM structure. The bottom layer of such a planar structure is typically designed to be an optically thick metal layer that is significantly thicker than the metal’s skin depth for complete zero transmission. The middle insulator

layer can also be chosen among different conventional dielectric materials because the refractive index of the dielectric is an important parameter in determining the resonance frequency of a cavity mode [11]. The top layer is designed to be optically thin, enabling incoming light to couple into the MIM cavity and then trapping light inside it with back-and-forth reflections from the metals. With each reflection in this asymmetric Fabry–Pérot cavity, the trapped light is partially absorbed, which finally results in enhanced absorbance. The equation that governs the resonance mode of such asymmetric Fabry–Pérot cavity created by this MIM device at normal incidence optical radiation is of the form [12]:

$$2\left(\frac{2\pi}{\lambda_{\text{res}}}\right)n_i d_i + \phi_b + \phi_t = 2\pi m, \quad (2.1)$$

where λ_{res} is the resonance wavelength, n_i and d_i are the refractive index and thickness of the middle dielectric layer, respectively, and m is an integer number that determines the order of cavity mode. The phase shifts obtained from the bottom and top metal layers are denoted by ϕ_b and ϕ_t , respectively. According to Eq. (2.1), higher-order cavity modes (m) resonate at smaller wavelengths due to their inverse relations. Notably, by increasing the n_i and d_i of the MIM structure, the resonant wavelength λ_{res} increases as well. Thus, the resonance wavelength red-shifts as the optical beam path expressed as $n_i d_i$, increases. As such, the wavelength of the resonantly absorbed optical field incident on a MIM structure is directly related to the insulator thickness of the structure as well as its dielectric properties. Therefore, one may employ dielectrics with various refractive indices or use an active mechanism to change its thickness following the desired absorption band to vary the center of the absorption band.

In recent times, there have been many advancements in using MIM structures as color filters in reflection or transmission [13–15], as well as researching other MIM-based applications [16, 17]. Researchers have shown interest in making MIM structures actively tunable, widening their applicability in light–matter interactions, and integrated optical devices [18] as well as electro-optical tuning mechanisms applications [19]. One approach is to use stimuli-responsive insulator layers that can actively alter the thickness or refractive index, thereby shifting the resonance of the MIM structure [20, 21]. Some examples of such materials are hydrogels and poly [methyl methacrylate] (PMMA), which respond to various stimuli and have the po-

tential to incorporate organic dye molecules (emitters) for improved light–matter interactions [22–25].

In the case of hydrogels, they swell remarkably in the presence of water and are responsive to humidity change, which increases the hydrogel’s volume. Secondly, some hydrogels exhibit a reversible volume phase transition at lower critical solution temperature (LCST) of the monomers crosslinked into the gel [26]. For gels, this temperature is also known as volume phase transition temperature (VPTT). This phase transition results in changing hydrogels from hydrophilic to hydrophobic above the transition temperature, which leads to the expulsion of previously absorbed water and the respective reduction in the hydrogel’s volume. These two volume–tuning mechanisms in hydrogels work oppositely – increasing humidity causes the hydrogel to absorb water and swell while increasing temperature causes it to expel water and contract [27]. These properties have brought hydrogels into the field of tunable plasmonic materials [28–33], structural coloration [34–36], and other optical elements [37–42]. PMMA as a prominent alternative in MIM structures is also responsive to organic vapor (saturated ethanol (EtOH) vapors) and induces polymer swelling when coupled to it. They reversibly interact with EtOH through hydrogen bonding and swell in the presence of these vapors [43]. PMMA are thereby, a potential synthetic polymer candidate that could be utilized in unstructured planar structures for active and tunable manipulation of emitters’ optical properties when embedded within, for efficient and advanced nanophotonic devices.

In summary, these interesting stimuli-responsive polymers can be designed and integrated into varied multilayered metamaterials to respond to a wide range of environmental signals such as changes in chemical composition, temperature, charge, and pressure, among other signals. Therefore, in this work for **P1**, we report on a bi-stimuli tunable hydrogel-based MIM structure to comprehend their interesting optical properties. We employ a poly(*N*-isopropylacrylamide)-acrylamidobenzophenone (PNIPAm-BP) hydrogel as the insulator layer, which reversibly changes dimensions under temperature and/or humidity stimuli control. The PNIPAm-based hydrogel has a good swelling ratio and good film-forming properties [44]. By applying temperature and humidity stimuli to the PNIPAm hydrogel incorporated into the MIM structure, we obtained continuous spectral tuning.

Figure 2.2 illustrates the schematic of the hydrogel-based MIM structure. The *dry* state, when hydrogel has no water absorbed, corresponds to a thinner hydrogel

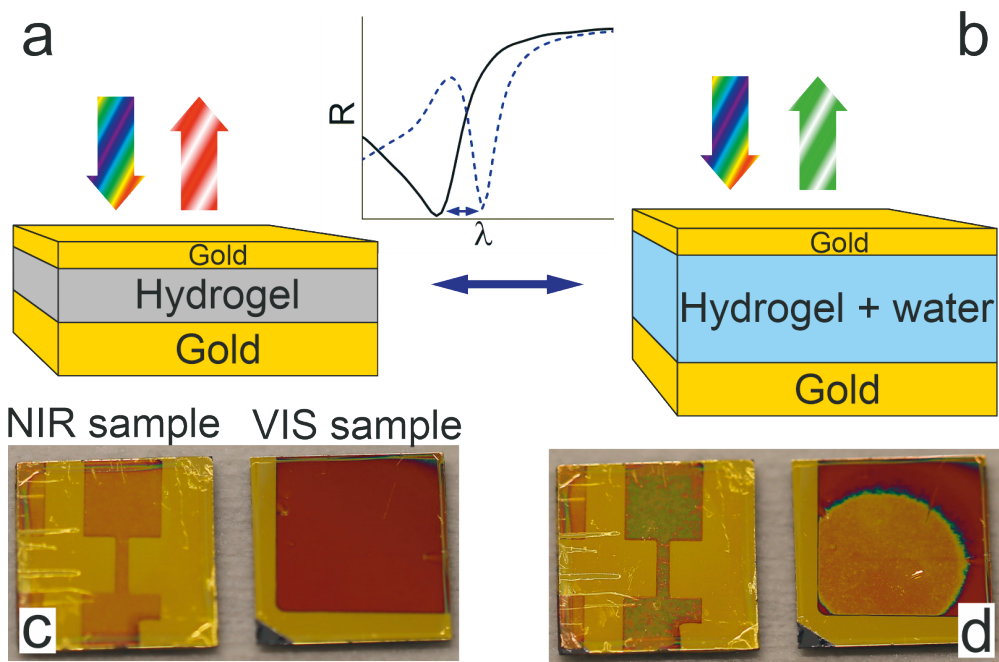


Figure 2.2 Top: schematic of the hydrogel MIM structure in a) *dry* and b) *wet* states. The inset graph illustrates the corresponding changes in the reflectance spectra between these two states. Bottom: images of the NIR and VIS samples in c) *dry* and d) *wet* states. Adapted from [P1].

layer (Fig. 2.2a). When the hydrogel absorbs water (the *wet* state), it swells and the resultant thickness increases (Fig. 2.2b), thereby leading to a corresponding change in the spectra illustrated as an inset in Fig. 2.2. Figure 2.2c,d show how the observable colors of the samples change between these two states. The inhomogeneities in the swelling mechanism of the hydrogel in Fig. 2.2d are due to the presence of local variations in the sputtered gold film porosity, along with defects arising from the spin-coating processes.

To comprehend the optical properties of the proposed hydrogel-based metal-insulator-metal (MIM) structures, mathematical calculations of the structures with different hydrogel layer thicknesses were performed and experimentally confirmed. Notably, it was observed that thicker hydrogel layers resulted in higher-order resonances, as depicted in Fig.2.3a. Specifically, when the thickness exceeded 250 nm, the 2nd order resonance appeared, and at 400–450 nm, the 3rd order resonance appeared, and so on. Comparing the electric field distributions for a 300 nm-thick hydrogel at resonant wavelengths 1082 nm and 568 nm (Fig. 2.3b and c, respectively), it can be

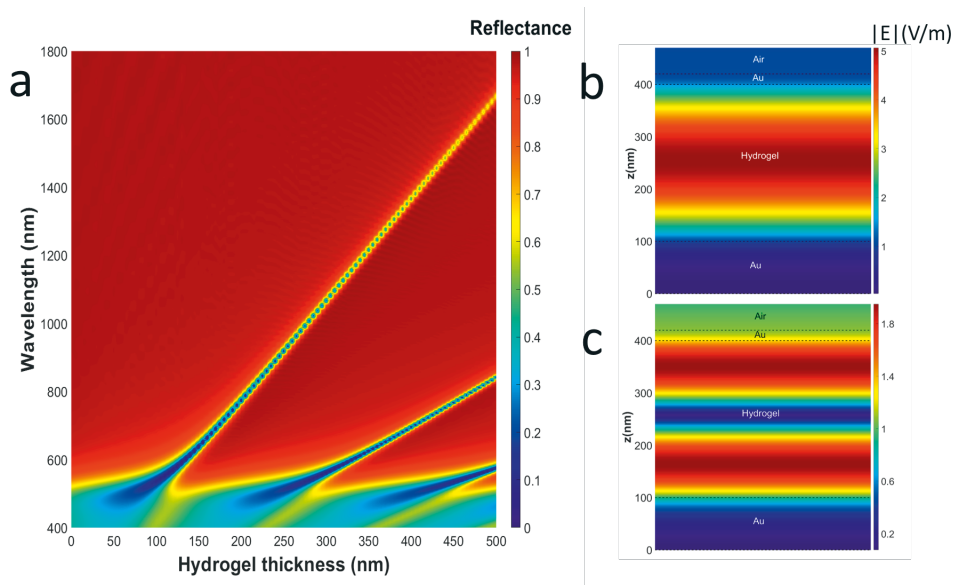


Figure 2.3 a) Calculated reflectance of MIM structure for different thicknesses of the hydrogel insulator layer. Note the presence and tunability of the several resonant orders. b,c) Electric field amplitudes for an MIM with a 300-nm thick hydrogel layer at 1082 nm (b) and 568 nm (c). Adapted from [P1].

concluded that the latter resonance is indeed the second order. Furthermore, these higher-order resonances can be tuned with the thickness change, although with less sensitivity compared to the first-order resonance.

2.1.2 Spectral changes via temperature and humidity control

Furthermore, to establish the continuous and reversible adjustment of the optical resonance in the hydrogel-based MIM structure, a temperature- and humidity-controlled chamber was employed. Reflectance spectra were continuously measured in a controlled environment, and the results are shown in Fig. 2.4. Both humidity and temperature stimuli were found to adjust the resonance wavelength of the MIM structure. As such, an increase in humidity at constant temperature results in hydrogel swelling, which corresponds to the redshift of the resonance of the MIM structure (transition from I to II in Fig. 2.4a,c), and vice versa – decreasing humidity “dries” the hydrogel and blueshifts the resonance (Fig. 2.4a,c V).

Another mechanism, unique to PNIPAm-based hydrogels, relied on the LCST

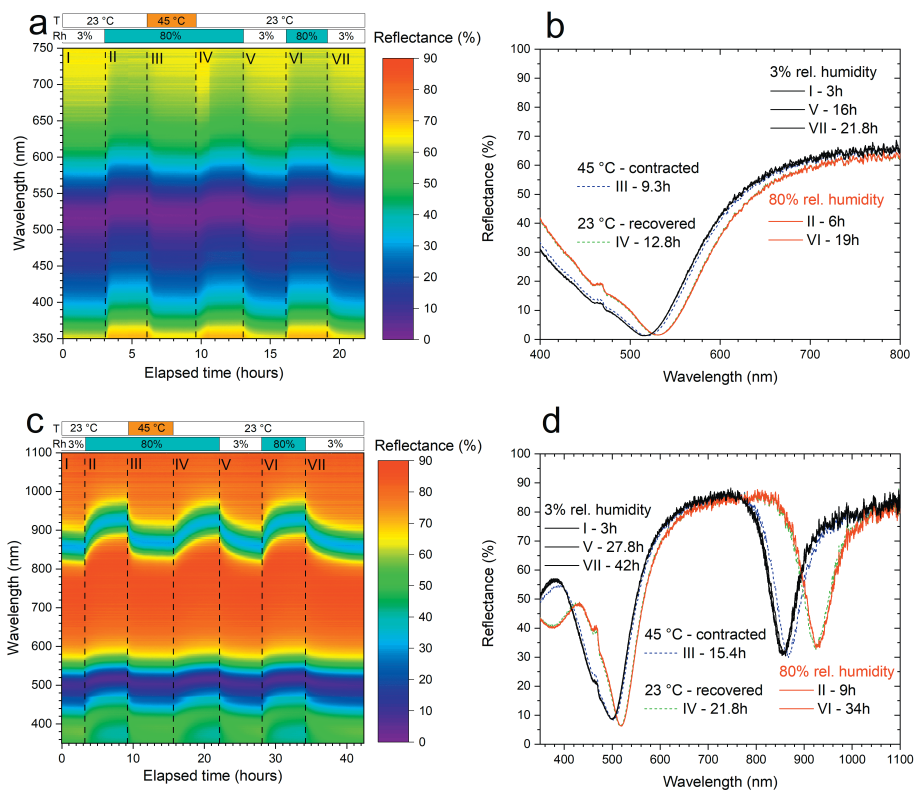


Figure 2.4 Reflectance spectra at varied environmental conditions: a,b) VIS sample, c,d) NIR sample. a,c) Time dependencies of the reflectance spectra, time steps II - VI are 3 hours (a) and 6 hours (c). The sample temperature and relative humidity of the environment at different times are shown in the bars at top of the graph. b,d) Reflectance spectra at the end of each time step. Adapted from [P1].

phase transition at temperatures approximately 32°C , over which the swollen hydrogel shrinks [45]. This process is reversible. To use this mechanism, the temperature of the MIM structure was altered while maintaining a constant humidity of 80% (Fig. 2.4a,c III - IV). At room temperature, the hydrogel was partly swollen at this humidity (Fig. 2.4a,c II). Notably, this transition was faster than the humidity-driven swelling/deswelling (compare the slope in Fig. 2.4c III and V). The reverse effect was also explored, i.e., lowering the temperature (while keeping 80% humidity) moved the resonance back to longer wavelengths (Fig. 2.4a,c IV). One more cycle of humidifying–drying was added to show the reproducibility of the hydrogel swelling/deswelling (Fig. 2.4a,c VI - VII). The spectra at the end of each step I -

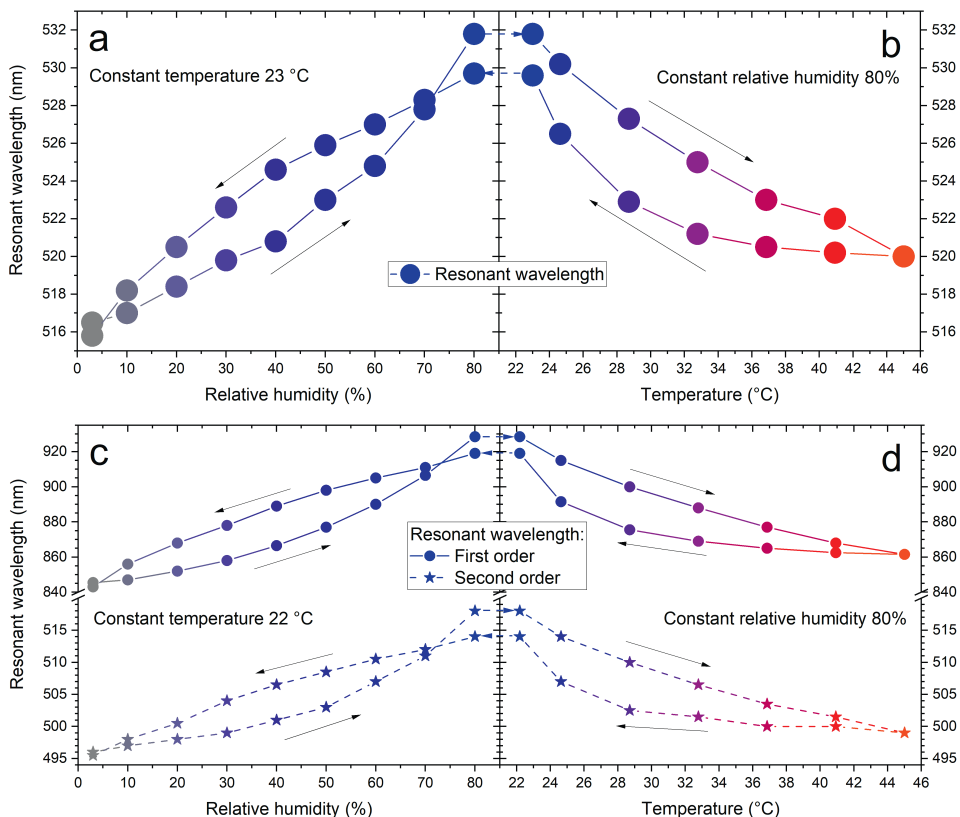


Figure 2.5 Dependence of the resonant wavelengths on a,c) humidity (at ambient temperature) and b,d) temperature (at 80% rel. humidity) for a,b) VIS and c,d) NIR samples. Note the different vertical scales in c, and d before and after the break. Lines are for eye-guiding only. Adapted from [P1].

VII in Fig. 2.4a,c are shown in Fig. 2.4b,d, respectively, illustrating the relative reproducibility of the tuning of the resonance during subsequent swelling-deswelling cycles.

Figure 2.5, on the other hand, shows the dependencies of the resonance in the samples when temperature and humidity are gradually changed between the same extreme values (3–80% RH, 23–45 °C, the system was let to stabilize at each value for 3 hours). Gradual changes in humidity allowed fine-tuning of the resonance with close to linear dependency (0.19 nm/% RH) with almost no hysteresis (Fig. 2.5a,c). At the same time, the temperature-induced changes at high humidity were also continuous, not step-like as one could expect from a phase-transition-induced process,

allowing continuous tuning as well (Fig. 2.5b,d).

These results, in principle, showed evidently, that changes in the thicknesses of a typical MIM structure can change their optical responses which can be tailored to couple with emitters (e.g. organic dye molecules) to enhance light–matter interactions. Figure 2.1 (b) under the planar section of the MHBLL, illustrates such a potential application of MIM structure as a sub-wavelength cavity coupled with organic molecules for enhanced light–matter interactions. Thus, by changing the thicknesses of the MIM structure, the resonance can be tuned across a wide spectral range which can be tailored to couple with the emission or absorption spectral regions of emitters to enhance light–matter interactions in dye molecules emission control. Detailed discussions of this study are presented in Ref. [3]. Nevertheless, we present in section 2.1.3 some discussion on spontaneous emission engineering and a summary of some of the relevant findings in Ref. [3] to elucidate the mechanism of enhanced spontaneous emission of emitters when coupled with MIM cavities. These insights pave the way for further exploration of multilayered thin films (hyperbolic media) in chapter 3 to exploit their interesting optical properties and broadband photonic density of states (PDOS) feature for enhancing spontaneous emission mechanisms.

2.1.3 Enhancing spontaneous emission in metamaterials

To begin with, we can define the process by which a quantum emitter (e.g. organic dye molecules, quantum dots) transitions from an excited state to a lower energy state by releasing energy in the form of a photon as spontaneous emission (SE). This process can be simplified to a two-level system where an emitter in its excited state E_2 spontaneously decays to a lower energy state E_1 by releasing a photon with energy equal to the difference between the two states as:

$$E_2 - E_1 = \hbar\omega, \quad (2.2)$$

where ω is the angular frequency of the photon and \hbar is the reduced Planck constant. The resultant photon has a random phase and is emitted in a random direction. The ability to enhance spontaneous emission of quantum sources (single atoms, ions or molecules, quantum dots, color and nitrogen-vacancy centers in diamond, defects in SiC, defects in monolayer transition metal dichalcogenides (TMDs), electron-hole pairs in quantum wells) is highly desirable in several research areas, including solid-

state lighting, optical communications, quantum computing with single photons, fluorescence imaging, and radiative engineering. Such a quantity relies on the electromagnetic environment in which the quantum emitter is located as well as the dipole moment μ of the transition. According to Fermi's Golden Rule, an excited state with 0 photons $|i, 0_{\mathbf{k}}\rangle$ at the beginning decays into a final state with 1 photon $|f, 1_{\mathbf{k}}\rangle$ of wavevector \mathbf{k} at a rate:

$$\Gamma_{fi} = \frac{2\pi}{\hbar} |\langle f, 1_{\mathbf{k}} | H_{\text{int}} | i, 0_{\mathbf{k}} \rangle|^2 \rho(\hbar\omega_{\mathbf{k}}), \quad (2.3)$$

where $H_{\text{int}} = \mu \cdot \mathbf{E}$ is the Hamiltonian of interaction between the dipole moment and the electric field \mathbf{E} and ρ is the density of states, namely the density of potential final photon states with frequency $\omega_{\mathbf{k}} = \omega_{fi}$, the transition frequency. By properly designing the emitter's surroundings, ρ can be increased in relation to its value inside a homogeneous dielectric medium, which is typically referred to as "free space".

Purcell was the first to quantify the SE rate in a cavity at radio frequencies and the SE rate in free space as $F_p = 3\lambda_0^3 Q / 4\pi^2 n^3 V$ [46] in order to investigate the idea of SE engineering. The quality factor Q and the mode volume V of a cavity with refractive index n are related to the SE enhancement at the resonant wavelength $\lambda = \lambda_0/n$ by the *Purcell factor* F_p formulation. This formalism has been utilized as a figure of merit for optical cavities with micrometric [47] and nanometric size, such as those created by semiconductor pillars coated with metal [48], defects in photonic crystals [49] as well as MIM cavities discussed in Ref. [3].

However, because nanoscale radiation confinement is inexact, Purcell enhancement is extracted either indirectly from lifetime measurements [49] or appropriately by redefining Q and V [48]. In Ref. [3], we illustrated the mechanism of an emitter embedded with an asymmetric Fabry-Pérot-like cavity tailored to couple with the emission and absorption of an emitter incorporated in a stimuli-responsive polymer. From [3], varied resonance response of the MIM cavities lead to different SE enhancement mechanisms of an emitter when coupled to it as well as under humidity controlled environment.

A physical alternative to the constructive interference used in cavities is provided by plasmonics for SE engineering. In the plasmonics regime, typically three competing mechanisms affect the relaxation of an emitter in an excited state when embedded in a dielectric medium coupled with the near-field of a metallic surface. These com-

peting mechanisms are the emission of a photon that propagates in the far field, the generation of lossy surface waves, that account for electron scattering and electron-hole excitation, and the emission of surface plasmon polariton bound to the metal/dielectric interface [50, 51]. The plasmon modes increase the photonic density of states by channeling the emission into k -vectors larger than those accessible with photons ($k > k_0$).

While plasmons and cavities have played significant roles in enhancing the emission response of coupled emitters in photonics applications, they do possess some limitations. These approaches are typically restricted to a narrow spectral range, and achieving enhanced photoluminescence (PL) responses necessitates passive or active adjustments of the spectral resonance to match the absorption and emission spectra of emitters embedded within. In other words, the resonant processes utilized in plasmons and cavities may not sufficiently overlap with the emission spectrum of the dye molecules coupled to it, thereby limiting their effectiveness.

In contrast, the utilization of hyperbolic media presents a potential solution to this limitation. These materials exhibit unique structural properties that will be thoroughly discussed in Chapter 3. By harnessing the properties of hyperbolic media, it may be possible to overcome the challenges associated with the restricted narrow spectral range of plasmons and cavities, thus opening up new avenues for achieving appreciable PL responses without the need for careful positioning of emitters or adjustments of the spectral resonances to match the emission and absorption characteristics of the emitters.

3 PLANAR METAMATERIAL

Multilayered structures composed of alternating subwavelength metal and dielectric layers have gained scientific interest recently due to their unique optical properties, which are useful for a wide range of advanced applications and devices. This surge in interest can be attributed, in part, to the emergence of new concepts such as transformation optics [52, 53], optical imaging [54], and metamaterials [55–59]. Multilayered systems exhibit anisotropic tensor behavior, which leads to interesting structural properties that do not occur naturally. In fact, one can even obtain a hyperbolic dispersion relationship in multilayered systems, where the permittivity along different axes of the medium are different [60]. Overall, the optical properties of metal-dielectric multilayered structures, as illustrated in Fig. 3.3, hold significant promise for advanced applications and devices, which will be discussed in the subsequent sections.

3.1 Hyperbolic media

The idea of a material with hyperbolic behavior originates from the optics of crystals. In such a media, the constitutive relations linking the electric displacement \mathbf{D} and the magnetic induction \mathbf{B} to the electric and magnetic fields \mathbf{E} and \mathbf{H} can be written

$$\mathbf{D} = \varepsilon_0 \bar{\varepsilon} \mathbf{E} \quad (3.1)$$

$$\mathbf{B} = \mu_0 \bar{\mu} \mathbf{H} \quad (3.2)$$

where ε_0 and μ_0 are the vacuum permittivity and permeability, and $\bar{\varepsilon}$ and $\bar{\mu}$ are the relative permittivity and permeability tensors. By considering a naturally occurring medium at the optical frequency with non-magnetic properties, we can assume $\bar{\mu} =$

I , where I is the identity tensor. Upon diagonalization, the permittivity tensor $\bar{\epsilon}$ can be expressed as

$$\bar{\epsilon} = \begin{bmatrix} \epsilon_{xx} & 0 & 0 \\ 0 & \epsilon_{yy} & 0 \\ 0 & 0 & \epsilon_{zz} \end{bmatrix} \quad (3.3)$$

in Cartesian coordinates with orientation along the principal axes of the media. The three diagonal components are all positive, and in general dependent on the angular frequency ω . The crystal is termed biaxial when $\epsilon_{xx} \neq \epsilon_{yy} \neq \epsilon_{zz}$, uniaxial when $\epsilon_{xx} = \epsilon_{yy} \neq \epsilon_{zz}$, and becomes isotropic when $\epsilon_{xx} = \epsilon_{yy} = \epsilon_{zz}$.

To determine the dispersion relation of an optical radiation in a medium described by Eq. (3.3), we considered the two Maxwell's equations in the absence of optical source expressed as

$$\nabla \times \mathbf{E} = -\frac{\partial \mathbf{B}}{\partial t} \quad (3.4)$$

$$\nabla \times \mathbf{H} = \frac{\partial \mathbf{D}}{\partial t} \quad (3.5)$$

By inserting the plane wave expression $\mathbf{E} = \mathbf{E}_0 e^{i(\omega t - \mathbf{k} \cdot \mathbf{r})}$ into Eq. (3.4) and Eq. (3.5) where \mathbf{k} is the wavevector, we obtain

$$\mathbf{k} \times \mathbf{E} = \omega \mu_0 \mathbf{H} \quad (3.6)$$

$$\mathbf{k} \times \mathbf{H} = -\omega \epsilon_0 \mathbf{E} \quad (3.7)$$

Substituting Eq. (3.6) into Eq. (3.7) results to the eigenvalue equation for the electric field \mathbf{E}

$$\mathbf{k} \times (\mathbf{k} \times \mathbf{E} + \omega^2 \mu_0 \epsilon_0 \bar{\epsilon} \mathbf{E}) = 0 \quad (3.8)$$

which can be written into the matrix form

$$\begin{bmatrix} k_0^2 \epsilon_{xx} - k_y^2 - k_z^2 & k_x k_y & k_x k_z \\ k_x k_y & k_0^2 \epsilon_{yy} - k_x^2 - k_z^2 & k_y k_z \\ k_x k_z & k_y k_z & k_0^2 \epsilon_{zz} - k_x^2 - k_y^2 \end{bmatrix} \begin{bmatrix} E_x \\ E_y \\ E_z \end{bmatrix} = 0, \quad (3.9)$$

where $k_0 = \omega/c$ is the magnitude of wavevector and $c = 1/\sqrt{\epsilon_0 \mu_0}$ is the speed of light in vacuum. We now focus our attention on uniaxial media, with optical

axis oriented along the \hat{z} direction, i.e., we set $\varepsilon_{xx} = \varepsilon_{yy} \equiv \varepsilon_{\parallel}$ and $k_{\parallel} = \sqrt{k_x^2 + k_y^2}$ and define the permittivity in the direction normal to the interface as $\varepsilon_{zz} \equiv \varepsilon_{\perp}$. Assuming Eq. (3.9), the non-trivial solutions leads to the dispersion relation

$$\left(k_{\parallel}^2 + k_z^2 - \varepsilon_{\parallel} k_0^2\right) \left(\frac{k_{\parallel}^2}{\varepsilon_{\perp}} + \frac{k_z^2}{\varepsilon_{\parallel}} - k_0^2\right) = 0. \quad (3.10)$$

These two equation representations in Eq. (3.10) correspond to a spherical and an ellipsoidal isofrequency surface in the k -space when solved, respectively [61]. The first equation describes waves polarized in the xy plane where $E_z = 0$ (ordinary or TE waves) and the second corresponds to waves polarized in a plane containing the optical axis, where $B_z = 0$ (extraordinary or TM waves). In common materials, the isofrequency contour (IFC) takes the form of a spherical surface (Fig. 3.1a) for the isotropic case, or an ellipsoid (Fig. 3.1b) for the anisotropic case, respectively.

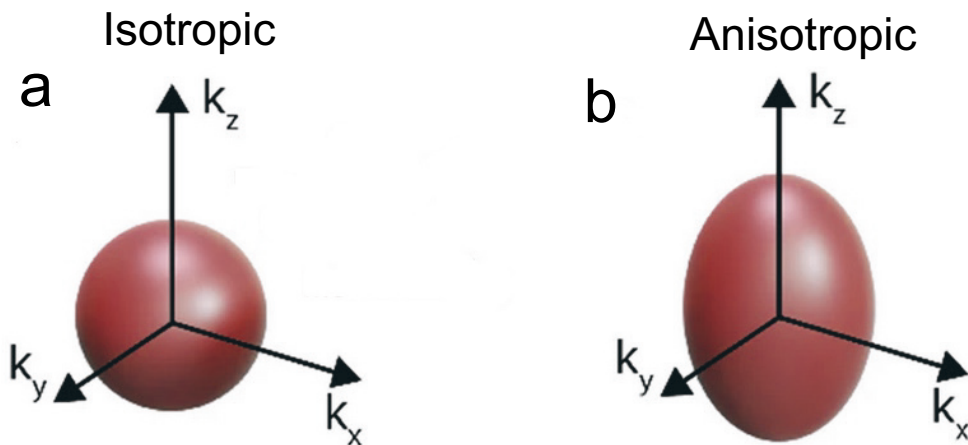


Figure 3.1 Isofrequency contour for (a) isotropic and (b) anisotropic media.

However, at extreme anisotropic behaviour where ε_{\parallel} or ε_{\perp} is negative, the dispersion relation changes substantially. As a result, opposite signs with the permittivity components leads to a hyperboloidal isofrequency surface for the extraordinary polarization, hence coined as hyperbolic media. As a result, waves with arbitrarily large wavevectors retain a propagating nature, while in isotropic materials they become evanescent due to the bounded IFC [62]. The choice of the permittivity components $\varepsilon_{\parallel} > 0$, $\varepsilon_{\perp} < 0$ relates to a two-fold hyperboloid, and the hyperbolic medium is called dielectric (with reference to its behavior in the xy plane) [60] or Type I.

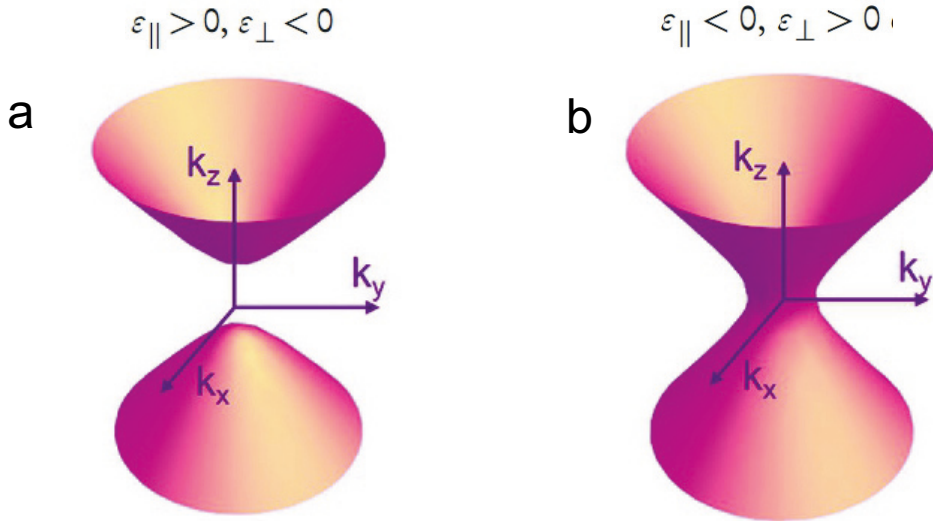


Figure 3.2 Hyperboloid isofrequency surface for a uniaxial medium with an extremely anisotropic dielectric response for (a) Type **I** and (b) Type **II** medium. They both can support waves with infinitely large wavevectors in the effective medium limit. However, such waves in a vacuum are evanescent and decay exponentially.

Alternatively, permittivity components $\epsilon_{\parallel} < 0, \epsilon_{\perp} > 0$ describes a one-fold hyperboloid, namely a metallic or Type **II** medium. The latter is relatively more reflective as it is more metallic than the Type **I** counterpart as shown in Fig. 3.2.

3.1.1 Building blocks of hyperbolic media

In principle, a metal–dielectric building block can be utilized for the practical realization of a hyperbolic medium. It is because a hyperbolic medium requires opposite signs of the effective permittivity components. As such, the medium has to combine the properties of a dielectric material in one direction and a reflective metal in the other for extreme anisotropic behavior [54, 63]. This can be achieved, for example, by designing metal–dielectric multilayer thin films with sub-wavelength thicknesses, as shown in Fig. 3.3 or by designing metallic nanorod arrays in a dielectric matrix [64]. Historically, the first attempt in this direction dates back to 1969, when permittivity engineering was proposed by restricting the motion of a magnetized electron plasma employing a constant magnetic field [65]. Yet, this approach was unpractical in terms of device portability and was limited in frequency and as such, utilizing

nanofabrication techniques to attain these metal–dielectric building blocks became of relevance.

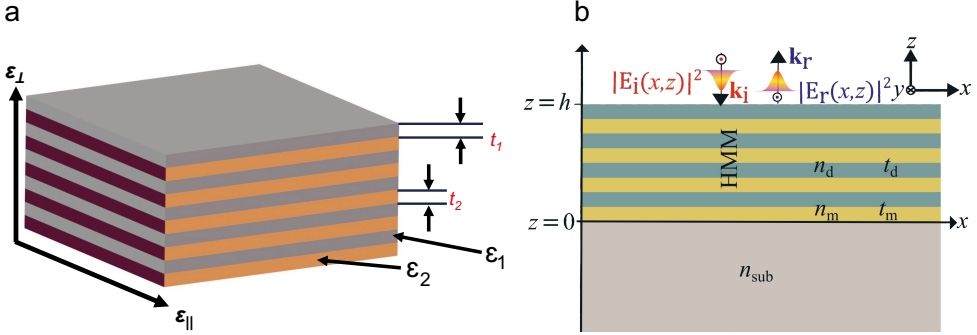


Figure 3.3 Uniaxial media schematic depicting alternating layers with permittivities ϵ_1 (dielectric) and ϵ_2 (metal) with thicknesses t_1 (t_d) and t_2 (t_m) and permittivity components ϵ_{\parallel} and ϵ_{\perp} . (a) 3D schematic and (b) 2D representation with refractive index n .

It is worth noting that the optical properties of metal–dielectric building blocks can usually be tuned from the ultraviolet spectral range to the mid-infrared by choosing appropriate materials [64]. Typically, a selected metal should have good metallic properties with low loss in the wavelength range under consideration. This can be achieved by choosing a metal with a high absolute value of the real part of the permittivity and a low value of the imaginary part, which determines the loss. Aluminium (Al) is so far used for applications in the ultraviolet spectral range, while metals such as silver (Ag) and gold (Au) are used in the visible spectrum in combination with a suitable dielectric such as aluminum oxide or a high refractive index material such as titanium oxide or silicon nitride [63, 66]. Albeit, Au has also been shown to be applicable in Type I nanorod-based hyperbolic metamaterials (HMMs) in the near-infrared wavelength range [67]. However, the high reflectivity of conventional plasmonic metals in the near-infrared spectral range causes high-impedance mismatches in metal–dielectric multilayers, thus reducing their transmittance. Alternative plasmonic materials in this spectral range with tailored lower plasma frequencies are being considered for hyperbolic media, such as transparent conducting oxides and transition metal nitrides [68]. At mid-infrared wavelengths, one option for metallic components in hyperbolic media is degenerately doped III–V semiconductors. However, the limit of doping concentration often restrains their ability to act as a metal

at near-infrared spectral regions, they are yet still ideally suitable in mid-infrared applications [68].

Furthermore, the source of propagating high-permittivity waves relies on microscopic metallic building blocks that create hyperbolic dispersion in the material. The polaritonic properties of the metal building blocks enable the desired light–matter coupling to generate high- k waves. In particular, phonon–polaritons (optically active phonons) or plasmonic–polariton metals (free electrons) are required to construct hyperbolic metamaterials. High- k modes are the result of the near-field coupling of surface plasmon polaritons (SPPs) at each metal–dielectric interface within the structure and are defined as Bloch modes in their superlattice. Further discussion on the origin of high- k modes will be detailed in section 3.1.3.

3.1.2 Hyperbolic media optical response

As the focus of the thesis is on multilayer metamaterials and their enhanced light–matter interaction, we will gear our discussions toward stacked metal–dielectric layers. In such hyperbolic media, their optical response can be homogenized using an effective medium theory (EMT) which results in a hyperbolic effective permittivity tensor. This model can be utilized when the unpatterned multilayer thin films satisfy the condition that the layers are relatively smaller than the interacting wavelength. As such, the effective permittivity components of the dielectric tensor in the limit of infinitesimal layer thickness for the multilayered structure can be obtained as

$$\varepsilon_{\parallel} = \varepsilon_2 \rho + (1 - \rho) \varepsilon_1 \quad (3.11)$$

$$\frac{1}{\varepsilon_{\perp}} = \frac{\rho}{\varepsilon_2} + \frac{1 - \rho}{\varepsilon_1} \quad (3.12)$$

assuming an average field displacement and utilizing electromagnetic boundary conditions. Here, ε_1 and ε_2 represent the permittivities of the two different alternating layers of the discontinuous uniaxial structure. The filling fraction $\rho = t_2 / (t_2 + t_1) \equiv t_m / (t_m + t_d)$ in the case of a metal–dielectric alternating layer, is defined as the volume percentage of the metallic material in a unit cell or period, and t_m and t_d are the relative thicknesses of the metal and dielectric, respectively. To reach the hyperbolic regime, the permittivity components are to be tuned such that $\varepsilon_{\parallel} \varepsilon_{\perp} < 0$. From Eqs. (3.11) and (3.12), the effective-medium approximations (EMA) un-

der long-wavelength limit results to an effective dielectric tensor ε_{eff} that can be expressed in matrix form as

$$\varepsilon_{\text{eff}} = \begin{bmatrix} \varepsilon_{\parallel} & 0 & 0 \\ 0 & \varepsilon_{\parallel} & 0 \\ 0 & 0 & \varepsilon_{\perp} \end{bmatrix} \quad (3.13)$$

However, in principle, the excitation of surface plasmon polaritons at the metal-dielectric interface causes the electric field to vary significantly on the period scale, although the vacuum wavelength is much larger than the period. Hence, the approximations, given by Eqs. (3.11) and (3.12), may not be valid for certain spectral ranges. As such, plasmonic modes can have IFC of more complex shapes that are neither elliptical nor hyperbolic. This produces both positive and negative refracted rays by light scattered at the metamaterial interface. Due to these effects, more accurate descriptions such as non-local EMT [NEMT] [69] and operator approach to effective-medium approximation (OEMA) [70] are being adopted to calculate the optical response of such media using a transfer-matrix method (TMM) presented in appendix A.1.

These non-local techniques of substituting an inhomogeneous periodic structure with its equivalent homogeneous medium by considering the spatial dispersion effect have been of great relevance to determining the optical properties of a local homogenized medium. Non-locality in this discussion refers to the behavior of a physical system at a given point depending on its state at another spatially separated region. Lately, Popov et al. [70] also developed an operator approach for effective medium analysis to overcome the breakdown of local homogenization and Lei et al. [71] built on the nonlocal model by introducing higher-order terms into the effective permittivity while Castaldi et al. [72] also applied a trace and anti-trace map formalism to model the higher-order terms in periodic multilayered metamaterials (PMMs) for non-local response correction. In this thesis, a simple yet robust closed-form effective-medium model for PMMs, in which the non-local effects are considered will be discussed [73]. Its derivation stems from the well-known Rytov's dispersion relation [74, 75] expressed as

$$k_{\text{effz}}(t_1 + t_2) = \arccos[\cos(k_{1z}t_1)\cos(k_{2z}t_2) - \gamma \sin(k_{1z}t_1)\sin(k_{2z}t_2)] \quad (3.14)$$

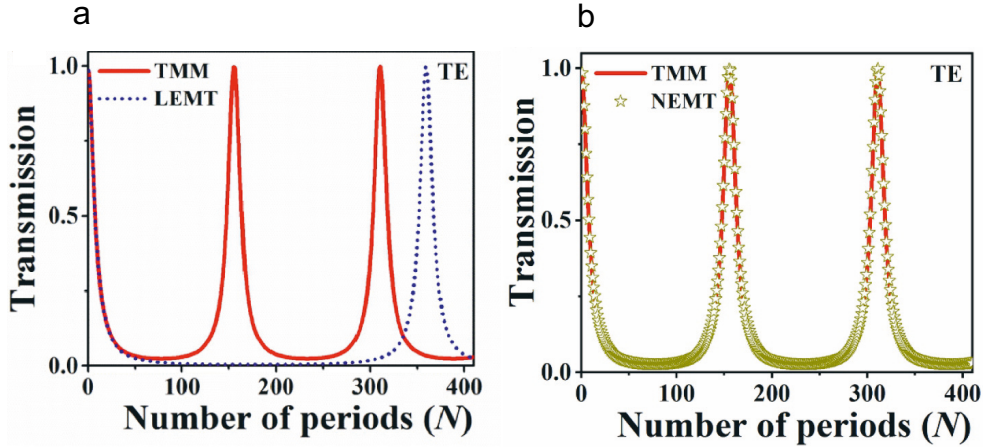


Figure 3.4 The error plot between TMM calculations (red solid lines) and the comparison between the local (blue dotted lines) and non-local EMT (star symbol) predictions versus the number of periods (N) and the $\theta_{\text{in}} = 59.98^\circ$ incident angle for TE polarized waves. Adapted from [73].

where γ is the polarization-specific parameter, i.e., $\gamma_{\text{TE}} = (k_{2z}/k_{1z} + k_{1z}/k_{2z})/2$ for TE polarized waves and $\gamma_{\text{TM}} = (\varepsilon_2 k_{1z}/\varepsilon_1 k_{2z} + \varepsilon_1 k_{2z}/\varepsilon_2 k_{1z})/2$ for transverse magnetic (TM) polarized waves. From this basis, the non-local effective permittivity components can be derived as [73]

$$\varepsilon_{\parallel}^{\text{NEMT}} = \frac{(\arccos \delta_{\text{TE}})^2}{k_0^2 (t_1 + t_2)^2} + \varepsilon_{\text{in}} \sin^2 \theta_{\text{in}} \quad (3.15)$$

$$\varepsilon_{\perp}^{\text{NEMT}} = \frac{\varepsilon_{\text{in}} \sin^2 \theta_{\text{in}} \left[(\arccos \delta_{\text{TE}})^2 + k_0^2 \varepsilon_{\text{in}} \sin^2 \theta_{\text{in}} (t_1 + t_2)^2 \right]}{(\arccos \delta_{\text{TE}})^2 - (\arccos \delta_{\text{TM}})^2 + k_0^2 \varepsilon_{\text{in}} \sin^2 \theta_{\text{in}} (t_1 + t_2)^2} \quad (3.16)$$

where $\delta_{\text{TE, TM}} = \cos(k_{1z} t_1) \cos(k_{2z} t_2) - \gamma_{\text{TE, TM}} \sin(k_{1z} t_1) \sin(k_{2z} t_2)$ and θ_{in} denotes the angle of incidence with effective thickness $t_{\text{eff}} = N(t_1 + t_2)$, where N is the number of periods of the multilayered structure.

By comparing these local and non-local techniques with the step-by-step TMM approach as presented in [73], one can see some error comparisons between these two approaches as shown in Fig. 3.4. The figure presents the difference between TMM calculations and the effective medium theories against the number of periods. It is evident that the non-local approach is more comparable with the layer-by-layer TMM approach as compared with the local homogenization technique. Although non-local effects are known to have a minor impact on linear optical responses of the

hyperbolic media, however, this condition can be relatively different when predicting the spontaneous emission properties of emitters located within such metamaterial, where the presence of an additional propagating mode within the media acts as a new decay channel for the emitters and fundamentally changes the local density of states.

3.1.3 High- k modes origin in a hyperbolic media

To elucidate the origin of high- k modes in a uniaxial media, it is relevant to understand the existence of SPPs in the conventional media utilized in building these multilayered stacked media. As such, we will discuss the interesting properties of the thin metal film component of the multilayered structure when it interacts with an electromagnetic field. Metals as conducting media interact with electromagnetic radiation via the movement of free electrons. In the optical regime, incident radiation with sufficiently high frequency can produce resonant charge density fluctuations of free electrons with no elastic restoring force as electrons are no longer bound to the atoms of a conducting medium. These charge oscillations are known as plasmons and can appear in metals as bulk or surface oscillations. SPPs are electromagnetic excitations propagating at the interface between a dielectric and a conductor (metal, semiconductor), and are confined at the interface and evanescent both in the propagation direction and the direction perpendicular to the interface [76, 77]. Thus, the oscillation of the free electrons in a conductor coupling with electromagnetic fields induces SPPs. From Maxwell's continuity equation for \mathbf{H} and \mathbf{E} at the interface of a metal–dielectric, the dispersion relation of SPPs can be expressed as

$$k_{x,\text{spp}} = \frac{\omega}{c} \sqrt{\frac{\epsilon_1 \epsilon_2}{\epsilon_1 + \epsilon_2}} \quad (3.17)$$

$$k_{z1,z2,\text{spp}} = \frac{\omega}{c} \sqrt{\frac{\epsilon_{1,2}^2}{\epsilon_1 + \epsilon_2}} \quad (3.18)$$

for TM polarized light considering the electromagnetic boundary conditions. From Eqs. (3.17) and (3.18), $k_{x,\text{spp}}$ and $k_{z1,z2,\text{spp}}$ represents the planar and perpendicular wavevector components, respectively.

Notably, the complex refractive index of metal and the loss supplied by such a

medium, causes the SPPs supported by a metal–dielectric interface to dissipate exponentially both along and perpendicular to the interface. As a result, reduced SPP attenuation is required to improve SPP utilization and achieve practical applications. The use of a thin metal sheet enclosed on both sides by the same dielectric is a typical technique for decreasing SPP attenuation. This can cause the excited SPPs on the two sides of the metal film to couple leading to mode hybridizations, i.e., symmetric or antisymmetric modes, illustrated as an inset in Fig. 3.5 (a). Based on the thick-

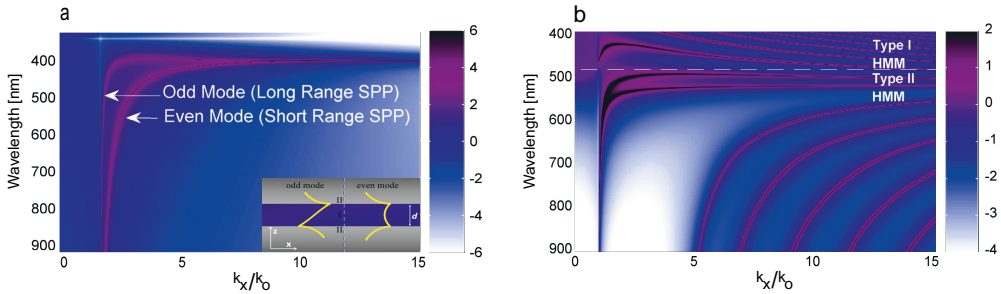


Figure 3.5 (a) TMM approach transmission (log scale) heatmap of a 30 nm low loss Ag layer sandwiched between two dielectric half-spaces with its schematic presented as an inset. Even (short-range SPP) and odd (long-range SPP) modes are realized through mode hybridization due to near-field interaction between the SPP at the top and bottom metal surfaces presented as the yellow-colored curve in the inset. Roman numbers I and II represents the core layer with thickness d and the claddings, respectively. (b) Similar heatmap for a 200 nm homogenized Ag-TiO₂ hyperbolic media. The high- k modes, which are the structure's Bloch waveguide modes, are shown by the bright bands in the Type I and Type II HMM areas.

ness of the metal slab sandwiched between the two dielectrics, even (short range) or odd (long range) mode hybridization can be excited. Odd SPP modes have extended propagation lengths and are less susceptible to larger metallic losses. Since propagation lengths of odd modes increase with decreasing metal thickness, they are known as long-range SPPs. Even modes, on the other hand, are short-range SPPs because their fields are more restricted to the metal. The confinement to the metal increases as the metal thickness decreases, reducing the propagation length of short-range SPPs. As such, increasing the number of metal–dielectric layers leads to an increasing number of coupled mode hybridization which is the origin of the high- k states (SPP hybridizations) in multilayer HMM architecture. Figure 3.5 (a) illustrates the odd and even hybridized SPP modes for a thin 30 nm silver film sandwiched between two dielectric halfspaces and (b) shows the corresponding Bloch modes in a hyperbolic media. Notably, the HMM modes exist as bright bands at large k_x values

which are normally evanescent in a vacuum/ conventional materials. The existence of these unique high- k modes in the HMM exhibit many potential applications due to its large photonic density of states.

3.1.4 Photonic density of states

In this section, we introduce the relation between an emitter and a hyperbolic medium complex and present the formulations utilized in calculating their spectral responses. Basically, engineering the optical environment around an emitter allows one to regulate the lifetime of spontaneous emission from that emitter. This is because there is a certain photonic density of states (PDOS) in the environment that can couple with the emitter. From section 2.1.3, we discussed that the rate of SE is proportional to the PDOS, which depends critically on the geometry of the near field. As such, the spontaneous decay rate of an emitter is increased (suppressed) when the number of possible photonic states increases (decreases), due to the higher (lower) available photonic modes [78, 79]. For instance, the spontaneous emission decay rate of an emitter placed near a photonic crystal or microcavity can be greatly increased for wavelengths that can couple into the resonant modes of the structure [80, 81]. Such a rate in engineered electromagnetic surroundings can greatly exceed that of a homogeneous dielectric environment, or “free space”, and the ratio of the two constitutes a figure of merit (FOM) known as *Purcell factor*. In contrast to resonant structures like cavities or single metallic/dielectric interfaces which require the adjustments of their restricted narrow resonances to match the absorption or emission of emitters coupled to it, hyperbolic media with a new family of guided plasmon mode (bulk plasmons with large k -vectors), have shown to be a practical tool to alleviate these constraints for radiative decay engineering, particularly in the area of quantum nanophotonics. This is due to the media’s interesting property of possessing high PDOS as they can accommodate infinitely high- k modes in the ideal limit [82]. In addition, they also exhibit a *Purcell factor* that is broadband and tunable in frequency [83].

To numerically determine the SE enhancement of a point source over an unpatterned planar multilayered structure, we utilized the model presented by Ford and Webers’ work on SE enhancement for single plasmonic interfaces [50], to the situation of our multilayered media. This semi-classical approach approximates ratios of

rates with ratios of powers and is comparable to a fully quantum theory in the weak coupling limit. In the model, the *Purcell factors* F_{\parallel} and F_{\perp} of a dipole oriented parallel (\parallel , “p-polarization”) or orthogonal (\perp , “s-polarization”) to the layers and located a distance d above the surface are expressed as

$$\begin{aligned} F_{\parallel} &= 1 - \eta_0 \left(1 - \frac{3}{4} \operatorname{Re} \int_0^{\infty} dk_{\parallel} D_{\parallel}(k_{\parallel}) \right), \\ F_{\perp} &= 1 - \eta_0 \left(1 - \frac{3}{2} \operatorname{Re} \int_0^{\infty} dk_{\parallel} D_{\perp}(k_{\parallel}) \right), \end{aligned} \quad (3.19)$$

where the power density spectra $D_{\parallel}(k_{\parallel})$ and $D_{\perp}(k_{\parallel})$ are

$$\begin{aligned} D_{\parallel} &= \frac{1}{k_z} \frac{k_{\parallel}}{\sqrt{\varepsilon_1} k_0} \left[1 + r_s e^{2ik_z d} + \left(\frac{k_z}{\sqrt{\varepsilon_1} k_0} \right)^2 (1 - r_p e^{2ik_z d}) \right] \\ D_{\perp} &= \frac{1}{k_z} \left(\frac{k_{\parallel}}{\sqrt{\varepsilon_1} k_0} \right)^3 (1 + r_p e^{2ik_z d}) \end{aligned} \quad (3.20)$$

In the above formulation, η_0 represents the internal quantum efficiency of the dipole in free space with real permittivity ε_1 , $k_0 = 2\pi/\lambda_0$, where, $k_{\parallel} = \sqrt{k_x^2 + k_y^2}$, and $k_z = \sqrt{\varepsilon_1 k_0^2 - k_{\parallel}^2}$ are the wavevector components along the in-plane and vertical direction of the structure. r_p, r_s also denote the reflection coefficients of the structure for TM or TE polarized plane wave (a different phenomenon from dipole polarization), retrieved with TMM formalism. Notably, dipoles occurring in nature are isotropic [84]; therefore a more appropriate *Purcell factor* F_{iso} is obtained through an average over F_{\parallel} and F_{\perp} represented as

$$F_{\text{iso}} = \frac{1}{3} (F_{\perp} + 2F_{\parallel}), \quad (3.21)$$

where the factor 2 accounts for the two orthogonal in-plane orientations. From these formulations, we can explore the interactions of emitters when coupled with a hyperbolic media to elucidate their interesting features close to the ENZ region of the multilayered structure which will be discussed in section 3.2. Nevertheless, since the relation of emitters’ radiation confinement and multilayered hyperbolic media configuration is not as strong as in a cavity as discussed in section 2.1.3, other suitable formulations of computing *Purcell factor* [$\text{FP} = \Gamma_{\text{HMM}}/\Gamma_0$, where Γ_{HMM} and

Γ_0 are the SE rates in the presence of the hyperbolic environment and in free space] can also be utilized. This ratio can be calculated using the dyadic Green function \tilde{G} , which describes how a point-like source emits radiation into its surroundings [84].

3.2 Epsilon-near-zero features of hyperbolic media

Amidst the interesting features of a hyperbolic media, there exists an ENZ window in their dispersion relation. This ENZ window is defined as a spectral range, where the effective permittivity of the media extends to zero [$Re\{\varepsilon_{||}\} < 1$]. The window exists between the transition of the media from the elliptical region to the hyperbolic domain (i.e., transition from being dielectric to the metallic regime) as discussed in the EMT formulation in section 3.1.2. In addition to the existence of zeros in the effective permittivity of the media, there exist resonant poles which are coined as epsilon-near-pole (ENP) [85]. The directions in which the resonances of the ENZ and ENP occurs is of great relevance, as it alters the spectral response of the media. ENZ in particular occurs parallel in the multilayered structures where the direction of free electron motion occurs according to the Drude plasma frequency. Conversely, the ENP behavior takes place when there is no continuous flow of the electrons. Within this ENZ spectral range, the hyperbolic media exhibits different physical phenomena such as an excitation of electromagnetic waves that propagate at long distances with negligible phase variations [86].

Although these exotic features of a hyperbolic medium are significant in many applications, the dissipation of coupled energy of emitters caused by a loss in the metal–dielectric building blocks has been a constraint in radiative decay engineering [87–89]. As a result, various design and engineering techniques have been put forth by various authors to overcome these limitations. These techniques include adiabatically tuning the filling fraction to tunnel trapped high- k modes, incorporating a high-index grating configuration on the HMM, and nanopatterning of the HMM slab to create hyper-crystals [64, 88, 90]. Additionally, theoretical research on loss-compensation and enhancement of spontaneous emission in active multilayered structures has been conducted using the geometry of the near fields as well as the multilayered structure’s dispersion relations [87, 91, 92]. The study of emitters coupled to multilayered structures made of metal and polymeric material has so far focused on loss compensation and transient technology, where a water-soluble and

biocompatible polymer were used to create a transient and flexible HMM structure [93, 94].

In **P2**, however, we proposed a polymer-based active HMM structure composed of alternating layers of a metal and PMMA medium to study the decay rate mechanism of emitters not only dispersed on the top layer but also in-between the PMMA layers. We engineered relatively thin PMMA films to serve as a dielectric medium to incorporate quantum emitters in the proposed structure. This active dye-doped HMM structure helped to compensate for the losses in a metal–dielectric structure due to the enhanced coupling of emitters dispersed on top and within the polymer-based HMM. The study provided insight into the radiative decay mechanisms of emitters coupled to the HMM structure and its relation to the ENZ region of the polymer-based HMM structure, which is prominent in efficient dipole engineering model design.

3.2.1 Structure design and modeling

We commence with the design of the proposed structure by numerically optimizing the thicknesses of the metal and dielectric layers (i.e., ρ - filling fraction). This optimization mechanism helped in attaining the required ENZ feature of the hyperbolic media to match it with the emission and absorption wavelengths of some selected emitters. Per the optimization conditions, we obtained a desired thickness of 9 nm for gold (Au) and 29 nm for PMMA. The latter is a versatile polymeric material and well suited for many applications such as protective coating, high-resolution positive resist, and as a sacrificial layer [95].

The obtained ENZ region of the proposed structure was comparable to the emission wavelength of the Rhodamine 590 (Rh590) dye molecule based on the optimized fill fraction ρ . From here, we numerically implemented the spectral response, PDOS, electric-field distribution, transmission dispersion relation, and *Purcell factor* calculations of the proposed structure. As a note, all calculations were conducted using a commercial Ansys Lumerical FDTD solutions software package and an in-house developed transfer-matrix method code with an experimental wavelength-dependent complex dielectric functions for Au [96] and PMMA [97].

Figure 3.6 (a) [Inside HMM] illustrates the schematic of the proposed Type II [58] HMM structure with emitters embedded within the polymeric PMMA layer.

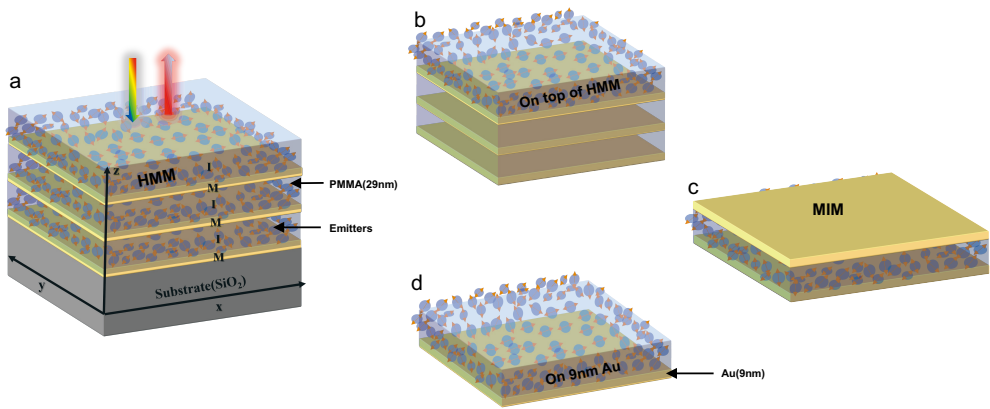


Figure 3.6 (a) Schematic of the Au-PMMA structure consisting of 9 nm thick Au and 29 nm thick PMMA layers. Three polymeric PMMA samples were incorporated with three different dyes each [HMM + 3L dye]. I-M represents the insulator-metal interface. M-I-M represents the metal-insulator-metal interface. (b) similar HMM structure with dye-doped PMMA on the top layer [HMM + 1L dye]. (c) schematic of the MIM structure. (d) similar representation of dye-doped PMMA on top of the 9 nm Au layer [1L Au + 1L dye]. Adapted from [P2].

Figure 3.6 (b) [on top of HMM], (c) [MIM] comparable to the Fabry-Pérot-like cavity in section 2.1.1, and (d) [on 9 nm Au] illustrate the schematic of the corresponding reference samples used to comprehend the decay rate mechanism and luminescence response of the proposed dye-doped HMM structure.

3.2.2 Sample fabrication and characterization

The proposed polymer-based HMM structure in P2 was fabricated using a metallic electron-beam (e-beam) evaporator and spin-coating techniques. The samples were fabricated on a fused silica (SiO₂) substrate with a refractive index of 1.45. Three active HMM samples were fabricated with each embedded with one of the different emitters (Rh590, Styryl-11 (LDS 798), and Pyromethene 650 (PYR650) dye-doped PMMA samples). Reference samples of each dye embedded in PMMA-A1 (1%wt PMMA and 99%wt anisole) spin-coated on a homogeneous glass substrate were also prepared. Each dye was also spin-coated at a speed of 2000 rpm for 30 secs, on a 9 nm Au film to serve as a reference to study the coupling effects of dye on a metal substrate. The thickness of the polymeric material was measured using a profilometer.

For the spectral characterization of the fabricated samples, a confocal Raman microscope from WiTec (alpha300R) was utilized. The reflectance and transmittance

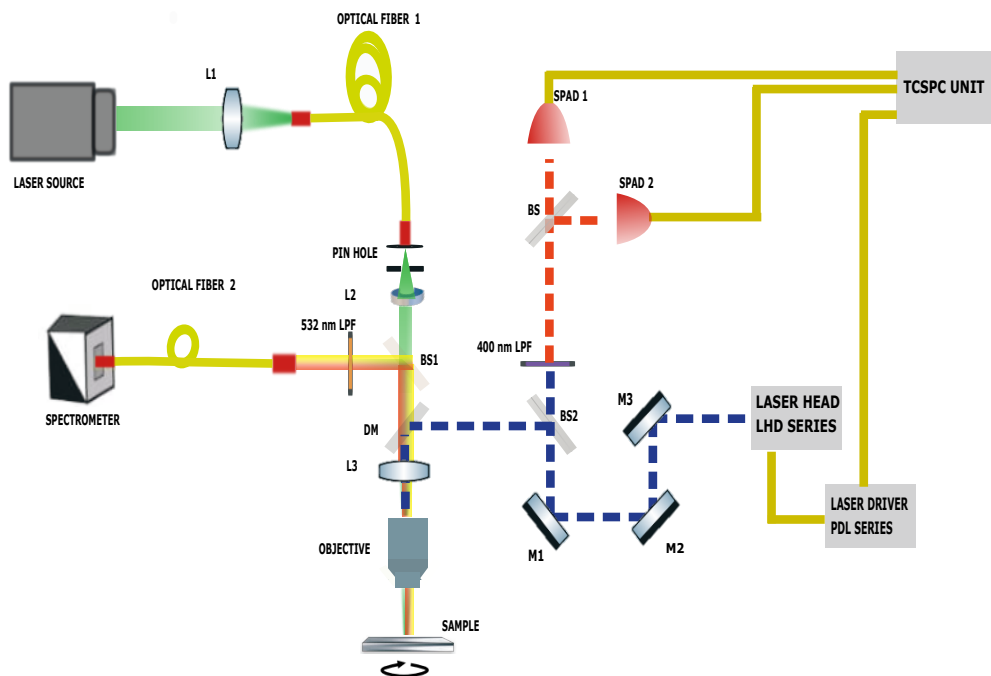


Figure 3.7 Experimental setup schematic for spectral response measurement by altering the left-hand configuration with a broadband optical source and removal of filters as they are required for the case of PL and fluorescence lifetime measurement. M, mirror, BS, beam splitter, L, lens, DM, dichroic mirror, and the rotating sign below the sample stage signifies a motorized scanning stage.

measurements were carried out using a broadband optical source (Energetiq EQ-99XFC LDLS, spectral range 190 - 2100 nm) to excite the samples. The optical spot is focused on the samples using a Zeiss "Epiplan-Neofluar" 20X objective with a numerical aperture ($NA = 0.4$) for both spectral measurements. To acquire the photoluminescence (PL) spectra of the samples, a 532 nm laser was used to excite the samples to attain signal counts of the emission peak intensity for the different dyes. A polarization-dependent 375 nm pulsed laser source (with a diffraction-limited spot size of $\approx 1.14 \mu\text{m}$) was utilized to attain the fluorescence lifetimes of the samples with the help of a Picoquant HydraHarp device and a single-photon avalanche diode (SPAD) detector.

All measurements were performed under optimal laboratory conditions. The response of the samples was coupled to an optical fiber connected to Ocean Optics Flame UV-VIS spectrometer for spectral response and PL measurement and a

SPAD detector for the fluorescence lifetime measurement as shown in the schematic of Fig. 3.7. In the case of the fluorescence lifetime measurement, a technique called time-correlated single photon counting (TCSPC) is utilized as illustrated on the right-hand side of Fig. 3.7. Using TCSPC, the time elapsed between a pulsed laser's excitation of the sample and the emitted photon's arrival into the detector is recorded. A defined "start" signal is provided by the electronics steering the laser pulse, and a defined "stop" signal are realized by detection using the SPAD detectors. The measurement of this time delay is repeated many times to account for the statistical nature of the fluorophore's emission. The delay times are then sorted into a histogram that plots the occurrence of emission over time after the excitation pulse.

3.2.3 Results and discussion

In (P2), we numerically calculated the dispersion relation of the proposed structure using both local and non-local EMT and the TMM approach as present in section 3.1.2 and appendix A.1 to determine the interesting wavevectors that are supported by the polymer-based hyperbolic metamaterial. The dispersion relation illustrated in Fig. 3.8 (a), (b), and (c) shows the transmission of evanescent waves through the proposed structure. The local EMT approach represents the multilayered structure

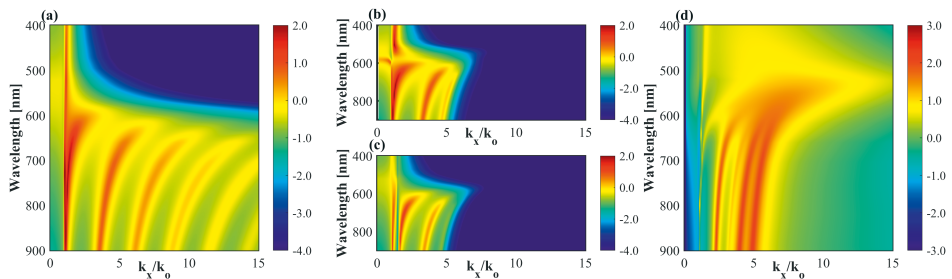


Figure 3.8 Dispersion relation of the polymer-based structure exhibiting high- k modes and the associated photonic density of states (PDOS). (a) Transmission of evanescent waves in logarithmic scale through the three bilayers of Au (9 nm)-PMMA (29 nm) multilayered structure using the local EMT approach. In the local effective medium limit, there are infinite high- k waves in a Type-II HMM due to the existence of strong spatial dispersion effects which can be corrected using the non-local EMT approach presented in (b). (c) Similar dispersion relation using the TMM approach. In this realistic case, the size of the unit cell imposes a cut-off to the tunneling of the high- k modes in the structure. (d) The corresponding PDOS of the polymer-based HMM composite using the TMM approach. Adapted from [P2].

as an effective bulk medium with hyperbolic dispersion as discussed in section 3.1.2.

As shown in Fig. 3.8 (a), infinitely large wavevectors can be transmitted through the entire bandwidth of this ideal structure. However, in a realistic structure with a finite number of layers and considering the inherent losses in the metal layers, there is a cutoff to the largest wavevector that can propagate through the HMM structure. This is also evident in the TMM dispersion relation illustrated in Fig. 3.8 (c), that shows two bright bands at $k_x/k_0 < 5$ and is comparable to the non-local EMT approach [73] illustrated in Fig. 3.8 (b). Non-local EMT approaches have been quite realistic in describing metal–dielectric hyperbolic metamaterials due to their spatial dispersion effects corrections as compared to the local EMT approach [69, 73, 98]. The existence of the bright bands in the dispersion relation of the polymer-based HMM structure shows that the medium supports bulk plasmon-polaritonic modes. As discussed above, the bright bands coined as the bulk plasmon modes are due to the coupling of SPPs at each metal–dielectric interface. These modes exhibit high electric-field intensity that overlaps with emitters placed close to the metamaterial, resulting in an increased PDOS which is presented in Fig. 3.8 (d). It is also noteworthy that the suggested material is a Type II HMM structure which shows several high- k modes as compared to Type I HMM which can support a lesser number of these modes [63].

3.2.3.1 Spectral response of the polymer-based hyperbolic metamaterial

In addition to the dispersion relation, we further calculated the field distribution through the polymer-based HMM structure using the TMM approach. Figure 3.9 (a) illustrates propagation mode along the multilayered metal–dielectric interface composed of three subdivisions with labels: IM [$0 \text{ nm} \leq Z \leq 38 \text{ nm}$], MIM1 [$29 \text{ nm} \leq Z \leq 76 \text{ nm}$], and MIM2 [$67 \text{ nm} \leq Z \leq 114 \text{ nm}$] layers. At the ENZ wavelength ($\lambda = 570 \text{ nm}$) of the suggested structure, we attained a significantly high electric-field intensity. However, the field intensity decays due to propagation losses, in particular at HMM thickness $Z > 60 \text{ nm}$, and inherent metallic losses of the multilayer HMM structure. As such, enhanced SE of the embedded emitters was envisaged to result mainly from the first PMMA at the top layer, while emitters in the other two layers contribute minimally due to the variations in the LDOS.

Furthermore, the FOM bandwidth constructed as indicated in Fig. 3.9 (b) corresponds to the enhanced spectral region of the electric field distribution presented in Fig. 3.9 (a). The FOM was defined as the ratio of the effective parallel ϵ_{\parallel} and

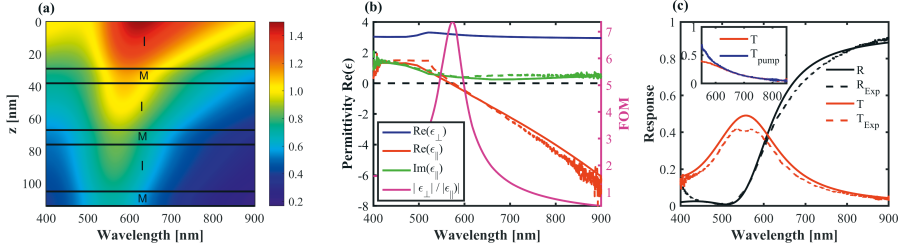


Figure 3.9 (a) P-polarized field (E_p) distribution through the HMM composite as a function of spectral wavelength. I-M corresponds to the insulator (PMMA) and metal (Au) interface. (b) Real [$\text{Re}(\epsilon_{\parallel})$, $\text{Re}(\epsilon_{\perp})$] and imaginary $\text{Im}(\epsilon_{\parallel})$ permittivities from local EMT, experimentally retrieved effective permittivity $\text{Ext}(\epsilon_{\parallel})$ [dashed lines] and the figure of merit (FOM) of the polymer-based HMM composite. ENZ wavelength is defined as the spectral wavelength where the structure permittivity crosses zero. (c) Spectral response of the polymer-based HMM material. Reflectance R and transmittance T acquired both numerically (using TMM) and experimentally (R_{Exp} , T_{Exp}). The inset depicts the experimentally measured transmission in the presence of a pump source T_{pump} and without a pump source T . Adapted from [P2].

perpendicular ϵ_{\perp} permittivities of the HMM structure acquired via local EMT. The FOM showed higher values at the ENZ wavelength ($\lambda = 570$ nm). Figure 3.9 (b) also shows the parallel ϵ_{\parallel} and perpendicular ϵ_{\perp} dielectric tensor as a function of wavelength. The dispersion relation above the ENZ window shows Type-II HMM behavior (i.e., $\text{Re}(\epsilon_{\parallel}) < 0$, $\text{Re}(\epsilon_{\perp}) > 0$) that exhibits, in principle, inherent optical losses and high impedance mismatch with respect to vacuum. In addition, we used inverse TMM formulations to compute the extracted effective permittivity $\text{Ext}(\epsilon_{\parallel})$ [dashed lines] of the fabricated polymer-based HMM structure based on the numerically computed and the experimentally attained spectral responses (i.e., reflection and transmission) of the HMM-dye complex structure. We identified that the extracted effective permittivity $\text{Ext}(\epsilon_{\parallel})$ [dashed lines] matches well with the calculated effective parallel ϵ_{\parallel} permittivity [solid lines] and possesses a similar ENZ wavelength as predicted numerically by EMT.

Figure 3.9 (c) illustrates the reflectance R and transmittance T of the polymer-based HMM structure obtained both numerically [solid lines] and experimentally (i.e., R_{Exp} , T_{Exp}) [dashed lines]. It can be seen that the spectral reflectance range above the ENZ wavelength is high as compared to the spectral range below ENZ. This role of a medium exhibiting dielectric (i.e., $\lambda < 570$ nm with $\text{Re}(\epsilon_{\parallel}) > 0$) and metallic behaviour (i.e., $\lambda > 570$ nm with $\text{Re}(\epsilon_{\parallel}) < 0$) shows the hyperbolic nature of

the HMM composite. As stated initially, this nature brings about the inherent losses which can be compensated by using a gain medium, shown as an inset in Fig 3.9 (c). The inset shows the enhancement of the optical transmission T response of the active polymer-based HMM structure in the presence of a pump source T_{pump} which complements the emitter's ability to help in the inherent metallic loss compensation.

3.2.3.2 Luminescence and lifetime measurement

After comprehending the loss compensation mechanism of the active polymer-based HMM structures, we extended the discussion to SE engineering based on the ENZ characteristics of the media. To realize these exotic effects of the active polymer-based HMM structure, we numerically calculated the *Purcell factor* and experimentally measured the luminescence and the fluorescence lifetimes for three different dyes (i.e., Rh590, LDS798, and PYR650) with a peak emission wavelength (i.e., $\lambda \approx 569$ nm, 621 nm, and 700 nm, respectively) within the polymer-based HMM structure. These dyes were selected due to their emission spectra having different amounts of overlap with the ENZ wavelength ($\lambda = 570$ nm) of the structure to determine their respective decay rate mechanisms when coupled to the polymer-based HMM structure.

In **P2**, we presented the luminescence measurement of Rh590 dye with a maximum emission wavelength of 569 nm which is close to the ENZ wavelength (570 nm) of the HMM structure. We further compared the emission of each dye on a 9 nm gold layer, on top of the HMM layers, and within the HMM layers, respectively to elucidate their decay rate mechanisms. We observed high luminescence counts of emitters on and within the HMM layers as compared to the metallic cases. This shows the non-radiative quenching of the emitters when placed on the metallic layers due to the inherent lossy nature of Au. These variations in luminescence spectra [not shown here] for the different configurations as shown in Fig. 3.6 are compared to elucidate the different decay rate mechanisms of the emitters.

In addition, we extended the discussion toward the experimentally attained fluorescence lifetime values for each of the three different dye-doped HMM structures. Table 3.1 contains the lifetime components and the corresponding amplitudes fitted to the measured TCSPC data as well as the calculated average lifetimes based on the amplitudes. For all dyes with ≈ 40 molecules/ $(10 \times 10 \times 29)$ nm³ in the presence of one gold layer, we observed shortening of the average lifetime by more than 50%,

	Rh590			PYR650			LDS798		
	Amplitudes	Lifetime components	Average	Amplitudes	Lifetime components	Average	Amplitudes	Lifetime components	Average
On fused silica	A ₁ : 4.54 A ₂ : 4.30	τ_1 : 4.06 ns τ_2 : 1.68 ns	2.91 ns	A ₁ : 7.70 A ₂ : 2.90	τ_1 : 1.60 ns τ_2 : 3.35 ns	2.08 ns	A ₁ : 23.0 A ₂ : 6.50	τ_1 : 0.55 ns τ_2 : 1.90 ns	0.85 ns
On 9 nm Au	A ₁ : 22.9 A ₂ : 0.12 A ₃ : 0.89	τ_1 : 0.70 ns τ_2 : 8.10 ns τ_3 : 2.30 ns	0.79 ns	A ₁ : 20.0 A ₂ : 1.29	τ_1 : 0.77 ns τ_2 : 2.46 ns	0.87 ns	A ₁ : 1.24 A ₂ : 0.05	τ_1 : 0.34 ns τ_2 : 2.00 ns	0.40 ns
On top of HMM	A ₁ : 28.0 A ₂ : 0.14 A ₃ : 0.72	τ_1 : 0.60 ns τ_2 : 6.70 ns τ_3 : 2.11 ns	0.66 ns	A ₁ : 19.0 A ₂ : 1.11	τ_1 : 0.73 ns τ_2 : 2.33 ns	0.81 ns	A ₁ : 3.94 A ₂ : 0.10	τ_1 : 0.34 ns τ_2 : 1.81 ns	0.40 ns
Inside HMM	A ₁ : 32.8 A ₂ : 0.13 A ₃ : 0.68	τ_1 : 0.59 ns τ_2 : 6.70 ns τ_3 : 2.20 ns	0.66 ns	A ₁ : 25.0 A ₂ : 1.52	τ_1 : 0.69 ns τ_2 : 2.22 ns	0.78 ns	A ₁ : 4.78 A ₂ : 0.10	τ_1 : 0.37 ns τ_2 : 2.01 ns	0.41 ns

Table 3.1 Lifetime measurements of the three dyes on a fused silica substrate, on 9 nm gold (Au) layer and, on top of the HMM structure and embedded within the polymer-based HMM structure. Adapted from [P2].

which further predicated the increased non-radiative decay due to near field absorption of the Au film. This is significant to note down when examining the lifetimes of dyes on top or embedded inside the polymer-based HMM, as the effect of dyes interacting with the thin Au film is also present in the HMM media. Nonetheless, in the polymer-based HMM, we observed even shorter lifetimes. From Fermi's golden rule, as described in section 2.1.3, the number of radiative decay channels depends on the number of PDOS available to the emitter [99]. Therefore, an increased PDOS can be experimentally verified by observing a shortened lifetime. Thus, these lifetime results act as evidence of coupling between the emitters (Rh590 and PYR650) and the high- k modes of the polymer-based HMM complex as well as coupling to the SPP modes at each metal-dielectric interface. This results in an additional increment to the non-radiative recombination rate of the emitters. However, for LDS798 dye molecules, we observed no additional shortening of lifetime in the HMM when compared with the metal case. This was due to the LDS798 dye molecules having the least overlap with the ENZ region of the proposed structure as presented in Fig. 3.8 (d). As a result, the coupling between the emitters of such dye and the exotic modes of the proposed structure was weak.

Furthermore, the resulting enhancement of the radiative decay rate due to the *Purcell* effect can also be observed through lifetime shortening. However, lifetime shortening can differ from a numerically calculated *Purcell factors*, since fluorescence lifetime is dependent mainly on the radiative and non-radiative rates. On the other hand, *Purcell factor* enhancements can be attributed to distinct factors such as local field intensity of the HMM structure, varied dye molecules orientations, as well as positions [100]. These different factors lead to variations between calculated *Purcell*

factor and experimentally attained decay rates in such a media. Also, it is noteworthy that emission lifetimes of the polymer-based HMM structure may vary at different characterization spots due to different emitter orientations and their various separation distances from the metallic layers. As such, to estimate reliable decay rate results, we measured the fluorescence lifetimes of each sample at several spots to attain their collective mean values and standard deviations. Average lifetime values of [$\approx 0.66 \pm 0.0064$, $\approx 0.78 \pm 0.0044$, and $\approx 0.41 \pm 0.0043$] ns were attained for (Rh590, PYR650, and LDS798) dyes inside HMM structures, respectively.

3.2.4 Summary

In conclusion, a study on a polymer-based planar HMM structure and its exotic features as well as its relation to emitters when coupled to it is presented. The existence of their non-radiative high- k modes per numerical formulations is also shown as well as a study of their ENZ features. From these features, **P2** illustrated how this interesting feature of the HMM structure can be extended to SE engineering by looking at the dynamics of the emission and decay rate of different dyes incorporated with a polymer-based HMM structure. Additionally, the increase in the non-radiative decay channels of the polymer-based HMM structure is demonstrated to be responsible for the average lifetime shortening and luminescence intensity rise of emitters embedded within and on top of the structure. With emitters spectrally closer (Rh590) to the ENZ region of the polymer-based HMM structure, **P2** illustrated a relatively strong shortening of the average lifetime as compared to other emitters spectrally close (PYR650) or far (LDS798) from the ENZ region. This observation confirmed the increase in non-radiative decay channels of the polymer-based HMM structure with a gain medium at the ENZ region. Furthermore, this work revealed that our proposed dye-doped polymer-based HMM structure compensates for the losses in a metal-dielectric HMM structure by observing an enhanced transmittance in the presence of a pump source and numerically implemented the sub-wavelength two dipoles resolution [not shown here] to emphasize the relevance of incorporating emitters into a passive polymer-based HMM structure. The interesting properties of our proposed polymer-based HMM structure could be a paradigm shift to enhance the relevance of HMM structures in nano-imaging and quantum optics applications.

4 CYLINDRICAL METAMATERIAL

In the previous discussions, we identified that the formations of planar metamaterials are one of the prominent engineering techniques that have helped to elucidate different classical or semi-classical optical phenomena in the nanoscale. Nevertheless, in real media; a total of approximately eight (8) layers are estimated to be the threshold to observe these interesting hyperbolic features [64] as stated in section 3.1.2. From the fabrication point of view, it is difficult and time-consuming to fabricate multilayered structures layer-by-layer. As such, using alternative measures to attain similar or advanced features with minimal layer depositions could be of great relevance. Therefore, research efforts to alleviate these fabrication constraints per planar metamaterials have generated a new paradigm shift in cylindrical metamaterials using self-rolling mechanisms, normally called rolled-up nanomembranes. These metamaterials will be discussed in the subsequent sections to elucidate some of their interesting properties both classically and in the quantum regime.

4.1 Rolling mechanism

Primarily, it is known that moment drives a static object to rotate in classical physics. As the formation of cylindrical metamaterials depends on a rolling process, a nonzero moment must exist to initiate the rolling-up mechanism in such metamaterials. From the continuum strain theory, this moment comes from either strain relaxation or external forces which act as the driving mechanisms for the formation of 3D structures in terms of rolled-up nanotechnology. As such, the most crucial component and deterministic aspect in rolled-up nanotechnology are the techniques to induce and manipulate strain gradients $\Delta\epsilon$, perpendicular to the nanomembranes system or external forces acting on the membranes.

Using the classical bending theory, Stoney et al. in 1909 [101], derived a mechanical model to explain the bending radius of a thick substrate with a thin strained layer

deposited on top of it as presented in Fig. 4.1 (a). From Fig. 4.1 (a), it is evident that depending on the stress on a film deposited on a substrate, the film can experience either tension or compression. As such, this model can help to estimate the stress in thin films by measuring the curvature of the film which can be expressed as

$$R_{St} = \frac{\rho \delta^2 d_2}{6\epsilon_s}, \quad (4.1)$$

where R_{St} is the bending radius, d_1 and d_2 are the thicknesses of the substrate and the thin film, and ϵ_s is the film strain. $\rho = Y_1/Y_2$ is the ratio of the strain Young's moduli and $\delta = d_1/d_2$ is the ratio of the thickness. Timoshenko [102], however, while studying heat-induced bimetal stripe (thermostat) bending with different thermal expansion coefficients, expanded the Stoney model for a substrate and film of equal thickness [See Fig. 4.1 (b)] with bending diameter:

$$D_{Ti} = \frac{d_2}{3(1+\nu)\epsilon_s} \frac{1 + 4\rho\delta + 6\rho\delta^2 + 4\rho\delta^3 + \rho^2\delta^4}{\rho\delta(1+\delta)}, \quad (4.2)$$

where ν is the Poisson's ratio and ϵ_s denotes the in-plane biaxial strain between the layers. This continuum mechanical model works well in predicting the diameters of rolled-up nanostructures by considering their intrinsic strain gradient as shown in Fig. 4.1 (b). From Eq. (4.2), it is evident that the bending curvature of a rolled-up nanomembrane depends on its strain gradient and thicknesses.

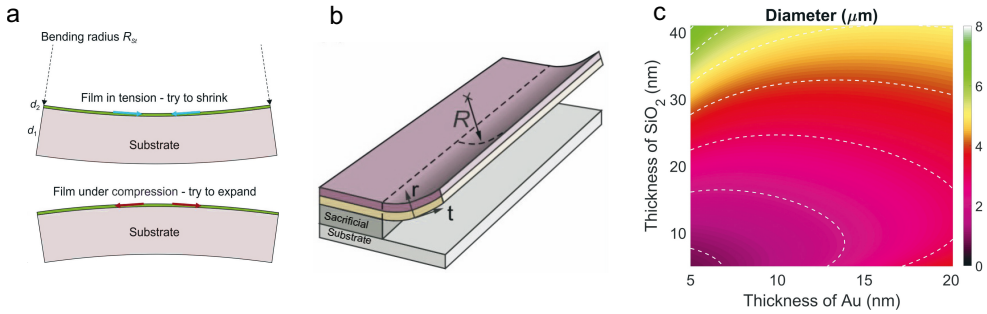


Figure 4.1 (a) Bending schematic of a thick substrate owing to tensile strained (top) and compressed (bottom) thin film. (b) Bent bilayer film schematic with a radius of curvature R and a strain gradient. (c). Numerically predicted diameters of a rolled-up structure composed of a metal (Au) and dielectric (SiO₂).

As such, selecting different thicknesses of a metal (Au) and dielectric (SiO₂) pos-

sessing varied intrinsic strain properties can generate varied diameters as shown in Fig. 4.1 (c). It can be seen that thicker materials could generate larger diameters [103]. Nevertheless, note that modification of this formulation can be investigated, by considering the effect of surface stress generated in ultrathin nanomembranes [104].

In this study, we will focus on strain engineering/relaxation as the driving mechanism for generating rolled-up nanomembranes. However, external forces also contribute to rolled-up nanotechnology by either enhancing or manipulating the total strain gradient or inducing the rolling process of some specific types of materials. These include ultrasonic treatment [105, 106], surface adsorption [107, 108], van der Waals forces [109], and surface tension [110, 111] mechanisms, among others.

4.1.1 Strain engineering techniques

In terms of strain engineering methods, the intrinsic property, strain gradient can be generated through different mechanisms such as lattice mismatch in a heteroepitaxial crystalline bilayer, thermal response properties of different materials, and/or non-epitaxial deposition techniques, among others. These techniques will be discussed in this section and geared toward the method implemented in this work.

Heteroepitaxial formed bilayer's strain gradient, for instance, originates from the different lattice constants of varied materials. An example of such is using GaAs-InAs bilayer system which was first reported by Prinz et al. [112] in 2000. Such epitaxially [molecular beam epitaxy (MBE)] grown semiconducting materials exhibit a strain gradient owing to their different lattice constants, thereby resulting in microtubes upon etching its sacrificial layer (AlAs). Regarding the lattice constant variations, indium (In) has a higher lattice constant than Ga [113]. Thus, when a layer of GaAs is epitaxially grown on the crystalline InAs, the upper layer would be stretched to fit the lattice constant of the lower which generates a tensile strain in the GaAs layer, while the InAs layer experiences a compressive strain. As a result, the InAs layer initiates a propensity to expand while the GaAs resist this expansion, thereby generating a net momentum that drives the planar structures into cylindrical microtubes. A similar mechanism can be realized in other epitaxy materials systems, such as AlN/GaN [114] and SiGe [115, 116].

Non-epitaxial methods such as electron-beam (e-beam) evaporation, magnetron sputtering, and ion plating are alternatives to heteroepitaxial-produced bilayers. Us-

ing these methods, it is also possible to create nanomembranes with a built-in strain gradient [117, 118]. An example of such a strained metal nanomembrane is Cr which can be deposited via electron-beam evaporation [119, 120]. However, non-epitaxial methods are not restricted to metal films and as such, insulators like Si_xN_y have also been at the forefront of this technique. Depending on the deposition conditions, the strain generated within Si_xN_y can either be tensile or compressive [121, 122].

Non-epitaxial techniques have clear advantages over epitaxial deposition techniques which require MBE mechanisms, in that, they are significantly less expensive and can accommodate materials with low refractive index. Per the discrepancies in deposition parameters of different materials in the non-epitaxial method, a strain gradient can be generated. This technique is employed in this work by utilizing a slow e-beam deposition rate for SiO_2 [layer 1] and a relatively high rate for Au [layer 2] to generate a strain gradient between the two layers. In such a configuration, as shown in Fig. 4.2 (a), the bottom layer and the top layer are deposited at different rates, and due to their different grain sizes, the two layers exert different stress levels which can induce rolling process when its sacrificial layer is etched. Fig. 4.2 (b) illustrates the schematic of the microtubes formed after the rolling process [103, 123]. However, these mechanisms also have their constraints as the deposition criteria require a strained nanomembrane besides the functional material of interest. This might influence the characterization of such functional materials of interest.

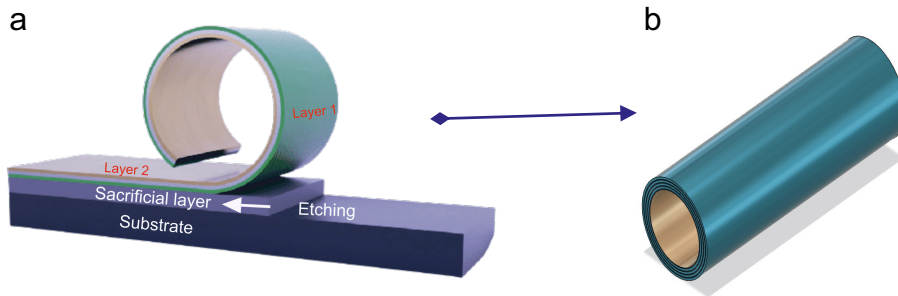


Figure 4.2 (a) Upward self-rolling process schematic based on the non-epitaxial technique. (b) A rolled-up and ready cylindrical metamaterial schematic.

Contrary to the two techniques outlined above, which introduce strain gradient during the deposition of nanomembranes, strain can also be generated inside a membrane system in response to an environmental change. Some of which in-

clude swelling strain [124] used in the construction of 4D mesostructures [125], thermal response strain [117, 126], strain from surface reconstruction [104, 127], and topochemical transformation strain [128], among others.

4.1.2 Release mechanism

Among the strain engineering approaches outlined in section 4.1.1, the fabrication process of rolled-up nanotechnology often necessitates a detach operation to free the generated nanomembranes from their substrate and mold them into 3D structures. During fabrication, a sacrificial layer is typically added between the nanomembranes and the substrate to help initiate the detach operation. This layer, in principle, separates the nanomembrane from its bulk, and the lateral etching of it detaches the freestanding membrane which results in the rolled-up structure. Here, we will discuss the release mechanisms (i.e., ultrasonic-treatment, dry, and dominant wet cases) utilized in rolled-up nanotechnology.

In the dry and ultrasonic-treatment release mechanisms, either a gaseous etchant or ultrasonication-generated forces [129] are needed to remove a selective sacrificial layer or to weaken the bonding between the nanomembranes and its substrate, respectively, to induce the rolling process. For example, the use of gaseous xenon difluoride (XeF_2) etchant to remove Ge sacrificial layer [130] or hydrogen fluoride (HF) in the vapor phase to etch SiO_2 sacrificial layer in the dry release mechanism [131]. Importantly, because these two mechanisms do not require use of photolithography processes, fabrication does not require use of cleanrooms. However, such fabrication processes, for instance, the dry release mechanisms use dangerous etchants that can be harmful to the environment. Alternatively, the ultrasonic-treatment release mechanisms are also limited to the number of nanomembranes and usage [129].

In the wet release mechanism, different chemical etchants have been employed for selective sacrificial layers to detach the nanomembranes from their respective substrates. An example is the removal of the AlAs sacrificial layer used in GaAs–InAs nanomembrane with a dilute HF solution [112], removal of Ge sacrificial layer used in Si/SiGe and SiN_x nanomembrane with an H_2O_2 solution [132, 133], the removal of buried oxide sacrificial layer utilized in compound materials on insulator (XOI)-based systems using HF solution [134, 135], and the removal of sacrificial aluminum layers in KOH-based etchant [136].

Also, the usage of polymers as a sacrificial layer in the wet release mechanism has been demonstrated to be a prominent detaching mechanism in non-epitaxial strained materials. This technique was demonstrated by Mie et al. [137] to alleviate the drawbacks in conventional fabrication, where the necessity for high etching selectivity has hampered the choice of materials. In this technique, varied inorganic materials including metals [138, 139], insulators [137], and their combinations [140, 141] can be employed to fabricate rolled-up nanomembranes. Per their fabrication criteria, a photoresist layer is first patterned on a substrate by photolithography. Non-epitaxial physical or chemical vapor deposition is then used to deposit the strain-engineered materials. The sacrificial photoresist dissolves in acetone or other organic solvents without corroding the inorganic components, and the nanomembrane rolls up into a tubular configuration. This technique has been realized in various applications including optical resonators [137], metal jet engines [142], gas detectors [143], and fluidic sensors [144], among others. Despite its numerous applications, the polymer-based mechanism also possesses some drawbacks in terms of accurately determining the strain gradient generated within the nanomembranes and having more control over the rolling process as well as attaining rolled-up nanomembranes with relatively smaller diameters. To overcome these constraints, we utilized a two-step lithography technique to fabricate our desired rolled-up tube and explored some of its interesting classical and quantum applications.

4.1.3 Two-step lithography technique

In terms of the two-step lithography process, a monolayer of Hexamethyldisilazane (HMDS) is coated to a cleaned silicon (Si) substrate at 125° Celsius (C) to improve the photoresist's adherence. Following that, we spin coat image reversal resist AZ5214E at 3000 rounds per minute (rpm) for 40 seconds (secs) and soft bake at 100 °C. The coated samples are exposed to ultraviolet light (UV) using a Suss MA6 mask aligner for 4 secs. The exposed samples are baked at 115 °C for 2 minutes (mins). For the image reversal process, the samples were exposed to UV light for 30 secs without a mask. The rectangular pattern ($25 \times 25 \mu\text{m}^2$) appears once the exposed samples were developed for 60 secs using MIF 726 developer and then rinsed three (3) times in deionized (DI) water. The developed samples are coated with 40 nm of Ge which serves as a sacrificial layer. The unwanted material is removed using the lift-off process, by

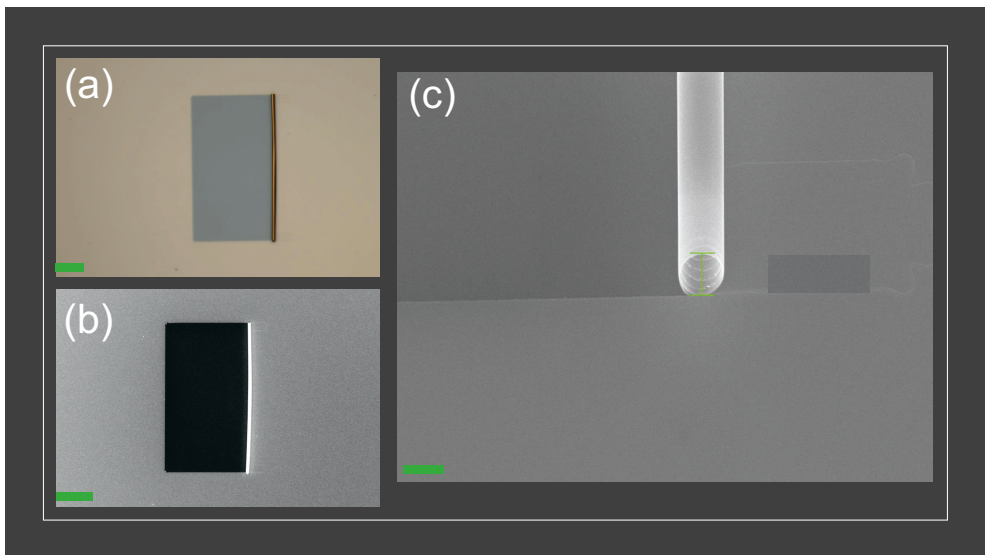


Figure 4.3 (a) Microscope and scanning-electron microscope image (b) of the full rolled-up nanostructure from the top and from the side (c) showing also the cross-section with a diameter of 700 nm. The green scale bar is 9 and $10\mu m$ for the microscope and scanning-electron microscope, respectively. Adapted from [P3].

leaving the samples in S1165 remover at $80\text{ }^{\circ}\text{C}$ and sonicated for 2 mins. Once rectangular structures of 40 nm of Ge are achieved the sample is again coated with HMDS and positive resist AZ3012E with the same speed and time. The coated samples are soft baked at $90\text{ }^{\circ}\text{C}$ for 90 secs and exposed to a second mask to create a window for etching the Ge layer. The exposed samples are hard-baked at $110\text{ }^{\circ}\text{C}$ for 60 secs. This time samples are developed for 1 min in MIF 726 developer and rinsed under the DI water. The developed samples are coated with 5 nm of SiO_2 , 1 nm of titanium (Ti) as an adhesive layer, and 10 nm of Au. The difference in the deposition rate and material densities during the deposition process inherits different strains as introduced in section 4.1.1. The SiO_2 undergoes compressive stress, while Au with a high deposition rate will have tensile stress. The two opposite stress conditions when released by etching the bottom Ge layer for 120 min in 35% H_2O_2 , will start rolling the SiO_2 and Au in the upward direction. Thus, in general, rolled-up nanotechnology can be used with a variety of material systems to generate 3D rolled-up tubes from a stack of two-dimensional (2D) structures as long as the desired nanomembrane and the sacrificial layer can be etched with a selective etchant. Notably, the thicknesses of the SiO_2/Au and the use of Ge as etch layer tightly roll the tubes to achieve a small diam-

eter of 700 nm, reported for the first time in **P3**. Microscope and scanning-electron microscope image of the full rolled-up nanostructure is shown in Fig. 4.3.

4.2 Applications

After elucidating the practical realization of the rolled-up nanotechnology using the two-step lithography processes in achieving a metamaterial with cylindrical geometries, we looked at some of its peculiar and intriguing characteristics as well as some practical applications in areas such as imaging, super-scattering, and ENZ properties.

4.2.1 High-resolution imaging

In imaging techniques, for instance, it is often not possible to image subwavelength features using conventional optics due to the diffraction limit. This limit causes the resolution of conventional imaging devices to be limited to a minimum distance, as described by the Rayleigh criterion [84]. To overcome this limitation, researchers have explored the use of hyperbolic media, which have interesting anisotropic dispersion and can support high- k modes that allow for the recovery of evanescent components in the far field [145]. These high- k modes discussed in chapter 3 can convey finer details of an object, while low k -vector components encode larger geometric characteristics. As a result, experimental efforts have included the use of rolled-up nanotechnology in hyperlens applications [146] due to the hyperbolic dispersion relation of these media.

In theory, a plane wave illuminating an object can be described mathematically as a Fourier superposition of plane waves that can be expressed in the basis of the cylindrical wave as

$$e^{ikx} = \sum_{m=-\infty}^{\infty} i^m J_m(kr) e^{im\theta}, \quad (4.3)$$

where k is the wavevector's magnitude, i is the imaginary unit, $J_m(kr)$ stands for the Bessel function of the first kind, m is the cylindrical wave's angular momentum mode number, and r and θ represent the cylindrical coordinates (i.e., distance from the origin and azimuthal angle, respectively). In this form, retrieving the scattering amplitudes and phase shifts of the various component angular momentum modes is analogous to reconstructing an image. This may be viewed as several information

channels through which the information about the object at the origin is conveyed to the far field.

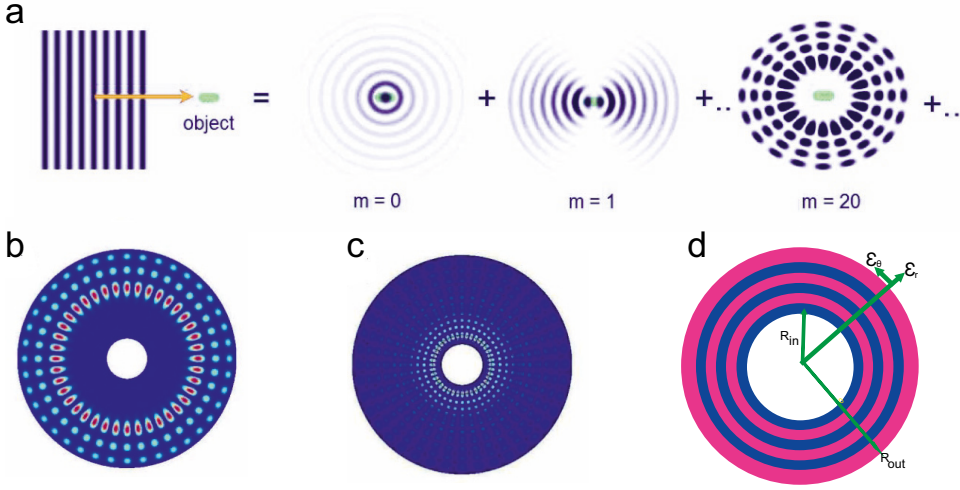


Figure 4.4 (a) Cylindrical wave basis expansion of a plane wave scattered by an object (in green). Low electric field intensity areas are depicted in light blue, whereas high electric field intensity areas are displayed in deep blue. (b) High angular momentum modes in an isotropic cylindrical medium and (c) in an anisotropic cylinder made of an effective hyperbolic medium with dielectric permittivities having different signs in the tangential and radial directions ($\epsilon_\theta > 0$, $\epsilon_r < 0$). (d) Front-view cross-section of a possible practical realization of a hyperlens, consisting of alternating concentric metal and dielectric layers. Adapted (a), (b), (c) from [145].

According to Fig. 4.4(a), the scattering of an incident plane wave to a target (in green) demonstrates different angular momentum modes, with the regions of high (low) intensity being portrayed as deep (light) blue field responses. The radial component of the electric field in a typical isotropic material as shown in the figure rapidly decays near the origin as m increases. This can be seen as a result of the conservation of angular momentum $m = k_\theta r$, which indicates that a larger tangential wavevector component corresponds to a gradually decreasing distance from the center where $k_\theta \approx 1/r$. As discussed in chapter 3, in an isotropic medium, the allowable radial and tangential components of the wave vector lie on a circle due to their dispersion relation

$$k_r^2 + k_\theta^2 = \epsilon \frac{\omega^2}{c^2}, \quad (4.4)$$

where the arbitrarily growing value of k_θ yields an imaginary or evanescent radial component k_r near the origin. Conversely, in a hyperbolic media with strong cylindrical anisotropy where the dielectric permittivities have different signs in the tan-

gential and radial directions ($\varepsilon_\theta > 0$, $\varepsilon_r < 0$), the dispersion relation of the extraordinary modes can be expressed as

$$\frac{k_r^2}{\varepsilon_\theta} - \frac{k_\theta^2}{|\varepsilon_r|} = \frac{\omega^2}{c^2}, \quad (4.5)$$

where the radial component ε_r of the wave vector grows as the tangential component ε_θ does in the direction of the center. This phenomenon arises due to unbounded values of wavevector k at a finite frequency, allowed by the hyperbolic dispersion relation in Eq. (4.5). Comparing the field distribution in an isotropic medium [Fig. 4.4 (b)] to that in a metamaterial [Fig. 4.4 (c)] with cylindrical hyperbolic anisotropy reveals that, in the latter case, in addition to the mode penetrating toward the core, the distance between the field nodes at the core gradually reduces, allowing for sub-wavelength probing of spatial details. As a result, utilizing the rolled-up nanotechnology technique to produce such a cylindrically-based system as discussed in section 4.1.3 with strong anisotropy [Fig. 4.4 (d)], can carry information about the detailed structure of an object placed within the core to the far field with a resolution factor of

$$\Delta \propto \frac{R_{\text{in}}}{R_{\text{out}}} \lambda. \quad (4.6)$$

R_{in} and R_{out} are the inner radius and outer radius of the cylindrical metamaterial. Likely, rolled-up nanotechnology can facilitate realizations of these systems with fast throughput and fewer deposition steps. Nevertheless, certain distinctive hyperbolic metamaterials with half-cylindrical orientation have also been used in these imaging techniques using electron-beam evaporation techniques [147, 148].

4.2.2 Enhanced scattering properties

In addition, cylindrical metamaterials can also be engineered to exhibit interesting scattering properties for varied photonic applications. These scattering properties of a cylindrical metamaterial describe how it interacts with incoming electromagnetic waves. The properties are influenced by several factors, including the geometry of the cylinder, the wavelength and polarization of the incident waves, the material composition and structure of the metamaterial, and more. For instance, a metamaterial with a high refractive index or a highly resonant response may show strong

scattering, while a metamaterial with a low refractive index or a weakly resonant response may display weak scattering [149]. Cylindrical metamaterials with these characteristics have been used in super-scattering applications, where the normalized scattering cross section (NSCS) of the system is greater than one. The high NSCS of these structures is due to constructive interference of multipolar resonances [150, 151].

Using the rolled-up nanotechnology approach, cylindrical multilayered metamaterials with superscattering capabilities can be created by designing the structure to have a high scattering cross-section, which is a measure of how well a material or structure scatters light. These metamaterials have the potential to be used in applications such as sensing, spectroscopy, imaging and others that require efficient manipulation of strong scattering or designed angular scattering patterns [150, 152].

To theoretically determine the scattering properties of a multilayered cylindrical structure, the same methods that were discussed in chapter 3 can be used, but with a cylindrical coordinate system (r, θ, z) as the basis. For instance, the core and shell of a simple cylindrical structure with radial anisotropy's relative permittivity tensors may be represented as [153]

$$\bar{\varepsilon}_i = \begin{bmatrix} \varepsilon_{ir} & 0 & 0 \\ 0 & \varepsilon_{i\theta} & 0 \\ 0 & 0 & \varepsilon_{iz} \end{bmatrix} \quad (4.7)$$

where ε_r and ε_θ are the radial tangential permittivity components. The governing equation for the magnetic field, H_z , after various analytical derivations based on Maxwell's equation is given as follows:

$$\frac{1}{r} \left[\frac{\partial}{\partial r} \left(\frac{r}{\varepsilon_{i\theta}} \frac{\partial H_z}{\partial r} \right) \right] + \frac{1}{r^2} \frac{\partial}{\partial \theta} \left(\frac{1}{\varepsilon_{ir}} \frac{\partial H_z}{\partial \theta} \right) + \omega^2 \varepsilon_0 \mu_0 \mu_{iz} H_z = 0 \quad (4.8)$$

where the μ_{iz} is the permeability tensor. Assuming $H_z = \Phi(r)e^{im\theta}$, the radial function $\Phi(r)$ is found to satisfy

$$r^2 \frac{d^2 \Phi(r)}{dr^2} + r \frac{d\Phi(r)}{dr} + \left(\omega^2 \varepsilon_0 \mu_0 \varepsilon_{i\theta} \mu_{iz} r^2 - m^2 \frac{\varepsilon_{i\theta}}{\varepsilon_{ir}} \right) \Phi(r) = 0. \quad (4.9)$$

As a result, the incident plane wave's magnetic field can be represented as [154]

$$H_{\text{in}} = \hat{z}H_0 \exp(ikx) = \hat{z}H_0 \sum_{m=-\infty}^{+\infty} i^m J_m(kr) \exp(im\theta), \quad (4.10)$$

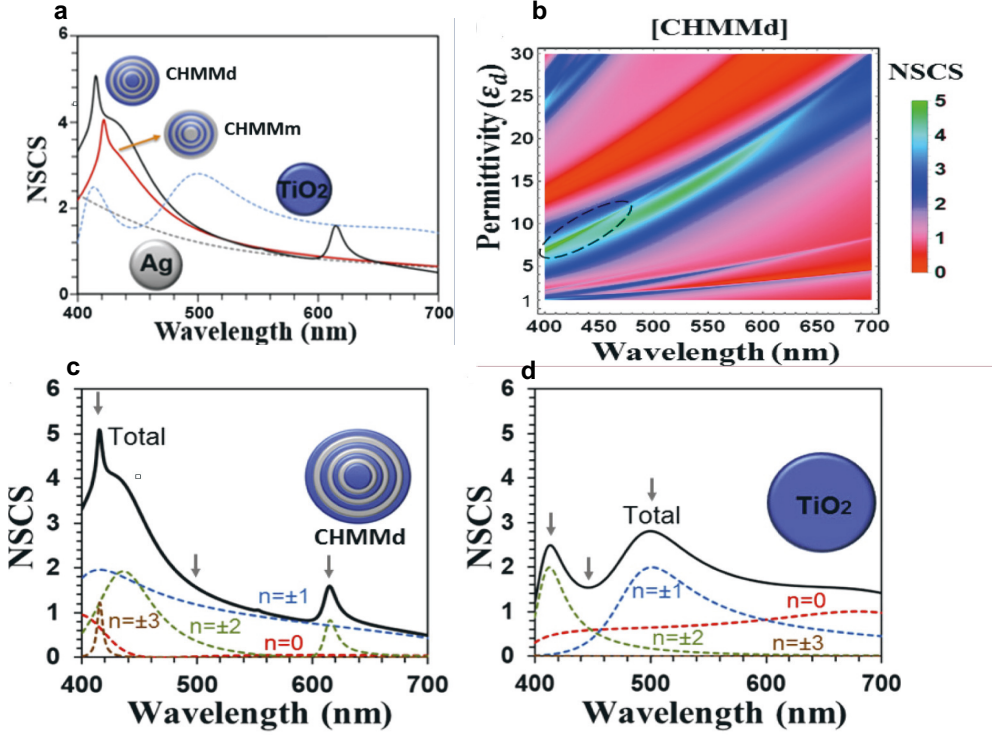


Figure 4.5 (a). NCS spectra for cylinder-shaped silver, TiO₂ and CHMM, with a similar outer diameter. (b). A density map of NCS as a function of wavelength and the dielectric permittivity for CHMMd. (c) and (d). Resonance modes overlap for CHMMd and TiO₂. Adapted from [150].

where r and θ are the cylindrical coordinates for the radial and azimuthal directions, H_0 is constant amplitude, J_m is the Bessel function of the first kind and mode order m , $k = k_0\sqrt{\epsilon}$, $k_0 = \omega/c$ is the wavenumber in a vacuum. For $r > r_N$, the scattered magnetic field in the environment medium can be written as

$$H_{\text{sca}} = \hat{z}_0 H_0 \sum_{m=-\infty}^{+\infty} d_m i^m H_m^{(1)}(kr) \exp(im\theta) \quad (4.11)$$

where the Hankel function of the first kind and mode order m is denoted by $H_m^{(1)}$ and accounts for the behavior of the wave at infinity. In the region within the medium,

however, the Bessel function is used to ensure that the wave remains finite at the center of the structure. The magnetic field in a given n -th layer of the rolled-up nanomembrane [for $r_{n-1} < r < r_n$] can also be written as

$$H_n = \hat{z}H_0 \sum_{m=-\infty}^{+\infty} i^m \left[b_{m,n} J_m(k_n r) + c_{m,n} H_m^{(1)}(k_n r) \right] \exp(im\theta), \quad (4.12)$$

where $k_n = k_0 \sqrt{\varepsilon_n}$. For $k_c = k_0 \sqrt{\varepsilon_c}$, ε_c represents permittivity of the core medium with a magnetic field expressed as [for $r < r_0$]

$$H_c = \hat{z}H_0 \sum_{m=-\infty}^{+\infty} i^m a_m J_m(k_c r) \exp(im\theta) \quad (4.13)$$

The coefficients $a_m, b_{m,n}, c_{m,n}$, and d_m are determined by imposing boundary conditions that ensure the continuity of electric and magnetic fields between the layers. These boundary conditions which are applied at the radius $r = r_n$ can be expressed in the matrix form as

$$D_{m,n}(r_n) \cdot \begin{bmatrix} b_{m,n} \\ c_{m,n} \end{bmatrix} = D_{m,n+1}(r_n) \cdot \begin{bmatrix} b_{m,n+1} \\ c_{m,n+1} \end{bmatrix}, \quad (4.14)$$

where the matrix $D_{m,n}(r_n) = \begin{bmatrix} \varepsilon_n J_m(k_n r_n) & \varepsilon_n H_m^{(1)}(k_n r_n) \\ \sqrt{\varepsilon_n} J'_m(k_n r_n) & \sqrt{\varepsilon_n} H_m'^{(1)}(k_n r_n) \end{bmatrix}$, with J'_m and $H_m'^{(1)}$ denoting the derivatives. Using the transfer matrix T_m as

$$T_m = \begin{bmatrix} T_{m,11} & T_{m,12} \\ T_{m,21} & T_{m,22} \end{bmatrix}, \quad (4.15)$$

$$T_m = D_{m,1}(r_0) \cdot \left\{ \prod_{n=1}^N [D_{m,n}(r_n)]^{-1} \cdot D_{m,n+1}(r_n) \right\},$$

relation between the scattering coefficients can be expressed as

$$\begin{bmatrix} a_m \\ d_m \end{bmatrix} = \frac{1}{T_{m,12}y - T_{m,22}x} \begin{bmatrix} -T_{m,11}T_{m,22} + T_{m,12}T_{m,21} \\ xT_{m,21} - yT_{m,11} \end{bmatrix}, \quad (4.16)$$

where, $x = \varepsilon_c J_m(k_c r_0)$, and $y = \sqrt{\varepsilon_c} J'_m(k_c r_0)$. Finally, the NSCS is expressed as

$$\sigma = \sum_{m=-\infty}^{+\infty} |d_m|^2 \quad (4.17)$$

From the above formulations, the full analytical NSCS of a multilayered cylindrical metamaterial can be determined as presented in Fig. 4.5. According to Fig. 4.5(a), the scattering spectra of various structures with the same outer diameter of 220 nm were compared to elucidate the enhanced scattering properties of the cylindrical multilayered structure as presented in [150]. It is evident that CHMMd (cylindrical multilayered metamaterial [CHMM] with both inner and outer layers made of a dielectric) and CHMMm (similar to CHMMd but with a metallic counterpart) exhibit an enhanced scattering peak at approximately 420 nm. The NSCS peak displays approximately twice the scattering intensity of bare silver (Ag) or TiO₂ cylinders with the same diameter. Based on these observations, it is evident that cylindrically rolled-up metamaterials can achieve superscattering properties which can be utilized in varied photonic applications [150]. Figure 4.5(b) also illustrates the heatmap of the CHMMd NSCs for different parametric permittivity sweeps. This shows that different materials utilized in this strain-engineering technique can possess different NSCS due to their varied permittivity values and Fig. 4.5 (c) and (d) illustrate the overlap of different resonance modes for CHMMd (a type of multi-layered structure) and a homogeneous TiO₂ cylinder. Evidently, the occurrence of the different resonance modes overlaps helps to attain the enhanced NSCS. These modes are described to be linked to the magnetic dipole ($n \equiv m = 0$), electric dipole ($m = \pm 1$), electric quadrupole ($m = \pm 2$) resonant modes, and other higher-order modes [155].

To analyze the optical properties of cylindrical multilayered structures (CHMMs) and reduce the computational effort required, researchers have developed alternative homogenization methods such as planar effective medium approximation (PEMA) and cylinder effective medium approximation (CEMA) [145, 154]. These methods enable the understanding of the optical properties of CHMMs while satisfying the condition $h \ll \lambda \ll r$, where h is the thickness of the layers in the structure and λ is the wavelength of light. In PEMA, the radial ε_r and azimuthal ε_θ is presented as

$$\varepsilon_r = (f_m/\varepsilon_m + f_d/\varepsilon_d)^{-1}, \quad \varepsilon_\theta = \varepsilon_z = f_m \varepsilon_m + f_d \varepsilon_d, \quad (4.18)$$

where f_m and f_d are the filling fractions of metal and dielectric layers in the structures, with permittivities ε_m and ε_d , respectively. This formulation however ignores the curvature of the layers, leading to limitations in its accuracy. In contrast, CEMA takes into account the curvature of the layers, making it a more accurate method for analyzing CHMMs. The CEMA model is also given as [150]

$$\varepsilon_r = \log(r_N/r_0) \left(\sum_{n=1}^N (\log(r_n/r_{n-1})/\varepsilon_n) \right)^{-1}, \quad (4.19)$$

$$\varepsilon_\theta = \varepsilon_z = (\log(r_N/r_0))^{-1} \left(\sum_{n=1}^N (\log(r_n/r_{n-1})\varepsilon_n) \right), \quad (4.20)$$

where r_N and r_0 illustrate the inner and outer radius of the multilayered cylinder with r_n denoting the radius of the n -th layer. The effective permittivities in the CEMA model depend on the radial distance of the individual layers, while the effective permittivities in the PEMA model only depend on the filling fraction of the materials. In our previous work [103], we used the CEMA formulation to determine the structural ENZ characteristics of different diameters of rolled-up metamaterials and elucidated some interesting optical responses of the structure. In addition, we studied some photonic properties of the structure by numerically predicting its employments in waveguide applications. In the subsequent section, we will discuss these in detail and see how the interesting properties of the fabricated rolled-up metamaterial can be extended into the quantum regime.

4.3 Near-zero-index feature of a cylindrical media

As mentioned earlier in **(P2)**, the integration of emitters into metamaterials opens an exciting opportunity to study emitters in tailorable dielectric or plasmonic environments, especially in the stretched mode ENZ medium. Rolled-up metamaterials, on the other hand, as discussed in **(P3)**, are also a type of 3D metamaterial that is created by stacking 2D planar structures and they possess interesting optical properties [156], as demonstrated in early studies on fishnet [140, 157, 158] and Terahertz (THz) metamaterials [159]. One potential application of these materials is using them as waveguide reservoirs for quantum emitters, which could increase the interaction between optical fields and quantum systems and exhibit enhanced energy

transfer and efficient inter-emitter interactions similar to other proposed plasmonic waveguides [160–162]. In particular, plasmonic waveguide channels with rectangular configurations have been found to support extraordinary optical transmission when excited and have been used in the subwavelength regime to mediate long-range interactions of quantum emitters [163, 164]. Li *et al.* [160] conducted a comparative study of ENZ and plasmonic waveguide channels to enhance efficient long-range resonance energy transfer and inter-emitter entanglement. While plasmonic waveguide types such as V-shaped grooves and cylindrical nanorods have been shown to outperform the sub-wavelength distance limitations of quantum emitters’ cooperative emission in a homogeneous medium, their usefulness in practical applications is limited due to their dependence on the spatial position of emitters [163]. As a result, various techniques have been implemented to overcome these challenges [160–163]. In this section, we explore the interesting properties of the rolled-up nanomembrane in the quantum regime.

To comprehend the possibility of employing rolled-up nanomembranes as quantum reservoirs, their photonic properties will be examined. This includes analyzing the corresponding zero-index mode (i.e., fundamental TE_{11} mode) at the cutoff wavelength, where there is minimal phase variation. As a guide to determine the fundamental mode of the rolled-up metamaterial composed of an alternating layer of metal and dielectric, we numerically implement the dispersion relation for a homogeneous circular waveguide with an air core [165]. The dispersion relation is mainly calculated to identify the cutoff wavelength, where the propagation constant $k = 0$. At this wavelength, the electromagnetic waves can be squeezed or tunneled through a waveguide to exhibit a similar response as zero-index materials [166]. This phenomenon relative to circular waveguides has been demonstrated theoretically by Pan *et al.* [167] to exhibit interesting electromagnetic tunneling which is independent of the waveguide length. In principle, the cutoff wavelength as a function of the effective mode index of a circular hollow waveguide can be expressed analytically as

$$n_{\text{eff}} = \sqrt{1 - \left(\frac{u_{\text{nm}}}{\pi}\right)^2 \left(\frac{\lambda}{2\rho}\right)^2}, \quad (4.21)$$

where n_{eff} is the effective index as a function of dielectric core diameter, u_{nm} is the root of the Bessel function, ρ is the radius of the circular core, and λ is the wavelength. The appropriate root of the Bessel function considered is 3.832 since our

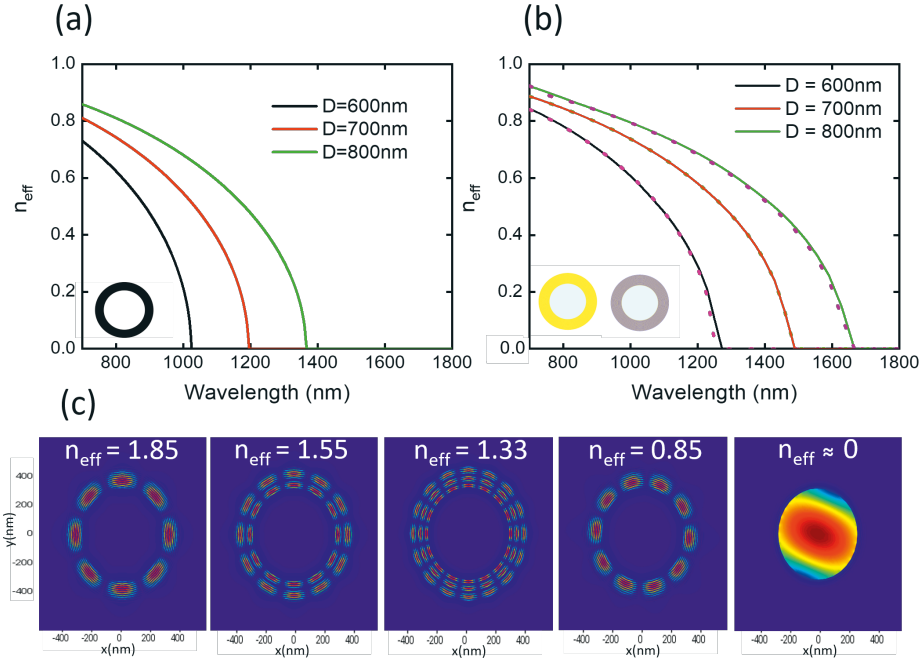


Figure 4.6 (a). The dispersion relation of a cylindrical hollow waveguide with different core diameters D . The black circular inset represents the schematic of the homogeneous circular waveguide. (b). The dispersion relation of the rolled-up zero-index waveguide (solid lines) [grey circular inset]. The dotted lines in (b) show similar dispersion calculated for the cylindrical hollow metallic waveguide [yellow circular inset]. The cutoff wavelength varies as a function of D in both figures (top panel). (c). The different electric $|E|$ field mode profiles excited in the rolled-up zero-index waveguide for different effective indices (n_{eff}) with $n_{\text{eff}} \approx 0$ depicting the fundamental TE_{11} mode. Adapted from [P3].

mode of interest is the fundamental TE_{11} mode.

Figure 4.6 (a) shows the analytical calculation of the dispersion relation of a cylindrical dielectric waveguide. This served as a benchmark as stated earlier, to determine the cutoff frequency of the rolled-up metamaterial dubbed rolled-up zero-index waveguide as presented in Fig. 4.6 (b) for different diameters D . The different core diameters of both the homogeneous cylindrical and zero-index hollow waveguides illustrated a redshift of the cutoff wavelength. This shows the dependence of the cutoff wavelength on the material dimensions. The dispersion of the cylindrical hollow metallic (Au) waveguide [dotted lines] follows a similar trend as the rolled-up zero-index waveguide, as shown in Fig. 4.6 (b). Figure 4.6 (c), however, shows the complex modes of the rolled-up zero-index waveguide at different effective indices.

Evidently, these modes are mostly confined to the metal–dielectric cladding region due to the excitation of plasmon modes, except for the fundamental mode with an effective index close to zero, which has a similar dispersion relation to the fundamental modes of the plasmonic hollow waveguide. This fundamental mode, with an effective index close to zero $n_{\text{eff}} \approx 0$, offers new ways to control and enhance the propagation of optical fields due to its infinite phase velocity of the tunneled electromagnetic wave as illustrated in Fig. 4.7. Based on these interesting properties of the rolled-up nanomembrane and its possible quantum emitters (qubits) integration techniques, we explored their quantum entanglement applications with qubits in **P3** and **P4** which will be discussed in the section below.

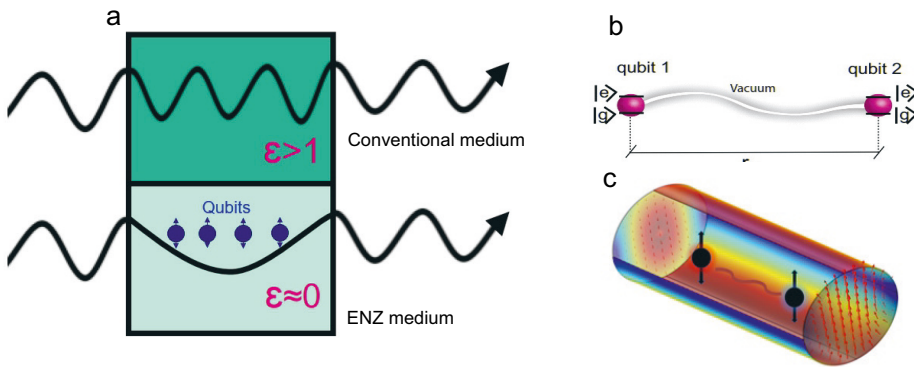


Figure 4.7 Schematics depicting (a) the mode propagation trends in a conventional and epsilon-near-zero (ENZ) medium. The inset in (a) depicts the quantum emitters. (b) qubit–qubit interactions in free space and (c) show similar interactions in a rolled-up ENZ waveguide.

4.3.1 Quantum extension

The concept of entanglement, or non-separability, between qubits, is important in various quantum processes such as quantum cryptography and teleportation [161, 162, 168, 169]. While entanglement has traditionally been observed in systems like atoms and ions, it is becoming increasingly accessible in other areas of quantum physics [163, 170]. Specifically, short-distance entanglement has been observed in quantum dots, nanotubes, and molecules, but long-range qubit–qubit interactions are necessary for long-distance information transfer [171–173]. One way to facilitate this is through the use of plasmonic waveguides, which are engineered to have interesting optical properties such as a near-zero refractive index and infinite phase

velocity at the nanoscale. Numerical studies on rectangular ENZ reservoir [160, 174] showed that ENZ media outperform the subwavelength distance limitations of qubits cooperative emission in a homogeneous medium. However, the difficulties to incorporate quantum emitters in a rectangular waveguide and their fabrication challenges in the nanoscale regime have hampered their practical use.

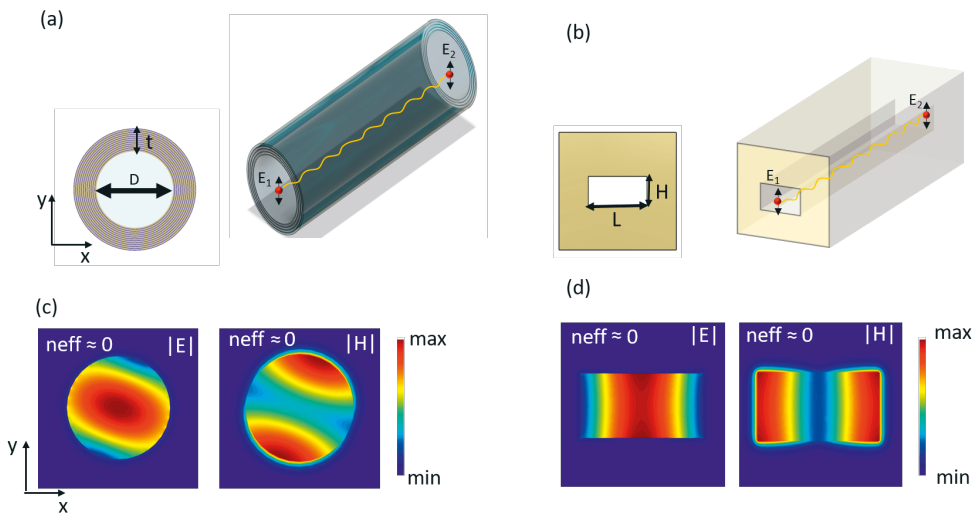


Figure 4.8 Schematics of (a) rolled-up ENZ, and (b) rectangular ENZ waveguide with their corresponding cross-section in the x - y plane. E_1 and E_2 represent the two quantum emitters interacting with the corresponding ENZ waveguides. (c) The electric $|E|$ and magnetic $|H|$ fields of the fundamental TE_{11} mode (zero-index mode) of the rolled-up ENZ waveguide, and (d) the fundamental TE_{10} mode (zero-index mode) of the rectangular ENZ waveguide. Reproduced from [P4], with the permission of AIP Publishing.

As a result, we introduced the rolled-up ENZ waveguide to serve as a reservoir to mediate qubit-qubit interactions at long distances and the emergence of driven steady-state entanglement under continuous double pumping. Based on these two experimentally validated ENZ waveguide channels [55, 175], we numerically computed their relations with quantum emitters when used as a quantum reservoir to ascertain the final state of the system. This study adopted ENZ waveguides into quantum systems which can be relevant in generating distinctive optical sources, robust entangled states, and other innovative optical applications in different fields of study.

In the numerical implementations, Ansys Lumerical software was used to determine the cutoff wavelength of both the rolled-up and rectangular ENZ waveguides

in order to ascertain the equivalent fundamental mode of the waveguide. Figure 4.8 demonstrates the schematics (top panel) and field distributions (lower panel) (i.e., electric $|E|$ and magnetic $|H|$ fields) of the rolled-up and the rectangular ENZ waveguide. As compared to the TE_{10} mode of the rectangular ENZ waveguide transverse to its propagation direction, the numerically calculated ENZ mode for the rolled-up ENZ waveguide exhibit TE_{11} mode with the existence of both radial and axial components of the transverse fields due to its symmetry. Also, the waveguide dimensions were optimized and set to attain the same cutoff wavelength of $\lambda_0 \approx 1400$ nm. The rolled-up ENZ waveguide has a diameter (D) of 700 nm and thickness (t) of 180 nm (i.e., 12 layers) with 5 nm of gold (Au) and 10 nm of SiO_2 . The corresponding plasmonic (Au) rectangular ENZ waveguide has a dimension of 650×350 nm² (i.e., width (L) and height (H)), respectively.

After identifying the photonic properties of the ENZ waveguide channels in **P4**, we initiated the entanglement calculations of qubits coupled with the corresponding ENZ reservoirs. To measure the entanglement of the qubits coupled to the reservoir [161, 163], we used the concurrence C metric formalism by Wootters [176]. However, to determine this metric formalism, it is important to obtain the dyadic response of an emitter coupled to the rolled-up ENZ waveguide in comparison to the rectangular ENZ waveguide to determine their respective coupling parameters.

In **P4**, two identical qubits with the same transition frequency ω_0 were considered and embedded within the ENZ channels as compared with **P3** with single qubit resonance enhancements. By combining the dyadic Green's function with the quantum master equation formalism, the dynamic evolution of quantum systems coupled to lossy plasmonic environments is elucidated. The dyadic Green's function, which was briefly introduced in chapter 3, is a classical quantity used to investigate the spontaneous decay of quantum emitters coupled to a quantum reservoir. The dynamics of the two-qubit system density matrix ρ near a reservoir were described by the quantum master equation. In principle, assuming a weak excitation and weak coupling regime, the Born–Markov, and rotating-wave approximations can be used to compute the master equation, which is expressed as [177]

$$\frac{\partial \rho}{\partial t} = \frac{1}{i\hbar} [H, \rho] - \frac{1}{2} \sum_{i,j=1}^2 \gamma_{ij} (\rho \sigma_i^\dagger \sigma_j + \sigma_i^\dagger \sigma_j \rho - 2\sigma_i \rho \sigma_j^\dagger), \quad (4.22)$$

where the Hamiltonian H describing the coherent part of the evolutionary dynam-

ics is expressed as

$$H = \sum_i \hbar(\omega_0 + g_{ii})\sigma_i^\dagger\sigma_i + \sum_{i \neq j} \hbar g_{ij}\cdot\sigma_i^\dagger\sigma_j \quad (4.23)$$

From Eq. (4.22), ρ depicts the density matrix of the two-qubit system. $\sigma(\sigma^\dagger)$ represents the destruction (creation) operator applied to the qubits. The photonic Lamb shift g_{ii} due to the self-interaction of each qubit embedded within the ENZ waveguide is usually minimal and neglected in our formulations. g_{ij} also represents the coherent dipole–dipole interactions of the two identical qubits expressed as

$$g_{ij} = (\omega_0^2/\varepsilon_0 \hbar c^2) \text{Re} \left[\boldsymbol{\mu}_i^* \cdot \mathbf{G}(\mathbf{r}_i, \mathbf{r}_j, \omega_0) \cdot \boldsymbol{\mu}_j \right], \quad (4.24)$$

where the dyadic Green's tensor $\mathbf{G}(\mathbf{r}_i, \mathbf{r}_j, \omega_0)$ satisfies the classical electromagnetic equations for a point dipole source located at a position \mathbf{r}_j . Also, γ_{ij} represents the dissipative and noncoherent term of the master equation which is expressed as a function of the imaginary part of the dyadic Green's function

$$\gamma_{ij} = (2\omega_0^2/\varepsilon_0 \hbar c^2) \text{Im} \left[\boldsymbol{\mu}_i^* \cdot \mathbf{G}(\mathbf{r}_i, \mathbf{r}_j, \omega_0) \cdot \boldsymbol{\mu}_j \right]. \quad (4.25)$$

To solve the master equation and to obtain the density matrix, a convenient basis for the two-qubit system vector space must be defined. It was more convenient to work in the Dicke basis: $|3\rangle = |e_1\rangle \otimes |e_2\rangle = |e_1, e_2\rangle$, $|0\rangle = |g_1\rangle \otimes |g_2\rangle = |g_1, g_2\rangle$, and $|\pm\rangle = 1/\sqrt{2}(|e_1, g_2\rangle \pm |g_1, e_2\rangle)$, when studying identical emitters in equivalent positions, i.e., $\gamma_{11} = \gamma_{22} = \gamma$, where, $|e_i\rangle$ ($|g_i\rangle$) represents the excited (ground) state of the i -th qubit. The selected basis can be used to characterize the response of the two-qubit system since it leads to a diagonalized Hamiltonian H . In general, the entanglement between two qubits can be quantified by computing the concurrence C introduced by Wootters [176] expressed as

$$C = \max(0, \sqrt{u_1} - \sqrt{u_2} - \sqrt{u_3} - \sqrt{u_4}), \quad (4.26)$$

where u_i represents the eigenvalues of the matrix $\rho\tilde{\rho}$. $\tilde{\rho} = \sigma_y \otimes \sigma_y \rho^* \sigma_y \otimes \sigma_y$ is the spin-flip density matrix and σ_y is the Pauli matrix. The degree of concurrence is determined between 1 (completely entangled state) and 0 (unentangled state). However, to gain insight into the entanglement process between two emitters when only

one of the emitters is excited, a transient concurrence formulation can be derived from the master equation which is expressed as

$$C(t) = 0.5 \sqrt{\left[e^{-(\gamma+\gamma_{12})t} - e^{-(\gamma-\gamma_{12})t} \right]^2 + 4e^{-2\gamma t} \sin^2(2g_{12}t)} \quad (4.27)$$

According to Eqn. (4.27), $C(0) = 0$, because at $t = 0$, the quantum system is initially at an unentangled state. As time progresses, $t > 0$, the concurrence becomes larger than zero, meaning that the emitters become entangled. However, at some point the concurrence starts to decay with time and becomes zero again, $C(t) = 0$, after a long period of time ($t \rightarrow \infty$). Thus, the system needs to be sustained by an external source to prolong the entanglement. External pumps with the same frequency (ω_p) can, therefore, be used to pump each emitter embedded within the ENZ waveguide channels, to prevent the transient concurrence from decaying after some time and to achieve steady-state entanglement. In that case, an additional term $1/i\hbar[V, \rho]$ needs to be introduced in the right-hand side of the quantum master equation, where the operator

$$V = - \sum_i^2 \hbar \left(\Omega_i e^{-i\Delta_i t} \sigma_i^\dagger + \Omega_i^* e^{i\Delta_i t} \sigma_i \right) \quad (4.28)$$

characterizes the interaction between the pump field and the emitter. The parameter $\Omega_i = \mu \cdot E_{0i} / \hbar$ is the effective Rabi frequency of the pump that depends on the induced electromagnetic field E_{0i} from the optical source pumping the i -th qubit. The parameter $\Delta_i = \omega_0 - \omega_p$ is the detuning parameter due to the pump frequency ω_p . After expressing ρ in the usual basis $|e_1, e_2\rangle, |e_1, g_2\rangle, |g_1, e_2\rangle$, and $|g_1, g_2\rangle$, one can calculate the steady-state concurrence C_{ss} by solving numerically the master equation where the Rabi frequency and detuning parameter due to the external pumping have been included.

Following the above theory, we numerically computed the dyadic Green's response of a single emitter coupled to the ENZ waveguide channels. From the dyadic Green's function, the decay rate ($\gamma_{1,2}$) and dipole-dipole coupling interactions (g_{12}) of the qubit coupled to the waveguide channels were obtained. These coupling parameters (i.e., γ_{12} , g_{12}) were used in the quantum master equation to determine the evolutionary dynamics of the quantum system. Figure 4.9 (a) and (b) depicts the normalized decay rate γ_{12}/γ and the dipole-dipole interactions g_{12}/γ of qubits coupled to the rolled-up ENZ waveguide and the rectangular ENZ waveguide channels,

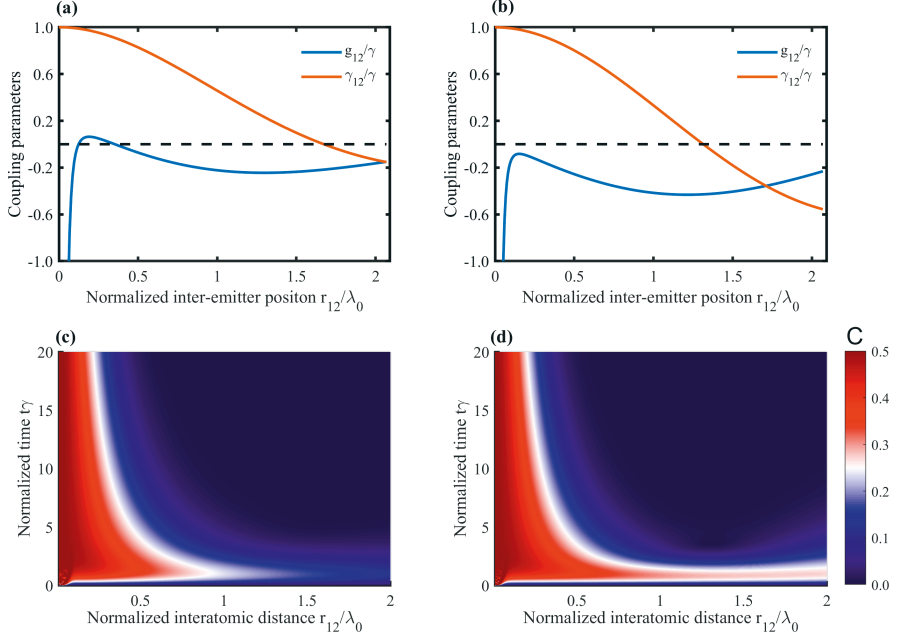


Figure 4.9 Normalized decay rate enhancement γ_{12}/γ and dipole–dipole interaction g_{12}/γ as a function of normalized interatomic emitter distance r_{12}/λ_0 of (a) rolled-up ENZ waveguide and (b) rectangular waveguide. The measure of entanglement as a function of concurrence C for (c) rolled-up ENZ tube and (d) rectangular ENZ waveguide. Adapted from [P4].

respectively. We discovered that the decay rate of the rectangular ENZ waveguide is faster as compared to the rolled-up ENZ waveguide. Compared to the rectangular ENZ waveguide, the decay rate of the rolled-up ENZ waveguide exceeds a normalized interatomic distance r_{12}/λ_0 of 1.5 before it goes to zero. Due to the high propagation and non-radiative losses of the rectangular waveguide, we see a faster decay rate $\gamma_{12}/\gamma = 0$ at normalized interatomic distance $r_{12}/\lambda_0 < 1.5$. Also, the normalized dipole–dipole interactions g_{12}/γ of the rolled-up ENZ waveguide increase appreciably above zero (0) at normalized interatomic emitter distance $r_{12}/\lambda_0 < 0.5$ as compared to the rectangular waveguide. Both waveguide channels exhibit a monotonic decrease in the spontaneous decay rate γ_{12} and dipole–dipole coupling g_{12} as a function of normalized interatomic distance r_{12}/λ_0 .

After identifying the coupling parameters relevant to the quantum master equation, we computed the concurrence C metric measure of entanglement as a function of normalized interatomic distance r_{12}/λ_0 and normalized evolution time $t\gamma$

as shown in Fig. 4.9 (c) and (d). We identified relatively good transient concurrence C in both the rolled-up ENZ waveguide shown in Fig. 4.9 (c) and the rectangular waveguide presented in Fig. 4.9 (d). However, in both cases, we saw a decrease in the concurrence as a function of time t which depicts the depopulation of emitters in the excited state due to both radiative and non-radiative losses. Typically, electron-phonon, ohmic loss, inherent losses of the excited ENZ mode, and propagation losses contribute to the transient nature of qubits entanglement mediated by an ENZ medium [160]. Also, the qubit-qubit dissipative coupling induces modified collective decay rates i.e., superradiant $\gamma + \gamma_{12}$ and subradiant states $\gamma - \gamma_{12}$ which exhibits pure superradiant emission when $\gamma = \gamma_{12}$ condition is satisfied [178].

In order to compensate for the depopulation of the emitter excited state, we introduced an external pump into the master equation to compute the steady-state concurrence C_{ss} as well as the population dynamics of the qubits. Figure 4.10 shows the population dynamics of the qubits embedded within the two ENZ reservoirs at a normalized interatomic distance $r_{12}/\lambda_0 = 0.5$. Figure 4.10 (a), (c), and (e) illustrates the population dynamics of qubits inside the rolled-up ENZ waveguide at different pump intensities (i.e., antisymmetric $\Omega_1 = 0.8\gamma, \Omega_2 = 0$, symmetric $\Omega_1 = \Omega_2 = 0.5\gamma$, and asymmetric $\Omega_1 = -\Omega_2 = 0.5\gamma$ pumping cases). The corresponding Fig. 4.10 (b), (d), and (f) shows similar dynamics for qubits embedded within a plasmonic rectangular waveguide reservoir.

We present here four density matrix elements $\rho_{gg}, \rho_{ee}, \rho_{ge},$ and ρ_{eg} , which represent the probability of both qubits to be in the ground state, both qubits being in the excited state, the first qubit being in the ground state and the second being in the excited state, and vice versa. Furthermore, we assumed an initial state $\rho_{eg} = 1$. It can be seen that the qubits embedded within the ENZ reservoirs show different population dynamics for different external pumping cases. The symmetric pumping case depicts a similar population steady-state $\rho_{eg} = \rho_{ge}$ due to the identical pumping of the quantum system. The antisymmetric and asymmetric pumping density elements grow appreciably at normalized time $t\gamma < 5$ and decays to a constant probability at normalized time $t\gamma > 5$. Yet, we obtained a weak population state in the symmetric pumping case, for both rolled-up ENZ waveguide and plasmonic ENZ reservoir, as shown in Fig. 4.10 (c) and (d), respectively. At a strong antisymmetric pumping case, we obtained an appreciable high probability of both qubits being in the excited state ρ_{ee} as compared to the other two coherent pump cases.

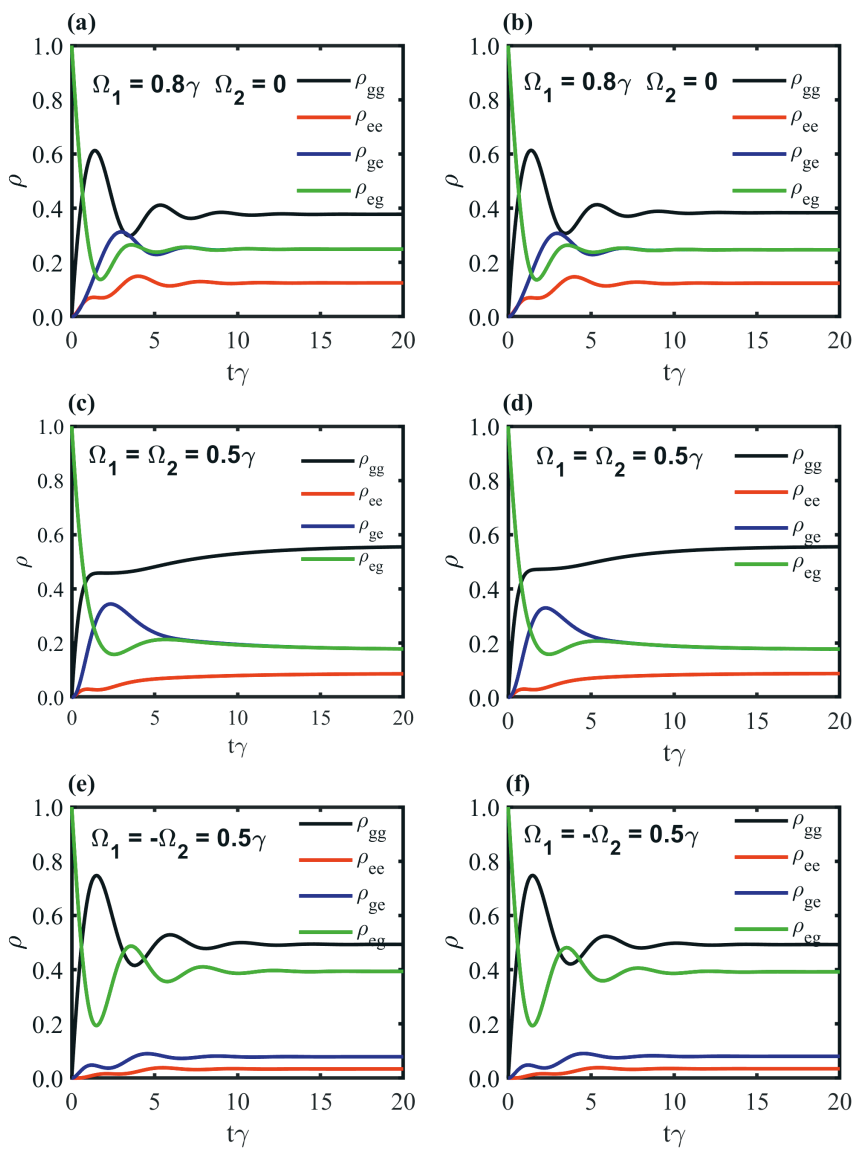


Figure 4.10 Dynamics of the density matrix elements for qubits under external pumping. (a), (c), and (e) Population dynamics of qubits inside the rolled-up ENZ waveguide. (b), (d), and (f) Similar dynamics of qubits inside the plasmonic rectangular waveguide at different pump intensities. Adapted from [P4].

The high probability signifies the effect of strong pumping on the dynamics of emitters coupled to a reservoir and how it affects entanglement between two qubits. It is evident that under strong pumping, the dynamics of qubits are defined by the external pumps and not only by the dipole–dipole interactions, thereby affecting the entanglement of qubits in such vicinity. In the asymmetric pump case, we see a high population state $\rho_{eg} > \rho_{ge}$ of the first qubit since the pump intensity for the second qubit is negated. The aforementioned dynamics of the different pump scenarios show the effect of pump intensities on emitters’ interactions and how high coherent pump intensities could potentially affect the entanglement property of qubits embedded within an ENZ reservoir with similar behavior observed with incoherent pumping [179, 180].

Figure 4.11 also illustrates the heatmaps of steady-state concurrence C_{ss} at normalized evolution time $t\gamma = 90$ as a function of two normalized pump intensities (i.e., $\Omega_1/\gamma, \Omega_2/\gamma$) at different normalized interatomic distances r_{12}/λ_0 . It is evident that the steady-state concurrence of the rolled-up ENZ waveguide (in the top panel of Fig. 4.11 (a), (b), (c)) shows a high measure of entanglement ($\max(C_{ss}) \approx 0.32$) as compared to the rectangular ENZ waveguide ($\max(C_{ss}) \approx 0.2$) shown in the lower panel (i.e., (d), (e), (f)) at $r_{12}/\lambda_0 = 0.5$. Similar results are presented for different normalized interatomic distances $r_{12}/\lambda_0 = 1.0$ and $r_{12}/\lambda_0 = 1.5$, respectively. The high entanglement in the rolled-up ENZ waveguide depicts its relevance to serving as a reservoir to mediate qubit entanglement as compared to the rectangular ENZ waveguide. Note that the high steady-state concurrence of the proposed ENZ waveguide channels is as a result of the large values of γ_{12} and small values of g_{12} . Also, the pump strength should not be too high to achieve strong steady-state entanglement between the qubits; otherwise, strong interactions between the pump and the qubits as well as the reservoir will occur, eventually leading to qubits decoupling and lasing.

In summary, we showed that the long-range quantum entanglement between a pair of qubits mediated by a rolled-up ENZ waveguide persists over extended periods and long distances. The response is compared to the corresponding plasmonic rectangular ENZ waveguide. The theory of both transient and steady-state quantum entanglement, quantified by computing the concurrence metric, was briefly introduced and utilized to determine the robust entanglement of qubits coupled to the ENZ waveguide channel. This concurrence metric formalism has a direct link with the cross-term second-order coherence function that can be extracted from an ex-

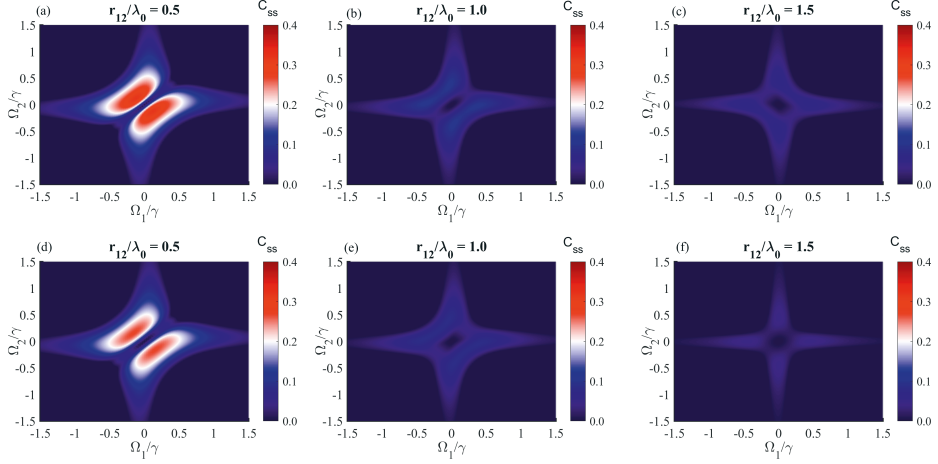


Figure 4.11 Two pumps steady-state entanglement at different inter-atomic distance r_{12}/λ_0 for (top panel) rolled-up ENZ waveguide and (bottom panel) rectangular waveguide. Adapted from [P4].

periment (i.e., Hanbury Brown and Twiss (HBT) effect or two-photon detection probability (PRR) measurement) [160, 178, 181]. We also showed ways to improve the entanglement of qubits coupled to the proposed reservoirs. We obtained that the rolled-up ENZ waveguide system demonstrates an improved quantum optical and long-range entanglement performance with $\max(C_{ss}) \approx 0.32$ compared to the rectangular ENZ waveguide channel.

These numerical formulations established the groundwork for the theoretical underpinnings of cylindrical metamaterials and their potential uses in both the classical and quantum regimes. To develop on these and further quantify some practical realizations of these rolled-up structures, we investigated the fabrication of rolled-up tubes coupled with emitters to comprehend some of their interesting photonic properties. In this technique, emitters are embedded on their planar composites before the initiation of the self-rolling mechanism to produce the rolled-up nanomembrane with emitters complex as shown in Fig. 4.12.

Figure 4.12 (a) shows a proof-of-concept of the rolled-up structure with an emitter complex composed of nitrogen-vacancy (NV) color centers present in nanodiamonds embedded within the rolled-up structure. These NV centers are mainly defects found in a diamond crystal that have interesting electronic and optical properties, making them useful for a variety of applications, including sensing, quantum

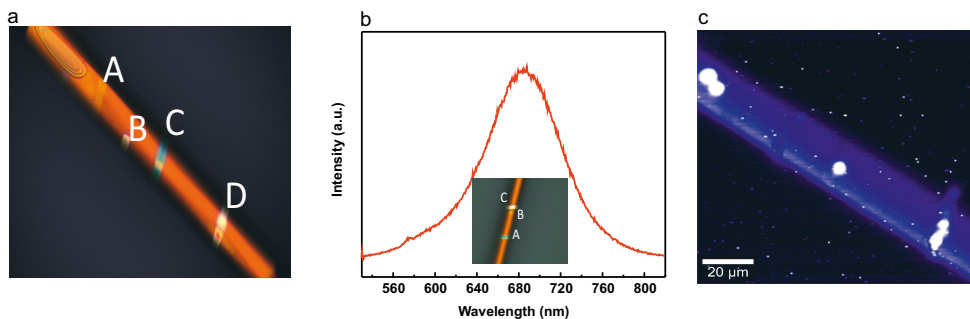


Figure 4.12 (a) Rolled-up nanomembranes embedded with quantum emitters labeled as [A, B, C, D] (b) Photoluminescence (PL) spectra of the NV-centers at label C on the rolled-up tube inset. (c) PL heatmap of the rolled-up tubes with bright spots depicting the location of the NV centers embedded.

computing, and imaging. Their electronic structure consists of a negatively charged nitrogen atom (N) and a nearby vacant lattice site (V), which creates a stable defect in the diamond lattice. The NV center has a ground state spin triplet ($S = 1$) and an excited state spin singlet ($S = 0$). The electronic transitions that occur between these states are governed by the spin-conserving transitions $\Delta S = 0$ and electric dipole transitions $\Delta m_s = \pm 1$ selection rules. This spin state can be manipulated and read out optically, making it a useful qubit for quantum computing. Additionally, the NV center has a strong electron spin resonance signal that makes it useful for sensing applications such as magnetic imaging as well as has usage in fluorescence-based imaging, as they can be excited with an external laser and emit light at a specific wavelength [182]. As such, integrating NV-centers which show quantum behavior at room temperature with rolled-up nanomembranes can exhibit interesting optical properties. Fig. 4.12 (b) and (c) show the preliminary PL spectral characteristics and heatmap of the rolled-up nanomembrane and NV emitter complex system inset with label [C]. This helped in comprehending the fluorescence emission of the NV defect diamonds coupled with the rolled-up structure. This complex structure also has the potential to offer other interesting photonic properties due to the combination of the interesting optical and electronic properties of the NV centers with the confinement and guidance provided by the rolled-up nanomembrane as well as create an iconic model system to develop a wide variety of quantum manipulation protocols. This proof of fabrication concept gives a flavour on some ongoing works and future directions we are currently working on.

5 SPHERICAL METAMATERIAL

From the previous sections, we identified that ENZ materials exhibit a dielectric permittivity approaching zero at a frequency close to the material's plasma frequency. Also, alternating layers of metal and dielectric were demonstrated to exhibit ENZ properties either in the planar domain or in the cylindrical morphology. Amidst these planar and cylindrical geometries which were established in the previous chapters, we next extend our discussion toward the spherical domain and look at some of its possible applications and ENZ properties. In general, spherical metamaterials are artificial materials that are designed to have specific electromagnetic properties. They can be made from a variety of materials, including metals, dielectrics, and semiconductors, and are often composed of a stack of thin layers arranged in a spherical configuration [183–185]. In **P5**, we explored these stacked spherically-shaped metastructures to elucidate some of their interesting properties.

5.1 Spherical nanoparticle

As the field of nanotechnology continues to advance, it is becoming increasingly prevalent in various domains such as healthcare, pharmacology, food science, information technology, electronics, energy, and the environment [186]. As a result, there is a growing need for the development of new, functional nanoparticles (NP) for use in these various fields, as well as numerical research to aid in the careful experimental design and interpretation of observed data. One area of particular interest is the use of metal NP in industry. These NP possess interesting optical, catalytic, electronic, and spectroscopic properties, making them useful in a wide range of applications [187–189]. They are characterized by a localized surface plasmon resonance (LSPR) absorption band, which can be influenced by factors such as the type of metal, size, shape, and dielectric environment of the particles [190–192]. LSPR is generally a phenomenon in which the polarizability of a nanometer-sized structure

is maximized, as described by the quasi-static approximation for small particles. An example of this is the static polarizability of a sphere, which is given by the equation:

$$\alpha = 4\pi\epsilon_0 R^3 \frac{\epsilon_d - \epsilon_m}{\epsilon_d + 2\epsilon_m}, \quad (5.1)$$

where R is the radius of the NP sphere, and α is the static polarizability. It can be inferred from Eq. (5.1) that α is maximized when $|\epsilon_d + 2\epsilon_m|$ is minimized, which demonstrates the strong relationship between the NPs' plasmonic properties and the dielectric function. These collective electron charge density oscillations in NPs result in enhanced near-field intensity at the resonance wavelength. Additionally,

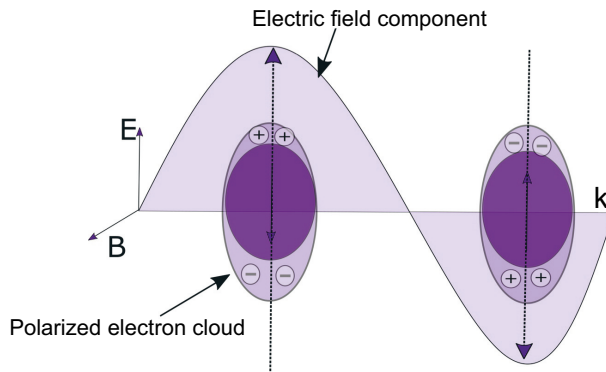


Figure 5.1 Metallic nanoparticles polarization depicting the classical interpretation of the excitation of plasmons.

NP composed of a metal–dielectric complex have been found to exhibit interesting light–matter interactions with many potential applications in physics and chemistry, such as scattering [193, 194] and nonlinear optics [195, 196], sensing [197, 198], fluorescence [199, 200], and up-conversion enhancement [201], surface plasmon amplification [202, 203], hydrogen generation [204], and solar energy harvesting [205, 206]. However, their ENZ properties have not been exploited. As such, in **P5**, we employed the effective medium approach to model the optical response of a multi-layer sphere as an effective bulk spherical medium, and compared the results with those obtained from the analytical method, to demonstrate the potential of utilizing NP as ENZ materials.

5.2 Epsilon-near-zero properties

The ENZ NP considered in **P5** is a bi-layer structure as shown schematically in Fig. 5.2. The inner dielectric core layer is made of silicon dioxide (SiO_2) and an outer metallic shell is made of silver (Ag). Noble metals, such as Ag, have high carrier concentration, electron mobility, and strong electromagnetic field confinement properties, which makes it a suitable choice for the outer shell [207]. To study

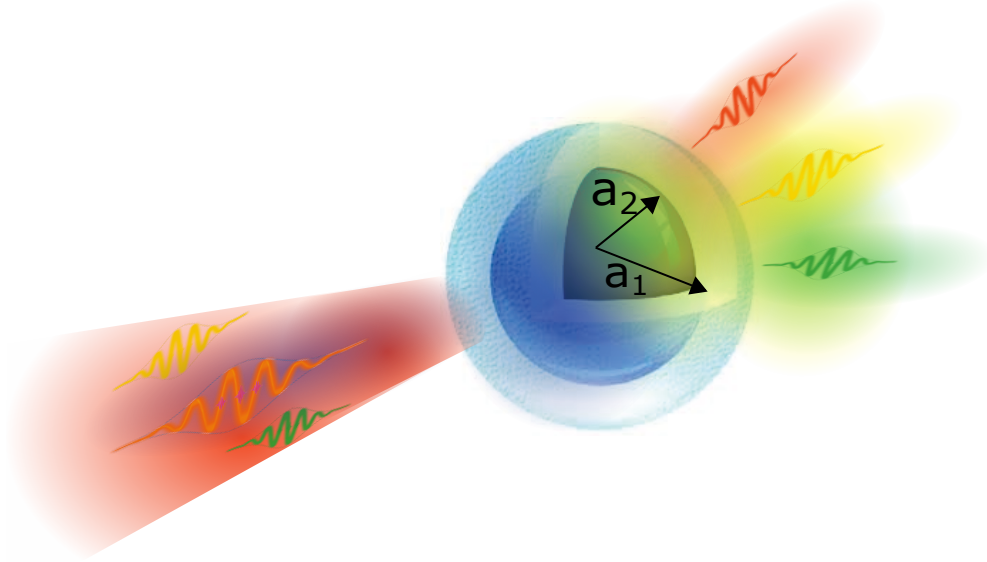


Figure 5.2 Schematic representation of the bi-layer spherical NP. a_2 and a_1 denote the inner and outer radius of the sphere. The inner, dark blue, sphere represents the dielectric core (SiO_2) of the NP, while the outer, light blue, shell represents the Ag coating. Adapted from **[P5]**.

the optical responses of ENZ NP, we use a transfer-matrix approach (based on the open-source STRATIFY code [208]). As a validation, we also implemented the optical response (i.e., scattering and absorption) for different materials [not reported here] and found that the Ag- SiO_2 bilayer structure gives us the required ENZ region of interest (i.e., visible to NIR). We first examined the effective ENZ optical responses of a bi-layer spherical NP embedded within a host medium (i.e., air), and then extended the effective permittivity approach to multilayer nanosphere composites. The wavelength-dependent complex dielectric functions for Ag and SiO_2 were obtained from the material data of Johnson and Christy [96]. The scattering, absorp-

tion, and electromagnetic near-field distribution were calculated using STRATIFY code, which is a recursive TMM (RTMM) MATLAB code.

In theory, the effective permittivity of a bi-layer spherical NP is derived by using an effective description of the electric permittivity of a metal–dielectric layered NP, following the methods presented in Ref. [209]. The chosen approach is the EMA, which assigns a single, effective permittivity to multi-layered NP. The NP is assumed to be a composite material, where the outer layer (the shell) plays the role of the host medium, whereas the inner layer (the core) is the inclusion. This assumption allows the use of the theory of effective media, reducing the problem to that of a single, homogeneous spherical NP with an effective permittivity. For the case of a metal–dielectric NP as depicted in Fig. 5.2, the electric field generated by the bilayered sphere in the host medium (air) is the same as that of a single sphere with radius a_1 and permittivity derived by solving the Laplace equation in the whole space [210]. By doing this, it is possible to assign an effective permittivity to the multi-layered NP as:

$$\tilde{\epsilon}_1 = \frac{1 - 2G}{1 + G} \epsilon_1, \quad (5.2)$$

where

$$G = \frac{\epsilon_1 - \epsilon_2}{2\epsilon_1 + \epsilon_2} \left(\frac{a_2}{a_1} \right)^3, \quad (5.3)$$

with ϵ_1 being the permittivity of the shell, ϵ_2 the permittivity of the core, and a_2 the radius of the inner sphere.

The above theory can then be generalized for multilayered structures by simply applying Eq. (5.2) recursively to each couple of layers, from the outer to the inner one [209], thus obtaining, for the general k -th layer

$$\tilde{\epsilon}_k = \frac{1 - 2G_k}{1 + G_k} \epsilon_k, \quad (5.4)$$

with

$$G_k = \frac{\epsilon_k - \tilde{\epsilon}_{k+1}}{2\epsilon_k + \tilde{\epsilon}_{k+1}} \left(\frac{a_{k+1}}{a_k} \right)^3. \quad (5.5)$$

Here, the layers are numbered from outside to inside so that $k = 1$ represents the outer layer and $k = N$ represents the inner one. The permittivity for each layer $k = \{N - 1, N - 2, \dots, 2, 1\}$ is expressed using the above equations.

5.2.1 Results and discussion

In **P5**, numerical calculations were used to determine the effective permittivity of a proposed spherical bilayer structure, in order to identify the ENZ points as a function of the core diameter with fixed outer layer thickness. By altering the radii of the bilayer nanospheres, we were able to attain different ENZ points. Figure 5.3 illustrates the effective permittivities for the different ENZ NP with different core diameters (i.e., $a_{2,1} = \{38, 40\}$, $a_{2,1} = \{68, 70\}$, and $a_{2,1} = \{98, 100\}$ nm, respectively) where $a_{2,1}$ denotes the radii of the inner and outer shells. In particular, for $a_{2,1} = \{38, 40\}$

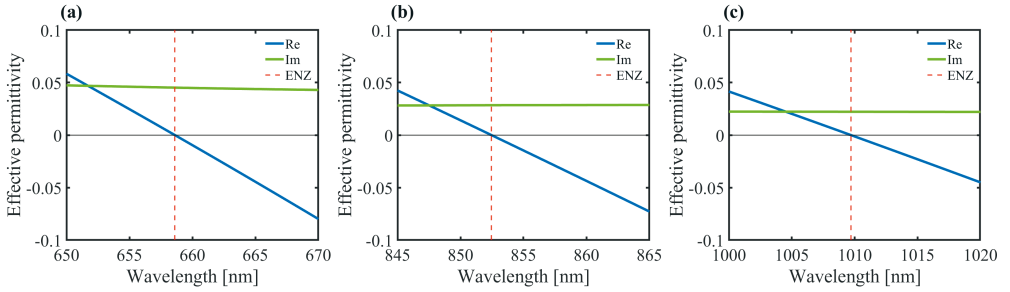


Figure 5.3 Effective permittivities of different bilayer spheres and their characteristic ENZ wavelengths, (a) $a_{2,1} = \{38, 40\}$, (b) $a_{2,1} = \{68, 70\}$, and (c) $a_{2,1} = \{98, 100\}$ nm. (Re) and (Im) denote the real and imaginary parts of effective permittivity. The ENZ wavelengths are marked with red dashed lines. Adapted from **[P5]**.

nm [Fig. 5.3(a)], the ENZ wavelength is found to be $\lambda_{\text{ENZ}} \approx 659$ nm. Similar to this, we identified a redshift of the ENZ wavelength to $\lambda_{\text{ENZ}} \approx 852$ nm [Fig. 5.3(b)] and $\lambda_{\text{ENZ}} \approx 1010$ nm [Fig. 5.3(c)], for $a_{2,1} = \{68, 70\}$ and $a_{2,1} = \{98, 100\}$, respectively. This showed that the ENZ wavelength can be tuned from the visible to the NIR region by changing the radii. We also found that the outer radius of the Ag-SiO₂ NP should fulfill $a_1 \leq \lambda_{\text{ENZ}}/10$ criteria to remain valid under the effective medium approach. This study also highlighted the importance of the parametric variations for the inner core and outer shell of the NP, as huge thickness variations between the two layers could affect the bilayer NP from exhibiting ENZ properties.

In addition, the electromagnetic field distribution of the proposed effective medium theory was compared with the complete analytical formulation to verify the reliability of the effective medium approach. The results, shown in Fig. 5.4, indicate that the electric field distribution outside the NP, as calculated using STRATIFY, is relatively similar for both the bilayer structure and the bulk sphere with effective

permittivity ϵ_{eff} at the ENZ wavelength. The small difference observed near the surface of the NP is attributed to the presence of surface waves in the actual bilayer structures, which locally modify the electric field. However, this difference does not undermine the validity of the effective medium approach as previously observed in similar situations in planar metal–dielectric-based metamaterials [211].

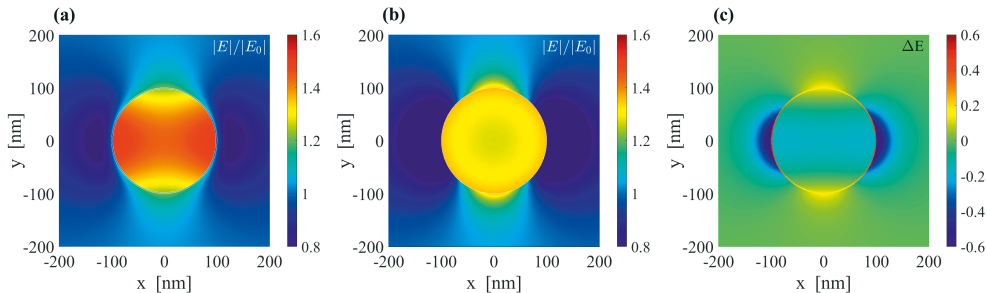


Figure 5.4 The electric field distribution for the bilayer structure, $a_{2,1} = \{98, 100\}$ nm at the ENZ wavelength. (a) The actual bilayer structure, and (b) the bulk effective medium structure. (c) The difference in the near-field distribution between (b) and (a). Adapted from [P5].

Moreover, we identified that a bilayer metal–dielectric structure is sufficient to achieve the desired ENZ properties. Although a full numerical optimization could be performed, the ENZ NP with radius $a_{2,1} = \{98, 100\}$ nm was considered, as it shows the capabilities of our approach shown in Fig. 5.4 and corresponds to experimentally potential NP [212].

Furthermore, the fundamental extinction cross-sections and the ENZ-dependent parametric sweep for different layers of the ENZ NP in the case of a plane wave incident on it using full permittivity (without any EMA) and the effective permittivity, coming from the effective medium formulation were numerically calculated. Figures 5.5 (a) and (b) show the calculated absorption and scattering cross-sections for three different ENZ NP using STRATIFY, i.e., $a_{2,1} = \{38, 40\}$ nm (purple), $a_{2,1} = \{68, 70\}$ nm (cyan), and $a_{2,1} = \{98, 100\}$ nm (orange), with absorption and scattering peak resonances at $\lambda \approx 913$ nm, 1206 nm, and 1466 nm, respectively. The maximum extinction resonance wavelengths for the proposed ENZ NP are redshifted, compared to their characteristic ENZ wavelengths which are presented in Table 5.1.

This is due to the resonant excitation of dipole surface plasmons on the ENZ NP. We note, in fact, that the obtained resonance enhancement for both scattering and absorption cross-section occurs when the condition $\epsilon_{\text{eff}} \approx -2$ (the so-called Fröhlich condition) for spherical NP is satisfied [213]. The absorption and scattering for the

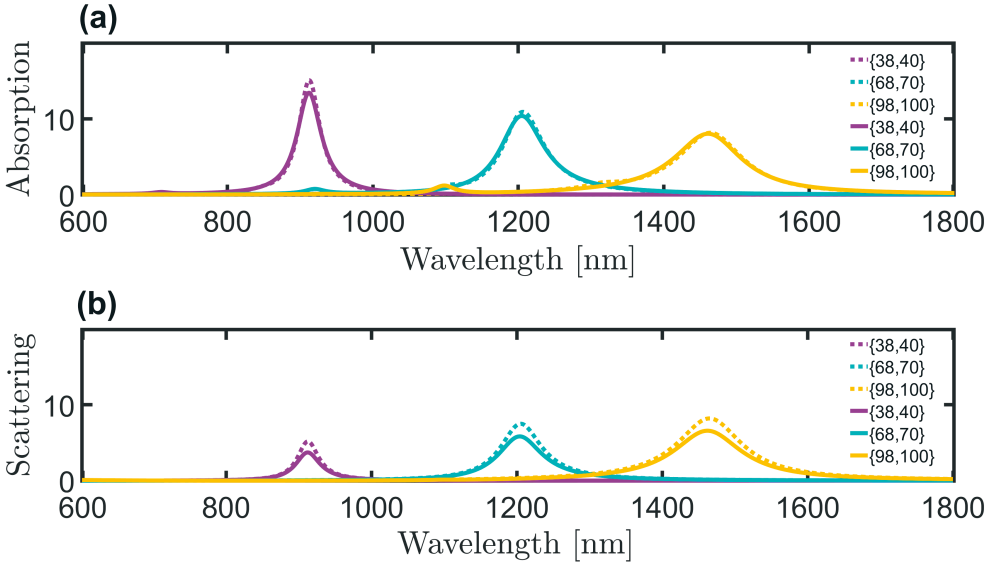


Figure 5.5 (a) Absorption and (b) Scattering cross-sections for the bilayered spherical NP with full permittivity (solid lines) and effective permittivity (dashed lines) for radii $a_{2,1} = \{38,40\}$ nm, $a_{2,1} = \{68,70\}$ nm, and $a_{2,1} = \{98,100\}$ nm. The values in the legend denote the radius values of the inner and outer spherical layers. Adapted from [P5].

NP size (nm)	λ_{ENZ}	$\lambda_{\text{Resonance}}$
{38, 40}	659 nm	913 nm
{68, 70}	852 nm	1206 nm
{98, 100}	1010 nm	1466 nm

Table 5.1 The ENZ NP with their characteristic ENZ wavelengths as well as their corresponding resonance wavelengths. Adapted from [P5].

ENZ NP $a_{2,1} = \{98,100\}$ nm have appreciably similar peak values. However, for the ENZ NP $a_{2,1} = \{38,40\}$ nm and $a_{2,1} = \{68,70\}$ nm, we obtained a relatively low scattering peak value, as compared to its corresponding absorption cross-section peak values. It is also interesting to note that by changing the filling ratio of the ENZ NP, a passive tuning of the λ_{ENZ} can be observed, which corroborates the shift in the NP's peak absorbance and scattering cross-sections. Intuitively, the redshift of the peak in the dipole resonance with increasing size could be linked to the weakening of their restoring force. Since the distance between charges on opposite sides of the ENZ NP increases with size, in fact, their corresponding interaction decrease.

In addition to the absorption and scattering cross-section of the ENZ NP, the

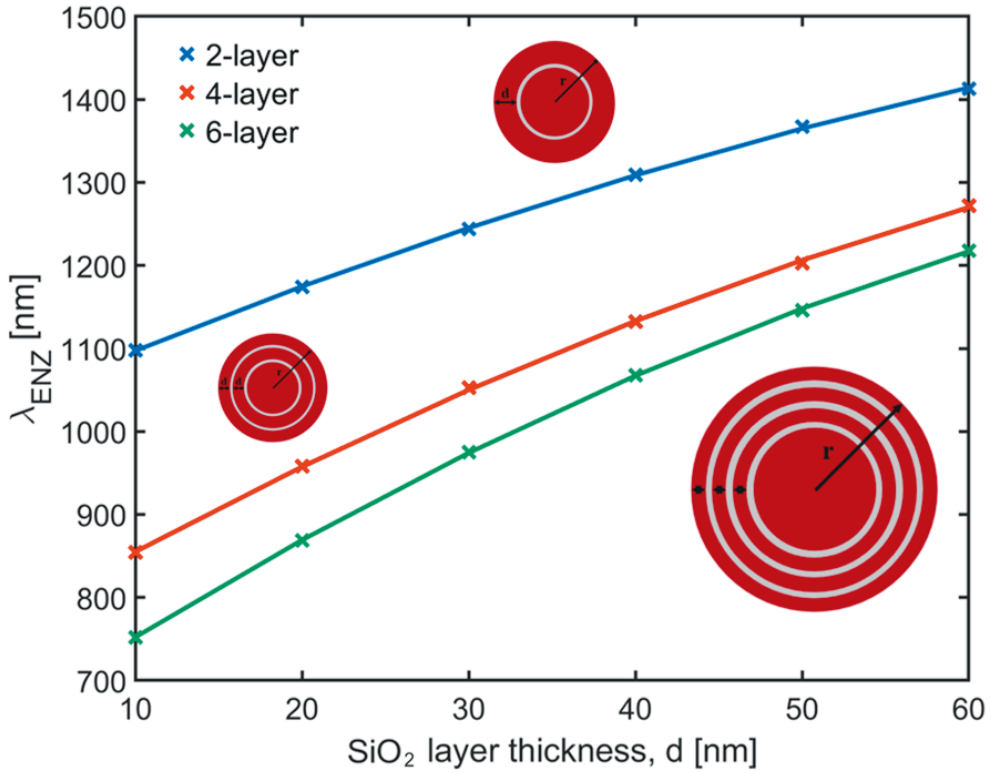


Figure 5.6 ENZ wavelengths calculated for three different structures of a set of SiO₂ layers, with varying thicknesses (d). The SiO₂ inner core and the Ag layers in between are fixed with a radius of $a_2 = \{98\}$ nm and a thickness of 2 nm. The compositions of the multilayer nanoparticles are schematically presented with red (SiO₂) and gray (Ag) circular layers, next to the relevant λ_{ENZ} plots, corresponding to 2 (blue), 4 (red), and 6 layers (green), respectively with thickness d values ranging from $\{10 - 60\}$ nm. Adapted from [P5].

ENZ wavelengths for different layered NP by parametrically varying the thickness of SiO₂ overlayed on the outer Ag shell were numerically calculated. The SiO₂ inner core and the Ag layers in between are fixed with a radius of $a_2 = \{98\}$ nm and a thickness of 2 nm. It is evident in Fig. 5.6 that by changing the thicknesses of the embedded SiO₂ layers, we attain different ENZ wavelengths for the other multilayered NP. For all the considered nanostructures, we see a linear trend that depicts that by varying the thicknesses of the SiO₂ layers, there is a corresponding shift in λ_{ENZ} for different layered structures. This signifies the possibility of extending the effective medium formulation of the bi-layered structure into multilayered NP.

5.2.2 Summary

In **P5**, we showed that the theory of effective media may be useful in understanding the unique optical properties of bilayer spherical NP. We found that by varying the diameter of the NP, we could shift its spectral absorbance and scattering properties. Our formulation for the effective permittivity of bilayer spherical structures worked relatively well and can be applied to more complex multilayer spherical structures. While we focused on Ag-SiO₂ NP, which are widely available commercially, this approach can be adapted to any combination of metal and dielectric materials, with the caveat that the condition $a_1 \leq \lambda_{\text{ENZ}}/10$ may need to be adjusted. Additionally, the choice of metal and dielectric can affect the spectrum and ENZ wavelength. Furthermore, for practical implementations, the proposed ENZ NP can be produced through inexpensive chemical synthesis techniques and could possess potential applications that take advantage of both ENZ and NP properties.

6 SUMMARY AND FUTURE WORK

In conclusion, the field of optics and photonics has been revolutionized by the development of metamaterials, which are materials with tailored optical properties created through artificial engineering. These materials have opened up new possibilities for light-matter interactions, enabling the engineering and creation of photonic devices with fascinating optical properties. They are designed by manipulating the subwavelength nanostructures of a material, to achieve specific optical properties, making them highly customizable and adaptable for various applications. This thesis explored the extensive range of applications that metamaterials have found in various fields, including energy harvesting, sensing, and quantum computing. The resonance and epsilon-near-zero (ENZ) properties of metamaterials have been a primary focus of this study, along with their coupling capabilities with emitters and the potential to serve as reservoirs for quantum systems.

The study began by investigating a lithography-free metal-insulator-metal structure, which demonstrated resonance properties and coupling capabilities with emitters that could enhance light-matter interactions. This simple three-layer-based structure provided a foundation for extending the discussion towards more complex multilayered structures, such as polymer-based hyperbolic metamaterials. The hyperbolic dispersion relations of these structures, the existence of high- k modes, their ENZ properties, and coupling mechanisms with emitters were all investigated to better comprehend their optical responses. With emitters spectrally closer to the ENZ region of the polymer-based HMM structure, a strong shortening of the average lifetime was identified which confirmed the increase in non-radiative decay channels at the ENZ region. Furthermore, the proposed dye-doped polymer-based HMM structure demonstrated to compensate for the losses in a metal-dielectric HMM structure by observing the enhanced transmittance in the presence of a pump source. In addition to studying the ENZ properties of planar structures, the thesis also explored cylindrical metamaterials. A self-rolling fabrication technique was used to

create three-dimensional (3D) rolled-up multilayered waveguides, which alleviated the constraints of multilayered planar structures from a fabrication point of view. The photonic properties and fabrication mechanism of these rolled-up structures were discussed, and their potential as waveguide reservoirs for quantum systems was also explored.

As the study delved further into the quantum regime, the importance of finding photonic media that could sustain the quantum properties of distantly spaced qubits became evident. This led to the introduction of the fabrication of a rolled-up zero-index waveguide with ENZ properties, which provided a medium that could address the drawbacks of optical interaction with a single quantum system. The waveguide reservoir illustrated the existence of unique extended modes that could be integrated with two emitters or an ensemble of emitters to exhibit interesting light-matter interactions and was compared with a rectangular ENZ waveguide. To expand the study even further, the ENZ features of spherical nanoparticles were also investigated using the effective medium approach to model the optical response of a multilayered sphere as an effective bulk spherical medium. The results of this study showcased the potential of planar multilayered structures, spherical nanoparticles, and cylindrical rolled-up waveguides for various classical and quantum applications, including optical filtering, radiative engineering, quantum communication, quantum information processing, and superradiance.

Overall, this thesis highlights the immense potential of metamaterials to shape the future of technology and science, paving the way for groundbreaking applications in various fields. With their unique optical properties and adaptability, metamaterials have opened up new possibilities for light-matter interactions. However, the potential for these materials goes beyond what has been explored so far.

Looking ahead, there are several exciting future directions for research in this field. One area of particular interest is the development of thin-film metamaterials with advanced functionalities, such as active tuning of their optical properties. This could be achieved through the integration of materials that can change their properties in response to external stimuli, such as electric or magnetic fields [214]. In addition, further exploration into self-rolling mechanisms for integrating tunable materials holds the promise of generating smart metamaterials with large wafer-scale fabrication capabilities. By combining rolled-up tubes with advanced lithography techniques, possibilities like microfluidic channels for sensing and out-of-plane meta-

surfaces with intricate metalens designs can be harnessed. Another important direction is the investigation of the quantum properties of metamaterials [215]. The study of quantum effects in these materials could lead to the development of new quantum technologies, such as quantum sensors and quantum computers. In addition, superradiance, the collective emission of radiation from an ensemble of quantum systems, is an area of research that could greatly benefit from the use of metamaterials. By controlling the coupling between emitters and ENZ mode activated rolled-up metamaterials, we can create materials that enhance superradiance, potentially leading to more efficient energy transfer and communication [216]. Furthermore, the development of metamaterials with tailored thermal properties is an important area of research. To sum up, the future of thin-film metamaterials research is exciting and holds great promise for advancing our understanding of light-matter interactions and for the development of new technologies that could have a significant impact on society.

REFERENCES

- [1] W. Cai and V. Shalaev. *Optical Metamaterials: Fundamentals and Applications*. Springer-Verlag New York, 2010.
- [2] E. Cortés, F. J. Wendisch, L. Sortino, A. Mancini, S. Ezendam, S. Saris, L. de S. Menezes, A. Tittl, H. Ren and S. A. Maier. Optical Metasurfaces for Energy Conversion. *Chemical Reviews* **122** (2022), 15082–15176.
- [3] D. Ghindani, I. Issah, S. Chervinskii, M. Lahikainen, K. Kuntze, A. Priimagi and H. Caglayan. Humidity-Controlled Tunable Emission in a Dye-Incorporated Metal–Hydrogel–Metal Cavity. *ACS Photonics* **9** (2022), 2287–2294.
- [4] T. Cao, C. Wei and M. J. Cryan. Low-loss dual-band double-negative chirped metamaterial. *JOSA B* **32** (2015), 108–113.
- [5] V. G. Veselago. The Electrodynamics of Substances with Simultaneously Negative Values of ϵ and μ . *Soviet Physics Uspekhi* **10** (1968), 509.
- [6] D. R. Smith, W. J. Padilla, D. C. Vier, S. C. Nemat-Nasser and S. Schultz. Composite Medium with Simultaneously Negative Permeability and Permittivity. *Phys. Rev. Lett.* **84** (2000), 4184–4187.
- [7] J. B. Pendry. Negative Refraction Makes a Perfect Lens. *Phys. Rev. Lett.* **85** (2000), 3966–3969.
- [8] J. B. Pendry. Focus Issue: Negative Refraction and Metamaterials. *Opt. Express* **11** (2003), 639–639.
- [9] N. Seddon and T. Bearpark. Observation of the Inverse Doppler Effect. *Science* **302** (2003), 1537–1540.
- [10] S. Xi, H. Chen, T. Jiang, L. Ran, J. Huangfu, B.-I. Wu, J. A. Kong and M. Chen. Experimental Verification of Reversed Cherenkov Radiation in Left-Handed Metamaterial. *Phys. Rev. Lett.* **103** (2009), 194801.

- [11] Z. Li, E. Palacios, S. Butun, H. Kocer and K. Aydin. Omnidirectional, broadband light absorption using large-area, ultrathin lossy metallic film coatings OPEN. *Scientific Reports* **5** (2015), 15137.
- [12] B. J. Lee and Z. M. Zhang. Design and fabrication of planar multilayer structures with coherent thermal emission characteristics. *Journal of Applied Physics* **100** (2006), 063529.
- [13] Z. Li, S. Butun and K. Aydin. Large-Area, Lithography-Free Super Absorbers and Color Filters at Visible Frequencies Using Ultrathin Metallic Films. *ACS Photonics* **2** (2015), 183–188.
- [14] M. Aalizadeh, A. Khavasi, B. Butun and E. Ozbay. Large-Area, Cost-Effective, Ultra-Broadband Perfect Absorber Utilizing Manganese in Metal-Insulator-Metal Structure. *Sci. Rep.* **8** (2018), 9162.
- [15] S. Banerjee. Simulation and Design of MIM Nanoresonators for Color Filter Applications. *J. Soc. Inf. Disp.* **24** (2016), 433–438.
- [16] Y. Li, Z. Liu, H. Zhang, P. Tang, B. Wu and G. Liu. Ultra-Broadband Perfect Absorber Utilizing Refractory Materials in Metal-Insulator Composite Multilayer Stacks. *Opt. Express* **27** (2019), 11809–11818.
- [17] C. Williams, G. Rughoobur, A. J. Flewitt and T. D. Wilkinson. Single-step Fabrication of Thin-film Linear Variable Bandpass Filters Based on Metal-Insulator-Metal Geometry. *Appl. Opt.* **55** (2016), 9237–9241.
- [18] Z. Yang, T. Albrow-Owen, W. Cai and T. Hasan. Miniaturization of Optical Spectrometers. *Science* **371** (2021), eabe0722.
- [19] M. Aalizadeh, A. E. Serebryannikov, A. Khavasi, G. A. E. Vandenbosch and E. Ozbay. Toward Electrically Tunable, Lithography-Free, Ultra-Thin Color Filters Covering the Whole Visible Spectrum. *Sci. Rep.* **8** (2018), 11316.
- [20] E.-S. Yu, S.-H. Lee, Y.-G. Bae, J. Choi, D. Lee, C. Kim, T. Lee, S.-Y. Lee, S.-D. Lee and Y.-S. Ryu. Highly Sensitive Color Tunability by Scalable Nanomorphology of a Dielectric Layer in Liquid-Permeable Metal–Insulator–Metal Structure. *ACS Appl. Mater. Interfaces* **10** (2018), 38581–38587.
- [21] S. A. Jewell, S. L. Cornford and J. R. Sambles. Dynamic Control of Visible Radiation by a Liquid Crystal Filled Fabry-Pérot Etalon. *J. Appl. Phys.* **102** (2007), 093108.

- [22] E. P. A. van Heeswijk, A. J. J. Kragt, N. Grossiord and A. P. H. J. Schenning. Environmentally Responsive Photonic Polymers. *Chem. Commun.* **55** (2019), 2880–2891.
- [23] L. Tang, L. Wang, X. Yang, Y. Feng, Y. Li and W. Feng. Poly(N-isopropylacrylamide)-Based Smart Hydrogels: Design, Properties and Applications. *Prog. Mater. Sci.* **115** (2021), 100702.
- [24] I. Tokarev and S. Minko. Stimuli-Responsive Hydrogel Thin Films. *Soft Matter* **5** (2009), 511–524.
- [25] I. Issah, T. Pihlava, A. R. Rashed and H. Caglayan. Mechanism of emitters coupled with a polymer-based hyperbolic metamaterial. *Opt. Express* **30** (2022), 8723–8733.
- [26] F. Muralter, F. Greco and A. M. Coclite. Applicability of Vapor-Deposited Thermo-responsive Hydrogel Thin Films in Ultrafast Humidity Sensors/Actuators. *ACS Appl. Polym. Mater.* **2** (2020), 1160–1168.
- [27] K. Matsumoto, N. Sakikawa and T. Miyata. Thermo-responsive gels that absorb moisture and ooze water. *Nat. Commun.* **9** (2018), 1–7.
- [28] T. Ding, C. Rüttiger, X. Zheng, F. Benz, H. Ohadi, G. A. E. Vandenbosch, V. V. Moshchalkov, M. Gallei and J. J. Baumberg. Fast Dynamic Color Switching in Temperature-Responsive Plasmonic Films. *Adv. Opt. Mater.* **4** (2016), 877–882.
- [29] N. Gisbert Quilis, M. van Dongen, P. Venugopalan, D. Kotlarek, C. Petri, A. Moreno Cencerrado, S. Stanescu, J. L. Toca Herrera, U. Jonas, M. Möller, A. Mourran and J. Dostalek. Actively Tunable Collective Localized Surface Plasmons by Responsive Hydrogel Membrane. *Adv. Opt. Mater.* **7** (2019), 1900342.
- [30] A. U. R. Khalid, J. Liu, Y. Han, N. Ullah, S. Jia and Y. Wang. Multipurpose Thermo-responsive Hydrogel: a Platform for Dynamic Holographic Display. *Opt. Lett.* **45** (2020), 479.
- [31] Y. Brasse, M. B. Müller, M. Karg, C. Kuttner, T. A. F. König and A. Fery. Magnetic and Electric Resonances in Particle-to-Film-Coupled Functional Nanostructures. *ACS Appl. Mater. Interfaces* **10** (2018), 3133–3141.

- [32] C. D. Sorrell, M. C. D. Carter and M. J. Serpe. Color Tunable Poly (N-Isopropylacrylamide)-co-Acrylic Acid Microgel–Au Hybrid Assemblies. *Adv. Funct. Mater.* **21** (2011), 425–433.
- [33] C. D. Sorrell and M. J. Serpe. Glucose Sensitive Poly (N-isopropylacrylamide) Microgel Based Etalons. *Anal. Bioanal. Chem.* **402** (2012), 2385–2393.
- [34] J. Shin, S. G. Han and W. Lee. Dually Tunable Inverse Opal Hydrogel Colorimetric Sensor with Fast and Reversible Color Changes. *Sensors and Actuators B: Chemical* **168** (2012), 20–26.
- [35] Y. Ohtsuka, T. Seki and Y. Takeoka. Thermally Tunable Hydrogels Displaying Angle-Independent Structural Colors. *Angewandte Chemie International Edition* **54** (2015), 15368–15373.
- [36] O. M. Wani, A. P. H. J. Schenning and A. Priimagi. A Bifacial Colour-tunable System via Combination of a Cholesteric Liquid Crystal Network and Hydrogel. *J. Mater. Chem. C* **8** (2020), 10191–10196.
- [37] Z. Wang, J. Zhang, J. Xie, Z. Wang, Y. Yin, J. Li, Y. Li, S. Liang, L. Zhang, L. Cui, H. Zhang and B. Yang. Polymer Bragg Stack as Color Tunable Photonic Paper. *J. Mater. Chem.* **22** (2012), 7887–7893.
- [38] E. Tian, J. Wang, Y. Zheng, Y. Song, L. Jiang and D. Zhu. Colorful Humidity Sensitive Photonic Crystal Hydrogel. *J. Mater. Chem.* **18** (2008), 1116–1122.
- [39] J. Shi, V. K. Hsiao, T. R. Walker and T. J. Huang. Humidity Sensing Based on Nanoporous Polymeric Photonic Crystals. *Sens. Actuators, B* **129** (2008), 391–396.
- [40] M. Kumoda, M. Watanabe and Y. Takeoka. Preparations and Optical Properties of Ordered Arrays of Submicron Gel Particles: Interconnected State and Trapped State. *Langmuir* **22** (2006), 4403–4407.
- [41] J. M. Weissman, H. B. Sunkara, A. S. Tse and S. A. Asher. Thermally Switchable Periodicities and Diffraction from Mesoscopically Ordered Materials. *Science* **274** (1996), 959–963.
- [42] X. Wang, X. Liu and X. Wang. Hydrogel Diffraction Grating as Sensor: A Tool for Studying Volume Phase Transition of Thermo-responsive Hydrogel. *Sens. Actuator B-Chem.* **204** (2014), 611–616.

- [43] H. Clevenson, P. Desjardins, X. Gan and D. Englund. High sensitivity gas sensor based on high-Q suspended polymer photonic crystal nanocavity. *Applied Physics Letters* **104** (2014), 241108.
- [44] M. E. Nash, W. M. Carroll, P. J. Foley, G. Maguire, C. O. Connell, A. V. Gorelov, S. Beloshapkin and Y. A. Rochev. Ultra-thin Spin Coated Crosslinkable Hydrogels for use in Cell Sheet Recovery—Synthesis, Characterisation to Application. *Soft Matter* **8** (2012), 3889–3899.
- [45] H. Schild. Poly(N-isopropylacrylamide): Experiment, Theory and Application. *Prog. Polym. Sci.* **17** (1992), 163–249.
- [46] E. M. Purcell. Spontaneous Emission Probabilities at Radio Frequencies. *Confined Electrons and Photons: New Physics and Applications*. Springer US, 1995, 839–839.
- [47] K. J. Vahala. Optical microcavities. *Nature* **424** (2003), 839–846.
- [48] M. Hill, Y. Oei, E. Smalbrugge, Y. Zhu, T. Vries, de, P. Veldhoven, van, F. Otten, van, T. Eijkemans, J. Turkiewicz, H. Waardt, de, E. Geluk, S.-H. Kwon, Y.-H. Lee, R. Nötzel and M. Smit. Lasing in metallic-coated nano-cavities. *Nature Photonics* **1** (2007), 589–594.
- [49] G. Shambat, B. Ellis, A. Majumdar, J. Petykiewicz, M. Mayer, T. Sarmiento, J. Harris, E. Haller and J. Vuckovic. Ultrafast Direct Modulation of a Single-Mode Photonic Crystal Nanocavity Light-Emitting Diode. *Nature communications* **2** (2011), 539.
- [50] G. Ford and W. Weber. Electromagnetic interactions of molecules with metal surfaces. *Physics Reports* **113** (1984), 195–287.
- [51] W. L. Barnes. Fluorescence near interfaces: The role of photonic mode density. *Journal of Modern Optics* **45** (1998), 661–699.
- [52] N. Lassaline, R. Brechbühler, S. J. W. Vonk, K. Ridderbeek, M. Spieser, S. Bisig, B. le Feber, F. T. Rabouw and D. J. Norris. Optical Fourier surfaces. *Nature* **582** (2020), 506–510.
- [53] X. Jiang, B. Liang, R.-q. Li, X.-y. Zou, L.-l. Yin and J.-c. Cheng. Ultra-broadband absorption by acoustic metamaterials. *Applied Physics Letters* **105** (2014), 243505.

- [54] V. P. Drachev, V. A. Podolskiy and A. V. Kildishev. Hyperbolic metamaterials: new physics behind a classical problem. *Opt. Express* **21** (2013), 15048–15064.
- [55] M. Habib, I. Issah, D. Briukhanova, A. R. Rashed and H. Caglayan. Wavefront Control with Nanohole Array-Based Out-of-Plane Metasurfaces. *ACS Applied Nano Materials* **4** (2021), 8699–8705.
- [56] I. I. Smolyaninov, Y. J. Hung and C. C. Davis. Two-dimensional metamaterial structure exhibiting reduced visibility at 500 nm. *Opt. Lett.* **33** (2008), 1342–1344.
- [57] I. Issah, F. Li, M. Baah, I. A. Otoo, L. Asilevi, P. Bawuah and B. O. Asamoah. Passive tunable and polarization-insensitive fan-like metamaterial absorber in the visible spectrum. *J. Opt. Soc. Am. B* **38** (2021), C1–C10.
- [58] Z. Guo, H. Jiang and H. Chen. Hyperbolic metamaterials: From dispersion manipulation to applications. *Journal of Applied Physics* **127** (2020), 071101.
- [59] S. Chervinskii, I. Issah, M. Lahikainen, A. R. Rashed, K. Kuntze, A. Priimagi and H. Caglayan. Humidity- and Temperature-Tunable Metal–Hydrogel–Metal Reflective Filters. *ACS Applied Materials & Interfaces* **13** (2021), 50564–50572.
- [60] S. Ishii, A. V. Kildishev, E. Narimanov, V. M. Shalaev and V. P. Drachev. Sub-wavelength interference pattern from volume plasmon polaritons in a hyperbolic medium. *Laser & Photonics Reviews* **7** (2013), 265–271.
- [61] A. Aigner, J. Dawes, S. Maier and H. Ren. Nanophotonics shines light on hyperbolic metamaterials. *Light: Science & Applications* **11** (2022), 2047–7538.
- [62] L. Novotny and B. Hecht. *Principles of Nano-Optics*. 2nd ed. Cambridge University Press, 2012, i–vi.
- [63] P. Shekhar, J. Atkinson and Z. Jacob. Hyperbolic metamaterials: fundamentals and applications. *Nano convergence* **1** (2014), 1–17.
- [64] C. L. Cortes, W. Newman, S. Molesky and Z. Jacob. Corrigendum: Quantum nanophotonics using hyperbolic metamaterials (2012 J. Opt. 14 063001). *Journal of Optics* **16** (2014), 129501.
- [65] R. K. Fisher and R. W. Gould. Resonance Cones in the Field Pattern of a Short Antenna in an Anisotropic Plasma. *Phys. Rev. Lett.* **22** (1969), 1093–1095.

- [66] D. Lu and Z. Liu. Hyperlenses and metalenses for far-field super-resolution imaging. *Nature communications* **3** (2012), 1205.
- [67] B. D. F. Casse, W. T. Lu, Y. J. Huang, E. Gultepe, L. Menon and S. Sridhar. Super-resolution imaging using a three-dimensional metamaterials nanolens. *Applied Physics Letters* **96** (2010), 023114.
- [68] G. V. Naik, J. Kim and A. Boltasseva. Oxides and nitrides as alternative plasmonic materials in the optical range. *Opt. Mater. Express* **1** (2011), 1090–1099.
- [69] L. Sun, Z. Li, T. S. Luk, X. Yang and J. Gao. Nonlocal effective medium analysis in symmetric metal-dielectric multilayer metamaterials. *Phys. Rev. B* **91** (2015), 195147.
- [70] V. Popov, A. V. Lavrinenko and A. Novitsky. Operator approach to effective medium theory to overcome a breakdown of Maxwell Garnett approximation. *Phys. Rev. B* **94** (2016), 085428.
- [71] X. Lei, L. Mao, Y. Lu and P. Wang. Revisiting the effective medium approximation in all-dielectric subwavelength multilayers: Breakdown and rebuilding. *Phys. Rev. B* **96** (2017), 035439.
- [72] G. Castaldi, A. Alù and V. Galdi. Boundary Effects of Weak Nonlocality in Multilayered Dielectric Metamaterials. *Phys. Rev. Applied* **10** (2018), 034060.
- [73] Z. Wen, H. Xu, W. Zhao, Z. Zhou, X. Li, S. Li, J. Zhou, Y. Sun, N. Dai and J. Hao. Nonlocal effective-medium theory for periodic multilayered metamaterials. *Journal of Optics* **23** (2021), 065103.
- [74] S. M. Rytov. *Electromagnetic Properties of a Finely Stratified Medium*. 2014.
- [75] H. Hemmati and R. Magnusson. Applicability of Rytov’s Full Effective-Medium Formalism to the Physical Description and Design of Resonant Metasurfaces. *ACS Photonics* **7** (2020), 3177–3187.
- [76] J. Zhang, L. Zhang and W. Xu. Surface plasmon polaritons: physics and applications. *Journal of Physics D: Applied Physics* **45** (2012), 113001.
- [77] V. G. Kravets, A. V. Kabashin, W. L. Barnes and A. N. Grigorenko. Plasmonic Surface Lattice Resonances: A Review of Properties and Applications. *Chemical Reviews* **118** (2018), 5912–5951.

- [78] Z. Jacob, I. I. Smolyaninov and E. E. Narimanov. Broadband Purcell effect: Radiative decay engineering with metamaterials. *Applied Physics Letters* **100** (2012), 181105.
- [79] M. A. Noginov, H. Li, Y. A. Barnakov, D. Dryden, G. Nataraj, G. Zhu, C. E. Bonner, M. Mayy, Z. Jacob and E. E. Narimanov. Controlling spontaneous emission with metamaterials. *Opt. Lett.* **35** (2010), 1863–1865.
- [80] P. Lodahl, A. van Driel, I. Nikolaev, A. Irman, K. Overgaag, D. Vanmaekelbergh and W. Vos. Controlling the dynamics of spontaneous emission from quantum dots by photonic crystals. *Nature* **430** (2004), 654–657.
- [81] S. Hughes. Enhanced single-photon emission from quantum dots in photonic crystal waveguides and nanocavities. *Opt. Lett.* **29** (2004), 2659–2661.
- [82] Z. Jacob and V. Shalaev. Plasmonics Goes Quantum. *Science* **334** (2011), 463–464.
- [83] S. Krasikov and I. V. Iorsh. Self-consistent Purcell factor and spontaneous topological transition in hyperbolic metamaterials. *Physica Status Solidi - Rapid Research Letters* **10** (2016), 769–773.
- [84] L. Novotny and B. Hecht. *Principles of Nano-Optics*. Cambridge University Press, 2006.
- [85] K. Halterman and J. M. Elson. Near-perfect absorption in epsilon-near-zero structures with hyperbolic dispersion. *Opt. Express* **22** (2014), 7337–7348.
- [86] A. Alù, M. G. Silveirinha, A. Salandrino and N. Engheta. Epsilon-near-zero metamaterials and electromagnetic sources: Tailoring the radiation phase pattern. *Phys. Rev. B* **75** (2007), 155410.
- [87] R. S. Savelev, I. V. Shadrivov, P. A. Belov, N. N. Rosanov, S. V. Fedorov, A. A. Sukhorukov and Y. S. Kivshar. Loss compensation in metal-dielectric layered metamaterials. *Phys. Rev. B* **87** (2013), 115139.
- [88] W. D. Newman, C. L. Cortes and Z. Jacob. Enhanced and directional single-photon emission in hyperbolic metamaterials. *J. Opt. Soc. Am. B* **30** (2013), 766–775.
- [89] J. R. Lakowicz. Radiative decay engineering 5: metal-enhanced fluorescence and plasmon emission. *Analytical Biochemistry* **337** (2005), 171–194.

- [90] Z. Jacob and E. E. Narimanov. Optical hyperspace for plasmons: Dyakonov states in metamaterials. *Applied Physics Letters* **93** (2008), 221109.
- [91] X. Ni, S. Ishii, M. D. Thoreson, V. M. Shalaev, S. Han, S. Lee and A. V. Kildishev. Loss-compensated and active hyperbolic metamaterials. *Opt. Express* **19** (2011), 25242–25254.
- [92] L. Ferrari, D. Lu, D. Lepage and Z. Liu. Enhanced spontaneous emission inside hyperbolic metamaterials. *Opt. Express* **22** (2014), 4301–4306.
- [93] H.-I. Lin, K.-C. Shen, S.-Y. Lin, G. Haider, Y.-H. Li, S.-W. Chang and Y.-F. Chen. Transient and Flexible Hyperbolic Metamaterials on Freeform Surfaces. *Scientific Reports* **8** (2018), 9469.
- [94] C. Rizza, A. Di Falco and A. Ciattoni. Gain assisted nanocomposite multilayers with near zero permittivity modulus at visible frequencies. *Applied Physics Letters* **99** (2011).
- [95] X. Wu. Perfect absorption in cascaded asymmetric hyperbolic metamaterial slabs. *Superlattices and Microstructures* **124** (2018), 10–16.
- [96] P. B. Johnson and R. W. Christy. Optical constants of the noble metals. *Physical Review B* **6** (1972), 4370–4379.
- [97] G. Beadie, M. Brindza, R. A. Flynn, A. Rosenberg and J. S. Shirk. Refractive index measurements of poly(methyl methacrylate) (PMMA) from 04–16 μm . *Applied Optics* **54** (2015), F139.
- [98] A. V. Chebykin, A. A. Orlov, A. V. Vozianova, S. I. Maslovski, Y. S. Kivshar and P. A. Belov. Nonlocal effective medium model for multilayered metal-dielectric metamaterials. *Phys. Rev. B* **84** (2011), 115438.
- [99] Z. Jacob, J.-Y. Kim, G. V. Naik, A. Boltasseva, E. E. Narimanov, V. M. Shalaev and A. Boltasseva. Engineering photonic density of states using metamaterials. *Appl Phys B* **100** (2010), 215–218.
- [100] A. Kinkhabwala, Z. Yu, S. Fan, Y. Avlasevich, K. Müllen and W. E. Moerner. Large single-molecule fluorescence enhancements produced by a bowtie nanoantenna. *Nature Photonics* **3** (2009), 654–657.
- [101] G. G. Stoney and C. A. Parsons. The tension of metallic films deposited by electrolysis. *Proceedings of the Royal Society of London. Series A, Containing Papers of a Mathematical and Physical Character* **82** (1909), 172–175.

- [102] S. Timoshenko. Analysis of Bi-Metal Thermostats. *J. Opt. Soc. Am.* **11** (1925), 233–255.
- [103] M. Habib, I. Issah, E. Bermúdez-Ureña and H. Caglayan. Self-Rolling SiO₂/Au Based Epsilon-Near-Zero Metamaterials. *Advanced Optical Materials* **10** (2022), 2200081.
- [104] J. Zang and F. Liu. Modified Timoshenko formula for bending of ultrathin strained bilayer films. *Applied Physics Letters* **92** (2008), 021905.
- [105] L. M. Viculis, J. J. Mack and R. B. Kaner. A Chemical Route to Carbon Nanoscrolls. *Science* **299** (2003), 1361–1361.
- [106] S. Meng and Y. Li. Graphene nanoscrolls made from isolated carbon nanotubes with line defects. *Japanese Journal of Applied Physics* **58** (2019), 050910.
- [107] D. Yu and F. Liu. Synthesis of carbon nanotubes by rolling up patterned graphene nanoribbons using selective atomic adsorption. *Nano letters* **7** (2007), 3046–3050.
- [108] M. Calvaresi, M. Quintana, P. Rudolf, F. Zerbetto and M. Prato. Rolling up a graphene sheet. *ChemPhysChem* **14** (2013), 3447–3453.
- [109] S. Kang, J.-B. Pyo and T.-S. Kim. Layer-by-layer assembly of free-standing nanofilms by controlled rolling. *Langmuir* **34** (2018), 5831–5836.
- [110] J. Li, J. Zhang, W. Gao, G. Huang, Z. Di, R. Liu, J. Wang and Y. Mei. Dry-Released Nanotubes and Nanoengines by Particle-Assisted Rolling. *Advanced Materials* **25** (2013), 3715–3721.
- [111] D. Gracias, V. Kavthekar, J. Love, K. Paul and G. Whitesides. Fabrication of Micrometer-Scale, Patterned Polyhedra by Self-Assembly. *Advanced Materials* **14** (2002), 235–238.
- [112] V. Prinz, V. Seleznev, A. Gutakovsky, A. Chehovskiy, V. Preobrazhenskii, M. Putyato and T. Gavrilova. Free-standing and overgrown InGaAs/GaAs nanotubes, nanohelices and their arrays. *Physica E: Low-dimensional Systems and Nanostructures* **6** (2000), 828–831.
- [113] C. Downs and T. E. Vandervelde. Progress in Infrared Photodetectors Since 2000. *Sensors* **13** (2013), 5054–5098.
- [114] X. Li. Self-rolled-up microtube ring resonators: a review of geometrical and resonant properties. *Advances in Optics and Photonics* **3** (2011), 366–387.

- [115] O. G. Schmidt and K. Eberl. Thin solid films roll up into nanotubes. *Nature* **410** (2001), 168–168.
- [116] O. Schmidt and N. Jin-Phillipp. Free-standing SiGe-based nanopipelines on Si (001) substrates. *Applied Physics Letters* **78** (2001), 3310–3312.
- [117] M. Huang, F. Cavallo, F. Liu and M. G. Lagally. Nanomechanical architecture of semiconductor nanomembranes. *Nanoscale* **3** (2011), 96–120.
- [118] W. Li, G. Huang, H. Yan, J. Wang, Y. Yu, X. Hu, X. Wu and Y. Mei. Fabrication and stimuli-responsive behavior of flexible micro-scrolls. *Soft Matter* **8** (2012), 7103–7107.
- [119] S. V. Golod, V. Y. Prinz, P. Wägli, L. Zhang, O. Kirfel, E. Deckhardt, F. Glaus, C. David and D. Grützmacher. Freestanding SiGe/Si/Cr and SiGe/Si/Si-xNy/Cr microtubes. *Applied Physics Letters* **84** (2004), 3391–3393.
- [120] F. Cavallo, W. Sigle and O. G. Schmidt. Controlled fabrication of Cr/Si and Cr/SiGe tubes tethered to insulator substrates. *Journal of Applied Physics* **103** (2008), 116103.
- [121] X. Yu, E. Arbabi, L. L. Goddard, X. Li and X. Chen. Monolithically integrated self-rolled-up microtube-based vertical coupler for three-dimensional photonic integration. *Applied Physics Letters* **107** (2015), 031102.
- [122] X. Yu, L. L. Goddard, X. Li and X. Chen. Enhanced axial confinement in a monolithically integrated self-rolled-up SiNx vertical microring photonic coupler. *Applied Physics Letters* **109** (2016), 111104.
- [123] I. Issah, M. Habib and H. Caglayan. Long-range qubit entanglement via rolled-up zero-index-waveguide. *Nanophotonics* **10** (2021), 4579–4589.
- [124] V. Luchnikov, O. Sydorenko and M. Stamm. Self-Rolled Polymer and Composite Polymer/Metal Micro- and Nanotubes with Patterned Inner Walls. *Advanced Materials* **17** (2005), 1177–1182.
- [125] A. Gladman, E. Matsumoto, R. Nuzzo, L. Mahadevan and J. Lewis. Biomimetic 4D printing. *Nature materials* **15** (2016).
- [126] D.-H. Kim, J.-H. Ahn, W. M. Choi, H.-S. Kim, T.-H. Kim, J. Song, Y. Y. Huang, Z. Liu, C. Lu and J. A. Rogers. Stretchable and foldable silicon integrated circuits. *Science* **320** (2008), 507–511.

- [127] F. Liu and M. Lagally. Interplay of stress, structure, and stoichiometry in Ge-covered Si (001). *Physical review letters* **76** (1996), 3156.
- [128] R. Ramachandran, D. Johnson-McDaniel and T. T. Salguero. Formation and scrolling behavior of metal fluoride and oxyfluoride nanosheets. *Chemistry of Materials* **28** (2016), 7257–7267.
- [129] H. Wang, J. G. S. Moo and M. Pumera. Tissue cell assisted fabrication of tubular catalytic platinum microengines. *Nanoscale* **6** (2014), 11359–11363.
- [130] G. D. Cole, Y. Bai, M. Aspelmeyer and E. A. Fitzgerald. Free-standing Al_xGa_{1-x}As heterostructures by gas-phase etching of germanium. *Applied Physics Letters* **96** (2010), 261102.
- [131] N. Sridi, B. Lebental, J. Azevedo, J. C. P. Gabriel and A. Ghis. Electrostatic method to estimate the mechanical properties of suspended membranes applied to nickel-coated graphene oxide. *Applied Physics Letters* **103** (2013), 051907.
- [132] P. Froeter, Y. Huang, O. V. Cangelaris, W. Huang, E. W. Dent, M. U. Gillette, J. C. Williams and X. Li. Toward Intelligent Synthetic Neural Circuits: Directing and Accelerating Neuron Cell Growth by Self-Rolled-Up Silicon Nitride Microtube Array. *ACS Nano* **8** (2014), 11108–11117.
- [133] W. Huang, Z. Yang, M. D. Kraman, Q. Wang, Z. Ou, M. M. Rojo, A. S. Yalamathy, V. Chen, F. Lian, J. H. Ni, S. Liu, H. Yu, L. Sang, J. Michaels, D. J. Sievers, J. G. Eden, P. V. Braun, Q. Chen, S. Gong, D. G. Senesky, E. Pop and X. Li. Monolithic mtesla-level magnetic induction by self-rolled-up membrane technology. *Science Advances* **6** (2020), eaay4508.
- [134] Q. Guo, G. Wang, D. Chen, G. Li, G. Huang, M. Zhang, X. Wang, Y. Mei and Z. Di. Exceptional transport property in a rolled-up germanium tube. *Applied Physics Letters* **110** (2017), 112104.
- [135] Z. Tian, B. Xu, B. Hsu, L. Stan, Z. Yang and Y. Mei. Reconfigurable vanadium dioxide nanomembranes and microtubes with controllable phase transition temperatures. *Nano Letters* **18** (2018), 3017–3023.
- [136] Y. V. Nastaushev, V. Y. Prinz and S. Svitashva. A technique for fabricating Au/Ti micro-and nanotubes. *Nanotechnology* **16** (2005), 908.

- [137] Y. Mei, G. Huang, A. A. Solovev, E. B. Ureña, I. Mönch, F. Ding, T. Reindl, R. K. Y. Fu, P. K. Chu and O. G. Schmidt. Inside Front Cover: Versatile Approach for Integrative and Functionalized Tubes by Strain Engineering of Nanomembranes on Polymers (Adv. Mater. 21/2008). *Advanced Materials* **20** (2008).
- [138] B. A. Ganji and B. Y. Majlis. Slotted capacitive microphone with sputtered aluminum diaphragm and photoresist sacrificial layer. *Microsystem technologies* **16** (2010), 1803–1809.
- [139] G. Zhao, A. Ambrosi and M. Pumera. Clean room-free rapid fabrication of roll-up self-powered catalytic microengines. *Journal of Materials Chemistry A* **2** (2014), 1219–1223.
- [140] D. Briukhanova, M. Habib, I. Issah and H. Caglayan. Low loss fishnet metamaterial via self-rolled nanotechnology. *Applied Physics Letters* **119** (2021), 141101.
- [141] Q. Wei, S. Tan, X. Liu, M. Yan, F. Wang, Q. Li, Q. An, R. Sun, K. Zhao, H. Wu and L. Mai. Energy Storage: Novel Polygonal Vanadium Oxide Nanoscrolls as Stable Cathode for Lithium Storage (Adv. Funct. Mater. 12/2015). *Advanced Functional Materials* **25** (2015), 1766–1766.
- [142] A. A. Solovev, Y. Mei, E. Bermúdez Ureña, G. Huang and O. G. Schmidt. Catalytic Microtubular Jet Engines Self-Propelled by Accumulated Gas Bubbles. *Small* **5** (2009), 1688–1692.
- [143] B. Xu, Z. Tian, J. Wang, H. Han, T. Lee and Y. Mei. Stimuli-responsive and on-chip nanomembrane micro-rolls for enhanced macroscopic visual hydrogen detection. *Science Advances* **4** (2018), eaap8203.
- [144] W. Li, G. Huang, J. Wang, Y. Yu, X. Wu, X. Cui and Y. Mei. Superelastic metal microsprings as fluidic sensors and actuators. *Lab Chip* **12** (2012), 2322–2328.
- [145] Z. Jacob, L. V. Alekseyev and E. Narimanov. Optical Hyperlens: Far-field imaging beyond the diffraction limit. *Opt. Express* **14** (2006), 8247–8256.
- [146] J. Kerbst, S. Schwaiger, A. Rottler, A. Koitmäe, M. Bröll, J. Ehlermann, A. Stemmann, C. Heyn, D. Heitmann and S. Mendach. Enhanced transmission in rolled-up hyperlenses utilizing Fabry-Pérot resonances. *Applied Physics Letters* **99** (2011), 191905.

- [147] Z. Liu, H. Lee, Y. Xiong, C. Sun and X. Zhang. Far-Field Optical Hyperlens Magnifying Sub-Diffraction-Limited Objects. *Science* **315** (2007), 1686–1686.
- [148] H. Lee, Z. Liu, Y. Xiong, C. Sun and X. Zhang. Development of optical hyperlens for imaging below the diffraction limit. *Opt. Express* **15** (2007), 15886–15891.
- [149] F. Monticone and A. Alù. Metamaterials and plasmonics: From nanoparticles to nanoantenna arrays, metasurfaces, and metamaterials. *Chinese Physics B* **23** (2014), 047809.
- [150] R. Kumar and K. Kajikawa. Superscattering from cylindrical hyperbolic metamaterials in the visible region. *Opt. Express* **28** (2020), 1507–1517.
- [151] Z. Ruan and S. Fan. Superscattering of Light from Subwavelength Nanostructures. *Phys. Rev. Lett.* **105** (2010), 013901.
- [152] F. Monticone, C. Argyropoulos and A. Alù. Multilayered Plasmonic Covers for Comblike Scattering Response and Optical Tagging. *Phys. Rev. Lett.* **110** (2013), 113901.
- [153] H. L. Chen and L. Gao. Tunability of the unconventional Fano resonances in coated nanowires with radial anisotropy. *Opt. Express* **21** (2013), 23619–23630.
- [154] R. Kumar and K. Kajikawa. Comparison of cylinder- and planar-effective medium approximations on calculation of scattering properties of cylindrical hyperbolic metamaterials. *J. Opt. Soc. Am. B* **36** (2019), 559–564.
- [155] W. Liu. Superscattering pattern shaping for radially anisotropic nanowires. *Phys. Rev. A* **96** (2017), 023854.
- [156] B. Edwards, A. Alú, M. E. Young, M. Silveirinha and N. Engheta. Experimental Verification of Epsilon-Near-Zero Metamaterial Coupling and Energy Squeezing Using a Microwave Waveguide. *Phys. Rev. Lett.* **100** (2008), 033903.
- [157] A. Rottler, M. Harland, M. Bröll, S. Schwaiger, D. Stickler, A. Stemmann, C. Heyn, D. Heitmann and S. Mendach. Rolled-up nanotechnology for the fabrication of three-dimensional fishnet-type GaAs-metal metamaterials with negative refractive index at near-infrared frequencies. *Applied Physics Letters* **100** (2012), 151104.

- [158] D. R. Smith, D. C. Vier, T. Koschny and C. M. Soukoulis. Electromagnetic parameter retrieval from inhomogeneous metamaterials. *Physical Review E - Statistical, Nonlinear, and Soft Matter Physics* **71** (2005), 036617.
- [159] I. V. Semchenko, S. A. Khakhomov, E. V. Naumova, V. Y. Prinz, S. V. Golod and V. V. Kubarev. Study of the properties of artificial anisotropic structures with high chirality. *Crystallography Reports* **56** (2011), 366–373.
- [160] Y. Li, A. Nemilentsau and C. Argyropoulos. Resonance energy transfer and quantum entanglement mediated by epsilon-near-zero and other plasmonic waveguide systems. *Nanoscale* **11** (2019), 14635–14647.
- [161] S. A. H. Gangaraj, A. Nemilentsau, G. W. Hanson and S. Hughes. Transient and steady-state entanglement mediated by three-dimensional plasmonic waveguides. *Optics Express* **23** (2015), 22330.
- [162] S. A. H. Gangaraj, G. W. Hanson and M. Antezza. Robust entanglement with three-dimensional nonreciprocal photonic topological insulators. *Physical Review A* **95** (2017), 063807.
- [163] A. Gonzalez-Tudela, D. Martin-Cano, E. Moreno, L. Martin-Moreno, C. Tejedor and F. J. Garcia-Vidal. Entanglement of two qubits mediated by one-dimensional plasmonic waveguides. *Physical Review Letters* **106** (2011), 020501.
- [164] I. DÁmico, D. G. Angelakis, F. Bussi eres, H. Caglayan, C. Couteau, T. Durt, B. Kolaric, P. Maletinsky, W. Pfeiffer, P. Rabl, A. Xuereb and M. Agio. Nanoscale quantum optics. *Rivista del Nuovo Cimento* **42** (2019), 153–195.
- [165] A. W. Snyder and J. D. Love. *Optical Waveguide Theory*. Kluwer Academic Publishers, 1983.
- [166] L. Vertchenko, C. DeVault, R. Malureanu, E. Mazur and A. Lavrinenko. Near-Zero Index Photonic Crystals with Directive Bound States in the Continuum. *Laser & Photonics Reviews* **15** (2021), 2000559.
- [167] Y. Pan and S. Xu. Energy tunnelling through an ultrasmall epsilon-near-zero channel in circular waveguide. *IET Microwaves, Antennas and Propagation* **3** (2009), 821–825.
- [168] M. O. Scully and M. S. Zubairy. *Quantum Optics*. Cambridge University Press, 1997.

- [169] P. Kok. Principles of quantum computation and information volume II. *Journal of Physics A: Mathematical and Theoretical* **40** (2007).
- [170] Y. Hao and G.-L. Long. Quantum information and quantum computing. *Fundamental Research* **1** (2021).
- [171] Quantum-state engineering with Josephson-junction devices. *Reviews of Modern Physics* **73** (2001).
- [172] R. Hanson, L. P. Kouwenhoven, J. R. Petta, S. Tarucha and L. M. Vandersypen. Spins in few-electron quantum dots. *Reviews of Modern Physics* **79** (2007).
- [173] B. Lienhard, T. Schröder, S. Mouradian, F. Dolde, T. T. Tran, I. Aharonovich and D. Englund. Bright and photostable single-photon emitter in silicon carbide. *Optica* **3** (2016).
- [174] R. Sokhoyan and H. A. Atwater. Quantum optical properties of a dipole emitter coupled to an ϵ -near-zero nanoscale waveguide. *Opt. Express* **21** (2013), 32279–32290.
- [175] E. J. R. Vesseur, T. Coenen, H. Caglayan, N. Engheta and A. Polman. Experimental verification of $n=0$ structures for visible light. *Physical Review Letters* **110** (2013), 013902.
- [176] W. K. Wootters. Entanglement of formation of an arbitrary state of two qubits. *Physical Review Letters* **80** (1998), 2245–2248.
- [177] H. T. Dung, L. Knöll and D.-G. Welsch. Resonant dipole-dipole interaction in the presence of dispersing and absorbing surroundings. *Phys. Rev. A* **66** (2002), 063810.
- [178] D. Martín-Cano, A. González-Tudela, L. Martín-Moreno, F. J. García-Vidal, C. Tejedor and E. Moreno. Dissipation-driven generation of two-qubit entanglement mediated by plasmonic waveguides. *Phys. Rev. B* **84** (2011), 235306.
- [179] E. del Valle. Strong and weak coupling of two coupled qubits. *Phys. Rev. A* **81** (2010), 053811.
- [180] C. A. Downing, J. C. L. Carreño, A. I. Fernández-Domínguez and E. del Valle. Asymmetric coupling between two quantum emitters. *Phys. Rev. A* **102** (2020), 013723.

- [181] E. Özgün, E. Ozbay and H. Caglayan. Tunable Zero-Index Photonic Crystal Waveguide for Two-Qubit Entanglement Detection. *ACS Photonics* **3** (2016), 2129–2133.
- [182] R. Schirhagl, K. Chang, M. Loretz and C. L. Degen. Nitrogen-Vacancy Centers in Diamond: Nanoscale Sensors for Physics and Biology. *Annual Review of Physical Chemistry* **65** (2014), 83–105.
- [183] A. Bhardwaj, V. Sridurai, S. A. Bhat, C. V. Yelamaggad and G. G. Nair. Photo-tunable epsilon-near-zero behavior in a self-assembled liquid crystal – nanoparticle hybrid material. *Nanoscale Adv.* **3** (2021), 2508–2515.
- [184] I. Ben Tahar, P. Fickers, A. Dziedzic, D. Płoch, B. Skóra and M. Kus-Liśkiewicz. Green pyomelanin-mediated synthesis of gold nanoparticles: Modelling and design, physico-chemical and biological characteristics. *Microbial Cell Factories* **18** (2019).
- [185] M. Mahmood, M. Abid, M. F. Nazar, M. N. Zafar, M. A. Raza, M. Ashfaq, A. M. Khan, S. H. Sumrera and M. Zubair. The wet chemical synthesis of surfactant-capped quasi-spherical silver nanoparticles with enhanced antibacterial activity. *Mater. Adv.* **1** (2020), 2332–2338.
- [186] T. Rambaran and R. Schirhagl. Nanotechnology from lab to industry – a look at current trends. *Nanoscale Adv.* **4** (2022), 3664–3675.
- [187] P. Yang, J. Zheng, Y. Xu, Q. Zhang and L. Jiang. Colloidal synthesis and applications of plasmonic metal nanoparticles. *Advanced materials* **28** (2016), 10508–10517.
- [188] L. Liu, X. Zhang, L. Yang, L. Ren, D. Wang and J. Ye. Metal nanoparticles induced photocatalysis. *National Science Review* **4** (2017), 761–780.
- [189] X. Wu, C. Hao, J. Kumar, H. Kuang, N. A. Kotov, L. M. Liz-Marzán and C. Xu. Environmentally responsive plasmonic nanoassemblies for biosensing. *Chemical Society Reviews* **47** (2018), 4677–4696.
- [190] N. G. Bastús, J. Comenge and V. Puntes. Kinetically controlled seeded growth synthesis of citrate-stabilized gold nanoparticles of up to 200 nm: size focusing versus Ostwald ripening. *Langmuir* **27** (2011), 11098–11105.

- [191] J. S. DuChene, W. Niu, J. M. Abendroth, Q. Sun, W. Zhao, F. Huo and W. D. Wei. Halide anions as shape-directing agents for obtaining high-quality anisotropic gold nanostructures. *Chemistry of Materials* **25** (2013), 1392–1399.
- [192] Y. Xia, Y. Xiong, B. Lim and S. E. Skrabalak. Shape-controlled synthesis of metal nanocrystals: simple chemistry meets complex physics?: *Angewandte Chemie International Edition* **48** (2009), 60–103.
- [193] C. Graf and A. van Blaaderen. Metallodielectric Colloidal Core-Shell Particles for Photonic Applications. *Langmuir* **18** (2002), 524–534.
- [194] K. Hasegawa, C. Rohde and M. Deutsch. Enhanced surface-plasmon resonance absorption in metal-dielectric-metal layered microspheres. *Opt. Lett.* **31** (2006), 1136–1138.
- [195] S. A. Scherbak and A. A. Lipovskii. Understanding the Second-Harmonic Generation Enhancement and Behavior in Metal Core–Dielectric Shell Nanoparticles. *The Journal of Physical Chemistry C* **122** (2018), 15635–15645.
- [196] Y. Pu, R. Grange, C.-L. Hsieh and D. Psaltis. Nonlinear Optical Properties of Core-Shell Nanocavities for Enhanced Second-Harmonic Generation. *Phys. Rev. Lett.* **104** (2010), 207402.
- [197] M. A. Ochsenkühn, P. R. T. Jess, H. Stoquert, K. Dholakia and C. J. Campbell. Nanoshells for Surface-Enhanced Raman Spectroscopy in Eukaryotic Cells: Cellular Response and Sensor Development. *ACS Nano* **3** (2009), 3613–3621.
- [198] P. K. Jain and M. A. El-Sayed. Surface Plasmon Resonance Sensitivity of Metal Nanostructures: Physical Basis and Universal Scaling in Metal Nanoshells. *The Journal of Physical Chemistry C* **111** (2007), 17451–17454.
- [199] C. Zhang, T. Zhang, Z. Zhang and H. Zheng. Plasmon Enhanced Fluorescence and Raman Scattering by [Au-Ag Alloy NP Cluster]@SiO₂ Core-Shell Nanostructure. *Frontiers in Chemistry* **7** (2019).
- [200] C. K. Chan, R. C. Flagan and J. H. Seinfeld. Resonance structures in elastic and Raman scattering from microspheres. *Appl. Opt.* **30** (1991), 459–467.
- [201] F. Zhang, G. B. Braun, Y. Shi, Y. Zhang, X. Sun, N. O. Reich, D. Zhao and G. Stucky. Fabrication of Ag@SiO₂@Y₂O₃:Er Nanostructures for Bioimaging: Tuning of the Upconversion Fluorescence with Silver Nanoparticles. *Journal of the American Chemical Society* **132** (2010), 2850–2851.

- [202] V. S. Zuev. SPASER laser and Purcell factor. *Optics and Spectroscopy* **109** (2010), 760–762.
- [203] M. A. Noginov, G. Zhu, A. M. Belgrave, R. Bakker, V. M. Shalaev, E. E. Narimanov, S. Stout, E. Herz, T. Suteewong and U. Wiesner. Demonstration of a spaser-based nanolaser. *Nature* **460** (2009), 1110–1112.
- [204] I. S. Curtis, R. J. Wills and M. Dasog. Photocatalytic hydrogen generation using mesoporous silicon nanoparticles: Influence of magnesiothermic reduction conditions and nanoparticle aging on the catalytic activity. *Nanoscale* **13** (2021), 2685–2692.
- [205] D. Rativa and L. A. Gómez-Malagón. Colloidal plasmonic structures for harvesting solar radiation. *Renewable Energy* **118** (2018), 947–954.
- [206] A. D. Phan, N. B. Le, N. T. Lien and K. Wakabayashi. Multilayered plasmonic nanostructures for solar energy harvesting. *Journal of Physical Chemistry C* **122** (2018), 19801–19806.
- [207] M. G. Blaber, M. D. Arnold and M. J. Ford. A review of the optical properties of alloys and intermetallics for plasmonics. *Journal of Physics Condensed Matter* **22** (2010), 143201.
- [208] I. L. Rasskazov, P. S. Carney and A. Moroz. STRATIFY: a comprehensive and versatile MATLAB code for a multilayered sphere. *OSA Continuum* **3** (2020), 2290–2306.
- [209] L. F. Chen, C. K. Ong and B. T. G. Tan. Effective Permittivity of Layered Dielectric Sphere Composites. *Journal of materials science* **33.24** (1998), 5891–5894.
- [210] J. D. Jackson. *Classical electrodynamics; 2nd ed.* New York, NY: Wiley, 1975.
- [211] Y. Guo, C. L. Cortes, S. Molesky and Z. Jacob. Broadband super-Planckian thermal emission from hyperbolic metamaterials. *Applied Physics Letters* **101** (2012), 131106.
- [212] X. Zhang, S. Ye, X. Zhang and L. Wu. Optical properties of SiO₂@M (M = Au, Pd, Pt) core-shell nanoparticles: material dependence and damping mechanisms. *J. Mater. Chem. C* **3** (2015), 2282–2290.
- [213] X. Fan, W. Zheng and D. J. Singh. Light scattering and surface plasmons on small spherical particles. *Light: Science & Applications* **3** (2014), e179.

- [214] N. Zheludev and Y. Kivshar. From Metamaterials to Metadevices. *Nature materials* **11** (2012), 917–24.
- [215] J. Q. Quach, C.-H. Su, A. M. Martin, A. D. Greentree and L. C. L. Hollenberg. Reconfigurable quantum metamaterials. *Opt. Express* **19** (2011), 11018–11033.
- [216] Y. Li and C. Argyropoulos. Multiqubit entanglement and quantum phase gates with epsilon-near-zero plasmonic waveguides. *Applied Physics Letters* **119**, 21 (2021), 211104.
- [217] C. C. Katsidis and D. I. Siapkas. General transfer-matrix method for optical multilayer systems with coherent, partially coherent, and incoherent interference. *Appl. Opt.* **41** (2002), 3978–3987.

A APPENDIX

A.1 Transfer matrix method

The transfer-matrix method (TMM) is a very prominent technique for multilayer thin films to elucidate the relation between an incident, reflected, and transmitted field on a media as compared with the Airy summation approach [217]. Using the boundary condition criteria where the tangential components of the magnetic and electric fields are continuous across a planar boundary, we can connect the fields at any interface to any other interface in the multilayer. The formulation presented below considers all the relevant information needed to attain some unique optical response of a multilayer media. Concerning the conditions stated earlier, we present the TM mode (p -polarized) optical field which can be easily extended to the TE mode. We assumed an optical field with no transverse momentum in the y -direction and as such, the propagation wavevector $\mathbf{k} = k_x \hat{x} + k_z \hat{z}$, where k_x^n and k_z^n are the projections of the propagation wavevector along the x - and z -directions which can be linked to the IFC relation as:

$$k_x^2 + k_z^2 = \epsilon(\omega/c)^2 \quad (\text{A.1})$$

If $k_x^2 > \epsilon(\omega/c)^2$, the condition: $\text{Im}[k_z] > 0$ must be satisfied so that amplitudes of the electric and magnetic fields decay as they propagate. P -polarized light only has a magnetic field in the y -direction such that in the n^{th} layer of the multilayered media, the magnetic field can be written as $\mathbf{H}^n = H_y^n \hat{y}$ with

$$H_y^n = a_+^n e^{j(k_x^n x + k_z^n z)} + a_-^n e^{j(k_x^n x - k_z^n z)}, \quad (\text{A.2})$$

where a_{\pm}^n are the complex amplitudes of the forward and backward propagating waves that are supported in the n^{th} layer of the media. From Maxwell's equations, the

relation of the x -component of the electric field from the magnetic field is obtained as:

$$E_x^n = \frac{k_z^n}{\epsilon_n k_o} a_+^n e^{j(k_x^n x + k_z^n z)} + \frac{-k_z^n}{\epsilon_n k_o} a_-^n e^{j(k_x^n x - k_z^n z)}, \quad (\text{A.3})$$

where $k_o = \omega/c = 2\pi/\lambda$ and ϵ_i is the permittivity of the n^{th} layer of the media. Using the boundary conditions, the components of the magnetic and electric field parallel to the interface, H_{\parallel} and E_{\parallel} , are required to be continuous across the interface. For these conditions to be satisfied: the transverse wavevector k_x is to be conserved the whole system: $k_x = k_x^n \forall n$.

$$\begin{aligned} E_x^n \Big|_{z=z_n} &= E_x^{n+1} \Big|_{z=z_n} \\ H_y^n \Big|_{z=z_n} &= H_y^{n+1} \Big|_{z=z_n}. \end{aligned} \quad (\text{A.4})$$

The boundary conditions for the n^{th} interface may be simplified to:

$$\begin{aligned} a_+^n e^{jk_z^n z_n} + a_-^n e^{-jk_z^n z_n} &= a_+^{n+1} e^{jk_z^{n+1} z_n} + a_-^{n+1} e^{-jk_z^{n+1} z_n} \\ \frac{k_z^n}{\epsilon_n} a_+^n e^{jk_z^n z_n} - \frac{k_z^n}{\epsilon_n} a_-^n e^{-jk_z^n z_n} &= \frac{k_z^{n+1}}{\epsilon_{n+1}} a_+^{n+1} e^{jk_z^{n+1} z_n} - \frac{k_z^{n+1}}{\epsilon_{n+1}} a_-^{n+1} e^{-jk_z^{n+1} z_n}. \end{aligned} \quad (\text{A.5})$$

which can be presented in a matrix form:

$$\begin{aligned} \begin{pmatrix} 1 & 1 \\ \frac{k_z^n}{\epsilon_n} & -\frac{k_z^n}{\epsilon_n} \end{pmatrix} \begin{pmatrix} e^{jk_z^n z_n} & 0 \\ 0 & e^{-jk_z^n z_n} \end{pmatrix} \begin{pmatrix} a_+^n \\ a_-^n \end{pmatrix} &= \begin{pmatrix} 1 & 1 \\ \frac{k_z^{n+1}}{\epsilon_{n+1}} & -\frac{k_z^{n+1}}{\epsilon_{n+1}} \end{pmatrix} \\ &\quad \begin{pmatrix} e^{jk_z^{n+1} z_n} & 0 \\ 0 & e^{-jk_z^{n+1} z_n} \end{pmatrix} \begin{pmatrix} a_+^{n+1} \\ a_-^{n+1} \end{pmatrix} \end{aligned} \quad (\text{A.6})$$

Equation (A.6) can be presented in a more concise form as:

$$D_n p_n \begin{pmatrix} a_+^n \\ a_-^n \end{pmatrix} = D_{n+1} p_{n+1} \begin{pmatrix} a_+^{n+1} \\ a_-^{n+1} \end{pmatrix} \quad (\text{A.7})$$

Additionally, this formulation can be extended to the $z = z_{n+1}$ interface such that

$$D_{n+1}P_{n+1} \begin{pmatrix} a_+^{n+1} \\ a_-^{n+1} \end{pmatrix} = D_{n+2}P_{n+2} \begin{pmatrix} a_+^{n+2} \\ a_-^{n+2} \end{pmatrix}. \quad (\text{A.8})$$

From Eqs. (A.7) and (A.8), the complex amplitudes of the n^{th} layer can be related to $i + 2^{\text{th}}$ layer as:

$$\begin{aligned} \begin{pmatrix} a_+^n \\ a_-^n \end{pmatrix} &= \begin{pmatrix} e^{jk_z^n z_n} & 0 \\ 0 & e^{-jk_z^n z_n} \end{pmatrix}^{-1} \begin{pmatrix} 1 & 1 \\ \frac{k_z^n}{\epsilon_n} & -\frac{k_z^n}{\epsilon_n} \end{pmatrix}^{-1} \begin{pmatrix} 1 & 1 \\ \frac{k_z^{n+1}}{\epsilon_{n+1}} & -\frac{k_z^{n+1}}{\epsilon_{n+1}} \end{pmatrix} \\ &\quad \begin{pmatrix} e^{jk_z^{n+1} z_n} & 0 \\ 0 & e^{-jk_z^{n+1} z_n} \end{pmatrix} \begin{pmatrix} e^{jk_z^{n+1} z_{n+1}} & 0 \\ 0 & e^{-jk_z^{n+1} z_{n+1}} \end{pmatrix}^{-1} \\ &\quad \begin{pmatrix} 1 & 1 \\ \frac{k_z^{n+1}}{\epsilon_{n+1}} & -\frac{k_z^{n+1}}{\epsilon_{n+1}} \end{pmatrix}^{-1} \begin{pmatrix} 1 & 1 \\ \frac{k_z^{n+2}}{\epsilon_{n+2}} & -\frac{k_z^{n+2}}{\epsilon_{n+2}} \end{pmatrix} \begin{pmatrix} a_+^{n+2} \\ a_-^{n+2} \end{pmatrix} \end{aligned} \quad (\text{A.9})$$

or equivalently,

$$\begin{pmatrix} a_+^n \\ a_-^n \end{pmatrix} = P_n^{-1} D_n^{-1} D_{n+1} P_{n+1} D_{n+1}^{-1} D_{n+2} P_{n+2} \begin{pmatrix} a_+^{n+2} \\ a_-^{n+2} \end{pmatrix} \quad (\text{A.10})$$

Here, P_{n+1} is the combination of the 4th and 5th matrices on the right hand side of the equation. We can now continue the same process as above by extending the formula from layer $i = 0$ to layer $i = N$ for a multilayered media. In this way, we move the boundary conditions from the interface $i = 0$ to the interface $i = N$ as:

$$\begin{pmatrix} a_+^0 \\ a_-^0 \end{pmatrix} = P_0^{-1} D_0^{-1} \left(\prod_{i=1}^N D_n P_n D_n^{-1} \right) D_{N+1} P_{N+1} \begin{pmatrix} a_+^{N+1} \\ a_-^{N+1} \end{pmatrix} \quad (\text{A.11})$$

Conclusively, suppose we define the first interface as the origin ($z_0 = 0$) and use the physical fields for the outer regions (incoming and reflected waves for the incident medium and only one outgoing wave is propagated into the final medium) then the

overall result for p -polarized (and s -polarized) light is given by:

$$\begin{pmatrix} 1 \\ r^{s,p} \end{pmatrix} = (D_0^{s,p})^{-1} T^{s,p} D_{N+1}^{s,p} \begin{pmatrix} t^{s,p} \\ 0 \end{pmatrix} \quad (\text{A.12})$$

where

$$T^{s,p} = \left(\prod_{i=1}^N D_n^{s,p} P_n (D_n^{s,p})^{-1} \right) \quad (\text{A.13})$$

and

$$D_n^p = \begin{pmatrix} 1 & 1 \\ \frac{k_z^n}{\epsilon_n} & -\frac{k_z^n}{\epsilon_n} \end{pmatrix}, D_n^s = \begin{pmatrix} 1 & 1 \\ k_z^n & -k_z^n \end{pmatrix}, P_n = \begin{pmatrix} e^{-jk_z^n d_n} & 0 \\ 0 & e^{jk_z^n d_n} \end{pmatrix}. \quad (\text{A.14})$$

The reflection and transmission coefficients are given by:

$$\begin{aligned} r^{s,p} &= \frac{M_{21}^{s,p}}{M_{11}^{s,p}} \\ t^{s,p} &= \frac{1}{M_{11}^{s,p}} \end{aligned} \quad (\text{A.15})$$

where $M = (D_0^{s,p})^{-1} T^{s,p} D_{N+1}^{s,p}$, which is the total transfer matrix of the multilayered media.

A.2 List of other publications

- I M. Habib, **I. Issah**, E. Bermúdez-Ureña and H. Caglayan. Self-Rolling SiO₂/Au Based Epsilon-Near-Zero Metamaterials. *Advanced Optical Materials*, 10 (2022).
- II M. Habib, **I. Issah**, D. Briukhanova, A. R. Rashed and H. Caglayan. Wave-front Control with Nanohole Array-Based Out-of-Plane Metasurfaces. *ACS Applied Nano Materials* 4, 9 (2021).
- III D. Briukhanova, M. Habib, **I. Issah** and H. Caglayan. Low loss fishnet metamaterial via self-rolled nanotechnology. *Applied Physics Letters* 119, 14 (2021).
- IV D. Ghindani, **I. Issah**, S. Chervinskii, M. Lahikainen, K. Kuntze, A. Primagi and H. Caglayan. Humidity-Controlled Tunable Emission in a Dye-

- Incorporated Metal–Hydrogel–Metal Cavity. *ACS Photonics* 9,7 (2022).
- V **I. Issah**, C. R. Fernández, M. Habib, S. Chervinskii, and H. Caglayan. Dual-Band Metal-Insulator-Metasurface Absorber. arXiv:2209.00867 (2022).
- VI **I. Issah**, F. Li, M. Baah, I. A. Otoo, L. Asilevi, P. Bawuah and B. O. Asamoah. Passive tunable and polarization-insensitive fan-like metamaterial absorber in the visible spectrum. *J. Opt. Soc. Am. B* 38, 9 (2021).
- VII F. Li, **I. Issah**, M. Baah, R. Amedalor, M. Quarshie, P. Bawuah and B. O. Asamoah. Polarization-dependent wideband metamaterial absorber for ultraviolet to near-infrared spectral range applications. *Opt. Express* 30, 15 (2022).
- VIII Gupta, R.K. (Ed.). (2023). *Nanowires: Applications, Chemistry, Materials, and Technologies* (1st ed.). CRC Press. (Featured)
- IX C. R. Fernández, **I. Issah**, M. J. Recio, J. C. Ferrer, M. Morias, D. J. Aberasturi, L. M. LizMarz, M. A. Cotta, and A. Cantarero. Observation of the LO forbidden vibrational mode of indium phosphide nanowires when excited by localised surface plasmon resonances in the near-field. (Paper in preparation)
- X C. R. Fernández, M. Habib, **I. Issah**, H. A. Fernández, H. Caglayan. Enhanced light-matter interaction in 2D materials coupled with metasurfaces. (Paper in preparation)

PUBLICATIONS

PUBLICATION

I

Humidity- and Temperature-Tunable Metal–Hydrogel–Metal Reflective Filters

S. Chervinskii, I. Issah, M. Lahikainen, A. R. Rashed, K. Kuntze, A. Priimagi and
H. Caglayan

ACS Applied Materials & Interfaces **13**(42) (2021), 50564–50572

DOI: 10.1021/acsami.1c15616

Publication reprinted with the permission of the copyright holders



Humidity- and Temperature-Tunable Metal–Hydrogel–Metal Reflective Filters

Semyon Chervinskii, Ibrahim Issah, Markus Lahikainen, Alireza R. Rashed, Kim Kuntze, Arri Priimagi,* and Humeyra Caglayan*

Cite This: <https://doi.org/10.1021/acsami.1c15616>

Read Online

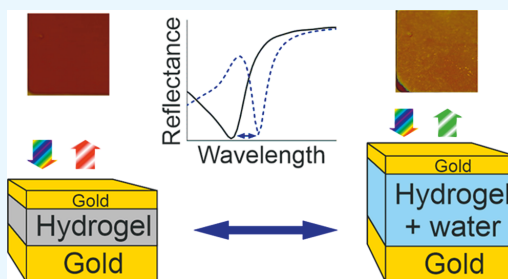
ACCESS |

Metrics & More

Article Recommendations

Supporting Information

ABSTRACT: A tunable reflectance filter based on a metal–hydrogel–metal structure responsive to humidity and temperature is reported. The filter employs a poly(*N*-isopropylacrylamide)–acrylamidobenzophenone (PNIPAm–BP) hydrogel as an insulator layer in the metal–insulator–metal (MIM) assembly. The optical resonance of the structure is tunable by water immersion across the visible and near-infrared range. Swelling/deswelling and the volume phase transition of the hydrogel allow continuous reversible humidity- and/or temperature-induced tuning of the optical resonance. This work paves the way toward low-cost large-area fabrication of actively tunable reversible photonic devices.



KEYWORDS: metal–insulator–metal, hydrogel, tunable color filter, stimuli-responsive material, active plasmonics, PNIPAm

1. INTRODUCTION

Since their emergence, plasmonic nanomaterials have been among the fastest-growing subfields of optical materials.^{1–3} Resonant optical absorption and support of highly localized strong electromagnetic fields have yielded many applications for these materials, such as active and passive optical elements, sensors, or energy conversion to mention but a few examples.^{4,5} One direction owing to the opportunity of tailoring the optical absorption⁶ is the development of various types of optical filters.^{4,7} For instance, customizing structural properties of plasmonic nanomaterials to design their spectral response has enabled high-quality color filters.⁸ However, in many cases, this has come with the cost of necessary top-down nanopatterning. To avoid that, lithography-free nanostructures have been developed, relying on thin film deposition and/or bottom-up self-assembly.^{9–11} Prominent examples of lithography-free nanostructures are metal–insulator–metal (MIM) structures¹² capable of resonant absorption of light and hence sometimes coined as “perfect absorbers”.¹³ The wavelength of the resonance is directly related to insulator thickness in this sandwich structure, as well as to its dielectric properties. Therefore, by changing this thickness, the resonance can be tuned across a wide spectral range.

Lately, there have been many advances in employing MIM structures as color filters in reflection or transmission,^{14–16} as well as studies of other MIM-based applications.^{17–19} There has been interest in making MIM structures actively tunable, widening their applicability in sensorics, optical filtering, and integrated optical devices.²⁰ An electrical tuning mechanism

was suggested using MIM with an electro-optical insulating layer.²¹ Another approach is using stimuli-responsive insulator layers, which would change the thickness or refractive index and therefore shift the resonance of the MIM structure.^{22,23} One example of such materials is hydrogels, which are responsive to several stimuli.^{24–26} First, they swell remarkably in the presence of water and are responsive to humidity change, which increases the hydrogel’s volume. Second, some hydrogels exhibit a reversible volume phase transition at a lower critical solution temperature (LCST) of the monomers cross-linked into the gel.²⁷ For gels, this temperature is also known as volume phase-transition temperature (VPTT). This phase transition results in changing hydrogels from hydrophilic to hydrophobic above the transition temperature, which leads to the expulsion of previously absorbed water and the respective reduction in the hydrogel’s volume. These two volume-tuning mechanisms in hydrogels work oppositely—increasing humidity causes the hydrogel to absorb water and swell, while increasing temperature causes it to expel water and contract.²⁸ In the last decade, these properties have brought hydrogels into the field of tunable plasmonic materials,^{29–34} structural coloration,^{35–37} and other optical elements.^{38–43} In

Received: August 16, 2021

Accepted: October 4, 2021

particular, Serpe *et al.* have worked extensively on tunable etalons where the dielectric layer comprises PNIPAm microgel, which in aqueous environment can rapidly respond to several stimuli, displaying a color-tuning range of hundreds of nanometers.^{35,44–49} Recently, Jang *et al.* have demonstrated a humidity-tunable optical transmittance filter for visible range based on a MIM structure with a chitosan hydrogel insulator layer at room temperature,⁵⁰ while Dong *et al.* have demonstrated a humidity-tunable reflectance filter using cellulose hydrogel.⁵¹ In both cases, only humidity-induced tuning was studied. To the best of our knowledge, no results have been reported so far combining both humidity and temperature stimuli on hydrogel-enabled mechanisms for optical tuning in air.

Here, we report a bistimuli-tunable hydrogel-based MIM reflection filter. We employ a poly(*N*-isopropylacrylamide)–acrylamidobenzophenone (PNIPAm–BP) hydrogel as the insulator layer, which reversibly changes dimensions under temperature and/or humidity control. The PNIPAm-based hydrogel has a good swelling ratio and good film-forming properties even in the desired 100 nm range.⁵² By applying temperature and humidity stimuli to the PNIPAm hydrogel incorporated into the MIM structure, we obtained continuous spectral tuning. The spectral tuning range amounted to 80 and 340 nm in the visible and near-infrared spectral range, respectively, depending on the initial thickness of the hydrogel. The proposed structures employ low-cost thin film deposition methods such as spin-coating and evaporation, which allows large-area devices and easy scalability. These simple-to-fabricate filters provide actively tunable reversible photonic devices, opening up a range of applications from nano- to macroscale.

2. RESULTS AND DISCUSSION

2.1. Filter Design. The MIM structures were fabricated from gold and PNIPAm–BP hydrogel (Figure 1). Gold was chosen for claddings as the nonoxidizing plasmonic layer. The thickness of the bottom layer was set to 100 nm to ensure high reflectivity, while for the top layer, a thickness of 30 nm was used to allow the collection of the reflected light. In this design, the resonant absorption characteristic of the MIM structure translates into the dip in the reflection spectrum; thus, we will

address this resonance as reflectance in this paper. Two sets of samples were fabricated, differing in the hydrogel layer thicknesses (80–100 and 200–300 nm). These hydrogel thicknesses correspond to the first-order resonance in the visible (VIS) and near-infrared (NIR) range, respectively, and will be hereon addressed as VIS and NIR samples.

The concept of the hydrogel-based tunable MIM reflective filters is schematically illustrated in Figure 1. The dry state, when hydrogel has no water absorbed, corresponds to a thinner hydrogel layer (Figure 1a). When the hydrogel absorbs water (the wet state), it swells and the resultant thickness increases, thus shifting the resonant reflection band of the MIM structure to longer wavelengths (Figure 1b). Figure 1c,d shows how the observable colors of the samples change between these two states, and the inset in Figure 1 illustrates the corresponding change in the spectra.

2.2. Modeling. To design MIM filters and predict their optical properties, we performed finite-difference time-domain (FDTD) calculations of the structures with different hydrogel layer thicknesses. The corresponding reflectance map is shown in Figure 2a. This MIM design allows tunability over a wide range of wavelengths, from just above the gold interband absorption up to at least 1.5 μm . For applications, it is important to consider the possible tuning range of the fabricated MIM structures, which in our case is limited by the swelling factor of the hydrogel (the ratio between wet and dry thicknesses). Assuming the swelling factor to be up to 2,⁵² we designed our VIS samples to have a dry thickness of around 100 nm and NIR one around 250 nm, which should correspond to the maximum achievable tuning range for the first-order resonance of about 550–700 and 900–1600 nm, respectively. It is worth noting that increasing the water content changes the refractive index of the insulator layer toward that of water. However, this difference is less than 0.1 (assuming a 1:1 water:hydrogel mixture for the maximum swelling with a factor of 2)⁵³ and therefore is not as influential as the thickness change, though it should slightly reduce the overall tuning range. Importantly, the thicker hydrogel layer also gives rise to higher-order resonances; e.g., in Figure 2a when the thickness exceeds 250 nm, the second order appears, and over 400–450 nm thickness also the third order, and so on. Comparing the electric field distributions for a 300 nm thick hydrogel (corresponding to the partly swollen NIR sample) at resonant wavelengths 1082 and 568 nm (Figure 2b,c, respectively), one can conclude that the latter resonance is indeed the second order. These higher-order resonances are also tunable with the thickness change, though with less sensitivity compared to the first-order resonance. However, this lesser sensitivity is compensated by the fact that a higher initial hydrogel thickness yields a higher absolute thickness change at the same swelling ratios.

2.3. Tuning by Water Immersion. To evaluate the maximum tuning range of the MIM structures, we compared their reflectance spectra at ambient conditions (26 °C, 30% relative humidity) and after immersion in deionized water for 20 min (Figure 3). The dry samples demonstrate reflectance dips almost to 0%, characteristic of MIM structures. The reflectance dips move to longer wavelengths after the samples are immersed in water; the corresponding color changes are evident in Videos S1 and S2. The penetration of water into the hydrogel layer is supposedly enabled by the porosity of the sputtered gold film,⁵⁴ and local variations of this porosity together with spin-coating defects (Figure S4) explain the

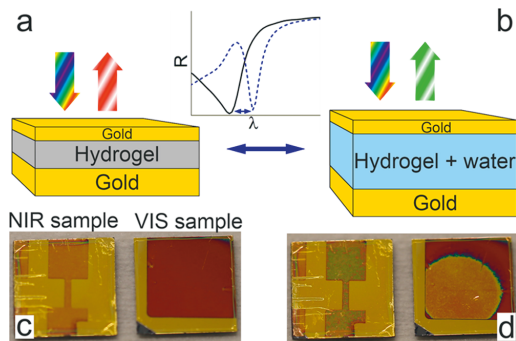


Figure 1. Top: schematic of the hydrogel MIM reflective filter in (a) dry and (b) wet states. The inset graph illustrates the corresponding changes in the reflectance spectra between these two states. Bottom: images of the NIR and VIS samples in (c) dry and (d) wet states.

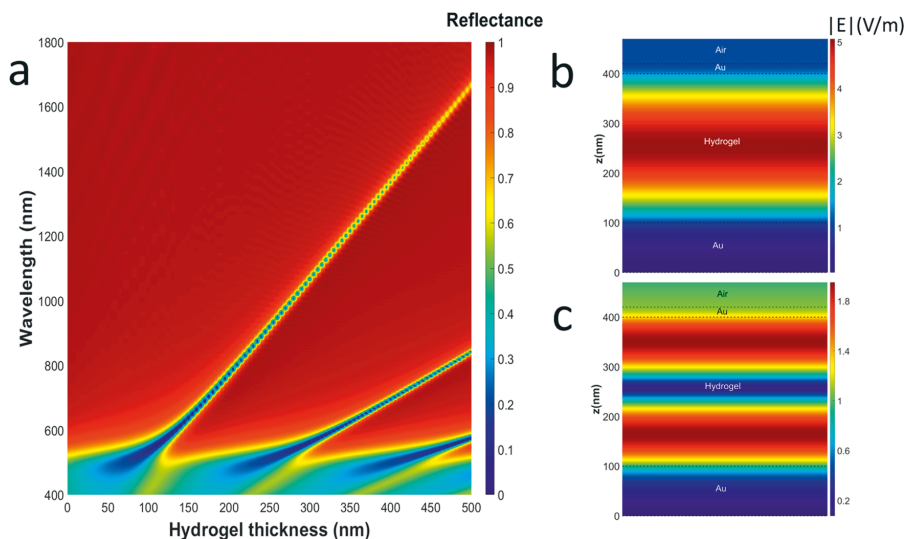


Figure 2. (a) Calculated reflectance of the MIM structure for different thicknesses of the hydrogel insulator layer. Note the presence and tunability of several resonant orders. (b, c) Electric field amplitudes for an MIM with a 300 nm thick hydrogel layer at 1082 nm (first order) (b) and 568 nm (second order) (c).

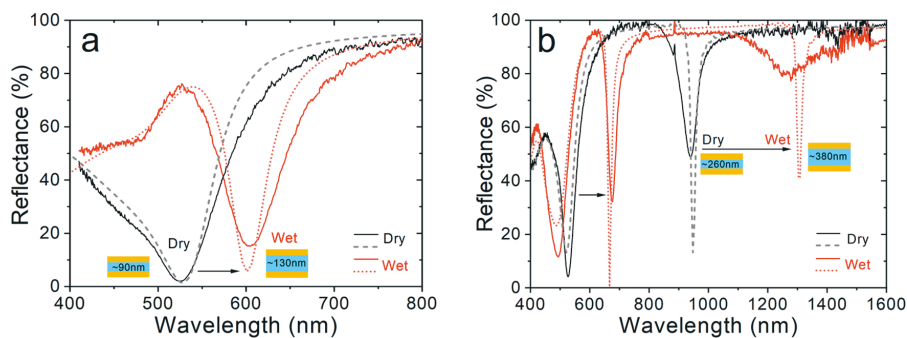


Figure 3. Reflectance of hydrogel-based MIM filters at ambient conditions and after immersion in water. (a) VIS sample and (b) NIR sample. Solid, experimental spectra; dashed and dotted, modeling. The arrows show the shift of the resonant dips.

observed inhomogeneities of swelling. The wavelength of the resonant absorbance of the MIM structure depends on the thickness of the insulator; therefore, swelling of the hydrogel increases the resonant wavelength of the filter.

The experimental results were fitted to the modeling presented in Figure 2. The validity of the model was confirmed by the perfect match between the reflectance spectra calculated for MIM structures with the hydrogel thicknesses of 90 and 260 nm and the experimental spectra for VIS and NIR samples with the measured hydrogel thicknesses of 85 ± 5 and 250 ± 10 nm, respectively. The observed broadening of the experimental resonances in comparison to the modeling, as well as the experimental data reported for solid-state MIMs elsewhere,¹⁵ can be explained by fabrication imperfections, originating mostly from spin-coating. Fitting the same model with different hydrogel layer thicknesses to the wet experimental spectra allowed us to estimate the thickness change. We considered a constant refractive index of 1.503 for

the hydrogel layer in all cases; therefore, the fitted thicknesses in the wet case are slightly underestimated.

The estimated change in the hydrogel thickness was from 90 to 130 nm for the VIS sample and from 260 to 380 nm for the NIR sample, which corresponds to a 1.4–1.5 swelling factor. The respective overall spectral shift of the resonance was 80 nm for the VIS sample (from 524 to 604 nm) and 340 nm for the NIR sample (from 940 to 1280 nm). In addition to that, the second-order resonance of the NIR sample shifted by 150 nm (from 524 to 674 nm). The latter illustrates that thicker hydrogel layers may be more beneficial for applications, as higher initial thickness allows a broader tuning range at a constant swelling ratio, while higher-order resonances give access to the visible wavelength range. Importantly, the swelling did not reduce the quality factors of the resonances: Q -factors ($Q = \lambda/\Delta\lambda$; Table S1) exceeded 10 in a 650–1000 nm wavelength range for both dry and wet states, and the maximum Q -factor of around 19 was measured for the second-

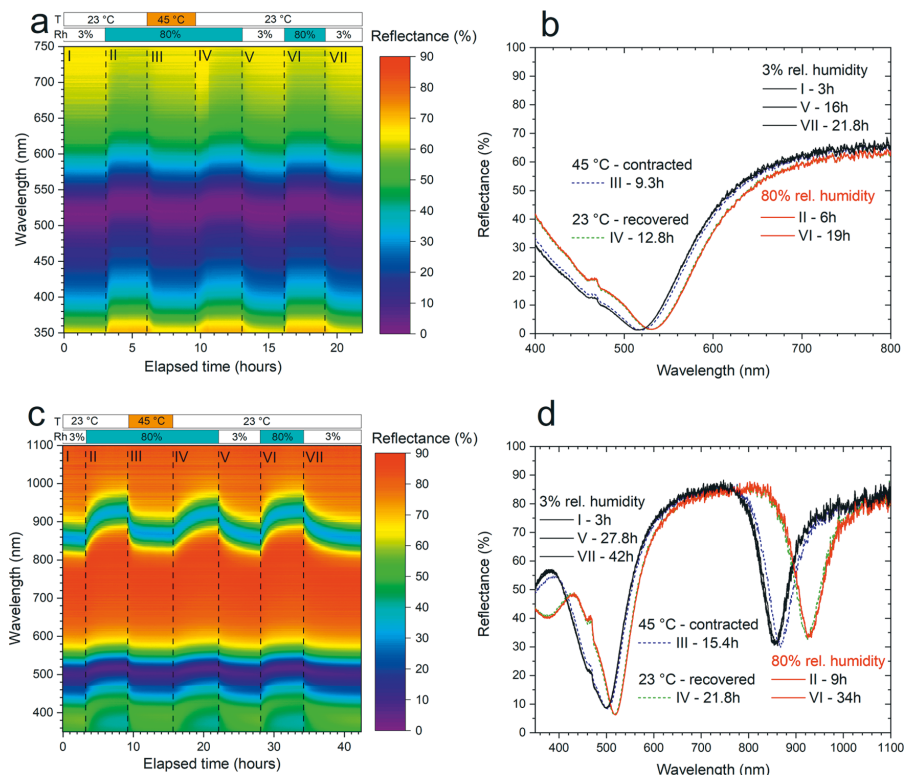


Figure 4. Reflectance spectra at varied environmental conditions: (a, b) VIS sample and (c, d) NIR sample. (a, c) Time dependencies of the reflectance spectra; time steps II–VI are 3 h (a) and 6 h (c). The sample temperature and relative humidity of the environment at different times are shown in the bars on top of the graph. (b, d) Reflectance spectra at the end of each time step.

order resonance in the wet state (dip at 675 nm in Figure 3b; FWHM = 35 nm). This is in line with the modeling predictions for the highest Q -factors in this wavelength region, with no regard to water presence, so it is solely defined by the MIM geometry. This value is reported for the first time for environment-responsive MIM structures, and it is close to Q -factors reported for traditional solid-state MIM structures^{3,14,18} and can supposedly be further improved with better uniformity of thin layer deposition.

2.4. Tuning by Temperature and Humidity Control.

We employed temperature- and humidity-controlled chambers to demonstrate continuous and reversible tuning of the optical resonance in the hydrogel MIM filter in air. Continuous measurements of the reflectance spectra in a controlled environment showed that both humidity and temperature can be used for tuning the reflectance of the fabricated structures (Figure 4). This employs two mechanisms. An increase in humidity at constant temperature results in hydrogel swelling, which corresponds to the red shift of the resonance of the MIM structure (transition from I to II in Figure 4a,c), and vice versa—decreasing humidity “dries” the hydrogel and blue-shifts the resonance (Figure 4a,c, V). Another mechanism specific to PNIPAM-based hydrogels is to utilize the LCST phase transition at a temperature around 32 °C,⁵⁵ above which the swollen hydrogel contracts. Importantly,

it is a reversible transition. To use this mechanism, we changed the temperature of the MIM structure while keeping a constant humidity of 80% (Figure 4a,c, III and IV). At room temperature, the hydrogel is partly swollen at this humidity (Figure 4a,c, II). However, increasing the temperature up to 45 °C resulted in the blue shift of the resonance to the values characteristic to the MIM with dry hydrogel (Figure 4a,c, III), meaning that the phase transition took place and the hydrogel contracted, expelling water from it. The close spectral match between the temperature-contracted (Figure 4a,c, III) and dry hydrogels (at 3% relative humidity; Figure 4a,c, I) indicates that the adsorbed water is almost completely gone at 45 °C. It is worth noting that this transition is faster than the humidity-driven swelling/deswelling (compare the slope in Figure 4c, III and V). We also demonstrated the reverse effect; i.e., lowering the temperature (while keeping 80% humidity) moved the resonance back to the longer wavelengths (Figure 4a,c, IV). One more cycle of humidifying-drying was added to show reproducibility of the hydrogel swelling/deswelling (Figure 4a,c, VI and VII). The spectra at the end of each step I–VII in Figure 4a,c are shown in Figure 4b,d, respectively, demonstrating perfect reproducibility of the tuning of the resonance during subsequent swelling–deswelling cycles. The overall spectral tuning range was up to 80/70 nm in the near-infrared and 22/18 nm in the visible region for humidity/temperature-

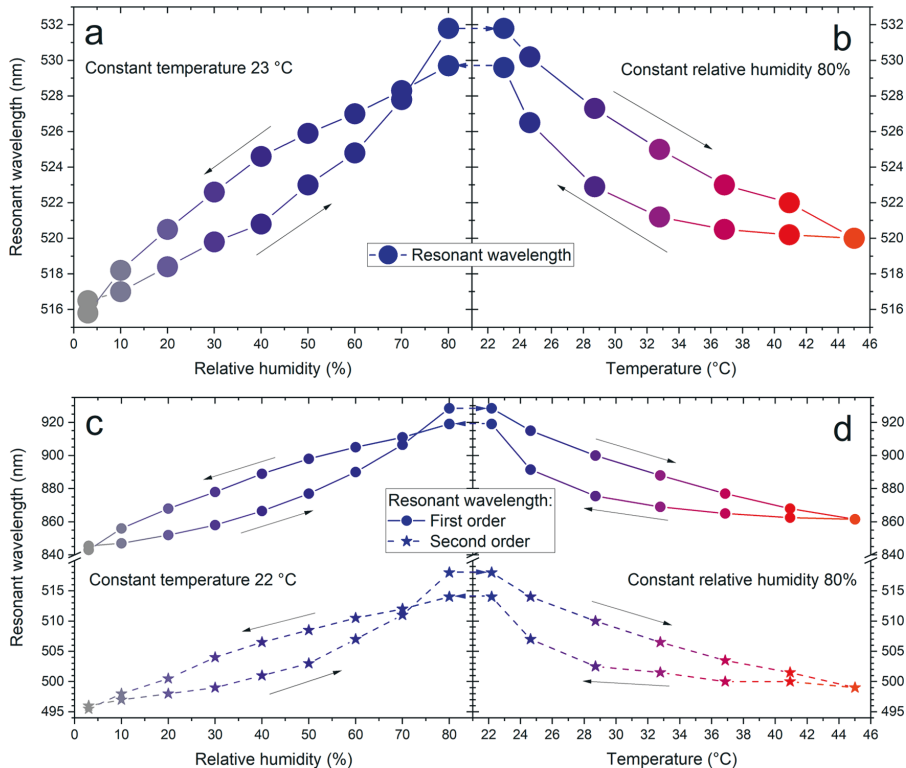


Figure 5. Dependency of the resonant wavelengths on (a, c) humidity (at ambient temperature) and (b, d) temperature (at 80% rel. humidity) for (a, b) VIS and (c, d) NIR samples. Note the different vertical scales in panels (c, d) before and after the break. Lines are for eye-guiding only. Raw measurements (spectra, humidity, and temperature) are available in SI, Figures S7 and S8.

induced mechanisms. These values were both achieved with the NIR sample (the first- and the second-order resonances, respectively); for the VIS sample, the tuning range was 15/12 nm. This supports the hypothesis that employing the higher-order resonances in the visible range using a thicker initial hydrogel layer may be beneficial for the maximal tuning range.

Figure 5 shows the dependencies of the resonance in the samples when temperature and humidity are gradually changed between the same extreme values (3–80% RH, 23–45 °C, the system was let to stabilize at each value for 3 h). A full spectroscopic map for this measurement is available in the Supporting Information. Gradual changes in humidity expectedly allow fine-tuning of the resonance with close to linear dependency (0.19 nm/% RH) with almost no hysteresis (Figure 5a,c). At the same time, the temperature-induced changes at high humidity are also continuous, not step-like as one could expect from a phase-transition-induced process, allowing continuous tuning as well (Figure 5b,d).

While PNIPAm-based hydrogels are generally known to undergo rapid LCST transition within a few °C range, this range, as well as the transition temperature, can be tuned by additives (e.g., comonomers).⁵⁶ In our experiments, we employed a benzophenone (BP) comonomer, the hydrophobicity of which is expected to lower the LCST. It also provides more linear temperature changes to the PNIPAm hydrogel.^{57,58} However, our hydrogel constitutes from 48:1

composition of PNIPAm:BP (further details in SI), so the influence of the comonomer is supposedly not strong enough to extend the transition range to a couple of tens of °C (in this ratio was in the range of 12:1). Additionally, the transition temperature is traditionally estimated for hydrogel in water, while it depends on the water content in the hydrogel,⁵⁹ which was significantly lower in our humidity-driven experiment. Finally, the temperature-tuning of the PNIPAm hydrogel volume above LCST has been reported;⁶⁰ however, the shrinking was irreversible, which differs from our samples.

We believe that the temperature hysteresis observed in Figure 5b,d can be explained by the formation of a dense skin layer at the beginning of the deswelling process, as reported elsewhere.⁶¹ To date, the temperature-induced volume changes in PNIPAm hydrogels have been mostly studied in water,^{62,63} while the mechanism of the observed changes in humid air across a wide range of temperatures is yet to be understood and it can broaden possible PNIPAm hydrogel applications beyond temperature-tunable color filters reported here.

3. CONCLUSIONS

We report a continuously tunable reflective color filter based on the metal–insulator–metal (MIM) structure with a hydrogel as an intermediate insulating layer. The device responds to two stimuli—humidity and temperature—by

reversibly changing the resonant wavelength. We obtained a spectral red shift of 22 nm in the visible range and 80 nm in the near-infrared range by changing the humidity from 3 to 80% for the initial hydrogel thickness at ambient conditions of 90 and 260 nm, respectively. The maximum resonance shift obtained by immersion of the hydrogel MIMs in water was 80 and 340 nm, respectively. These shifts are attributed to the reversible swelling of hydrogel in the presence of water and deswelling when water is removed. The temperature-tuning mechanism employed the LCST phase transition when swollen (wet) hydrogel contracts at elevated temperatures expelling water from it. We show that changing the temperature from ambient to 45 °C at a constant 80% humidity results in the continuous blue shift of the resonant wavelength with the maximum shift of 18 nm in the visible range and 70 nm in the near-infrared, and these changes are reversible. We also demonstrate that for better tunability it is beneficial to employ the higher-order resonances, as in our experiments the second-order resonance outperformed the first-order one in the overall tuning range and thus in humidity and temperature sensitivity. The best experimental quality factor of around 19 was obtained in the visible range for the second-order resonance in MIM with the swollen hydrogel, indicating that swelling does not reduce the quality of the resonances. The reported tunable filter opens new perspectives for plasmonic devices such as contactless (optical) sensors of humidity or temperature of the liquid. Another possible direction is using the proposed structure as a tunable cavity for emitters embedded in the hydrogel.

While our samples demonstrated good resonant properties, it is possible to further improve the optical properties by improving the deposition quality. We believe that further extension of the tuning range is possible using higher-refractive-index liquids in addition to water, the aqueous mixtures of which can be compatible with bistimuli tuning in a certain range of concentrations. An important advantage of the lithography-free MIM structures is that they do not require nano- or micropatterning, relying only on thin film deposition methods, which makes these structures potentially scalable for roll-to-roll industrial manufacturing.^{64,65} The demonstrated stimuli-responsive structures can be applied as humidity sensors or immersed temperature sensors—in both cases, sensing would be optical and therefore contactless. Leaning on plasmon resonances, MIMs can also be used as Raman-enhancing substrates,^{66,67} which in combination with temperature/humidity sensing opportunities gives rise to potential integrated applications, e.g., in lab-on-chip.

4. METHODS

4.1. Numerical Calculations. The reflectance spectra of the metal–hydrogel–metal thin film, as well as E-field distributions under the plane-wave irradiation, were simulated using the two-dimensional (2D) finite-difference time-domain (FDTD) method with commercial software (Lumerical FDTD Solutions). The modeled structure comprised five layers (from bottom to top): (1) semi-infinite glass substrate, (2) 100 nm thick gold, (3) hydrogel of a varied thickness (0–500 nm), (4) 30 nm thick gold, and (5) semi-infinite free-space superstrate. The refractive indices of the glass, the hydrogel, and the superstrate were taken as 1.46, 1.503 (see Supporting Information, Figure S10), and 1, respectively, while the complex index of gold was in accordance with Johnson and Christy data.⁶⁸ The plane-wave excitation was incident from the superstrate perpendicular to the layers (along the *x*-direction). A power monitor was placed at a distance of half the maximum wavelength behind the radiation source

to measure the reflectance spectra. The mesh refinement was set to the conformal variant 0 with a minimum mesh set of 0.25 nm. Perfectly matched layer (PML) boundary conditions were set along the *x*-direction, and the antisymmetric boundary condition was set along the *y*-direction. The number of layers was increased to prevent any divergence in the simulation due to the dispersive Au unit cell. The auto-shutoff min was set to 1e-6, which was enough for the incident field to decay completely, as well as prevent any ripples in the reflectance spectra. The attained simulated results were used to fit the experimentally measured reflectance spectra of the samples in both dry and wet cases.

4.2. Hydrogel Material Synthesis. The *N*-isopropylacrylamide–acrylamidobenzophenone copolymer (PNIPAm–BP) was synthesized from commercial *N*-isopropylacrylamide and freshly synthesized 4-acrylamidobenzophenone via free-radical polymerization initiated by azobisisobutyronitrile (AIBN). The composition of the polymer was confirmed by ¹H NMR spectroscopy to be (NIPAm₄₈BP₁)_{*n*}, well in line with the monomer ratio before polymerization. Details of the synthetic protocols and characterization of the synthesis products are given in Supporting Information, Figures S1 and S3.

4.3. Hydrogel Layer Fabrication. PNIPAm–BP copolymer was diluted in 94% ethanol in concentrations 20 and 40 mg/mL; for better dissolution, the magnetic stirring at 50 °C was used for 1 h. Before spin-coating, the solutions were filtered through PTFE membranes with 0.45 μm pores. The substrates were cleaned by consecutive sonication in acetone, isopropanol, and deionized water (10 min each). After that, they were activated by plasma treatment (20 min, 30 W RF power, 1000 mTorr O₂) and immediately forwarded to spin-coating. Spin-coating included two steps: (1) 10 s at 150 rpm during which the PNIPAm–BP solution was dispensed and predistributed and (2) 30 s at 1000–6000 rpm to form the final coating. The deposition was followed by drying for 1 h at 40 °C in a vacuum and cross-linking under UV light (365 nm from CoolLED pE-4000 focused into a circle of ca. 2 cm in diameter) for 40 min. Complete cross-linking at these conditions was confirmed by the disappearance of the 301 nm peak in the optical transmittance spectra of the reference hydrogel coatings on glass (see the Supporting Information for more information).

4.4. MIM Structure Fabrication. The samples were fabricated on Si wafer square pieces. After consecutive sonication in acetone, isopropanol, and deionized water (10 min each), the substrates were blow-dried with nitrogen. After that, the adhesive layer of 1 nm Ti followed by a 100 nm layer of Au was deposited by e-beam evaporation. The hydrogel layer was fabricated as described before. The final gold layer (20–30 nm) was made by thermal sputtering. The thicknesses of all gold and hydrogel depositions were verified at the reference samples with the Dektak profilometer at cleanroom conditions (21 °C, 20–25% relative humidity). The resulting thicknesses were 100 nm Au/85 ± 5 nm hydrogel/30 nm Au for VIS samples and 100 nm Au/250 ± 10 nm hydrogel/26 nm Au for NIR samples.

4.5. Optical Measurements. Microscopic reflectance measurements were performed with a multifunctional WITec alpha300C confocal microscope. The samples were illuminated by a broad-band light source (LDLS EQ-99X) through a Zeiss EC “Epiplan” DIC, 20× air objective (NA = 0.4, WD = 3.0 mm); the reflected light was collected through the same objective and coupled to spectrometers via an optical fiber. For the spectral range of 400–800 nm, we used a WITec UHTS300 spectrometer equipped with 150 lines/mm grating and a TE-cooled CCD camera (Andor DV 401-BV-351). For the NIR spectral range (800–1600 nm), an Ocean Insight NIRQUEST 512-XR FLAME spectrometer equipped with an InGaAs linear array detector was used. Samples were measured at room conditions (26 °C, 30% r.h., dry state) and after immersion in deionized water for 1 h (wet state). An extended set of experimental spectra fitted with modeling results are shown in Figures S5 and S6.

Measurements in a controlled temperature and humidity environment were performed using the Linkam Scientific LTS420-H stage with an RH95 humidity controller, providing precise humidifying/dehumidifying of the air in the sample chamber, and a T96-S

temperature controller for heating the sample. The temperature of the sample was verified using an IR camera (Figure S9). Optical reflectance, in this case, was measured with the help of a Thorlabs RP29 reflectance fiber probe, which was connected to both an Ocean Optics DH-2000-BAL light source (halogen and deuterium lamps) and Avantes AvaSpec-2048L fiber spectrometer. The light to/from the fiber was coupled with a Thorlabs RC08SMA-F01 reflective collimator and weakly focused with Thorlabs LA4600 fused silica lens. The illuminated area on the sample was roughly 0.5 mm in diameter.

In all experiments, the reference intensity (reflected light source) and background/dark intensity were measured using a silver mirror with the light sources being, respectively, on and off. The reflectance of the sample was calculated as follows

$$\text{Reflectance} = 100\% \times \frac{I_{\text{Sample}} - I_{\text{Background}}}{I_{\text{Source}} - I_{\text{Background}}} \quad (1)$$

where I_{Sample} is the measured intensity of the light reflected from the sample, I_{Source} is the reference light source intensity, and $I_{\text{Background}}$ is the background intensity.

The absorbance of the reference hydrogel layers on the glass was measured with Agilent Technologies Cary 60 UV–vis spectrophotometer with a custom-built sample chamber.

■ ASSOCIATED CONTENT

Supporting Information

The Supporting Information is available free of charge at <https://pubs.acs.org/doi/10.1021/acsami.1c15616>.

Hydrogel material synthesis and characterization; metal–hydrogel–metal samples; spectral measurement in the temperature- and humidity-controlled environment; and refractive index of the PNIPAm hydrogel (PDF)

Video S1 of color changes in VIS and NIR samples when water is being added and removed (MP4)

Microscopic video S2 of color changes in the VIS sample when water is being added and removed (MP4)

■ AUTHOR INFORMATION

Corresponding Authors

Arri Priimagi – Faculty of Engineering and Natural Sciences, Tampere University, 33720 Tampere, Finland; orcid.org/0000-0002-5945-9671; Email: arri.priimagi@tuni.fi

Humeyra Caglayan – Faculty of Engineering and Natural Sciences, Tampere University, 33720 Tampere, Finland; orcid.org/0000-0002-0656-614X; Email: humeyra.caglayan@tuni.fi

Authors

Semyon Chervinskii – Faculty of Engineering and Natural Sciences, Tampere University, 33720 Tampere, Finland; orcid.org/0000-0002-8560-5679

Ibrahim Issah – Faculty of Engineering and Natural Sciences, Tampere University, 33720 Tampere, Finland; orcid.org/0000-0001-7663-4972

Markus Lahikainen – Faculty of Engineering and Natural Sciences, Tampere University, 33720 Tampere, Finland; orcid.org/0000-0002-4891-5352

Alireza R. Rashed – Faculty of Engineering and Natural Sciences, Tampere University, 33720 Tampere, Finland

Kim Kuntze – Faculty of Engineering and Natural Sciences, Tampere University, 33720 Tampere, Finland

Complete contact information is available at: <https://pubs.acs.org/doi/10.1021/acsami.1c15616>

Author Contributions

S.Ch. fabricated the samples, performed environmentally controlled measurements, analyzed the data, and wrote the main manuscript. I.I. performed FDTD modeling and fitting of the experimental data. M.L. and K.K. prepared the PNIPAm–BP material. A.R.R. performed spectral measurements before and after water immersion. A.P. and H.C. developed the idea and supervised the project. All authors contributed to the manuscript and approved the final version.

Notes

The authors declare no competing financial interest.

■ ACKNOWLEDGMENTS

The authors acknowledge the support of the Academy of Finland Flagship Programme (PREIN, Decision Number 321065). The authors thank Pertti Pääkkönen for ellipsometry measurements and Dipa Ghindani for SEM characterization. S.Ch. is grateful to Suvi Lehtimäki and Matti Virkki for their help with the experimental arrangements. M.L. is thankful to the Emil Aaltonen Foundation for the funding support. A.P. acknowledges the financial support of the European Research Council (Starting Grant Project PHOTOTUNE, Decision Number 679646) and the Academy of Finland (P-Cap Project, Decision Number 324353). H.C. acknowledges financial support of the European Research Council (Starting Grant project aQUARiUM; Agreement No. 802986).

■ REFERENCES

- (1) Maier, S. A. *Plasmonics: Fundamentals and Applications*; Springer: New York, NY, USA, 2007; pp 1–223.
- (2) Stockman, M. I.; Kneipp, K.; Bozhevolnyi, S. I.; Saha, S.; Dutta, A.; Ndukaife, J.; Kinsey, N.; Reddy, H.; Guler, U.; Shalae, V. M.; Boltasseva, A.; Gholipour, B.; Krishnamoorthy, H. N. S.; MacDonald, K. F.; Soci, C.; Zheludev, N. I.; Savinov, V.; Singh, R.; Groß, P.; Lienau, C.; Vadai, M.; Solomon, M. L.; Barton, D. R.; Lawrence, M.; Dionne, J. A.; Boriskina, S. V.; Esteban, R.; Aizpurua, J.; Zhang, X.; Yang, S.; Wang, D.; Wang, W.; Odom, T. W.; Accanto, N.; de Roque, P. M.; Hancu, I. M.; Piatkowski, L.; van Hulst, N. F.; Kling, M. F. Roadmap on Plasmonics. *J. Opt.* **2018**, *20*, No. 043001.
- (3) Wang, B.; Yu, P.; Wang, W.; Zhang, X.; Kuo, H.-C.; Xu, H.; Wang, Z. M. High-Q Plasmonic Resonances: Fundamentals and Applications. *Adv. Opt. Mater.* **2021**, *9*, No. 2001520.
- (4) Klimov, V. *Nanoplasmonics*; Jenny Stanford Publishing: New York, NY, USA, 2014.
- (5) Barbillon, G. *Nanoplasmonics - Fundamentals and Applications*; InTechOpen: London, UK, 2017.
- (6) Cai, W.; Shalae, V. *Optical Metamaterials: Fundamentals and Applications*; Springer-Verlag New York: NY, USA, 2010.
- (7) Cui, Y.; He, Y.; Jin, Y.; Ding, F.; Yang, L.; Ye, Y.; Zhong, S.; Lin, Y.; He, S. Plasmonic and Metamaterial Structures as Electromagnetic Absorbers. *Laser Photonics Rev.* **2014**, *8*, 495–520.
- (8) Ji, C.; Lee, K.-T.; Xu, T.; Zhou, J.; Park, H. J.; Guo, L. J. Engineering Light at the Nanoscale: Structural Color Filters and Broadband Perfect Absorbers. *Adv. Opt. Mater.* **2017**, *5*, No. 1700368.
- (9) Ghobadi, A.; Hajian, H.; Butun, B.; Ozbay, E. Strong Light–Matter Interaction in Lithography-Free Planar Metamaterial Perfect Absorbers. *ACS Photonics* **2018**, *5*, 4203–4221.
- (10) Coppens, Z. J.; Kravchenko, I. I.; Valentine, J. G. Lithography-Free Large-Area Metamaterials for Stable Thermophotovoltaic Energy Conversion. *Adv. Opt. Mater.* **2016**, *4*, 671–676.
- (11) Ghobadi, A.; Dereshgi, S. A.; Hajian, H.; Birant, G.; Butun, B.; Bek, A.; Ozbay, E. 97 Percent Light Absorption in an Ultrabroadband Frequency Range Utilizing an Ultrathin Metal Layer: Randomly Oriented, Densely Packed Dielectric Nanowires as an Excellent Light Trapping Scaffold. *Nanoscale* **2017**, *9*, 16652–16660.

- (12) Yan, M. Metal–Insulator–Metal Light Absorber: a Continuous Structure. *J. Opt.* **2013**, *15*, No. 025006.
- (13) Kenanakis, G.; Mavidis, C. P.; Vasilaki, E.; Katsarakis, N.; Kafesaki, M.; Economou, E. N.; Soukoulis, C. M. Perfect Absorbers Based on Metal–Insulator–Metal Structures in the Visible Region: a Simple Approach for Practical Applications. *Appl. Phys. A: Mater. Sci. Process.* **2017**, *123*, No. 77.
- (14) Li, Z.; Butun, S.; Aydin, K. Large-Area, Lithography-Free Super Absorbers and Color Filters at Visible Frequencies Using Ultrathin Metallic Films. *ACS Photonics* **2015**, *2*, 183–188.
- (15) Aalizadeh, M.; Khavasi, A.; Butun, B.; Ozbay, E. Large-Area, Cost-Effective, Ultra-Broadband Perfect Absorber Utilizing Manganese in Metal-Insulator-Metal Structure. *Sci. Rep.* **2018**, *8*, No. 9162.
- (16) Banerjee, S. Simulation and Design of MIM Nanoresonators for Color Filter Applications. *J. Soc. Inf. Disp.* **2016**, *24*, 433–438.
- (17) Li, Y.; Liu, Z.; Zhang, H.; Tang, P.; Wu, B.; Liu, G. Ultra-Broadband Perfect Absorber Utilizing Refractory Materials in Metal-Insulator Composite Multilayer Stacks. *Opt. Express* **2019**, *27*, 11809–11818.
- (18) Williams, C.; Rughoobur, G.; Flewitt, A. J.; Wilkinson, T. D. Single-step Fabrication of Thin-film Linear Variable Bandpass Filters Based on Metal-Insulator-Metal Geometry. *Appl. Opt.* **2016**, *55*, 9237–9241.
- (19) Ghindani, D.; Rashed, A. R.; Caglayan, H. Unveiling Spontaneous Emission Enhancement Mechanisms in Metal-Insulator-Metal Nanocavities. *Photon. Res.* **2021**, *9*, 237–242.
- (20) Yang, Z.; Albrow-Owen, T.; Cai, W.; Hasan, T. Miniaturization of Optical Spectrometers. *Science* **2021**, *371*, No. eabe0722.
- (21) Aalizadeh, M.; Serebryannikov, A. E.; Khavasi, A.; Vandebosch, G. A. E.; Ozbay, E. Toward Electrically Tunable, Lithography-Free, Ultra-Thin Color Filters Covering the Whole Visible Spectrum. *Sci. Rep.* **2018**, *8*, No. 11316.
- (22) Yu, E.-S.; Lee, S.-H.; Bae, Y.-G.; Choi, J.; Lee, D.; Kim, C.; Lee, T.; Lee, S.-Y.; Lee, S.-D.; Ryu, Y.-S. Highly Sensitive Color Tunability by Scalable Nanomorphology of a Dielectric Layer in Liquid-Permeable Metal–Insulator–Metal Structure. *ACS Appl. Mater. Interfaces* **2018**, *10*, 38581–38587.
- (23) Jewell, S. A.; Cornford, S. L.; Sambles, J. R. Dynamic Control of Visible Radiation by a Liquid Crystal Filled Fabry-Pérot Etalon. *J. Appl. Phys.* **2007**, *102*, No. 093108.
- (24) van Heeswijk, E. P. A.; Kragt, A. J. J.; Grossiord, N.; Schenning, A. P. H. J. Environmentally Responsive Photonic Polymers. *Chem. Commun.* **2019**, *55*, 2880–2891.
- (25) Tang, L.; Wang, L.; Yang, X.; Feng, Y.; Li, Y.; Feng, W. Poly(N-isopropylacrylamide)-Based Smart Hydrogels: Design, Properties and Applications. *Prog. Mater. Sci.* **2021**, *115*, No. 100702.
- (26) Tokarev, I.; Minko, S. Stimuli-Responsive Hydrogel Thin Films. *Soft Matter* **2009**, *5*, 511–524.
- (27) Muralter, F.; Greco, F.; Coclite, A. M. Applicability of Vapor-Deposited Thermoresponsive Hydrogel Thin Films in Ultrafast Humidity Sensors/Actuators. *ACS Appl. Polym. Mater.* **2020**, *2*, 1160–1168.
- (28) Matsumoto, K.; Sakikawa, N.; Miyata, T. Thermo-Responsive Gels that Absorb Moisture and Ooze Water. *Nat. Commun.* **2018**, *9*, No. 2315.
- (29) Ding, T.; Rüttiger, C.; Zheng, X.; Benz, F.; Ohadi, H.; Vandebosch, G. A. E.; Moshchalkov, V. V.; Gallei, M.; Baumberg, J. J. Fast Dynamic Color Switching in Temperature-Responsive Plasmonic Films. *Adv. Opt. Mater.* **2016**, *4*, 877–882.
- (30) Gisbert Quilis, N.; van Dongen, M.; Venugopalan, P.; Kotlarek, D.; Petri, C.; Moreno Cencerrado, A.; Stanescu, S.; Toca Herrera, J. L.; Jonas, U.; Möller, M.; Mourran, A.; Dostalek, J. Actively Tunable Collective Localized Surface Plasmons by Responsive Hydrogel Membrane. *Adv. Opt. Mater.* **2019**, *7*, No. 1900342.
- (31) Khalid, A. U. R.; Liu, J.; Han, Y.; Ullah, N.; Jia, S.; Wang, Y. Multipurpose Thermoresponsive Hydrogel: a Platform for Dynamic Holographic Display. *Opt. Lett.* **2020**, *45*, 479.
- (32) Brasse, Y.; Müller, M. B.; Karg, M.; Kuttner, C.; König, T. A. F.; Fery, A. Magnetic and Electric Resonances in Particle-to-Film-Coupled Functional Nanostructures. *ACS Appl. Mater. Interfaces* **2018**, *10*, 3133–3141.
- (33) Sorrell, C. D.; Carter, M. C. D.; Serpe, M. J. Color Tunable Poly (N-Isopropylacrylamide)-co-Acrylic Acid Microgel–Au Hybrid Assemblies. *Adv. Funct. Mater.* **2011**, *21*, 425–433.
- (34) Sorrell, C. D.; Serpe, M. J. Glucose Sensitive Poly (N-isopropylacrylamide) Microgel Based Etalons. *Anal. Bioanal. Chem.* **2012**, *402*, 2385–2393.
- (35) Shin, J.; Han, S. G.; Lee, W. Dually Tunable Inverse Opal Hydrogel Colorimetric Sensor with Fast and Reversible Color Changes. *Sens. Actuators, B* **2012**, *168*, 20–26.
- (36) Ohtsuka, Y.; Seki, T.; Takeoka, Y. Thermally Tunable Hydrogels Displaying Angle-Independent Structural Colors. *Angew. Chem., Int. Ed.* **2015**, *54*, 15368–15373.
- (37) Wani, O. M.; Schenning, A. P. H. J.; Priimagi, A. A Bifacial Colour-tunable System via Combination of a Cholesteric Liquid Crystal Network and Hydrogel. *J. Mater. Chem. C* **2020**, *8*, 10191–10196.
- (38) Wang, Z.; Zhang, J.; Xie, J.; Wang, Z.; Yin, Y.; Li, J.; Li, Y.; Liang, S.; Zhang, L.; Cui, L.; Zhang, H.; Yang, B. Polymer Bragg Stack as Color Tunable Photonic Paper. *J. Mater. Chem.* **2012**, *22*, 7887–7893.
- (39) Tian, E.; Wang, J.; Zheng, Y.; Song, Y.; Jiang, L.; Zhu, D. Colorful Humidity Sensitive Photonic Crystal Hydrogel. *J. Mater. Chem.* **2008**, *18*, 1116–1122.
- (40) Shi, J.; Hsiao, V. K.; Walker, T. R.; Huang, T. J. Humidity Sensing Based on Nanoporous Polymeric Photonic Crystals. *Sens. Actuators, B* **2008**, *129*, 391–396.
- (41) Kumoda, M.; Watanabe, M.; Takeoka, Y. Preparations and Optical Properties of Ordered Arrays of Submicron Gel Particles: Interconnected State and Trapped State. *Langmuir* **2006**, *22*, 4403–4407.
- (42) Weissman, J. M.; Sunkara, H. B.; Tse, A. S.; Asher, S. A. Thermally Switchable Periodicities and Diffraction from Mesoscopically Ordered Materials. *Science* **1996**, *274*, 959–963.
- (43) Wang, X.; Liu, X.; Wang, X. Hydrogel Diffraction Grating as Sensor: A Tool for Studying Volume Phase Transition of Thermoresponsive Hydrogel. *Sens. Actuators, B* **2014**, *204*, 611–616.
- (44) Xu, W.; Gao, Y.; Serpe, M. J. Electrochemically Color Tunable Poly(N-isopropylacrylamide) Microgel-based Etalons. *J. Mater. Chem. C* **2014**, *2*, 3873–3878.
- (45) Ahiabu, A.; Serpe, M. J. Rapidly Responding pH- and Temperature-Responsive Poly (N-Isopropylacrylamide)-Based Microgels and Assemblies. *ACS Omega* **2017**, *2*, 1769–1777.
- (46) Carter, M. C. D.; Sorrell, C. D.; Serpe, M. J. Deswelling Kinetics of Color Tunable Poly(N-isopropylacrylamide) Microgel-Based Etalons. *J. Phys. Chem. B* **2011**, *115*, 14359–14368.
- (47) Hu, L.; Serpe, M. J. Color-Tunable Etalons Assembled from Poly (N-isopropylacrylamide) Based Microgels. *Polymers* **2012**, *4*, 134–149.
- (48) Sorrell, C. D.; Serpe, M. J. Reflection Order Selectivity of Color-Tunable Poly(N-isopropylacrylamide) Microgel Based Etalons. *Adv. Mater.* **2011**, *23*, 4088–4092.
- (49) Gao, Y.; Serpe, M. J. Light-Induced Color Changes of Microgel-Based Etalons. *ACS Appl. Mater. Interfaces* **2014**, *6*, 8461–8466.
- (50) Jang, J.; Kang, K.; Raeis-Hosseini, N.; Ismukhanova, A.; Jeong, H.; Jung, C.; Kim, B.; Lee, J.; Park, I.; Rho, J. Self-Powered Humidity Sensor Using Chitosan-Based Plasmonic Metal–Hydrogel–Metal Filters. *Adv. Opt. Mater.* **2020**, *8*, No. 1901932.
- (51) Dong, Y.; Akinoglu, E. M.; Zhang, H.; Maasoumi, F.; Zhou, J.; Mulvaney, P. An Optically Responsive Soft Etalon Based on Ultrathin Cellulose Hydrogels. *Adv. Funct. Mater.* **2019**, *29*, No. 1904290.
- (52) Nash, M. E.; Carroll, W. M.; Foley, P. J.; Maguire, G.; Connell, C. O.; Gorelov, A. V.; Beloshapkin, S.; Rochev, Y. A. Ultra-thin Spin Coated Crosslinkable Hydrogels for use in Cell Sheet Recovery—Synthesis, Characterisation to Application. *Soft Matter* **2012**, *8*, 3889–3899.
- (33) Li, M.; Bresson, B.; Cousin, F.; Fretigny, C.; Tran, Y. Submicrometric Films of Surface-Attached Polymer Network with

Temperature-Responsive Properties. *Langmuir* **2015**, *31*, 11516–11524.

(54) Schwartzkopf, M.; Santoro, G.; Brett, C. J.; Rothkirch, A.; Polonsky, O.; Hinz, A.; Metwalli, E.; Yao, Y.; Strunskus, T.; Faupel, F.; Müller-Buschbaum, P.; Roth, S. V. Real-Time Monitoring of Morphology and Optical Properties during Sputter Deposition for Tailoring Metal–Polymer Interfaces. *ACS Appl. Mater. Interfaces* **2015**, *7*, 13547–13556.

(55) Schild, H. Poly(N-isopropylacrylamide): Experiment, Theory and Application. *Prog. Polym. Sci.* **1992**, *17*, 163–249.

(56) Liu, R.; Fraylich, M.; Saunders, B. R. Thermoresponsive Copolymers: From Fundamental Studies to Applications. *Colloid Polym. Sci.* **2009**, *287*, 627–643.

(57) Kim, J.; Hanna, J. A.; Byun, M.; Santangelo, C. D.; Hayward, R. C. Designing Responsive Buckled Surfaces by Halftone Gel Lithography. *Science* **2012**, *335*, 1201–1205.

(58) Zhou, Y.; Hauser, A. W.; Bende, N. P.; Kuzyk, M. G.; Hayward, R. C. Waveguiding Microactuators Based on a Photothermally Responsive Nanocomposite Hydrogel. *Adv. Funct. Mater.* **2016**, *26*, 5447–5452.

(59) Afroze, F.; Nies, E.; Berghmans, H. Phase Transitions in the System Poly(N-isopropylacrylamide)/Water and Swelling Behaviour of the Corresponding Networks. *J. Mol. Struct.* **2000**, *554*, 55–68.

(60) Bischofberger, I.; Trappe, V. New Aspects in the Phase Behaviour of Poly-N-isopropyl Acrylamide: Systematic Temperature Dependent Shrinking of PNiPAM Assemblies Well Beyond the LCST. *Sci. Rep.* **2015**, *5*, No. 15520.

(61) Salzmann, P.; Perrotta, A.; Coclite, A. M. Different Response Kinetics to Temperature and Water Vapor of Acrylamide Polymers Obtained by Initiated Chemical Vapor Deposition. *ACS Appl. Mater. Interfaces* **2018**, *10*, 6636–6645.

(62) Otake, K.; Inomata, H.; Konno, M.; Saito, S. Thermal Analysis of the Volume Phase Transition with N-isopropylacrylamide Gels. *Macromolecules* **1990**, *23*, 283–289.

(63) Qiu, Y.; Park, K. Environment-Sensitive Hydrogels for Drug Delivery. *Adv. Drug Delivery Rev.* **2001**, *53*, 321–339.

(64) Mitra, K. Y.; Weise, D.; Hartwig, M.; Baumann, R. R. Infra-red Curing Methodology for Roll-to-Roll (R2R) Manufacturing of Conductive Electrodes through Inkjet Technology Applicable for Devices in the Field of Flexible Electronics. *MRS Online Proc. Libr.* **2015**, *1791*, 1–6.

(65) Ok, J. G.; Seok Youn, H.; Kyu Kwak, M.; Lee, K.-T.; Jae Shin, Y.; Jay Guo, L.; Greenwald, A.; Liu, Y. Continuous and Scalable Fabrication of Flexible Metamaterial Films via Roll-to-Roll Nanoimprint Process for Broadband Plasmonic Infrared Filters. *Appl. Phys. Lett.* **2012**, *101*, No. 223102.

(66) Yan, Z.; Du, W.; Tu, L.; Gu, P.; Huang, Z.; Zhan, P.; Liu, F.; Wang, Z. A Facile High-performance SERS Substrate Based on Broadband Near-perfect Optical Absorption. *J. Raman Spectrosc.* **2015**, *46*, 795–801.

(67) Yang, Y.; Hu, Z.; Wang, Y.; Wang, B.; Zhan, Q.; Zhang, Y.; Ao, X. Broadband SERS Substrates by Oblique Angle Deposition Method. *Opt. Mater. Express* **2016**, *6*, 2644–2654.

(68) Johnson, P. B.; Christy, R. W. Optical Constants of the Noble Metals. *Phys. Rev. B* **1972**, *6*, 4370–4379.

PUBLICATION

II

Mechanism of emitters coupled with a polymer-based hyperbolic metamaterial

I. Issah, T. Pihlava, A. R. Rashed and H. Caglayan

Opt. Express **30**(6) (2022), 8723–8733

DOI: 10.1364/OE.451960

Publication reprinted with the permission of the copyright holders

Mechanism of emitters coupled with a polymer-based hyperbolic metamaterial

IBRAHIM ISSAH, ^{id} TUOMAS PIHLAVA, ALIREZA RAHIMI RASHED, ^{id}
AND HUMEYRA CAGLAYAN* ^{id}

Faculty of Engineering and Natural Science, Photonics, Tampere University, 33720 Tampere, Finland
**humeyra.caglayan@tuni.fi*

Abstract: We study a polymer-based hyperbolic metamaterial (HMM) structure composed of three Au-polymer bilayers with a hyperbolic dispersion relation. Using an effective refractive index retrieval algorithm, we obtain the effective permittivity of the experimentally fabricated polymer-based structure. In particular, the unique polymer-based HMM shows the existence of high-k modes that propagate in the metal-dielectric multilayered structure due to the excitation of bulk plasmon-polaritonic modes. Moreover, we compare the experimental luminescence and fluorescence lifetime results of the multilayered Au and a dye-doped polymer (PMMA) to investigate the dynamics of three different emitters, each incorporated within the unique polymer-based HMM structure. With emitters closer to the epsilon-near-zero region of the HMM, we observed a relatively high shortening of the average lifetime as compared to other emitters either close or far from the epsilon-near-zero region. This served as evidence of coupling between the emitters and the HMM as well as confirmed the increase in the non-radiative recombination rate of the different emitters. We also show that the metallic losses of a passive polymer-based HMM can be greatly compensated by a gain material with an emission wavelength close to the epsilon-near-zero region of the HMM. These results demonstrate the unique potential of an active polymer-based hyperbolic metamaterial in loss compensation, quantum applications, and sub-wavelength imaging techniques.

© 2022 Optica Publishing Group under the terms of the [Optica Open Access Publishing Agreement](#)

1. Introduction

In recent years, there has been a surge in scientific interest in metal-dielectric multilayered structures, owing in part to the new and related concepts of transformation optics [1,2], optical imaging [3], and metamaterials [4–8]. These multilayered structures composed of alternating subwavelength metal and dielectric layers provide unique optical properties useful for a wide range of advanced applications and devices. Typically, one can obtain a hyperbolic dispersion relationship in multilayered systems where the permittivity along different axes of the medium are different [9]. This anisotropic tensor behavior of the multilayered systems exhibits unique structural properties that do not exist naturally [9–11].

Note, the term hyperbolic metamaterial (HMM) was coined to describe a hyperbolic dispersion relation of a medium [10]. The unique property of HMMs has increased their applicability in numerous fields, such as negative refraction [12,13], superlenses [14,15], hyper-lenses [16], sub-diffraction imaging [17], remarkable waveguiding [18–20], and thermal emission engineering [11]. In addition, the effective permittivity of such media extends to zero within a certain spectral range known as epsilon-near-zero (ENZ) region. Within this spectral range, the HMM structure exhibits different physical phenomena such as an excitation of electromagnetic waves which propagates at long distances with negligible phase variations [21].

However, the fundamental constraint in the application of HMMs is the intrinsic loss of the metal layers. Nonetheless, the intrinsic loss can be overcome by the presence of a gain medium in the polymer-based HMM composite. Gain media have been experimentally incorporated into a variety of plasmonic and metamaterial systems, a technique relevant in quantum nanophotonics

and radiative decay engineering. The incorporation of gain within a multilayer HMM system compensates for metallic loss and could potentially enhance the robustness of HMM applications as compared to the passive HMM applications [22]. Moreover, HMMs have been shown by many authors to exhibit bulk plasmon modes which enhance its photonic density of state (PDOS) [23–25]. An increase in the PDOS property of HMMs has been identified to support subwavelength Bloch modes which could be quenched by the intrinsic metallic loss of the structure. Thereby embedding emitters in HMMs could compensate for these losses. Also, the existence of the high-k resonant modes in HMMs generates enormous enhancement of PDOS [10,26,27]. As a result of the continuum high-k modes of HMMs, a broadening of the Purcell factor full width at half maximum (FWHM) is exhibited in HMM and emitter complex structure. This could potentially be applicable in broadband single-photon generation [28–31]. Note that the emission rate of a spontaneous emitter embedded in a hyperbolic structure relative to the free-space decay rate is referred to as the Purcell factor [26,32,33].

HMM also possess additional states (i.e., propagating modes, plasmon modes) that are also prominent in HMM applications such as subwavelength imaging and sensing [34]. Although these exotic properties of HMM are prominent in various applications, the dissipation of coupled energy of emitters due to loss in the metal-dielectric complex has been a constraint in radiative decay engineering [22,27,35]. As such, various design and engineering techniques including adiabatic tuning of filling fraction to tunnel trapped high-k modes, incorporating a high-index grating configuration on the HMM, and nanopatterning of HMM slab known as hyper-crystals have been proposed by many authors to overcome these constraints [10,14,27]. In particular, loss-compensation and enhancement of spontaneous emission in active multilayered structures have been theoretically studied based on the dispersion relations of the multilayered structure as well as the geometry of the near fields [22,36,37]. Thus far, the practical realization of emitters coupled to a multilayered structure consisting of metal and a polymeric material have been studied with a focus on transient technology whereby a water-soluble and biocompatible polymer is utilized in forming a transient and flexible HMM structure [38].

Here, we propose a polymer-based active HMM structure composed of alternating layers of a metal and polymethyl methacrylate (PMMA) medium to study the decay rate mechanism of emitters not only dispersed on the top layer but also in-between the PMMA layers. We engineered relatively thin PMMA films to serve as a dielectric medium to incorporate quantum emitters in the proposed structure. This active dye-doped HMM structure is envisaged to compensate for the losses in a metal-dielectric structure due to the enhanced coupling of emitters dispersed on top and within the polymer-based HMM. This provides insight into the radiative decay mechanisms of emitters coupled to the HMM structure and its relation to the ENZ region of the polymer-based HMM structure, which is prominent in efficient dipole engineering model design.

2. Methods

2.1. Structure Design and modelling

Numerical optimization for thicknesses of the metal and dielectric layers (i.e. filling fraction) was implemented to attain the required epsilon-near-zero (ENZ) region with high PDOS and high phase velocity electromagnetic waves and match it with the emission and absorption wavelengths of the selected emitters. A desired thickness of 9 nm of gold (Au) and 29 nm of PMMA was attained using the aforementioned optimization codes. PMMA is a versatile polymeric material that is well suited for many applications such as high-resolution positive resist, protective coating, and as a sacrificial layer [39]. Based on the thickness values, we obtained an ENZ region comparable to the emission wavelength of Rhodamine 590 (Rh590) dye molecule. The spectral response, PDOS, Electric (E) field distribution, transmission dispersion relation, and Purcell factor calculations were numerically implemented using a commercial Ansys Lumerical FDTD solutions software package and an in-house developed transfer matrix method (TMM) code.

Experimental wavelength-dependent complex dielectric functions for Au [40] and PMMA [41] were used for the numerical calculations. Figure 1(a) [Inside HMM] illustrates the schematic of the proposed type-2 [7] HMM structure with emitters embedded within the polymeric PMMA layer. Fig. 1(b) [on top of HMM], (c) [MIM], and (d) [on 9nm Au] illustrate the schematic of the corresponding reference samples used to comprehend the decay rate mechanism and luminescence response of the proposed dye-doped HMM structure.

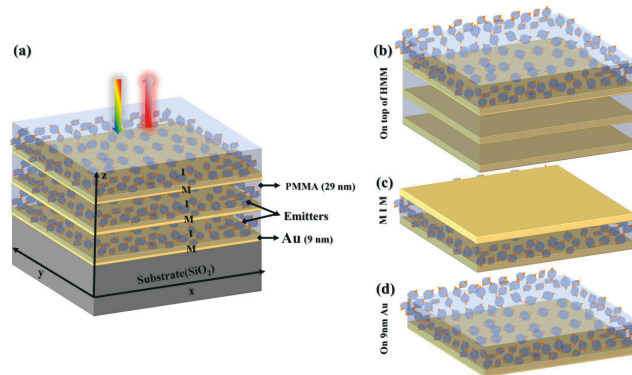


Fig. 1. (a) Schematic of the Au-PMMA structure consisting of 9 nm thick Au and 29 nm thick PMMA layers. Three polymeric PMMA samples were incorporated with three different dyes each [HMM + 3L dye]. I-M represents the insulator-metal interface. M-I-M represents the metal-insulator-metal interface. (b) similar HMM structure with dye-doped PMMA on the top layer [HMM + 1L dye]. (c) schematic of the MIM structure. (d) similar representation of dye-doped PMMA on top of the 9 nm Au layer [1L Au + 1L dye].

2.2. Sample fabrication and characterization

The proposed polymer-based HMM structure was fabricated using a metallic electron-beam (e-beam) evaporator and spin-coating techniques. The samples were fabricated on a fused silica (SiO₂) substrate with a refractive index of 1.45. Three active HMM samples were fabricated with each embedded with one of the different emitters. Reference samples of each dye embedded in PMMA-A1 (1%wt PMMA and 99%wt anisole) spin-coated on a homogeneous glass substrate were also prepared. Each dye was also spin-coated on a 9 nm Au film to serve as a reference to study the coupling effects of dye on a metal substrate. Rh590, Styryl-11 (LDS 798), and Pyromethene 650 (PYR650) dye-doped PMMA samples were fabricated for characterization. The PMMA with dyes complex were spin-coated on the Au layers at a speed of 2000 rpm for 30secs. The thickness of the polymeric material was measured using a profilometer.

A Confocal Raman microscope from WiTec (alpha300R) was used for the characterization of the fabricated samples. The reflectance and transmittance measurements were carried out using a broadband optical source (Energetiq EQ-99XFC LDLS, spectral range 190-2100 nm) to excite the samples. The optical spot is focused on the samples using a Zeiss "Epiplan-Neofluar" 20X objective (Numerical aperture (NA=0.4)) for both reflectance and transmittance measurements. To acquire the photoluminescence (PL) of the samples, a 532 nm laser was used to excite the samples to attain signal counts of the emission peak intensity for the different dyes. A polarization-dependent 375 nm pulsed laser source (with a diffraction-limited spot size of $\approx 1.14 \mu\text{m}$) was utilized to attain the fluorescence lifetimes of the samples with the help of a Picoquant

HydraHarp device and a single-photon avalanche diode (SPAD) detector. All measurements were performed under optimal laboratory conditions. The response of the samples was coupled to an optical fiber connected to Ocean Optics Flame UV-VIS spectrometer for spectral response and PL measurement and a SPAD detector for the fluorescence lifetime measurement.

3. Results and discussion

Before the experimental characterization, we numerically calculated the dispersion relation of the proposed structure using both local and non-local effective medium theory (EMT) and the TMM approach to determine the wavevectors that are supported by the polymer-based hyperbolic metamaterial. The dispersion relation illustrated in Fig. 2(a), (b) and (c) shows the transmission of evanescent waves through the proposed structure. The local EMT approach represents the multilayered structure as an effective bulk medium with hyperbolic dispersion. As shown in Fig. 2(a), infinitely large wavevectors can be transmitted through the entire bandwidth of this ideal structure. However, in a realistic structure with a finite number of layers and considering the inherent losses in the metal layers, there is a cutoff to the largest wavevector that can propagate through the HMM structure. This is evident in the TMM dispersion relation illustrated in Fig. 2(c), which shows two bright bands at $k_x/k_0 < 5$ and is comparable to the non-local EMT approach [42] illustrated in Fig. 2(b). Non-local EMT approaches have been quite realistic in describing metal-dielectric hyperbolic metamaterials due to their spatial dispersion effects corrections as compared to the local EMT approach [42–44]. The existence of the bright bands in the dispersion relation of the polymer-based HMM structure shows that the medium supports bulk plasmon-polaritonic modes. The bright bands coined as the bulk plasmon modes are due to the coupling of surface-plasmon-polaritons at each metal-dielectric interface. These modes also exhibit high electric field intensity that overlaps with emitters placed close to the metamaterial, resulting in an increased photonic density of states (PDOS) which is presented in Fig. 2(d). It is also interesting to note that the proposed material is a type 2 HMM structure which shows several high-k modes as compared to type 1 HMM which can support a lesser number of these modes [45].

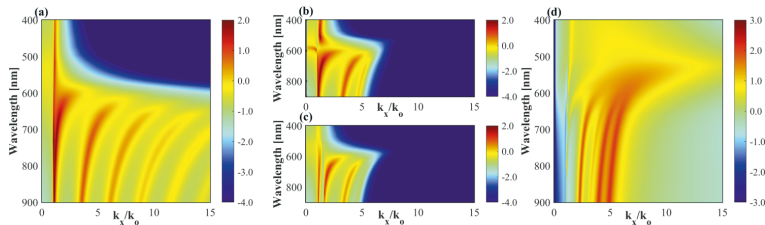


Fig. 2. Dispersion relation of the polymer-based structure exhibiting high-k modes and the associated photonic density of states (PDOS). (a) Transmission of evanescent waves in logarithmic scale through the three bilayers of Au (9 nm)-PMMA (29 nm) multilayered structure using the local EMT approach. In the local effective medium limit, there are infinite high-k waves in a type 2 HMM due to the existence of strong spatial dispersion effects which can be corrected using the non-local EMT approach presented in (b). (c) Similar dispersion relation using the TMM approach. In this realistic case, the size of the unit cell imposes a cut-off to the tunneling of the high-k modes in the structure. (d) The corresponding PDOS of the polymer-based HMM composite using the TMM approach.

3.1. Spectral response of the polymer-based hyperbolic metamaterial

In addition to the dispersion relation, we calculated the field distribution through the polymer-based HMM structure using the TMM approach. Figure 3(a) illustrates propagation mode along the multilayered metal-dielectric interface composed of three subdivisions with labels: IM [$0 \text{ nm} \leq Z \leq 38 \text{ nm}$], MIM1 [$29 \text{ nm} \leq Z \leq 76 \text{ nm}$], and MIM2 [$67 \text{ nm} \leq Z \leq 114 \text{ nm}$] layers. We obtained appreciably high electric field intensity at the ENZ wavelength of the proposed structure. However, the field intensity decays due to propagation losses and inherent metallic losses of the multilayer HMM structure. Note that at the HMM structure thickness $Z > 60 \text{ nm}$, enhanced electric field intensity decays along the metal-dielectric layer thickness. Thus, emission of the embedded emitters results mainly from the first PMMA layer, while emitters in the other two layers contribute minimally. The enhanced spectral region of the electric field distribution shown in Fig. 3(a) correlates to the figure of merit (FOM) bandwidth as shown in Fig. 3(b). The FOM is defined as the ratio of the effective parallel ϵ_{\parallel} and perpendicular ϵ_{\perp} permittivities of the HMM structure acquired via local EMT. The FOM shows higher values at the ENZ wavelength ($\lambda = 570 \text{ nm}$). Figure 3(b) also shows the parallel ϵ_{\parallel} and perpendicular ϵ_{\perp} dielectric tensor as a function of wavelength. The dispersion relation above the ENZ wavelength shows type 2 HMM behavior (i.e., $\text{Re}(\epsilon_{\parallel}) < 0$, $\text{Re}(\epsilon_{\perp}) > 0$) with inherent optical losses and high impedance mismatch with respect to vacuum. In addition, we obtained the extracted effective permittivity $\text{Ext}(\epsilon_{\parallel})$ [dashed lines] of the fabricated polymer-based HMM structure by implementing an inverse TMM code and applying it on the attained spectral response of the HMM-dye complex structure. It is evident that the extracted effective permittivity $\text{Ext}(\epsilon_{\parallel})$ [dashed lines] matches well with the calculated effective parallel ϵ_{\parallel} permittivity [solid lines] possessing a similar ENZ wavelength as predicted numerically by EMT. Figure 3(c) illustrates the reflectance R and transmittance T of the polymer-based HMM structure obtained both numerically [solid lines] and experimentally (i.e., R_{Exp} , T_{Exp}) [dashed lines]. It can be seen that the spectral reflectance range above the ENZ wavelength is high as compared to the spectral range below ENZ. This role of a medium exhibiting dielectric (i.e., $\lambda < 570 \text{ nm}$ with $\text{Re}(\epsilon_{\parallel}) > 0$) and metallic behaviour (i.e., $\lambda > 570 \text{ nm}$ with $\text{Re}(\epsilon_{\parallel}) < 0$) shows the hyperbolic nature of the HMM composite. As stated initially, this nature brings about the inherent losses which can be compensated by using a gain medium, shown as an inset in Fig. 3(c). The inset shows the enhancement of the optical transmission T response of the active polymer-based HMM structure in the presence of a pump source T_{pump} which complements the emitter's ability to help in the inherent metallic loss compensation.

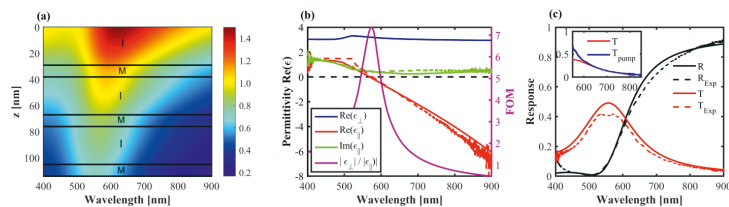


Fig. 3. (a) P-polarized field (E_p) distribution through the HMM composite as a function of spectral wavelength. I-M corresponds to the insulator (PMMA) and metal (Au) interface. (b) Real [$\text{Re}(\epsilon_{\parallel})$, $\text{Re}(\epsilon_{\perp})$] and imaginary [$\text{Im}(\epsilon_{\parallel})$] permittivities from local EMT, experimentally retrieved effective permittivity $\text{Ext}(\epsilon_{\parallel})$ [dashed lines] and the figure of merit (FOM) of the polymer-based HMM composite. ENZ wavelength is defined as the spectral wavelength where the structure permittivity crosses zero. (c) Spectral response of the polymer-based HMM material. Reflectance R and transmittance T acquired both numerically (using TMM) and experimentally (R_{Exp} , T_{Exp}). The inset depicts the experimentally measured transmission in the presence of a pump source T_{pump} and without a pump source T .

3.2. Purcell enhancement calculations

In addition to the spectral response implementations, we numerically calculated the Purcell factor and experimentally measured the photoluminescence of the polymer-based HMM structure to determine the decay rate mechanism of emitters coupled to the polymer-based HMM structure. We considered three scenarios in the numerical implementation. First, we numerically calculated the spectral-dependent far-field power density $W/(m^2 \times sr)$ at polar angle $\theta = 0$ of emitters embedded within the polymer-based HMM structure at different dipole positions Z . Note that $Z = 0 \text{ nm}$ corresponds to an unpolarized dipole placed at the topmost insulator part of the IM layer as shown in Fig. 3. $Z = 105 \text{ nm}$ also corresponds to the bottom insulator layer of the polymer-based HMM structure. The far-field power density calculations helped to determine the directional extraction effectiveness of emitters embedded within the polymer-based HMM as well as to numerically optimize the position of the dipoles embedded within the polymer-based HMM structure. Figure 4(a) delineates the far-field distribution of emitters embedded within the polymer-based HMM structure. We obtained high Purcell power density values at near-field which depicts that emitters close to the edge of the HMM medium exhibit high Purcell enhancement factor due to the high PDOS of the exotic HMM structure at the ENZ region. Also, to comprehend the emitter decay dynamics of the active HMM structure, we numerically placed three unpolarized dipoles (averaged x and y orientations) each at the central part of the three dielectric layers of the HMM structure to calculate their corresponding Purcell factors F_{rad}/F_0 . Figure 4(b) presents the emitter decay rate mechanism at the three corresponding layers (i.e., IM, MIM1, MIM2). Note that MIM1 and MIM2 are similar as shown in Fig. 3(a), labeled as MIM layers. Evidently, due to the inherent lossy nature of metals, we see a weak Purcell factor in the IM layer as compared to the resonant metal-insulator-metal (MIM) case of the multilayered HMM structure. We assumed a collective emitter decay mechanism by taking the average of the Purcell factor [Mean Purcell Factor] at the corresponding layers. We obtained a high Purcell factor as compared to the IM case which we compared with the experimental PL measurement as we shall see in Fig. 5. Figure 4(c) also shows the collective logarithmic scale Purcell enhancement heatmap of multiple emitters embedded within the MIM layer of the polymer-based HMM structure. It is evident that the large thickness of the dielectric and lossy nature of the structure inhibits the coupling of the spontaneous decay of emitters embedded within the layers. This predicts that the unique property of high wavevectors and photonic density of states potentially also play a role in compensating for the lossy nature of the type 2 HMM structure.

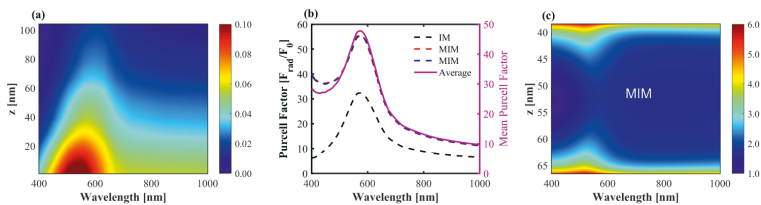


Fig. 4. Purcell factor calculation of the polymer-based HMM structure. (a) Spectral dependent far-field power density $W/(m^2 \times sr)$ distribution of emitters embedded within the polymer-based HMM composite. (b) Purcell enhancement factor F_{rad}/F_0 for three different positions of emitters coupled to the polymer-based HMM structure. IM represents the insulator-metal interface. (c) Collective logarithmic scale Purcell factor enhancement for multiple dipoles placed in the MIM layer of the multilayered HMM structure.

3.3. Luminescence and lifetime measurement

To realize these exotic effects of the active polymer-based HMM structure, we experimentally measured the luminescence and the fluorescence lifetimes for three different dyes (i.e., Rh590, LDS798, and PYR650) within the polymer-based HMM structure. These dyes were selected due to their emission spectra having different amounts of overlap with the ENZ wavelength ($\lambda = 570\text{nm}$) of the structure. Figure 5(a) presents the luminescence measurement of Rh590 dye with a maximum emission wavelength of 569 nm which is close to the ENZ wavelength (570 nm) of the HMM structure. We compared the emission of each dye on a 9 nm gold layer (IL Au + 1L dye), on top of the HMM layers (HMM + 1L dye), and within the HMM layers (HMM + 3L dye), respectively. We obtained high luminescence counts on and within the HMM layers as compared to the metallic cases. Evidently, we identified non-radiative quenching of the emitters when placed on the metallic layers due to the inherent lossy nature of Au. However, in the polymer-based HMM, we obtained improved luminescence counts as compared with the metallic case. This is due to the gold film absorbing the emitted waves with large k-vectors in the near field. On the other hand, in the HMM, these waves are mainly converted into propagating waves which help in compensating the loss of the metal (Au). Furthermore, the field confinement between the metal layers gives rise to emission rate enhancement of the emitters via Purcell effect. The improved luminescence within the polymer-based HMM structure is also compared to the luminescence counts of each dye on top of the HMM structure to compare their luminescence trends. It is noteworthy that the unique nature of the active polymer-based HMM structure compensates for the inherent losses as compared with the metal (Au) layer, yet possesses relatively similar luminescence counts either within or on top of the HMM layers. Figure 5(b) and (c) illustrate similar trend for PYR560 and LDS798 dye molecules. It must be pointed out that the emission wavelength of PYR650 is around 621 nm which is far from the ENZ wavelength of the polymer-based HMM. As a result of the hyperbolic nature of the HMM structure in such a spectral region, we obtained a relatively higher luminescence trend for the PYR650 dye molecules as compared to the Rh590 dye molecules. Figure 5(c) also shows similar results for LDS798 dye molecule depicting weaker luminescence counts with emission wavelength of LDS798 dye far from the ENZ wavelength of the polymer-based HMM structure.

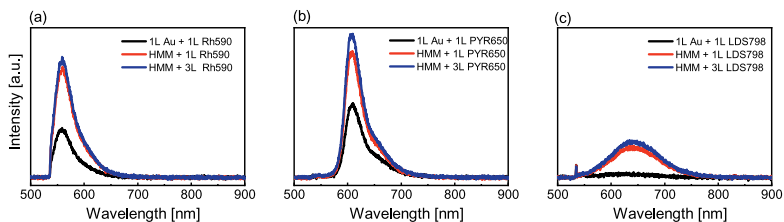


Fig. 5. Spectral luminescence measurement of emitters embedded within the polymer-based HMM composite. (a) Luminescence measurement of Rh590 dye molecule active polymer-based HMM structure. L represents the layers of emitters and metal-dielectric used, respectively. IL Au + 1L dye represents one layer of dye (0.01% concentration)-doped PMMA spin-coated on one layer of metal (Au) on top of a substrate. HMM + 1L dye depicts one layer of dye-doped PMMA spin-coated on top of the HMM structure. HMM + 3L dyes represent a polymer-based HMM structure with dyes doped at each PMMA layer of the HMM structure (3L). Similar measurement for (b) PYR650 dye-doped and (c) LDS798 dye-doped polymer-based HMM structure.

In addition, we compared the experimentally attained fluorescence lifetime values for each of the three different dye-doped HMM structures. Table 1 contains the lifetime components

and the corresponding amplitudes fitted to the measured time-correlated single-photon counting (TCSPC) data as well as the calculated average lifetimes based on the amplitudes. For all dyes (≈ 40 molecules/ $(10 \times 10 \times 29 \text{ nm}^3)$) in the presence of one gold layer, we observed shortening of the average lifetime by more than a half, which is attributed to increased non-radiative decay due to near field absorption of the gold film. This is important to keep in mind when inspecting the lifetimes of dyes on top or embedded inside the polymer-based HMM, as the effect of dyes interacting with the thin gold film is also present in the HMM. Nonetheless, in the polymer-based HMM we observe even shorter lifetimes. Fermi's golden rule states that the number of radiative decay channels depends on the number of PDOS available to the emitter [23]. Therefore, an increased PDOS can be experimentally verified by observing a shortened lifetime. Thus, these lifetime results act as evidence of coupling between the emitters (Rh590 and PYR650) and the high-k modes of the polymer-based HMM complex as well as coupling to the surface plasmon polariton modes at each metal-dielectric interface. This results in an additional increment to the non-radiative recombination rate of the emitters. However, for LDS798 no additional shortening of lifetime is observed in the HMM when compared with the metal case. As seen from Fig. 2(d), the increase in PDOS is highest near the ENZ wavelength. As the emission of LDS798 has the least overlap with that region, the coupling between the emitters and the high-k modes is weakest, thus not resulting in further shortening of the lifetime. Additionally, as seen in Fig. 3(a), the structure exhibits field confinement in the polymeric region between the gold layers spectrally overlapping with the ENZ wavelengths. The resulting enhancement of the radiative decay rate due to the Purcell effect can also be observed through lifetime shortening. However, lifetime shortening can differ from the calculated Purcell factor, since fluorescence lifetime is dependent mainly on the radiative and non-radiative rates. On the other hand, Purcell factor enhancements can be attributed to distinct factors such as local field intensity of the HMM structure, varied dye molecules orientations, as well as positions [46]. This accounts for the difference between the calculated Purcell factor and the experimental decay rates of the polymer-based HMM structure. Furthermore, the emission lifetimes of the polymer-based HMM structure may vary at different characterization spots due to different emitter orientations and their various separation distances

Table 1. Lifetime measurements of the three dyes on fused silica substrate, on 9 nm gold (Au) layer and, on top of the HMM structure and embedded within the polymer-based HMM structure.

	Rh590			PYR650			LDS798		
	Amplitudes	Lifetime components	Average	Amplitudes	Lifetime components	Average	Amplitudes	Lifetime components	Average
On fused silica	A ₁ : 4.54	τ_1 : 4.06 ns	2.91 ns	A ₁ : 7.70	τ_1 : 1.60 ns	2.08 ns	A ₁ : 23.0	τ_1 : 0.55 ns	0.85 ns
	A ₂ : 4.30	τ_2 : 1.68 ns		A ₂ : 2.90	τ_2 : 3.35 ns		A ₂ : 6.50	τ_2 : 1.90 ns	
On 9 nm Au	A ₁ : 22.9	τ_1 : 0.70 ns	0.79 ns	A ₁ : 20.0	τ_1 : 0.77 ns	0.87 ns	A ₁ : 1.24	τ_1 : 0.34 ns	0.40 ns
	A ₂ : 0.12	τ_2 : 8.10 ns		A ₂ : 1.29	τ_2 : 2.46 ns		A ₂ : 0.05	τ_2 : 2.00 ns	
	A ₃ : 0.89	τ_3 : 2.30 ns							
On top of HMM	A ₁ : 28.0	τ_1 : 0.60 ns	0.66 ns	A ₁ : 19.0	τ_1 : 0.73 ns	0.81 ns	A ₁ : 3.94	τ_1 : 0.34 ns	0.40 ns
	A ₂ : 0.14	τ_2 : 6.70 ns		A ₂ : 1.11	τ_2 : 2.33 ns		A ₂ : 0.10	τ_2 : 1.81 ns	
	A ₃ : 0.72	τ_3 : 2.11 ns							
Inside HMM	A ₁ : 32.8	τ_1 : 0.59 ns	0.66 ns	A ₁ : 25.0	τ_1 : 0.69 ns	0.78 ns	A ₁ : 4.78	τ_1 : 0.37 ns	0.41 ns
	A ₂ : 0.13	τ_2 : 6.70 ns		A ₂ : 1.52	τ_2 : 2.22 ns		A ₂ : 0.10	τ_2 : 2.01 ns	
	A ₃ : 0.68	τ_3 : 2.20 ns							

from the metallic layers. As such, we measured the fluorescence lifetimes of each sample at several spots to attain their collective mean values and standard deviations. Average lifetime values of [$\approx 0.66 \pm 0.0064$, $\approx 0.78 \pm 0.0044$, and $\approx 0.41 \pm 0.0043$] ns were attained for (Rh590, PYR650, and LDS798) dyes inside HMM structures, respectively.

3.4. Polymer-based HMM for subwavelength imaging application

To emphasize the relevance of the proposed active polymer-based HMM structure, we further calculated the subwavelength resolution of two-dipoles with a separation distance of 50 nm ($\approx \lambda/12$) placed at 10 nm away from the polymer-based HMM medium as shown in Fig. 6. We compared the passive (a), (b), and (c) and the active (d), (e), and (f) polymer-based HMM structures at three different wavelengths ($\lambda = 570 \text{ nm}$, 621 nm , and 700 nm) which are comparable to the emission wavelength of the dye molecules embedded within. It is evident that the active polymer-based HMM medium (d), (e), and (f) depicts enhanced field amplitude as compared to the passive (a), (b), and (c) HMM. Figure 6(a) shows the dipole resolved field distribution along the propagation axis (Z) for the passive HMM structure at resonance wavelength $\lambda = 570 \text{ nm}$. Similar results are shown in Fig. 6(b) and (c) at different spectral regions which correlate to the emission wavelength of PYR650 and LDS798 dyes, respectively. Evidently, incorporating dye molecules in the passive polymer-based HMM structure compensates for the metallic losses in the HMM and enhances the field distribution illustrated in Fig. 6(d), (e), and (f). The polymer-based HMM structure's ability to transmit high order evanescent waves from the near-field to the far-field and the existence of a gain medium embedded within enhances its applications in subwavelength resolution imaging. Thus utilizing the proposed polymer-based HMM structure breaks the diffraction limit and enhances dipole subwavelength resolution as well as projecting an image with subwavelength details into the far-field. This unique nature of the polymer-based HMM structure could be utilized in relevant photonic applications such as hyperlenses.

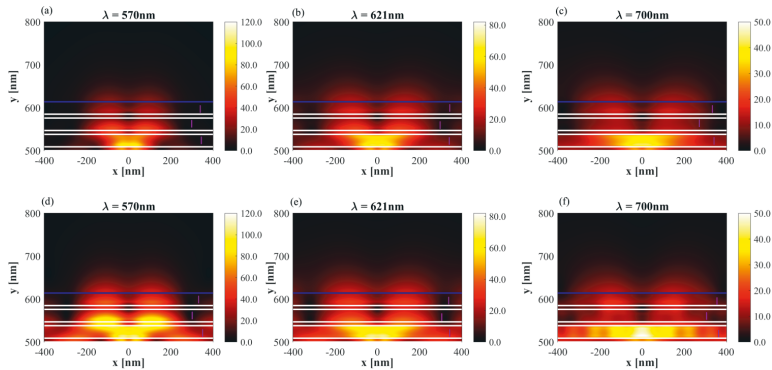


Fig. 6. (a), (b), and (c) Sub-wavelength resolved two dipole sources using a passive polymer-based HMM structure and their corresponding active case (d), (e), and (f) at different wavelengths (i.e., 570 nm , 621 nm , 700 nm) comparable to the emission wavelength of the dye molecules. In between the two white lines represents the metal layers and the blue line depicts the topmost layer of the polymer-based HMM layers. The insulator layer is also represented as I.

4. Conclusion

In summary, we have shown the dynamics of emission and decay rate of different dyes incorporated with a polymer-based HMM structure and numerically predicted the existence of its corresponding non-radiative high-k modes. We illustrated the shortening of the average lifetime and increment in the luminescence intensity of emitters embedded within and on top of the polymer-based HMM structure which are due to the increase in the non-radiative decay channels of the proposed structure. With emitters spectrally closer (Rh590) to the ENZ region of the polymer-based HMM structure, we observed a relatively high shortening of the average lifetime as compared to other emitters spectrally close (PYR650) or far (LDS798) from the ENZ region. This observation confirms the increase in non-radiative decay channels of the polymer-based HMM structure with a gain medium at the ENZ region. We also showed that our proposed dye-doped polymer-based HMM structure compensates for the losses in a metal-dielectric HMM structure by observing an enhanced transmittance in the presence of a pump source and numerically implemented the sub-wavelength two dipoles resolution to emphasize the relevance of incorporating emitters into a passive polymer-based HMM structure. The unique properties of our proposed polymer-based HMM structure could be a paradigm shift to enhance the robustness of HMM structures in nano-imaging and quantum optics applications.

Funding. H2020 European Research Council (802986); Academy of Finland (320165).

Acknowledgments. We acknowledge the financial support of the European Research Council (Starting Grant project aQUARIUM, Agreement No. 802986) and Academy of Finland Flagship Programme (PREIN) (320165).

Disclosures. The authors declare no conflicts of interest.

Data availability. Data underlying the results are presented in the paper.

References

1. N. Lassaline, R. Brechtbühler, S. J. W. Vonk, K. Ridderbeek, M. Spieser, S. Bisig, B. le Feber, F. T. Rabouw, and D. J. Norris, "Optical Fourier surfaces," *Nature* **582**(7813), 506–510 (2020).
2. X. Jiang, B. Liang, R.-q. Li, X.-y. Zou, L.-l. Yin, and J.-c. Cheng, "Ultra-broadband absorption by acoustic metamaterials," *Appl. Phys. Lett.* **105**(24), 243505 (2014).
3. V. P. Drachev, V. A. Podolskiy, and A. V. Kildishev, "Hyperbolic metamaterials: new physics behind a classical problem," *Opt. Express* **21**(12), 15048–15064 (2013).
4. M. Habib, I. Issah, D. Briukhanova, A. R. Rashed, and H. Caglayan, "Wavefront Control with Nanohole Array-Based Out-of-Plane Metasurfaces," *ACS Appl. Nano Mater.* **16**, 28 (2021).
5. I. I. Smolyaninov, Y. J. Hung, and C. C. Davis, "Two-dimensional metamaterial structure exhibiting reduced visibility at 500 nm," *Opt. Lett.* **33**(12), 1342–1344 (2008).
6. I. Issah, F. Li, M. Baah, I. A. Otoo, L. Asilevi, P. Bawuah, and B. O. Asamoah, "Passive tunable and polarization-insensitive fan-like metamaterial absorber in the visible spectrum," *J. Opt. Soc. Am. B* **38**(9), C1–C10 (2021).
7. Z. Guo, H. Jiang, and H. Chen, "Hyperbolic metamaterials: From dispersion manipulation to applications," *J. Appl. Phys.* **127**(7), 071101 (2020).
8. S. Chervinskii, I. Issah, M. Lahikainen, A. R. Rashed, K. Kuntze, A. Priimagi, and H. Caglayan, "Humidity- and temperature-tunable metal-hydrogel-metal reflective filters," *ACS Appl. Mater. Interfaces* **13**(42), 50564–50572 (2021).
9. S. Ishii, A. V. Kildishev, E. Narimanov, V. M. Shalaev, and V. P. Drachev, "Sub-wavelength interference pattern from volume plasmon polaritons in a hyperbolic medium," *Laser Photonics Rev.* **7**(2), 265–271 (2013).
10. C. L. Cortes, W. Newman, S. Molesky, and Z. Jacob, "Corrigendum: Quantum nanophotonics using hyperbolic metamaterials (2012 j. opt. 14 063001)," *J. Opt.* **16**(12), 129501 (2014).
11. Y. Guo, W. Newman, C. L. Cortes, and Z. Jacob, "Applications of Hyperbolic Metamaterial Substrates," *Adv. Optoelectron.* **2012**, 1–9 (2012).
12. W. Cai and V. Shalaev, *Optical metamaterials: Fundamentals and applications* (Springer, 2010).
13. D. Briukhanova, M. Habib, I. Issah, and H. Caglayan, "Low loss fishnet metamaterial via self-rolled nanotechnology," *Appl. Phys. Lett.* **119**(14), 141101 (2021).
14. Z. Jacob and E. E. Narimanov, "Optical hyperspace for plasmons: Dyakonov states in metamaterials," *Appl. Phys. Lett.* **93**(22), 221109 (2008).
15. W. Du, W. Kong, H. Liu, K. Liu, C. Wang, and X. Luo, "Design of a Structured Bulk Plasmon Illumination Source for Enhancing Plasmonic Cavity Superlens Imaging," *Plasmonics* **13**(4), 1387–1392 (2018).
16. S. Schwaiger, A. Rottler, and S. Mendach, "Rolled-up metamaterials," *Adv. Optoelectron.* **2012**, 1–10 (2012).

17. M. Kim, S. So, K. Yao, Y. Liu, and J. Rho, "Deep sub-wavelength nanofocusing of UV-visible light by hyperbolic metamaterials," *Sci. Rep.* **6**(1), 38645 (2016).
18. A. Poddubny, I. Iorsh, P. Belov, and Y. Kivshar, "Hyperbolic metamaterials," *Nat. Photonics* **7**(12), 948–957 (2013).
19. I. Issah, M. Habib, and H. Caglayan, "Long-range qubit entanglement via rolled-up zero-index-waveguide," *Nanophotonics* **10**(18), 4579–4589 (2021).
20. I. Issah and H. Caglayan, "Qubit–qubit entanglement mediated by epsilon-near-zero waveguide reservoirs," *Appl. Phys. Lett.* **119**(22), 221103 (2021).
21. A. Alù, M. G. Silveirinha, A. Salandrino, and N. Engheta, "Epsilon-near-zero metamaterials and electromagnetic sources: Tailoring the radiation phase pattern," *Phys. Rev. B* **75**(15), 155410 (2007).
22. R. S. Savelev, I. V. Shadrivov, P. A. Belov, N. N. Rosanov, S. V. Fedorov, A. A. Sukhorukov, and Y. S. Kivshar, "Loss compensation in metal-dielectric layered metamaterials," *Phys. Rev. B* **87**(11), 115139 (2013).
23. Z. Jacob, J.-Y. Kim, G. V. Naik, A. Boltasseva, E. E. Narimanov, V. M. Shalaev, and A. Boltasseva, "Engineering photonic density of states using metamaterials," *Appl. Phys. B* **100**(1), 215–218 (2010).
24. Z. Jacob, I. I. Smolyaninov, and E. E. Narimanov, "Broadband Purcell effect: Radiative decay engineering with metamaterials," *Appl. Phys. Lett.* **100**(18), 181105 (2012).
25. M. A. Noginov, H. Li, Y. A. Barnakov, D. Dryden, G. Nataraj, G. Zhu, C. E. Bonner, M. Mayy, Z. Jacob, and E. E. Narimanov, "Controlling spontaneous emission with metamaterials," *Opt. Lett.* **35**(11), 1863 (2010).
26. S. Krasikov and I. V. Iorsh, "Self-consistent Purcell factor and spontaneous topological transition in hyperbolic metamaterials," *Phys. Status Solidi RRL* **10**(10), 769–773 (2016).
27. W. D. Newman, C. L. Cortes, and Z. Jacob, "Enhanced and directional single-photon emission in hyperbolic metamaterials," *J. Opt. Soc. Am. B* **30**(4), 766–775 (2013).
28. O. A. Makarova, M. Y. Shalaginov, S. Bogdanov, A. V. Kildishev, A. Boltasseva, and V. M. Shalaev, "Patterned multilayer metamaterial for fast and efficient photon collection from dipolar emitters," *Opt. Lett.* **42**(19), 3968–3971 (2017).
29. A. P. Slobozhanyuk, P. Ginzburg, D. A. Powell, I. Iorsh, A. S. Shalin, P. Segovia, A. V. Krasavin, G. A. Wurtz, V. A. Podolskiy, P. A. Belov, and A. V. Zayats, "Purcell effect in hyperbolic metamaterial resonators," *Phys. Rev. B* **92**(19), 195127 (2015).
30. R. Chandrasekar, Z. Wang, X. Meng, S. I. Azzam, M. Y. Shalaginov, A. Lagutchev, Y. L. Kim, A. Wei, A. V. Kildishev, A. Boltasseva, and V. M. Shalaev, "Lasing action with gold nanorod hyperbolic metamaterials," *ACS Photonics* **4**(3), 674–680 (2017).
31. F. A. Inam, N. Ahmed, M. J. Steel, and S. Castelletto, "Hyperbolic metamaterial resonator–antenna scheme for large, broadband emission enhancement and single-photon collection," *J. Opt. Soc. Am. B* **35**(9), 2153–2162 (2018).
32. D. Lu, J. J. Kan, E. E. Fullerton, and Z. Liu, "Enhancing spontaneous emission rates of molecules using nanopatterned multilayer hyperbolic metamaterials," *Nat. Nanotechnol.* **9**(1), 48–53 (2014).
33. L. Novotny and B. Hecht, *Principles of Nano-Optics* (Cambridge University Press, 2006).
34. K. V. Sreekanth, A. De Luca, and G. Strangi, "Experimental demonstration of surface and bulk plasmon polaritons in hypergratings," *Sci. Rep.* **3**(1), 3291 (2013).
35. J. R. Lakowicz, "Radiative decay engineering 5: metal-enhanced fluorescence and plasmon emission," *Anal. Biochem.* **337**(2), 171–194 (2005).
36. X. Ni, S. Ishii, M. D. Thoreson, V. M. Shalaev, S. Han, S. Lee, and A. V. Kildishev, "Loss-compensated and active hyperbolic metamaterials," *Opt. Express* **19**(25), 25242–25254 (2011).
37. L. Ferrari, D. Lu, D. Lepage, and Z. Liu, "Enhanced spontaneous emission inside hyperbolic metamaterials," *Opt. Express* **22**(4), 4301–4306 (2014).
38. H.-I. Lin, K.-C. Shen, S.-Y. Lin, G. Haider, Y.-H. Li, S.-W. Chang, and Y.-F. Chen, "Transient and Flexible Hyperbolic Metamaterials on Freeform Surfaces," *Sci. Rep.* **8**(1), 9469 (2018).
39. X. Wu, "Perfect absorption in cascaded asymmetric hyperbolic metamaterial slabs," *Superlattices Microstruct.* **124**, 10–16 (2018).
40. P. B. Johnson and R. W. Christy, "Optical constants of the noble metals," *Phys. Rev. B* **6**(12), 4370–4379 (1972).
41. G. Beadie, M. Brindza, R. A. Flynn, A. Rosenberg, and J. S. Shirk, "Refractive index measurements of poly(methyl methacrylate) (PMMA) from 04–16 μm ," *Appl. Opt.* **54**(31), F139 (2015).
42. Z. Wen, H. Xu, W. Zhao, Z. Zhou, X. Li, S. Li, J. Zhou, Y. Sun, N. Dai, and J. Hao, "Nonlocal effective-medium theory for periodic multilayered metamaterials," *J. Opt.* **23**(6), 065103 (2021).
43. A. V. Chebykin, A. A. Orlov, A. V. Vozianova, S. I. Maslovski, Y. S. Kivshar, and P. A. Belov, "Nonlocal effective medium model for multilayered metal-dielectric metamaterials," *Phys. Rev. B* **84**(11), 115438 (2011).
44. L. Sun, Z. Li, T. S. Luk, X. Yang, and J. Gao, "Nonlocal effective medium analysis in symmetric metal-dielectric multilayer metamaterials," *Phys. Rev. B* **91**(19), 195147 (2015).
45. P. Shekhar, J. Atkinson, and Z. Jacob, "Hyperbolic metamaterials: fundamentals and applications," *Nano Convergence* **1**(1), 14–17 (2014).
46. A. Kinkhabwala, Z. Yu, S. Fan, Y. Avlasevich, K. Müllen, and W. E. Moerner, "Large single-molecule fluorescence enhancements produced by a bowtie nanoantenna," *Nat. Photonics* **3**(11), 654–657 (2009).

PUBLICATION

III

Long-range qubit entanglement via rolled-up zero-index waveguide

I. Issah, M. Habib and H. Caglayan

Nanophotonics 10(18) (2021), 4579–4589

DOI: 10.1515/nanoph-2021-0453

Publication reprinted with the permission of the copyright holders



Research Article

Ibrahim Issah, Mohsin Habib and Humeyra Caglayan*

Long-range qubit entanglement via rolled-up zero-index waveguide

<https://doi.org/10.1515/nanoph-2021-0453>

Received August 17, 2021; accepted November 1, 2021;
published online November 16, 2021

Abstract: Preservation of an entangled state in a quantum system is one of the major goals in quantum technological applications. However, entanglement can be quickly lost into dissipation when the effective interaction among the qubits becomes smaller compared to the noise-injection from the environment. Thus, a medium that can sustain the entanglement of distantly spaced qubits is essential for practical implementations. This work introduces the fabrication of a rolled-up zero-index waveguide which can serve as a unique reservoir for the long-range qubit–qubit entanglement. We also present the numerical evaluation of the concurrence (entanglement measure) via Ansys Lumerical FDTD simulations using the parameters determined experimentally. The calculations demonstrate the feasibility and supremacy of the experimental method. We develop and fabricate this novel structure using cost-effective self-rolling techniques. The results of this study redefine the range of light-matter interactions and show the potential of the rolled-up zero-index waveguides for various classical and quantum applications such as quantum communication, quantum information processing, and superradiance.

Keywords: concurrence; decay rate channels; entanglement; rolled up metamaterials; zero-index mode.

1 Introduction

Metamaterials are defined as artificially engineered structures with different material properties as compared to naturally existing materials [1, 2]. From their inception, these materials have played enormous roles in the manipulation

of electromagnetic fields in many disciplines [3, 4]. The unique properties of these materials have been identified to serve as means to enhance dipole-dipole interactions, energy harvesting, and long-range interactions of quantum emitters (i.e., quantum dots and diamonds (NV defect centers)) embedded within their waveguide-like meta-structures [5–8]. These physical systems find use in many quantum technologies such as quantum communication, quantum information processing [9], and single-photon generation [10, 11].

Other unique properties of metamaterials are related to the high enhancement of quantum emitter's response coupled with such a medium. These responses of emitters coupled to such an environment can be described by the dyadic Green's function which is related to the local density of states (LDOSs) formulations. This further leads to enhanced Purcell effects independent of the emitter position along and within the waveguide-like meta-structures. Experimental verifications of such material have been realized for a rectangular epsilon-near-zero (ENZ) waveguide using cathodoluminescence measurement techniques [12]. Fleury et al. [13] explored that the flexibility of dipole positions in ENZ waveguide channels at the cutoff wavelength is not the only relevance of these channels but could also boost Dicke superradiance effects which leads to a high collective coherent emission of the quantum emitters.

Plasmonic waveguide channels have also been identified to support extraordinary optical transmission when excited and have been implemented in the subwavelength regime to mediate long-range interactions of quantum emitters [14, 15]. Recently, Li et al. [16] presented a comparative study of ENZ and plasmonic waveguide channels used to enhance efficient long-range resonance energy transfer and inter-emitter entanglement. Although plasmonic waveguide types such as V-shaped grooves and cylindrical nanorods have been identified to outperform the sub-wavelength distance limitations of quantum emitters cooperative emission in a homogeneous medium, yet, quantum emitters entangled states mediated by these waveguides suffer from practical applications due to their dependence on the spatial position of emitters [14]. As

*Corresponding author: Humeyra Caglayan, Faculty of Engineering and Natural Science, Photonics, Tampere University, Tampere 33720, Finland, E-mail: humeyra.caglayan@tuni.fi. <https://orcid.org/0000-0002-0656-614X>

Ibrahim Issah and Mohsin Habib, Faculty of Engineering and Natural Science, Photonics, Tampere University, Tampere 33720, Finland. <https://orcid.org/0000-0001-7663-4972> (I. Issah), <https://orcid.org/0000-0002-6109-9468> (M. Habib)



a result, different techniques have been implemented by many authors to overcome these challenges [14, 16–18].

Note, due to the inherently short-range nature of the dipole-dipole interactions of quantum emitters in a homogeneous medium, it is relevant to identify different reservoirs that can be used to enhance the cooperative effects of quantum emitters [19]. The excitation of zero-index mode in such reservoirs makes it possible to enhance long-range interactions of quantum emitters as well as strong entanglement at farther distances. These waveguide channels, zero-index mode, exhibit a uniform field amplitude along the propagation axis which is independent of the axial dipole position due to the integrally large phase velocity [1, 20, 21].

These realizations of zero-index waveguide channels have intrigued much interest in the study of decay rate enhancement and cooperative emission of quantum emitters mediated by these channels [6]. Thereby, relevant to the practical realization of such zero-index waveguide channels with minimal constraints that can be used to enhance resonance energy transfer and long-range entanglement between two-level quantum fluorescence atoms (qubits) [22]. However, the difficulty to integrate quantum emitters in rectangular zero-index waveguide materials as well as the fabrication difficulties in the nanoscale regime has inhibited their practical applications [23]. To fulfill these zero-index features, the integration requires a controllable and feasible 3D fabrication process. The latter, while extremely pertinent from a fundamental perspective, poses limitations due to difficulties in sample fabrication, which may result in a reduced zero-index response or create a nonaccessible medium for integration and excitation of emitters.

Therefore, in this study, a self-assembled three-dimensional rolled-up zero-index waveguide will be our choice to overcome these deficiencies. We designed, fabricated, and numerically simulated, based on the parameters attained experimentally, alternating layers of metal and dielectric rolled-up zero-index waveguide to serve as an environment to mediate the cooperative emission of emitters embedded within it. We anticipate that the proposed rolled-up zero-index waveguide will enhance long-range dipole-dipole interactions and the preservation of entangled states due to its exotic properties to enhance super coupling within the cutoff region. To study these properties, we implemented the concept of rigorous dyadic Green's function relative to macroscopic quantum electrodynamics (QED) techniques to describe the response of a single fluorescence quantum emitter coupled to the rolled-up zero-index waveguide reservoir.

Also, we used the quantum master equation presented in the Supplementary section to numerically calculate the transient and steady-state entanglement between two-level atoms mediated by rolled-up zero-index waveguide using Wootters' concurrence formalism. Before the entanglement property calculations of the rolled-up zero-index waveguide, we first studied the photonic properties of the zero-index waveguide using Ansys Lumerical Finite Element EigenMode (FEEM) solver.

2 Zero-index waveguide modes

Ostensibly, long-distance entanglement between two quantum bits (qubits) is known to be mediated by photons. However, the recent emergence of the application of surface plasmons generation in different resonators and plasmonic waveguides has attracted researchers to delve into plasmon mediated entanglement between qubits in the nanoscale regime [13, 14]. This technique to confine optical fields in the subwavelength regime is fundamental in the application of surface plasmons in quantum optics. However, the sinusoidal phase change variations in propagating surface plasmon (SPP) mode of a waveguide channel limit the free distribution of quantum emitters in its corresponding environment [24]. It is thereby pertinent to use alternative means to examine other plasmonic channels with near-zero index properties and with the ability to enhance the entanglement of two qubits coupled with its excited zero-index waveguide mode.

Here, we investigate the fundamental TE_{11} mode of a rolled-up zero-index structure at the cutoff wavelength where there is minimal phase variation between two quantum emitters. Before investigating the fundamental mode, we examined the photonic properties of a traditional cylindrical hollow waveguide.

2.1 Cylindrical hollow waveguide

To serve as a guide to determine the fundamental mode of the rolled-up zero-index waveguide composed of an alternating layer of metal and dielectric, we numerically implement the analytical equation for a homogeneous circular waveguide with an air core [25]. The dispersion relation of the rolled-up zero-index waveguide is initially calculated to identify the cutoff wavelength, where the propagation constant $k = 0$. At this wavelength, the electromagnetic waves can be squeezed or tunneled through a waveguide to exhibit a similar response as zero-index materials. This phenomenon relative to circular waveguides has been

demonstrated theoretically by Pan et al. [26] to exhibit unique electromagnetic tunneling which is independent of the waveguide length.

From the Helmholtz eigenvalue equation, the cutoff wavelength as a function of the effective mode index of a circular hollow waveguide can be expressed analytically as

$$n_{\text{eff}} = \sqrt{1 - \left(\frac{u_{nm}}{\pi}\right)^2 \left(\frac{\lambda}{2\rho}\right)^2}, \quad (1)$$

where n_{eff} is the effective index as a function of dielectric core diameter, u_{nm} is the root of the Bessel function, ρ is the radius of the circular core, and λ is the wavelength. Since our mode of interest is the fundamental TE_{11} mode, the corresponding root of the Bessel function selected is 3.832. The analytical calculation of the dispersion relation of a cylindrical dielectric waveguide is shown in Figure 1(a). This served as a benchmark to determine the

cutoff frequency of the rolled-up zero-index waveguide presented in Figure 1(b) for different diameters D .

For different core diameters D of both the cylindrical and zero-index hollow waveguides, we obtained a redshift of the cutoff wavelength. This shows the dependence of the cutoff wavelength on the material dimensions. The dispersion of the cylindrical hollow metallic (i.e., gold (Au)) waveguide (dotted lines) superimposed on Figure 1(b) shows a similar dispersion relation as the rolled-up zero-index waveguide. Figure 1(c) illustrates the unique and complex modes of the rolled-up zero-index waveguide at different effective indices (n_{eff}). The complex mode profiles with effective cladding index ($n_{\text{eff}} \neq 0$) are mostly confined in the metal-dielectric cladding region due to the excitation of plasmon modes. However, the fundamental mode of the waveguide with $n_{\text{eff}} \approx 0$ confined in the core possesses a similar dispersion relation with the fundamental

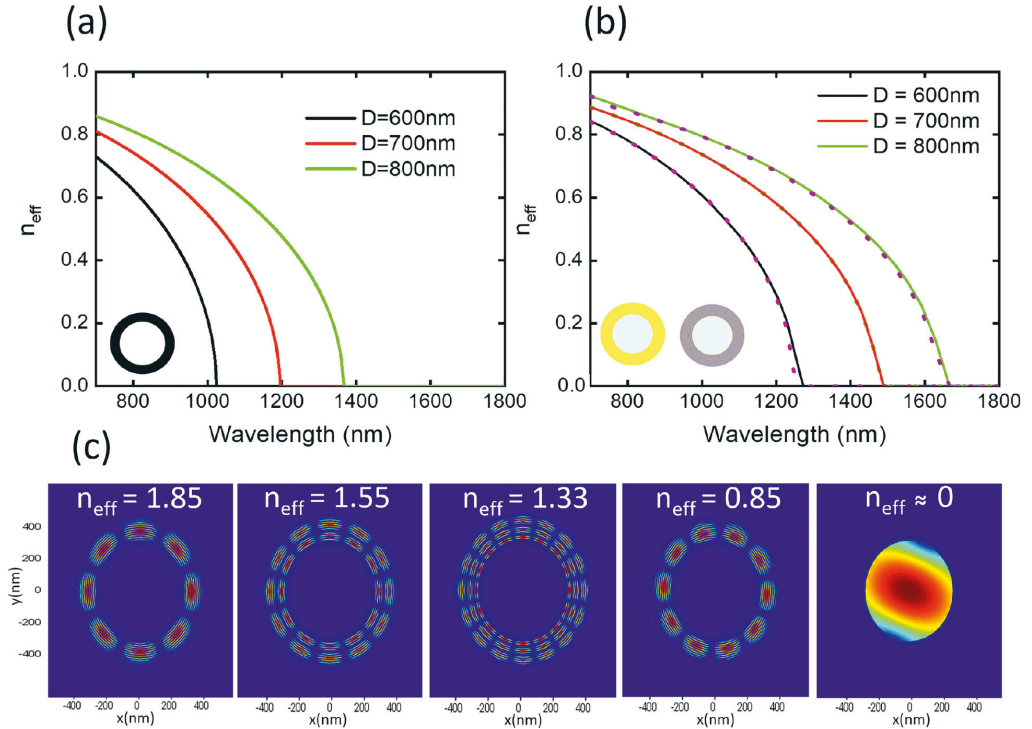


Figure 1: Photonic properties of a cylindrical hollow waveguide and a rolled-up zero-index waveguide with its corresponding mode profiles. (a) The dispersion relation of a cylindrical hollow waveguide with different core diameters D . The schematic of the homogeneous circular waveguide is represented by the black circular inset. (b) The dispersion relation of the rolled-up zero-index waveguide (solid lines). The dotted lines in the same figure show similar dispersion calculated for the cylindrical hollow metallic waveguide. The yellow circular inset represents the cylindrical hollow metallic waveguide and the rolled-up tube is represented by the multilayer gray circular inset. The cutoff wavelength varies as a function of the core diameter D in both figures (top panel). (c) The different mode profiles excited in the rolled-up zero-index waveguide ($D = 700$ nm) for different effective indices (n_{eff}) with $n_{\text{eff}} \approx 0$ depicting the fundamental TE_{11} mode.

modes of the plasmonic hollow waveguide. This waveguide fundamental mode with an effective index near zero introduces novel ways of controlling optical field propagation and enhancement due to the infinite phase velocity of the tunneled electromagnetic wave.

2.2 Rolled-up zero-index waveguide

In this section, we described how the proposed structure can be fabricated.

The first rolled-up tubes were fabricated by Prinz et al. using strained InAs/GaAs bilayer with lattice mismatch [27]. The layers start to roll as the sacrificial layer beneath them is released by an etchant. However, semiconductor-based rolled-up tubes are not suitable for our purpose, due to the high refractive indices of materials as compared to near-zero refractive index material required for this study. In this study, we adopted a similar strained induced self-rolling mechanism to obtain a three-dimensional rolled-up zero-index waveguide of Au and SiO₂ on a silicon (Si) substrate using germanium (Ge) as a sacrificial layer (see Supplementary for details). Figure 2(a) illustrates the schematics of the proposed design. Figure 2(b) depicts the scanning electron microscope (SEM) image of the fabricated rolled-up zero-index waveguide. The structure has a

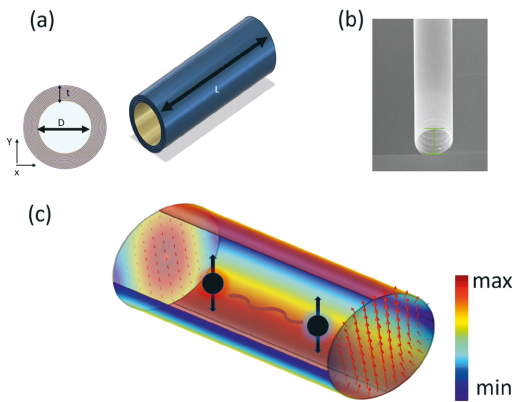


Figure 2: Rolled-up zero-index waveguide schematics and fabricated sample.

(a) Schematic of the rolled-up zero-index waveguide (b) SEM images of the fabricated waveguide. The green line corresponds to a diameter of 700 nm and the length of the waveguide is 25 μm . (c) The volumetric display of the normalized fundamental TE₁₁ mode propagation in the rolled-up zero-index waveguide. The embedded dipoles (qubits) are denoted by the black spheres with arrows. The interaction between the dipoles mediated by the zero-index mode is represented by the curvy lines. The surface vector plot shows the field distribution of the fundamental mode.

core diameter (D) of 700 nm, consisting of 12 alternating bi-layers, 10 nm of Au and 5 nm of glass silica (SiO₂) thick, and length (L) of 25 μm .

The benefit of the rolled-up zero-index waveguide over other plasmonic waveguide channels is that it offers different emitters integration techniques into the core of the waveguide. For example, injection techniques of colloidal nanoemitters using microsyringe technique. In such a case, the driving of nanoemitters is mediated by capillary forces [28]. Another method of integrating quantum emitters to the core of the rolled-up zero-index waveguide is to deposit emitters on the planar bilayer before initiating the rolling process.

We now move to the numerical calculations based on the parameters of the fabricated structure. However, due to the existence of the nonradiative and propagation losses, the 25 μm length of the fabricated waveguide is approximated to be 3 μm in the simulation. Moreover, the 3 μm was identified to suffice for determining the coupling parameters of an emitter positioned at the central part of the rolled-up zero-index waveguide. It is worth noting that the numerical calculation suggests that for a dipole placed at the central part of the waveguide, its decay rate vanishes beyond 3 μm as we shall see in Figure 4.

The core diameter of the rolled-up structure is filled with a material permittivity of one. Material dispersion of Au from Johnson and Christy [29] material dispersion data and Palik [30] data for the SiO₂ layers were used in the modeling. Figure 2(c) also shows the volumetric display of the fundamental mode of the rolled-up zero-index waveguide at the cutoff wavelength $\lambda \approx 1450$ nm. The embedded dipoles represent the quantum emitters mediated by the zero-index mode of the rolled-up zero-index waveguide, and the vector surface plot shows the field distribution of the fundamental TE₁₁ mode. Note that in the case of the fundamental TE₁₁ mode both radial and axial components of the transverse fields exist resulting in the distribution of total electric and magnetic field in the rolled-up zero-index waveguide cross-section.

3 Decay rate enhancement of the rolled-up waveguide

As stated initially, advances in plasmonic materials (i.e., V-shaped grooves, cylindrical nanorods) and ENZ plasmonic metamaterials (i.e., plasmonic planar waveguide) have availed the opportunity to enhance superradiant effects of a collective quantum emitter which outperforms the weak interaction of emitters in a homogeneous medium [13].

The superradiance effect known as the collective effect of quantum emitters arranged close to each other was proposed by Dicke [31] to show the relationship between the radiation intensity of quantum emitters and the number of quantum sources. This radiant effect is linked to the exotic properties of the reservoir to which the quantum emitters are coupled to.

At the cutoff wavelength region of the rolled-up zero-index waveguide channel, we foresee a high LDOS of the quantum emitter embedded in the waveguide structure. This enhancement at the cutoff wavelength is insensitive to the emitter axial position and thereby exhibits the aforementioned inherent flexibility of emitters position in zero-index metamaterials [16, 32, 33].

To verify the high LDOS at the cutoff wavelength, we computed the Purcell factor of the proposed rolled-up zero-index waveguide channels as a function of different waveguide core diameters D . Figure 3 presents the corresponding Purcell factor calculation. It can be seen that the spectral resonance response of a single quantum emitter coupled to a rolled-up zero-index waveguide is dependent on the core diameter D . As the diameter increases the spectral density response redshifts to a higher wavelength similar to the dispersion relation in Figure 1(b). For the waveguide channel with a core diameter of $D = 700$ nm, the peak enhancement is around the cutoff wavelength (i.e., $\lambda \simeq 1450$ nm).

Above the cutoff wavelength, the decay rate is predominantly quenched by the environment as there is a very low density of states due to the quenched propagating modes in the waveguide. However, below the cutoff wavelength, there is monotonic build-up in the decay rate

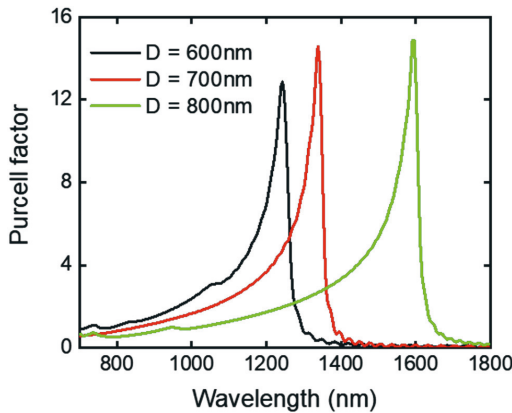


Figure 3: Decay rate enhancement for different core diameters D of the rolled-up zero-index waveguide.

reaching a maximum at the cutoff wavelength. Close to the cutoff wavelength, the decay rate is not only enhanced but remains uniform along the waveguide channel. This uniformity is due to the nonresonant mode distribution at the cutoff wavelength [12].

4 Rolled-up zero-index waveguide dipole-dipole coupling and decay rate

To determine the key parameters (i.e., decay rate (γ_{12}) and dipole-dipole coupling ($\pm g_{12}$)) to solve the quantum master equation in Eq. (S3), we calculate the γ_{12} and $\pm g_{12}$ of an emitter embedded within the rolled-up zero-index waveguide using the dyadic Green's function obtained from FDTD simulations (see Supplementary for details). We study these parameters of the quantum master equation at three different wavelengths (i.e., the cutoff wavelength ($\lambda = 1450$ nm) and at two other wavelengths: close ($\lambda = 1300$ nm) and far ($\lambda = 1250$ nm) from the cutoff wavelength).

Figure 4(a) depicts the dipole-dipole interactions of quantum emitters embedded in the rolled-up zero-index waveguide at three different wavelengths as a function of interatomic distance (r_{12}/λ_0). At the cutoff wavelength, the dipole interactions increase appreciably at short-range and decay exponentially as a function of interatomic distance as compared to the other two wavelengths. At $\lambda = 1250$ nm and $\lambda = 1300$ nm, we identified an oscillatory behavior of the dipole-interactions as compared to the cutoff wavelength. This oscillatory behavior of the two wavelengths relative to the cutoff wavelength is also shown in the spontaneous decay rate of the quantum emitter as shown in Figure 4(b). Figure 4(c)–(e) presents the energy transfer resonance, which is dependent on the dyadic Green's function of the qubits inside the rolled-up zero-index waveguide [34]. This shows that, at the cutoff wavelength, the rolled-up zero-index waveguide provides modes with a longer wavelength and minimal phase variations to enhance strong entanglements of two qubits placed at farther distances.

At the cutoff wavelength $\lambda_0 = 1450$ nm, we also see a long-range decay rate as a function of interatomic distance which enhances qubit entanglement. It is evident that the comparison between the normalized decay rate and the dipole-dipole interaction at the cutoff wavelength satisfies the condition of attaining high entanglement

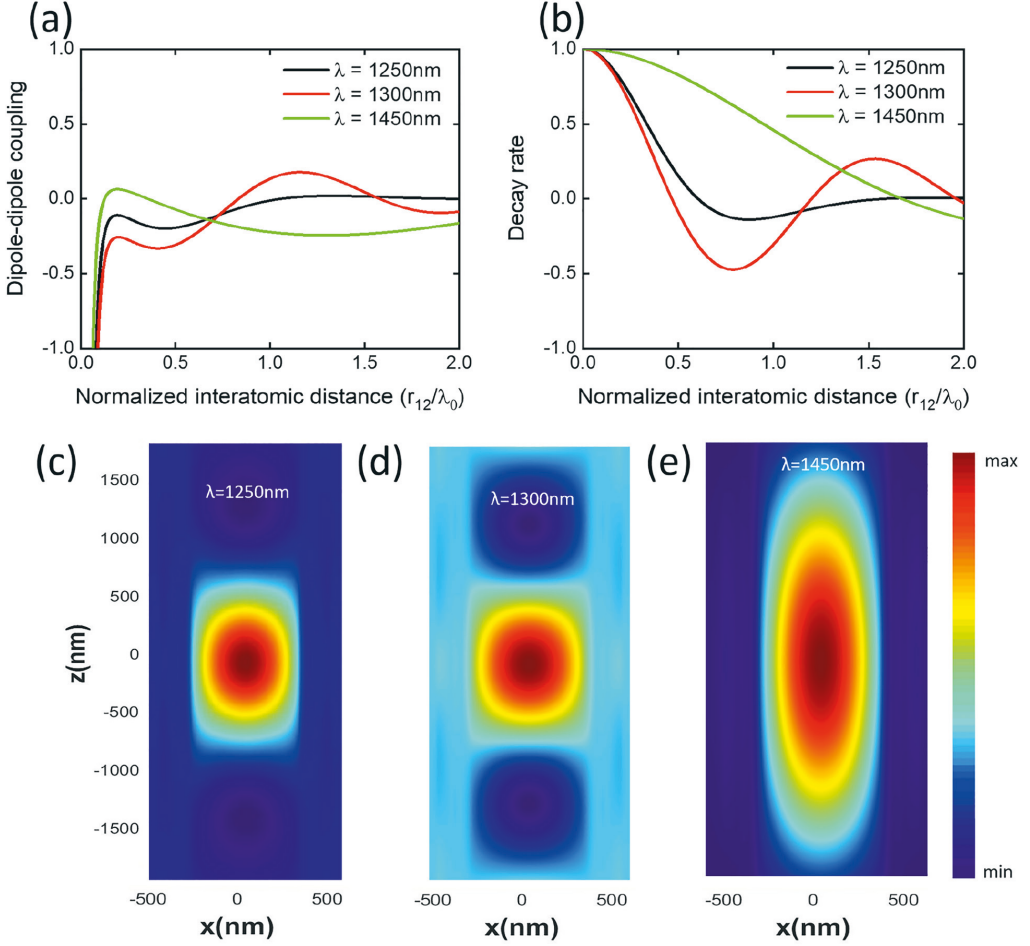


Figure 4: Coupling parameters of the rolled-up zero-index waveguide.

(a) The dipole-dipole interaction and (b) the decay rate of emitters coupled to the rolled-up zero-index waveguide at different excitation wavelengths. Energy transfer resonance (ETR) of the rolled-up zero-index waveguide for the different excitation wavelengths: (c) 1250 nm, (d) 1300 nm, and (e) 1450 nm.

performance i.e., $g_{12} \ll \gamma$ and $\gamma = \gamma_{12}$ as shown in Figure 4(a) and (b). Note that the emitter's decay time at the cutoff wavelength is normalized by its maximum value of approximately 10^{-5} s at normalized interatomic distance $r_{12}/\lambda_0 = 0$. The maximum value of the decay time is represented by the qubit self-interaction term γ . We also observed that $r_{12}/\lambda_0 = 0$ to $r_{12}/\lambda_0 = 1$, there is an appreciable high decay ratio γ_{12}/γ which results in a suppression of the subradiant decay state $|-\rangle$ as compared to the super-radiant $|+\rangle$ state (i.e., superradiant $\gamma + \gamma_{12}$ and subradiant

$\gamma - \gamma_{12}$ decay rates) (see Supplementary for details). Based on the coupling parameters (Figure 4(a) and (b)) and energy transfer resonance (Figure 4(e)) predicts strong long-range interaction of qubits and high persistence of entangled states in the rolled-up zero-index waveguide at the cutoff wavelength.

4.1 Measure of entanglement

Using the decay rate (γ_{12}) and the dipole-dipole interactions ($\pm g_{12}$) of the qubits inside the rolled-up

zero-index waveguide, we calculated the corresponding concurrence metric measure of entanglement (transient and steady-state) using Eqs. (S8) and (S9) (see Supplementary for details). This measure of entanglement is relevant to determine the long-range interactions of quantum emitters and their duration.

4.1.1 Transient entanglement mediated by rolled-up zero-index waveguide

Using the cutoff wavelength λ_0 and self-interactions γ as a normalization factor for both the interatomic distance r_{12} , and evolution time t , we calculated the concurrence metric of the quantum emitters as a function of normalized time

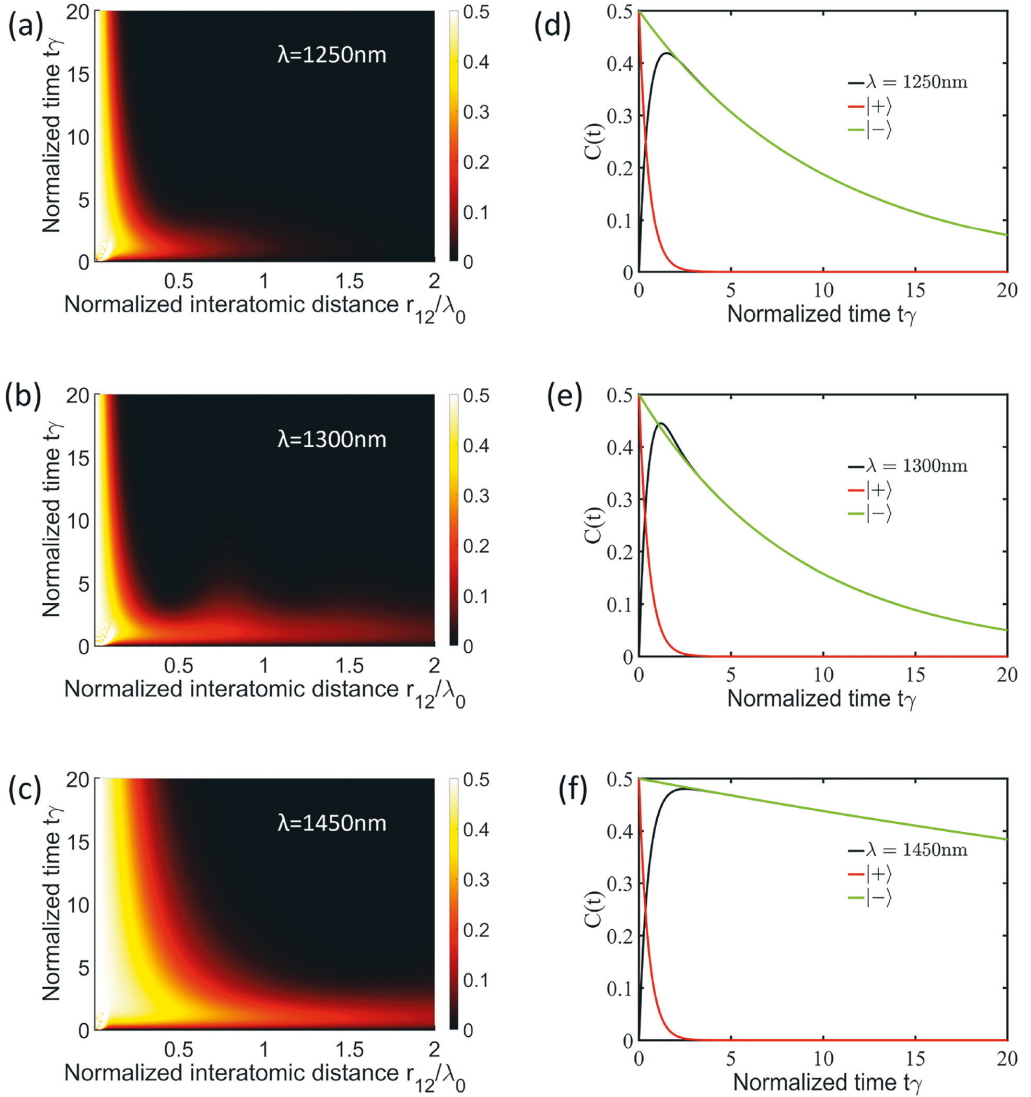


Figure 5: The measure of entanglement between qubits embedded within the rolled-up zero-index waveguide. (a)–(c) The concurrence metric heatmap for different wavelengths: (a) 1250 nm, (b) 1300 nm, and (c) 1450 nm (zero-index wavelength). (d) and (e) Similar concurrence metric plot at normalized interatomic distance ($r_{12}/\lambda_0 = 0.1$) and their corresponding symmetric $|+\rangle$ and antisymmetric $|-\rangle$ states.

γt and interatomic distance r_{12}/λ_0 at different wavelengths using Eq. (S8) (see Supplementary for details).

Figure 5(a)–(c) illustrates the measure of entangled states using the concurrence metric formalism for the different wavelengths. It is evident that the concurrence metric is higher at the cutoff wavelength as compared to the other two wavelengths. The high concurrence as a function of time and inter-emitter distance is due to the excitation of the zero-index mode of the waveguide which mediates the long-range interactions of the quantum emitters. At $\lambda = 1300$ nm, which is closer to the cutoff wavelength ($\lambda = 1450$ nm), shows a higher entanglement as compared to the concurrence for $\lambda = 1250$ nm.

The excited mode at $\lambda = 1250$ nm wavelength region has efficient entanglement at short-range but decreases monotonically as a function of inter-emitter distance due to the confined field as shown in Figure 4(c). However, at the cutoff wavelength, we obtain a large homogeneous electromagnetic field as shown in Figure 4(e). This results in a large decay rate value and small dipole-dipole interactions and thereby leads to a higher concurrence independent of the emitter position. To appreciate the latter effect, we plotted the concurrence metric at $r_{12}/\lambda_0 = 0.1$ as a function of normalized time γt for the different wavelengths, i.e., $\lambda = 1250$ nm, $\lambda = 1300$ nm, and $\lambda_0 = 1450$ nm, respectively, as shown in Figure 5(d), (e), and (f). It is clear that at the cutoff wavelength, we have high concurrence which persists for an appreciable time as compared to the other wavelengths. This effect is a consequence of the suppressed subradiant state $|-\rangle$ as compared with the high superradiant $|+\rangle$ decay channels which are superimposed on the concurrence plot in Figure 5(d)–(f). Clearly, a decrease in the population dynamics of the subradiant state $|-\rangle$ at $\lambda = 1250$ nm and $\lambda = 1300$ nm wavelengths results in a lower persistence of entanglement over time. Comparatively, the dependence of the subradiant $|-\rangle$ population of states is appreciably high at the cutoff wavelength which leads to a high concurrence state.

4.1.2 Steady-state entanglement mediated by rolled-up zero-index waveguide

Up until now, we have justified the relevance of concurrence metric key parameters (i.e., γ_{12} , $\pm g_{12}$) which can be beneficial to achieve appreciable entanglement useful for quantum information processing and communication. We have also demonstrated the concurrence as a function of normalized time and interatomic distance as well as illustrate the flexibility of emitter axial positions at the cutoff wavelength for the rolled-up

zero-index waveguide. However, this entanglement decays with time as shown in Figure 5(d)–(f). In the case of Figure 5(f), we can visualize the reduction in concurrence as a function of the gradual monotonic decay of the subradiant $|-\rangle$ population of states as compared to the sharp decay of Figure 5(d) and (e). This transient effect of entanglement between emitters embedded within a rolled-up zero-index waveguide is due to decoherence which is attributed to radiation losses and depopulation of emitters in the excited states [16]. To attain a steady entangled state $C(t \rightarrow \infty)$, it is relevant to compensate for the depopulation of the excited states by pumping the qubits with an external source. It is also interesting to note that to achieve strong steady-state entanglement between the qubits, the pump strength should not be too large; otherwise, strong interactions between the pump and the qubits as well as the pump and the zero-index channel may occur. This could eventually lead to qubit decoupling and lasing or strong resonances which may affect the decay channel of the emitter embedded within the waveguide channel [18]. In the current case, we utilized a weak pumping scenario and considered the effect of the pump on the zero-index waveguide negligible. We used pump intensities optimal to compensate for the depopulation of emitters in the excited states to enhance long-range entangled states.

We also assume a detuning parameter, $\Delta_i = \omega_0 - \omega_p = 0$, by utilizing an external source with a resonance frequency ω_p similar to the transition frequency ω_0 of the quantum emitters embedded in the rolled-up zero-index waveguide. Figure 6(a)–(c) shows the heatmap of the steady-state concurrence as a function of varied normalized Rabi frequencies Ω_1/γ for a single pump with the second pump kept constant ($\Omega_2/\gamma = 0$). We present here the steady entangled states at different interatomic distances $r_{12}/\lambda_0 = 0.5$, $r_{12}/\lambda_0 = 1.0$, and $r_{12}/\lambda_0 = 1.5$, respectively. The heatmap shows a high concurrence at $r_{12}/\lambda_0 = 0.5$ which corresponds to the high decay ratio γ_{12}/γ and minimal dipole-dipole interaction g_{12} which satisfy the aforementioned criteria for qubits entanglement. It can be seen that as the decay ratio γ_{12}/γ decreases relative to the interatomic distances r_{12}/λ_0 , the concurrence decreases. Note that the normalized interatomic distance $r_{12}/\lambda_0 = 0.5$, $r_{12}/\lambda_0 = 1.0$, and $r_{12}/\lambda_0 = 1.5$ correspond to a qubit separation of $r_{12} = 725$ nm, $r_{12} = 1450$ nm, and $r_{12} = 2175$ nm, respectively, which exceeds the resonance energy transfer of quantum emitters in vacuum.

Figure 6(d)–(f) also shows the concurrence of quantum emitters in the presence of a coherent pump source at three normalized interatomic distances $r_{12}/\lambda_0 = 0.5$, $r_{12}/\lambda_0 = 1.0$, $r_{12}/\lambda_0 = 1.5$. Similar calculations for vacuum

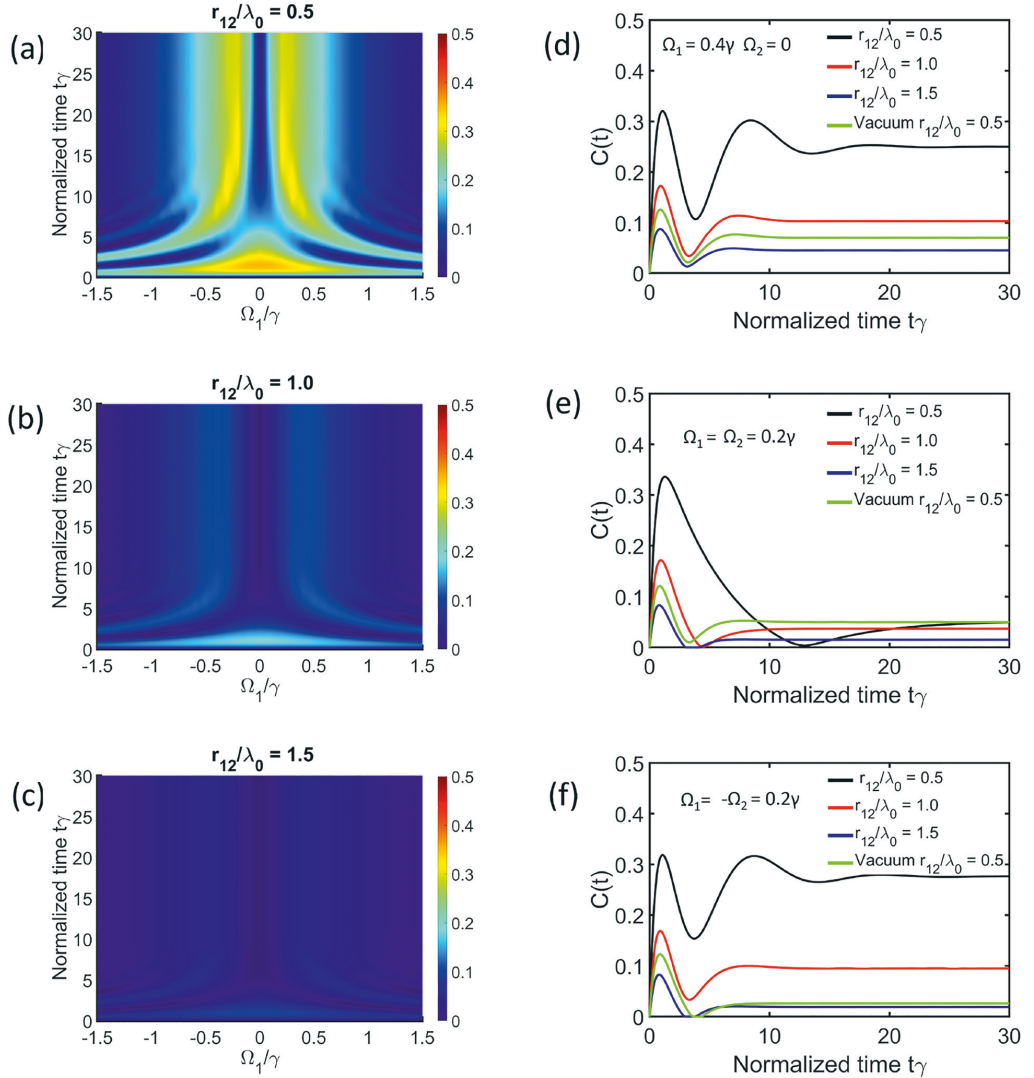


Figure 6: Persistent time dependent concurrence as a function of an external coherent source. The time dependent concurrence for different Rabi frequencies Ω_1/γ of a single pump source ($\Omega_2/\gamma = 0$) for different normalized interatomic distances (a) $r_{12}/\lambda_0 = 0.5$, (b) $r_{12}/\lambda_0 = 1.0$, and (c) $r_{12}/\lambda_0 = 1.5$. Time dependent concurrence between two quantum emitters at different normalized interatomic distances for different external pumping (d) asymmetric ($\Omega_1 = 0.4\gamma$, $\Omega_2 = 0$), (e) symmetric ($\Omega_1 = \Omega_2 = 0.2\gamma$), and (f) antisymmetric ($\Omega_1 = -\Omega_2 = 0.2\gamma$). Similar plot of the homogeneous medium is illustrated by the plot legend vacuum $r_{12}/\lambda_0 = 0.5$

reservoir ($r_{12}/\lambda_0 = 0.5$) (see Supplementary for details) are illustrated in the corresponding figures for reference purposes. We implement three types of pumps namely, asymmetric with Rabi frequencies $\Omega_1 \neq 0, \Omega_2 = 0$, symmetric with $\Omega_1 = \Omega_2$, and antisymmetric pumping with Rabi frequencies $\Omega_1 = -\Omega_2$. As expected, we obtain high

steady-state concurrence at $r_{12}/\lambda_0 = 0.5$ to $r_{12}/\lambda_0 = 1.0$, as compared to the vacuum medium. This shows that the zero-index rolled-up waveguide attains high entangled states at the cutoff wavelength and enhance long-range interactions of quantum emitters. From all the aforementioned pumping states, we see a persistent concurrence as a result of

the external source which compensates for the depopulation of the entangled states. Figure 6(d) and (f) (i.e., asymmetric and antisymmetric pumping) show quite identical steady-state concurrence with high entangled states in the proposed zero-index rolled-up waveguide at different interatomic distances r_{12}/λ_0 . In addition, the symmetric pumping criteria sustains the concurrence to normalized time $t\gamma = 15$ at $r_{12}/\lambda_0 = 0.5$. The high and persistent concurrence for the different pumping criteria (i.e., asymmetric and antisymmetric pumping) illustrates that one can achieve steady entangled states $C(t \rightarrow \infty)$ by compensating for the depopulation of the excited states through pumping of the qubits with a coherent external source (i.e., monochromatic laser source).

5 Conclusions

We have presented an alternate, more practical, and experimentally attainable rolled-up zero-index waveguide using a unique self-rolling mechanism. Based on the parameters attained experimentally, we implemented numerical methods to study the photonic properties of the rolled-up zero-index waveguide. The numerical calculations demonstrate that, at the cutoff wavelength, the rolled-up zero-index waveguide can serve as a reservoir to mediate dipole-dipole interactions and long-range entangled states. Moreover, the calculations establish that the rolled-up zero-index waveguide design will enhance resonance energy transfer and transient entanglement of qubits at the cutoff wavelength. We also demonstrate that the transient entanglement of qubits mediated by this novel rolled-up zero-index waveguide could reach its steady-state by using an external pump source. The different pumping systems compensate for the depopulation of the emitter excited states in the rolled-up zero-index waveguide. Our design and numerical calculations have established the feasibility of the rolled-up zero-index waveguide to serve as a unique reservoir for quantum entanglement. The practical realization of the proposed design is also experimentally novel and relevant to pursue in our subsequent works. We also envision that this rolled-up zero-index waveguide could overcome the practical challenges of quantum emitters integration. This will open a new avenue to explore entanglement in zero-index mediums practically, which is promising for quantum teleportation, computing, and communication.

Supporting information available

The version of the codes used to generate the transient entanglement calculations are provided here: link (i.e.,

<https://github.com/issahi62/Rolled-up-ENZ-Waveguide>) and users of this code are kindly requested to cite its use in their work. Supplementary Information (SI) includes Entanglement theory of qubits coupled with a rolled-up zero-index waveguide, Unbounded vacuum dipole-dipole coupling and decay rate, Modelling, and Fabrication. This material is available free of charge via the Internet at <http://pubs.acs.org/>.

Author contribution: All the authors have accepted responsibility for the entire content of this submitted manuscript and approved submission.

Research funding: This work was funded by H2020 European Research Council (Starting Grant project aQUARium; Agreement No. 802986), Academy of Finland Flagship Programme, (PREIN), (320165).

Conflict of interest statement: The authors declare no conflicts of interest regarding this article.

References

- [1] Y. Liu and X. Zhang, "Metamaterials: a new Frontier of science and technology," *Chem. Soc. Rev.*, vol. 40, pp. 2494–2507, 2011.
- [2] R. W. Ziolkowski and N. Engheta, *Metamaterials: Physics and Engineering Explorations*, Hoboken, NJ, John Wiley & Sons, 2006.
- [3] M. Kadic, G. W. Milton, M. van Hecke, and M. Wegener, "3D metamaterials," *Nat. Rev. Phys.*, vol. 1, pp. 198–210, 2019.
- [4] V. M. Shalaev, W. Cai, U. K. Chettiar, et al., "Negative index of refraction in optical metamaterials," *Opt. Lett.*, vol. 30, p. 3356, 2005.
- [5] C. M. Soukoulis and M. Wegener, "Past achievements and future challenges in the development of three-dimensional photonic metamaterials," *Nat. Photonics*, vol. 5, pp. 523–530, 2011.
- [6] R. Sokhoyan and H. A. Atwater, "Quantum optical properties of a dipole emitter coupled to an ϵ -near-zero nanoscale waveguide," *Opt. Express*, vol. 21, p. 32279, 2013.
- [7] J. Ren, T. Wu, and X. Zhang, "Multifrequency multi-qubit entanglement based on plasmonic hot spots," *Sci. Rep.*, vol. 5, p. 13941, 2015.
- [8] W. Ding, L. Y. Hsu, C. W. Heaps, and G. C. Schatz, "Plasmon-coupled resonance energy transfer II: exploring the peaks and dips in the electromagnetic coupling factor," *J. Phys. Chem. C*, vol. 122, pp. 22650–22659, 2018.
- [9] P. K. Jha, N. Shitrit, J. Kim, X. Ren, Y. Wang, and X. Zhang, "Metasurface-mediated quantum entanglement," *ACS Photonics*, vol. 5, pp. 971–976, 2018.
- [10] S. A. Biehs, V. M. Menon, and G. S. Agarwal, "Long-range dipole-dipole interaction and anomalous Förster energy transfer across a hyperbolic metamaterial," *Phys. Rev. B*, vol. 93, p. 245439, 2016.
- [11] R. Loudon, *The Quantum Theory of Light*, New York, Oxford University Press, 1983.

- [12] E. J. R. Vespeur, T. Coenen, H. Caglayan, N. Engheta, and A. Polman, "Experimental verification of $n=0$ structures for visible light," *Phys. Rev. Lett.*, vol. 110, p. 013902, 2013.
- [13] R. Fleury and A. Alù, "Enhanced superradiance in epsilon-near-zero plasmonic channels," *Phys. Rev. B Condens. Matter*, vol. 87, p. 201101[R], 2013.
- [14] A. Gonzalez-Tudela, D. Martín-Cano, E. Moreno, L. Martín-Moreno, C. Tejedor, and F. J. García-Vidal, "Entanglement of two qubits mediated by one-dimensional plasmonic waveguides," *Phys. Rev. Lett.*, vol. 106, p. 020501, 2011.
- [15] I. D'Amico, D. G. Angelakis, F. Bussièrès, et al., "Nanoscale quantum optics," *Riv. Nuovo Cimento*, vol. 42, pp. 153–195, 2019.
- [16] Y. Li, A. Nemilentsau, and C. Argyropoulos, "Resonance energy transfer and quantum entanglement mediated by epsilon-near-zero and other plasmonic waveguide systems," *Nanoscale*, vol. 11, pp. 14635–14647, 2019.
- [17] S. A. H. Gangaraj, A. Nemilentsau, G. W. Hanson, and S. Hughes, "Transient and steady-state entanglement mediated by three-dimensional plasmonic waveguides," *Opt. Express*, vol. 23, p. 22330, 2015.
- [18] S. A. H. Gangaraj, G. W. Hanson, and M. Antezza, "Robust entanglement with three-dimensional nonreciprocal photonic topological insulators," *Phys. Rev. A*, vol. 95, p. 063807, 2017.
- [19] M. O. Scully and M. S. Zubairy, *Quantum Optics*, New York, Cambridge University Press, 1997.
- [20] S. S. Islam, M. R. I. Faruque, and M. T. Islam, "An object-independent ENZ metamaterial-based wideband electromagnetic cloak," *Sci. Rep.*, vol. 6, p. 33624, 2016.
- [21] B. C. Yildiz and H. Caglayan, "Epsilon-near-zero media coupled with localized surface plasmon modes," *Phys. Rev. B*, vol. 102, p. 165303, 2020.
- [22] D. Martín-Cano, A. González-Tudela, L. Martín-Moreno, F. J. García-Vidal, C. Tejedor, and E. Moreno, "Dissipation-driven generation of two-qubit entanglement mediated by plasmonic waveguides," *Phys. Rev. B Condens. Matter*, vol. 84, p. 235306, 2011.
- [23] Y. Li and C. Argyropoulos, "Controlling collective spontaneous emission with plasmonic waveguides," *Opt. Express*, vol. 24, p. 26696, 2016.
- [24] D. Martín-Cano, L. Martín-Moreno, F. J. García-Vidal, and E. Moreno, "Resonance energy transfer and superradiance mediated by plasmonic nanowaveguides," *Nano Lett.*, vol. 10, pp. 3129–3134, 2010.
- [25] A. W. Snyder and J. D. Love, *Optical Waveguide Theory*, London, Chapman and Hall, 1983.
- [26] Y. Pan and S. Xu, "Energy tunnelling through an ultrasmall epsilon-near-zero channel in circular waveguide," *IET Microw., Antennas Propag.*, vol. 3, pp. 821–825, 2009.
- [27] V. Prinz, V. Seleznev, A. Gutakovskiy, et al., "Free-standing and overgrown InGaAs/GaAs nanotubes, nanohelices and their arrays," *Phys. E Low-dimens. Syst. Nanostruct.*, vol. 6, pp. 828–831, 2000.
- [28] C. Strelow, S. Kietzmänn, A. Schramm, et al., "AllnP-based rolled-up microtube resonators with colloidal nanocrystals operating in the visible spectral range," *Appl. Phys. Lett.*, vol. 101, p. 113114, 2012.
- [29] P. B. Johnson and R. W. Christy, "Optical constants of the noble metals," *Phys. Rev. B*, vol. 6, pp. 4370–4379, 1972.
- [30] E. Palik, *Handbook of Optical Constants of Solids*, Burlington, Academic Press, 1997.
- [31] R. H. Dicke, "Coherence in spontaneous radiation processes," *Phys. Rev.*, vol. 93, pp. 99–110, 1954.
- [32] E. Özgün, E. Ozbay, and H. Caglayan, "Tunable zero-index photonic crystal waveguide for two-qubit entanglement detection," *ACS Photonics*, vol. 3, pp. 2129–2133, 2016.
- [33] E. Özgün and E. Ozbay, "Epsilon-near-zero waveguides for quantum information applications: a theoretical approach for n-qubits," *J. Phys. Soc. Jpn.*, vol. 87, p. 2129, 2018.
- [34] J. Ren, T. Wu, B. Yang, and X. Zhang, "Simultaneously giant enhancement of Förster resonance energy transfer rate and efficiency based on plasmonic excitations," *Phys. Rev. B*, vol. 94, p. 125416, 2016.

Supplementary Material: The online version of this article offers supplementary material (<https://doi.org/10.1515/nanoph-2021-0453>).

PUBLICATION

IV

**Qubit-qubit entanglement mediated by epsilon-near-zero waveguide
reservoirs**

I. Issah and H. Caglayan

Applied Physics Letters **119**(22) (2021), 221103

DOI: 10.1063/5.0073134

Publication reprinted with the permission of the copyright holders

Qubit-qubit entanglement mediated by epsilon-near-zero waveguide reservoirs

Cite as: Appl. Phys. Lett. **119**, 221103 (2021); doi: [10.1063/5.0073134](https://doi.org/10.1063/5.0073134)

Submitted: 28 September 2021 · Accepted: 9 November 2021 ·

Published Online: 29 November 2021





View Online



Export Citation



CrossMark

Ibrahim Issah  and Humeyra Caglayan ^{a)} 

AFFILIATIONS

Faculty of Engineering and Natural Science, Photonics, Tampere University, 33720 Tampere, Finland

Note: This paper is part of the APL Special Collection on Zero-index Metamaterials for Classical and Quantum Light.

^{a)}Author to whom correspondence should be addressed: humeyra.caglayan@tuni.fi

ABSTRACT

This work investigates qubit entanglement in rolled-up and plasmonic rectangular epsilon-near-zero (ENZ) waveguide reservoirs. We explore the robust entanglement of qubits coupled to these reservoirs using the concurrence metric formalism and the emergence of driven steady-state entanglement under continuous pumping. The results indicate that the proposed rolled-up ENZ waveguide shows a high long-range entanglement of qubits embedded within as compared to the rectangular ENZ waveguide channel.

Published under an exclusive license by AIP Publishing. <https://doi.org/10.1063/5.0073134>

Entanglement or non-separability of qubits is relevant in quantum cryptography, quantum teleportation, and other two-qubit quantum processes.^{1–4} Entanglement, which was initially used in systems, such as optics, atoms, and ions, is becoming increasingly accessible in quantum physics.^{5,6} Short distance entanglement, in particular, has been realized for spin degrees of freedom in quantum dots, nanotubes, or molecules.^{7–9} However, long-range qubit–qubit interactions are required for long-distance information transfer. As a result, the correlation between the two qubits could be mediated by a reservoir composed of artificially engineered metamaterials that can support unique virtual bosons.

Metamaterial formations are one of the prominent engineering techniques that help to explore the classical, semi-classical, and quantum phenomena in the nanoscale. They are coined as tailoring the optical properties of a material to the desired value by designing its subwavelength nanostructures that help in attaining interesting optical phenomena.^{10,11} From its inception, numerous techniques have been implemented to study their unique optical properties.^{12–16} In particular, epsilon-near-zero (ENZ) metamaterials have been a material of interest due to their unique optical properties, such as near-zero refractive index, decoupling of electricity and magnetism, large nonlinearity effect, and infinite phase velocity.^{17,18} ENZ waveguides operating around its cutoff wavelength excites an effective zero-index mode. Typically, plasmonic waveguides excite unique extended ENZ modes at their corresponding cutoff wavelengths and can be integrated with quantum emitters to exhibit interesting atomic-field interactions. Numerical studies on rectangular ENZ reservoir^{19,20} showed that ENZ

mediums outperform the subwavelength distance limitations of qubits cooperative emission in a homogeneous medium. However, the difficulties to incorporate quantum emitters in a rectangular waveguide and their fabrication challenges in the nanoscale regime have hampered their practical use. As a result, achieving zero-index features necessitates a controlled and practical 3D manufacturing method. Rolled-up tubes have been shown to be easily fabricated using a self-rolling mechanism that could be practically utilized to incorporate emitters within.^{16,21–24} Recently, Habib *et al.*¹⁶ experimentally fabricated a cost-effective rolled-up tube composed of gold (Au) and SiO₂ using a self-rolling mechanism as compared to the rectangular ENZ waveguide with fabrication challenges.²⁵ These rolled-up waveguides have been shown to provide enhanced resonance energy transfer and good entanglement of qubits at their corresponding cutoff wavelength as compared to qubit–qubit cooperative emission in a homogeneous medium.²⁶

Here, we focus on rolled-up and rectangular ENZ waveguides serving as reservoirs to mediate qubit–qubit interactions at long distances and the emergence of driven steady-state entanglement under continuous double pumping. Based on these two experimentally proven ENZ waveguide channels, we numerically calculated their relations with quantum emitters when used as a quantum reservoir to determine the final state of a quantum system. We envisage that the different reservoirs seen by quantum emitters (qubits) will lead to different dyadic responses and, therefore, result in different long-range entanglements. Our study adopts ENZ waveguides into quantum systems, which are foreseen to generate unique optical sources, durable

entangled states, and other novel optical applications in different fields of study.

To determine the fundamental mode of the corresponding ENZ waveguide, numerical Finite Element Eigen Mode (FEEM) simulations were implemented in Ansys Lumerical software to determine the cutoff wavelength of both the rolled-up and rectangular ENZ waveguide. Figure 1 illustrates the schematics (top panel) and field distributions (lower panel) (i.e., electric $|E|$ and magnetic $|H|$ fields) of the rolled-up and the rectangular ENZ waveguide. The numerically calculated fundamental modes of the proposed quantum reservoirs exhibit TE_{11} mode for the rolled-up ENZ waveguide with the existence of both radial and axial components of the transverse fields due to its symmetry as compared to the TE_{10} mode of the rectangular ENZ waveguide transverse to its propagation direction. The dimensions of the waveguides were set and optimized to attain the same cutoff wavelength of $\lambda_0 \approx 1400$ nm. The rolled-up ENZ waveguide has a diameter (D) of 700 nm and a thickness (t) of 180 nm (i.e., 12 layers) with 5 nm of gold (Au) and 10 nm of SiO_2 . The corresponding plasmonic (Au) rectangular ENZ waveguide has a dimension of 650×350 nm² [i.e., width (L) and height (H)], respectively.

Additionally, to confirm the obtained cutoff wavelength of the ENZ waveguide channels, we simulated the radiative power of a single qubit embedded within the waveguide as a function of different dipole positions and spectral wavelengths. Figure 2 corresponds to the total average power (W) emitted from the dipole (qubits) as a function of the dipole's axial position along the rolled-up and rectangular ENZ waveguide reservoirs at different orthogonal orientations (i.e., vertically and horizontally polarized). The heatmap of the rectangular waveguide shows dipole emission power above the cutoff wavelength due to its sharp edge effects compared to the rolled-up ENZ waveguide. The results show a uniform emitted power and, hence, a

uniform decay rate enhancement along the axis of the waveguide at a cutoff wavelength of $\lambda_0 \approx 1400$ nm where the refractive index of the corresponding waveguide $n \approx 0$. This zero-index medium exhibits a uniform field amplitude along the waveguide channel and is envisioned to mediate the long-range interaction of qubits embedded within these waveguide channels.

After identifying the photonic properties of the ENZ waveguide channels, we initiated the entanglement calculations of qubits coupled with the corresponding ENZ reservoirs. Note that the measure of entanglement of qubits coupled to a reservoir^{2,6} can be described by the concurrence C metric formalism by Wootters.²⁷ To determine the concurrence C metric formalism, it is pertinent to obtain the dyadic response of an emitter coupled to the rolled-up ENZ waveguide compared to the rectangular ENZ waveguide to evaluate their respective coupling parameters.

To start with, we considered two identical qubits with the same transition frequency ω_0 embedded within the aforementioned ENZ channels. The dynamic evolution of quantum systems coupled to lossy plasmonic environments is described by the dyadic Green's function in conjunction with the quantum master equation formalism. Note that the dyadic Green's function is a classical quantity used to study the spontaneous decay of quantum emitters coupled to a quantum reservoir. The quantum master equation describes the dynamics of the density matrix ρ of a two-qubit system near a reservoir. Assuming a weak excitation and weak coupling regime, the Born–Markov, and rotating wave approximations can be used to compute the master equation, which is expressed as²⁸

$$\frac{\partial \rho}{\partial t} = \frac{1}{i\hbar} [H, \rho] - \frac{1}{2} \sum_{i,j=1}^2 \gamma_{ij} \left(\rho \sigma_i^\dagger \sigma_j + \sigma_i^\dagger \sigma_j \rho - 2 \sigma_i \rho \sigma_j^\dagger \right), \quad (1)$$

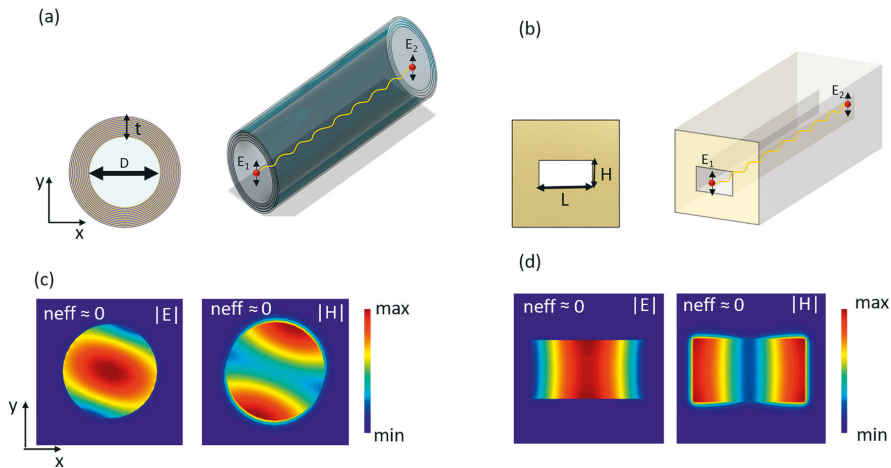


FIG. 1. Schematics of (a) rolled-up ENZ and (b) rectangular ENZ waveguide with their corresponding cross section in the x - y plane. E_1 and E_2 represent the two quantum emitters interacting with the corresponding ENZ waveguides. (c) The electric $|E|$ and magnetic $|H|$ fields of the fundamental TE_{11} mode (zero-index mode) of the rolled-up ENZ waveguide and (d) the fundamental TE_{10} mode (zero-index mode) of the rectangular ENZ waveguide.

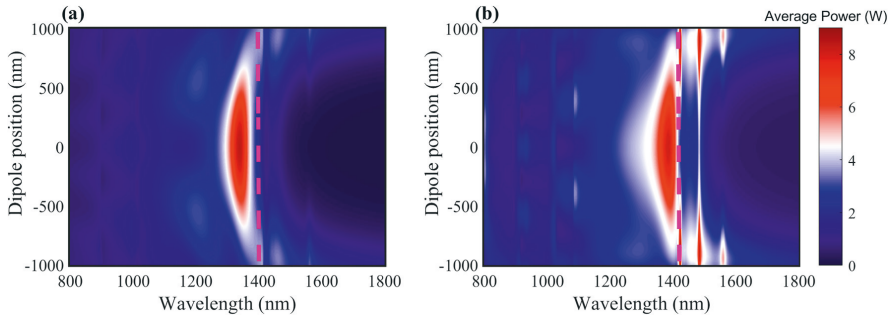


FIG. 2. Dipole emission average power (W) as a function of position along the (a) rolled-up waveguide and (b) rectangular waveguide at different spectral regions. The dash line represent the cutoff wavelength of the two ENZ waveguides.

where the Hamiltonian describing the coherent part of the evolutionary dynamics is expressed as

$$H = \sum_i \hbar(\omega_0 + g_{ii})\sigma_i^\dagger \sigma_i + \sum_{i \neq j} \hbar g_{ij} \sigma_i^\dagger \sigma_j. \quad (2)$$

From Eq. (1), ρ depicts the density matrix of the two-qubit system. $\sigma(\sigma^\dagger)$ represents the destruction (creation) operator applied to the qubits. The photonic Lamb shift g_{ii} due to the self-interaction of each qubit embedded within the ENZ waveguide is usually minimal and neglected in our formulations. g_{ij} also represents the coherent dipole-dipole interactions of the two identical qubits expressed as

$$g_{ij} = (\omega_0^2 / \epsilon_0 \hbar c^2) \text{Re} [\boldsymbol{\mu}_i^* \cdot \mathbf{G}(\mathbf{r}_i, \mathbf{r}_j, \omega_0) \cdot \boldsymbol{\mu}_j], \quad (3)$$

where the dyadic Green's tensor $\mathbf{G}(\mathbf{r}_i, \mathbf{r}_j, \omega_0)$ satisfies the classical electromagnetic equations for a point dipole source located at a position \mathbf{r}_j .

Also, γ_{ij} represents the dissipative and noncoherent term of the master equation, which is expressed as a function of the imaginary part of the dyadic Green's function:

$$\gamma_{ij} = (2\omega_0^2 / \epsilon_0 \hbar c^2) \text{Im} [\boldsymbol{\mu}_i^* \cdot \mathbf{G}(\mathbf{r}_i, \mathbf{r}_j, \omega_0) \cdot \boldsymbol{\mu}_j]. \quad (4)$$

To solve the master equation and to obtain the density matrix, a convenient basis for the two-qubit system vector space must be defined. It is easier to work in the Dicke basis, $|3\rangle = |e_1\rangle \otimes |e_2\rangle = |e_1, e_2\rangle$, $|0\rangle = |g_1\rangle \otimes |g_2\rangle = |g_1, g_2\rangle$, and $|\pm\rangle = 1/\sqrt{2}(|e_1, g_2\rangle \pm |g_1, e_2\rangle)$, when studying identical emitters in equivalent positions, i.e., $\gamma_{11} = \gamma_{22} = \gamma$, where $|e_i\rangle$ ($|g_i\rangle$) represents the excited (ground) state of the i th qubit. The basis selected is appropriate to characterize the response of the two-qubit system since it leads to a diagonalized Hamiltonian. In general, the entanglement between two qubits can be quantified by computing the concurrence C introduced by Wootters²⁷ expressed as

$$C = \max(0, \sqrt{u_1} - \sqrt{u_2} - \sqrt{u_3} - \sqrt{u_4}), \quad (5)$$

where u_i represents the eigenvalues of the matrix $\rho \tilde{\rho}$. $\tilde{\rho} = \sigma_y \otimes \sigma_y \rho^* \sigma_y \otimes \sigma_y$ is the spin-flip density matrix and σ_y is the Pauli matrix. The degree of concurrence is determined between 1

(completely entangled state) and 0 (unentangled state). However, to gain insight about the entanglement process between two emitters when only one of the emitter is excited, a transient concurrence formulation can be derived from the master equation, which is expressed as

$$C(t) = 0.5 \sqrt{[e^{-(\gamma+\gamma_{12})t} - e^{-(\gamma-\gamma_{12})t}]^2 + 4e^{-2\gamma t} \sin^2(2g_{12}t)}. \quad (6)$$

Note that the pure dephasing term γ' normally part of Eq. (6)² is considered to be relatively small compared to the radiative decay rate of qubits coupled to an ENZ structure at low temperatures.^{29,30} Thus, its contribution is insubstantial and considered as zero in our formulation. Interestingly, Vovchenko *et al.*³⁰ have recently showed that higher dephasing contributes to entanglement. Thus, dephasing is not only linked to the relaxation of the non-diagonal terms of the density matrix but can potentially lead to transitions between super- and sub-radiant states, thereby leading to entangled states. Also, from Eq. (6), $C(0) = 0$, since at $t = 0$, the quantum system is initially at an unentangled state. As time progresses, $t > 0$, the concurrence becomes larger than zero, meaning that the emitters become entangled. However, at some point, the concurrence starts to decay with time and becomes zero again, $C(t) = 0$, after a long period of time ($t \rightarrow \infty$). Thus, the system needs to be sustained by an external source to prolong the entanglement.

External pumps with the same frequency (ω_p) can, therefore, be used to pump each emitter embedded within the ENZ waveguide channels, to prevent the transient concurrence from decaying after some time and to achieve steady-state entanglement. In that case, an additional term $1/i\hbar[V, \rho]$ needs to be introduced in the right-hand side of the quantum master equation, where the operator,

$$V = - \sum_i^2 \hbar (\Omega_i e^{-i\Delta_i t} \sigma_i^\dagger + \Omega_i^* e^{i\Delta_i t} \sigma_i), \quad (7)$$

characterizes the interaction between the pump field and the emitter. The parameter $\Omega_i = \boldsymbol{\mu} \cdot \mathbf{E}_{0i} / \hbar$ is the effective Rabi frequency of the pump that depends on the induced electromagnetic field E_{0i} from the optical source pumping the i th qubit. The parameter

$\Delta_i = \omega_0 - \omega_p$ is the detuning parameter due to the pump frequency ω_p . After expressing ρ in the usual basis $|e_1, e_2\rangle, |e_1, g_2\rangle, |g_1, e_2\rangle$, and $|g_1, g_2\rangle$, one can calculate the steady-state concurrence C_{ss} by solving numerically the master equation where the Rabi frequency and detuning parameter due to the external pumping have been included.

From the above theory, we numerically compute the dyadic Green's response of a single emitter coupled to the ENZ waveguide channels. From the dyadic Green's function, we obtain the decay rate ($\gamma_{1,2}$) and dipole-dipole coupling interactions (g_{12}) of the qubit coupled to the waveguide channels. These coupling parameters (i.e., γ_{12} , g_{12}) are used in the quantum master equation to determine the evolutionary dynamics of the quantum system. Figures 3(a) and 3(b) illustrate the normalized decay rate γ_{12}/γ and the dipole-dipole interactions g_{12}/γ of qubits coupled to the rolled-up ENZ waveguide and the rectangular ENZ waveguide channels, respectively. We obtain that the decay rate of the rectangular ENZ waveguide is faster as compared to the rolled-up ENZ waveguide. It can be seen that the decay rate of the rolled-up ENZ waveguide exceeds a normalized interatomic distance r_{12}/λ_0 of 1.5 before it goes to zero as compared to the rectangular ENZ waveguide. Due to the high propagation and non-radiative losses of the rectangular waveguide as compared to the rolled-up ENZ waveguide, we see a faster decay rate $\gamma_{12}/\gamma = 0$ at normalized interatomic distance $r_{12}/\lambda_0 < 1.5$. Also, the normalized dipole-dipole interactions g_{12}/γ of the rolled-up ENZ waveguide increase appreciably above zero (0) at normalized interatomic emitter distance

$r_{12}/\lambda_0 < 0.5$ as compared to the rectangular waveguide. Both waveguide channels exhibit a monotonic decrease in the spontaneous decay rate γ_{12} and dipole-dipole coupling g_{12} as a function of normalized interatomic distance r_{12}/λ_0 .

After identifying the coupling parameters relevant for the quantum master equation, we compute the concurrence C metric measure of entanglement as a function of normalized interatomic distance r_{12}/λ_0 and normalized evolution time $t\gamma$ as shown in Figs. 3(c) and 3(d). We see relatively good transient concurrence C in both the rolled-up ENZ waveguide shown in Fig. 3(c) and the rectangular waveguide presented in Fig. 3(d). However, in both cases, we see a decrease in the concurrence as a function of time t , which depicts the depopulation of emitters in the excited state due to both radiative and non-radiative losses. Typically, electron-phonon, Ohmic loss, inherent losses of the excited ENZ mode, and propagation losses contribute to the transient nature of qubits entanglement mediated by an ENZ medium.²⁰ Also, the qubit-qubit dissipative coupling induces modified collective decay rates, i.e., superradiant $\gamma + \gamma_{12}$ and sub-radiant states $\gamma - \gamma_{12}$, which exhibits pure superradiant emission when $\gamma = \gamma_{12}$ condition is satisfied.²⁹

In order to compensate for the depopulation of the emitter excited state, we introduce an external pump into the master equation to compute the steady-state concurrence C_{ss} as well as the population dynamics of the qubits. Figure 4 shows the population dynamics of the qubits embedded within the two ENZ reservoirs at a normalized interatomic distance $r_{12}/\lambda_0 = 0.5$. Figures 4(a), 4(c), and 4(e) illustrate the

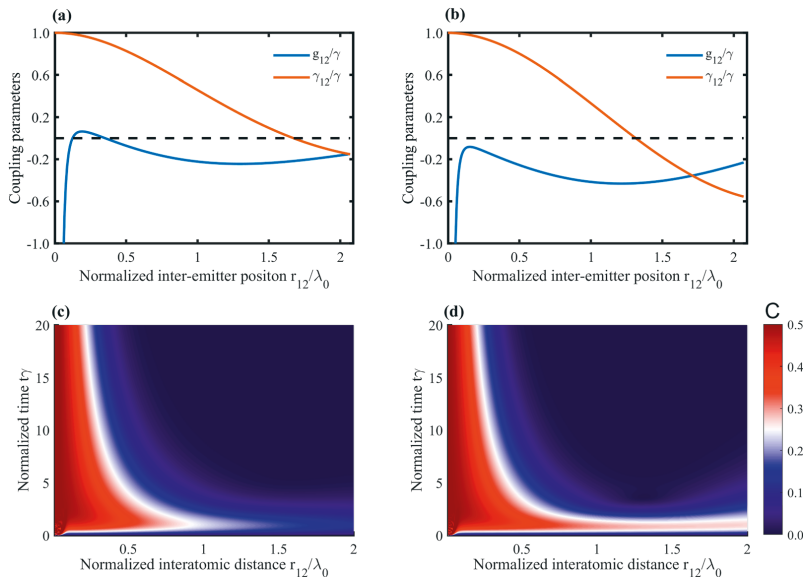


FIG. 3. Normalized decay rate enhancement γ_{12}/γ and dipole-dipole interaction g_{12}/γ as a function of normalized interatomic emitter distance r_{12}/λ_0 of (a) rolled-up ENZ waveguide and (b) rectangular waveguide. Measure of entanglement as a function of concurrence C for (c) rolled-up ENZ tube and (d) rectangular ENZ waveguide.

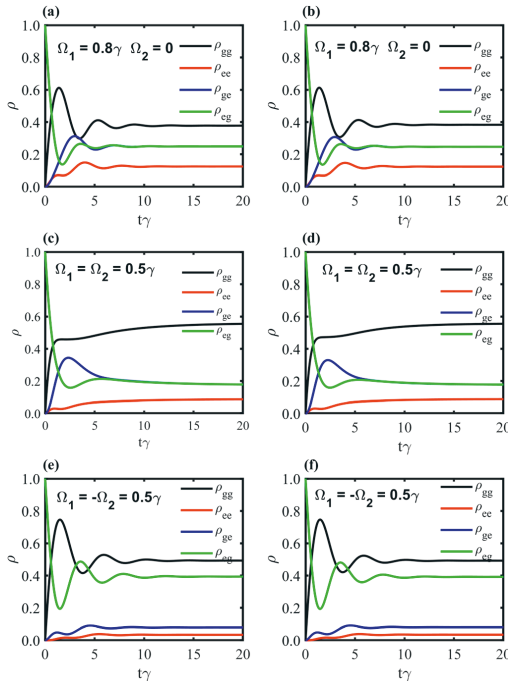


FIG. 4. Dynamics of the density matrix elements for qubits under external pumping. [(a), (c), and (e)] Population dynamics of qubits inside the rolled-up ENZ waveguide. [(b), (d), and (f)] Similar dynamics of qubits inside the plasmonic rectangular waveguide at different pump intensities.

population dynamics of qubits inside the rolled-up ENZ waveguide at different pump intensities (i.e., antisymmetric $\Omega_1 = 0.8\gamma, \Omega_2 = 0$, symmetric $\Omega_1 = \Omega_2 = 0.5\gamma$, and asymmetric $\Omega_1 = -\Omega_2 = 0.5\gamma$ pumping cases). The corresponding Figs. 4(b), 4(d), and 4(f) show similar dynamics for qubits embedded within a plasmonic rectangular waveguide reservoir.

We present here four density matrix elements $\rho_{gg}, \rho_{ee}, \rho_{ge}$, and ρ_{eg} , which represent the probability of both qubits to be in the ground state, both qubits being in the excited state, the first qubit being in the ground state, and the second being in the excited state, and vice versa. Furthermore, we assumed an initial state $\rho_{eg} = 1$. It can be seen that the qubits embedded within the ENZ reservoirs show different population dynamics for different external pumping cases. The symmetric pumping case depicts a similar population steady-state $\rho_{eg} = \rho_{ge}$ due to the identical pumping of the quantum system. The antisymmetric and asymmetric pumping density elements grow appreciably at normalized time $t\gamma < 5$ and decays to a constant probability at normalized time $t\gamma > 5$. Yet, we obtained a weak population state in the symmetric pumping case, for both rolled-up ENZ waveguide and plasmonic ENZ reservoir,

as shown in Figs. 4(c) and 4(d), respectively. At a high antisymmetric pumping case, we obtain an appreciable high probability of both qubits being in the excited state ρ_{ee} as compared to the other two coherent pump cases.

The high probability signifies the effect of strong pumping on the dynamics of emitters coupled to a reservoir and how it affects entanglement between two qubits. It is evident that under strong pumping, the dynamics of qubits are defined by the external pumps and not only by the dipole-dipole interactions, thereby affecting the entanglement of qubits in such vicinity. In the asymmetric pump case, we see a high population state $\rho_{eg} > \rho_{ge}$ of the first qubit since the pump intensity for the second qubit is negated. The aforementioned dynamics of the different pump scenarios show the effect of pump intensities on emitters' interactions and how high coherent pump intensities could potentially affect the entanglement property of qubits embedded within an ENZ reservoir with similar behavior observed with incoherent pumping.^{31,32}

Figure 5 also illustrates the heatmaps of steady-state concurrence C_{ss} at normalized evolution time $t\gamma = 90$ as a function of two normalized pump intensities (i.e., $\Omega_1/\gamma, \Omega_2/\gamma$) at different normalized interatomic distances r_{12}/λ_0 . It is evident that the steady-state concurrence of the rolled-up ENZ waveguide [in the top panel of Figs. 5(a)–5(c)] shows a high measure of entanglement [$\max(C_{ss}) \approx 0.32$] as compared to the rectangular ENZ waveguide [$\max(C_{ss}) \approx 0.2$] shown in the lower panel [i.e., (d)–(f)] at $r_{12}/\lambda_0 = 0.5$. Similar results are presented for different normalized interatomic distances $r_{12}/\lambda_0 = 1.0$ and $r_{12}/\lambda_0 = 1.5$, respectively. The high entanglement in the rolled-up ENZ waveguide depicts its relevance to serve as a reservoir to mediate qubit entanglement as compared to the rectangular ENZ waveguide. Note that the high steady-state concurrence of the proposed ENZ waveguide channels is as a result of the large values of γ_{12} and small values of g_{12} . Also, the pump strength should not be too high to achieve strong steady-state entanglement between the qubits; otherwise, strong interactions between the pump and the qubits as well as the reservoir will occur, eventually leading to qubits decoupling and lasing.

To conclude, we have shown the long-range quantum entanglement between a pair of qubits mediated by a rolled-up ENZ waveguide, which persists over extended periods and long distances. The response is compared to the corresponding plasmonic rectangular ENZ waveguide. The theory of both transient and steady-state quantum entanglement, quantified by computing the concurrence metric, is briefly introduced and utilized to determine the robust entanglement of qubits coupled to the ENZ waveguide channel. This concurrence metric formalism has a direct link with the cross term second-order coherence function that can be extracted from an experiment [i.e., Hanbury Brown and Twiss (HBT) effect or two-photon detection probability P_{RR} measurement].^{20,29,33} We also showed ways to improve the entanglement of qubits coupled to the proposed reservoirs. We obtain that the rolled-up ENZ waveguide system demonstrates an improved quantum optical and long-range entanglement performance with $\max(C_{ss}) \approx 0.32$ compared to the rectangular ENZ waveguide channel. This study could open new avenues to explore entanglement for quantum network applications, quantum information processing, cryptography, and the development of ultra-sensitive subwavelength metrology devices.

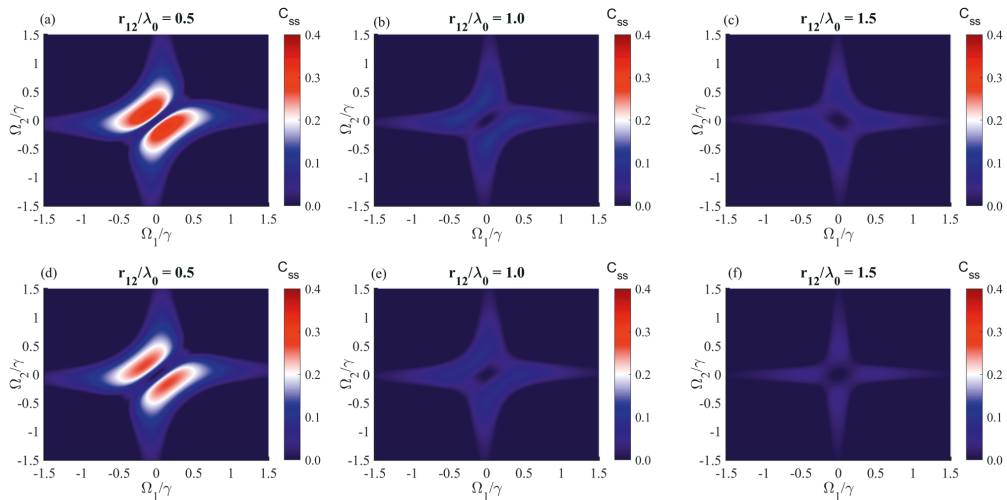


FIG. 5. Two pumps steady-state entanglement at different interatomic distance r_{12}/λ_0 for (top panel) rolled-up ENZ waveguide and (bottom panel) rectangular waveguide.

The authors acknowledge the financial support of the European Research Council (Starting Grant project aQUARiUM; Agreement No. 802986) and Academy of Finland Flagship Programme (PREIN) (No. 320165).

AUTHOR DECLARATIONS

Conflict of Interest

The authors have no conflicts of interest to disclose.

DATA AVAILABILITY

The data that support the findings of this study are available from the corresponding author upon reasonable request. The codes used for this study are openly available in GitHub at <https://github.com/issahi62/Rolled-up-ENZ-Waveguide>, Ref. 34.

REFERENCES

- M. O. Scully and M. S. Zubairy, *Quantum Optics* (Cambridge University Press, 1997).
- S. A. H. Gangaraj, A. Nemilentsau, G. W. Hanson, and S. Hughes, "Transient and steady-state entanglement mediated by three-dimensional plasmonic waveguides," *Opt. Express* **23**, 22330 (2015).
- S. A. H. Gangaraj, G. W. Hanson, and M. Antezza, "Robust entanglement with three-dimensional nonreciprocal photonic topological insulators," *Phys. Rev. A* **95**, 063807 (2017).
- P. Kok, "Principles of quantum computation and information volume II," *J. Phys. A* **40**, 12256 (2007).
- Y. Hao and G.-L. Long, "Quantum information and quantum computing," *Fundam. Res.* **1**, 2 (2021).
- A. Gonzalez-Tudela, D. Martin-Cano, E. Moreno, L. Martin-Moreno, C. Tejedor, and F. J. Garcia-Vidal, "Entanglement of two qubits mediated by one-dimensional plasmonic waveguides," *Phys. Rev. Lett.* **106**, 020501 (2011).
- Y. Makhlin, G. Schön, and A. Shnirman, "Quantum-state engineering with Josephson-junction devices," *Rev. Mod. Phys.* **73**, 357 (2001).
- R. Hanson, L. P. Kouwenhoven, J. R. Petta, S. Tarucha, and L. M. Vandersypen, "Spins in few-electron quantum dots," *Rev. Mod. Phys.* **79**, 1217 (2007).
- B. Lienhard, T. Schröder, S. Mouradian, F. Dolde, T. T. Tran, I. Aharonovich, and D. Englund, "Bright and photostable single-photon emitter in silicon carbide," *Optica* **3**, 768 (2016).
- Y. Liu and X. Zhang, "Metamaterials: A new frontier of science and technology," *Chem. Soc. Rev.* **40**, 2494–2507 (2011).
- Y. Li and C. Argyropoulos, "Controlling collective spontaneous emission with plasmonic waveguides," *Opt. Express* **24**, 26696 (2016).
- M. A. Noginov, H. Li, Y. A. Barnakov, D. Dryden, G. Nataraj, G. Zhu, C. E. Bonner, M. Mayy, Z. Jacob, and E. E. Narimanov, "Controlling spontaneous emission with metamaterials," *Opt. Lett.* **35**, 1863 (2010).
- T. Tumkur, G. Zhu, P. Black, Y. A. Barnakov, C. E. Bonner, and M. A. Noginov, "Control of spontaneous emission in a volume of functionalized hyperbolic metamaterial," *Appl. Phys. Lett.* **99**, 151115 (2011).
- J. Kerbst, S. Schwaiger, A. Rottler, A. Koitmäe, M. Brill, J. Ehlmann, A. Stemmann, C. Heyn, D. Heitmann, and S. Mendach, "Enhanced transmission in rolled-up hyperlenses utilizing Fabry-Pérot resonances," *Appl. Phys. Lett.* **99**, 191905 (2011).
- D. R. Smith, D. C. Vier, T. Koschny, and C. M. Soukoulis, "Electromagnetic parameter retrieval from inhomogeneous metamaterials," *Phys. Rev. E* **71**, 036617 (2005).
- M. Habib, I. Issah, D. Briukhanova, A. R. Rashed, and H. Caglayan, "Wavefront control with nanohole array-based out-of-plane metasurfaces," *ACS Appl. Nano Mater.* **4**, 8699 (2021).
- E. J. Smith, Z. Liu, Y. Mei, and O. G. Schmidt, "Combined surface plasmon and classical waveguiding through metamaterial fiber design," *Nano Lett.* **10**, 1–5 (2010).
- B. Edwards, A. Alù, M. E. Young, M. Silveirinha, and N. Engheta, "Experimental verification of epsilon-near-zero metamaterial coupling and energy squeezing using a microwave waveguide," *Phys. Rev. Lett.* **100**, 033903 (2008).
- R. Sokhoyan and H. A. Atwater, "Quantum optical properties of a dipole emitter coupled to an ϵ -near-zero nanoscale waveguide," *Opt. Express* **21**, 32279–32290 (2013).

- ²⁰Y. Li, A. Nemilentsau, and C. Argyropoulos, "Resonance energy transfer and quantum entanglement mediated by epsilon-near-zero and other plasmonic waveguide systems," *Nanoscale* **11**, 14635–14647 (2019).
- ²¹S. M. Harazim, W. Xi, C. K. Schmidt, S. Sanchez, and O. G. Schmidt, "Fabrication and applications of large arrays of multifunctional rolled-up SiO/SiO₂ microtubes," *J. Mater. Chem.* **22**, 2878–2884 (2012).
- ²²E. Bermúdez-Ureña and U. Steiner, "Self-rolled multilayer metasurfaces," *ACS Photonics* **6**, 2198–2204 (2019).
- ²³V. Y. Prinz, E. V. Naumova, S. V. Golod, V. A. Seleznev, A. A. Bocharov, and V. V. Kubarev, "Terahertz metamaterials and systems based on rolled-up 3D elements: Designs, technological approaches, and properties," *Sci. Rep.* **7**, 43334 (2017).
- ²⁴D. Briukhanova, M. Habib, I. Issah, and H. Caglayan, "Low loss fishnet metamaterial via self-rolled nanotechnology," *Appl. Phys. Lett.* **119**, 141101 (2021).
- ²⁵E. J. R. Vesseur, T. Coenen, H. Caglayan, N. Engheta, and A. Polman, "Experimental verification of $n=0$ structures for visible light," *Phys. Rev. Lett.* **110**, 013902 (2013).
- ²⁶I. Issah, M. Habib, and H. Caglayan, "Long-range qubit entanglement via rolled-up zero-index waveguide," *Nanophotonics* **2021**, 1.
- ²⁷W. K. Wootters, "Entanglement of formation of an arbitrary state of two qubits," *Phys. Rev. Lett.* **80**, 2245–2248 (1998).
- ²⁸H. T. Dung, L. Knöll, and D.-G. Welsch, "Resonant dipole-dipole interaction in the presence of dispersing and absorbing surroundings," *Phys. Rev. A* **66**, 063810 (2002).
- ²⁹D. Martín-Cano, A. González-Tudela, L. Martín-Moreno, F. J. García-Vidal, C. Tejedor, and E. Moreno, "Dissipation-driven generation of two-qubit entanglement mediated by plasmonic waveguides," *Phys. Rev. B* **84**, 235306 (2011).
- ³⁰I. V. Vovchenko, V. Y. Shishkov, and E. S. Andrianov, "Dephasing-assisted entanglement in a system of strongly coupled qubits," *Opt. Express* **29**, 9685–9698 (2021).
- ³¹E. del Valle, "Strong and weak coupling of two coupled qubits," *Phys. Rev. A* **81**, 053811 (2010).
- ³²C. A. Downing, J. C. L. Carreño, A. I. Fernández-Domínguez, and E. del Valle, "Asymmetric coupling between two quantum emitters," *Phys. Rev. A* **102**, 013723 (2020).
- ³³E. Özgün, E. Ozbay, and H. Caglayan, "Tunable zero-index photonic crystal waveguide for two-qubit entanglement detection," *ACS Photonics* **3**, 2129–2133 (2016).
- ³⁴Metaplasmonics group/aQUARIUM-ERC STG Project (2021). "Rolled-up ENZ waveguide" GitHub. <https://github.com/issahi62/Rolled-up-ENZ-Waveguide>

PUBLICATION

V





Epsilon-near-zero nanoparticles

I. Issah, J. Pietila, T. Kujala, M. Koivurova, H. Caglayan and M. Ornigotti

Phys. Rev. A 107(2023), 023501

DOI: 10.1103/PhysRevA.107.023501

Publication reprinted with the permission of the copyright holders

Epsilon-near-zero nanoparticlesIbrahim Issah , Jesse Pietila , and Tommi Kujala *Faculty of Engineering and Natural Sciences, Tampere University, 33720 Tampere, Finland*Matias Koivurova *Tampere Institute for Advanced Study, Tampere University, 33100 Tampere, Finland
and Faculty of Engineering and Natural Sciences, Tampere University, 33720 Tampere, Finland*Humeyra Caglayan * and Marco Ornigotti †*Faculty of Engineering and Natural Sciences, Tampere University, 33720 Tampere, Finland* (Received 9 August 2022; revised 4 November 2022; accepted 12 January 2023; published 1 February 2023)

In this work we propose epsilon-near-zero (ENZ) nanoparticles formed of metal and dielectric bilayers and employ the effective-medium approach for multilayered nanospheres to study their optical response. We obtain a passive tunable ENZ region by varying the radii of the proposed bilayer nanospheres, ranging from visible to near IR. In addition, we present the absorption and scattering cross section of ENZ nanoparticles using open-source transfer-matrix-based software (STRATIFY). The proposed ENZ nanoparticle is envisioned to be experimentally realized using chemical synthesis techniques.

DOI: 10.1103/PhysRevA.107.023501

I. INTRODUCTION

Epsilon-near-zero (ENZ) materials exhibit a dielectric permittivity approaching zero at a frequency close to the material's plasma frequency [1,2]. Transparent conductive oxides such as indium tin oxide are naturally occurring ENZ materials with ENZ wavelengths in near-infrared and midinfrared regions [3]. A metamaterial composed of alternating layers of metal and a dielectric was also demonstrated to exhibit ENZ properties in the visible region [4,5].

Notably, ENZ materials studied by many authors consist of nanostructures or meta-atoms, which require fabrication techniques such as focused ion beam milling, laser ablation, atomic layer deposition, and electron-beam lithography [6,7]. On the other hand, the synthesis of nanoparticles and their incorporation into materials are among the most studied topics in chemistry, physics, and material science. Furthermore, it has been demonstrated that localized surface plasmon resonance (LSPR) depends on the size, shape, and material of the nanoparticles. For example, small Au nanoparticles (between 5 and 10 nm) have the LSPR band around 520 nm, while for bigger particles (between 50 and 100 nm), this peak is redshifted up to 570 nm. Other materials such as transparent conductive oxides, transition metal nitrides [8], organic conductive materials [9], and highly doped semiconductors have also been identified to exhibit plasmonic behavior at

different spectral regions. In addition, nanoparticles composed of a metal-dielectric complex have been shown to exhibit interesting light-matter interactions with many vital applications in physics and chemistry, such as scattering [10,11] and nonlinear optics [12,13], sensing [14,15], fluorescence [16,17], and up-conversion enhancement [18], surface plasmon amplification [19,20], hydrogen generation [21], and solar energy harvesting [22,23].

Although planar films made of similar materials have been investigated as an ENZ medium for many applications, nanoparticles have not been considered ENZ materials. We envision that the ENZ nanoparticles could provide a new design solution for low-cost tunable ENZ materials, which have wide prospects for application in photonics.

In this work we propose the possibility of the utilization of nanoparticles as ENZ materials. To verify this approach, we employ the effective-medium approach to model the optical response of a multilayer sphere as an effective bulk spherical medium. In particular, by varying the structural properties of the nanospheres, we show how the ENZ character of such multilayered nanoparticles can be easily tuned from the visible to the near-IR region of the electromagnetic spectrum.

II. STRUCTURE DESIGN AND MODELING

The ENZ nanoparticles we consider in this work are bilayer structures consisting of an inner dielectric core, for which we employ SiO₂, and an outer metallic shell, as shown schematically in Fig. 1. Due to the high carrier concentration, electron mobility, and strong electromagnetic-field confinement property of noble metals [24], we choose silver for the outer shell.

To analyze the absorption and scattering of the aforementioned ENZ nanoparticles, we use a transfer-matrix approach (based on the open-source STRATIFY code [25]). As a sanity check, we also implement the optical response (i.e., scattering

*humeyra.caglayan@tuni.fi

†marco.ornigotti@tuni.fi

Published by the American Physical Society under the terms of the Creative Commons Attribution 4.0 International license. Further distribution of this work must maintain attribution to the author(s) and the published article's title, journal citation, and DOI.

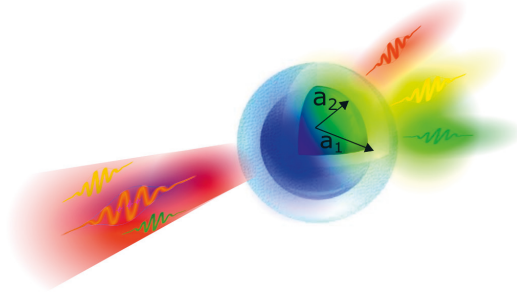


FIG. 1. Schematic representation of the bilayer spherical nanoparticles. Here a_2 and a_1 represent the inner and outer radii of the sphere. The inner, dark blue, sphere represents the dielectric core (SiO_2) of the nanoparticle, while the outer, light blue, shell represents the silver coating.

and absorption) for different materials and identify that the Ag- SiO_2 bilayer structure gives us the required ENZ region of interest (i.e., visible to near IR). First, we focus on the effective ENZ optical responses of a bilayer spherical nanoparticle embedded within a host medium (i.e., air) and later extend the effective permittivity approach to multilayer nanosphere composites.

The wavelength-dependent complex dielectric functions for Ag and SiO_2 are taken from the material data of Johnson and Christy [26]. The scattering, absorption, and electromagnetic near-field distribution are calculated using STRATIFY (i.e., recursive transfer-matrix method MATLAB code).

III. THEORY

In this section we briefly present the theoretical background needed to derive the effective permittivity of the bilayer spherical nanoparticle. Our approach makes use of an effective description of the electric permittivity of a metal-dielectric layered nanoparticle, following the methods presented in Ref. [27]. Although there are many different analytical methods available in the literature to describe the interaction of electromagnetic waves with layered media, such as dyadic Green's functions [28] or vector spherical harmonics decomposition in layered media [29], we choose to use the effective-medium approximation for its unique ability to assign a single effective permittivity to the multilayered nanoparticles. This method has been successfully applied in the past to effectively describe the properties of hyperbolic metamaterials [30,31] in an easy-to-engineer manner. Inspired by this, we decided to use the effective-medium approximation to provide easy-to-engineer ENZ properties of layered nanoparticles. To start with, we assume that a bilayer (and, by simple generalization, a multilayer) nanoparticle can be seen as a composite material, where the outer layer (the shell) plays the role of the host medium, whereas the inner layer (the core) is the inclusion. This assumption allows us to use the theory of effective media to simplify the complex problem of a multilayered spherical nanoparticle, reducing it to the simpler one of a single homogeneous spherical nanoparticle, described via an effective permittivity.

For the case of a metal-dielectric nanoparticle like the one depicted in Fig. 1, for example, this can be easily done using standard methods of electrostatics, i.e., by placing the nanoparticle in a homogeneous electric field and solving the Laplace equation for the electrostatic potential in the whole space [32]. By using this procedure, one can easily show that the electric field generated by the bilayered sphere in the host medium (air, in the case of Fig. 1) is the same as that of a single sphere with radius a_1 and permittivity

$$\tilde{\epsilon}_1 = \frac{1 - 2G}{1 + G} \epsilon_1, \quad (1)$$

with

$$G = \frac{\epsilon_1 - \epsilon_2}{2\epsilon_1 + \epsilon_2} \left(\frac{a_2}{a_1} \right)^3, \quad (2)$$

with ϵ_1 the permittivity of the shell, ϵ_2 the permittivity of the core, and a_2 the radius of the inner sphere.

The above theory can then be generalized for multilayered structures by expressing the multilayered permittivities by simply applying Eq. (1) recursively to each couple of layers, from the outer to the inner one [27], thus obtaining, for the general k th layer,

$$\tilde{\epsilon}_k = \frac{1 - 2G_k}{1 + G_k} \epsilon_k, \quad (3)$$

with

$$G_k = \frac{\epsilon_k - \tilde{\epsilon}_{k+1}}{2\epsilon_k + \tilde{\epsilon}_{k+1}} \left(\frac{a_{k+1}}{a_k} \right)^3. \quad (4)$$

Here the layers are numbered from outside to inside so that $k = 1$ represents the outer layer and $k = N$ represents the inner one. The permittivity for each layer $k = \{N - 1, N - 2, \dots, 2, 1\}$ is expressed using the above equations.

IV. RESULTS AND DISCUSSION

From the above theory, we determined the effective permittivity for the proposed spherical bilayer structure to obtain the ENZ points as a function of the varied core diameters with outer layer thicknesses fixed at 2 nm. Figure 2 shows the effective permittivities for the different ENZ nanoparticles with different core diameters (i.e., $a_{2,1} = \{38, 40\}$, $a_{2,1} = \{68, 70\}$, and $a_{2,1} = \{98, 100\}$ nm). Here $a_{2,1}$ represents the radii of the inner and outer shells, respectively. We obtained different ENZ points by changing the radii of the bilayer nanospheres.

In particular, for $a_{2,1} = \{38, 40\}$ nm [Fig. 2(a)], the ENZ wavelength is found to be $\lambda_{\text{ENZ}} \approx 659$ nm. Similarly, by changing the inner and outer radii of the ENZ nanoparticle, we observe a redshift of the ENZ wavelength to $\lambda_{\text{ENZ}} \approx 852$ nm [Fig. 2(b)] and $\lambda_{\text{ENZ}} \approx 1010$ nm [Fig. 2(c)], respectively. This is the first main result of our work which extends to the numerical calculations of the nanosphere's near-field enhancement, absorption, and scattering cross sections as well as exploiting the possibility of using the effective-medium formulations of bilayer nanospheres into multilayer ENZ nanoparticles.

Ag- SiO_2 nanoparticles clearly show ENZ behavior in the visible and near-IR spectral regimes. The position of the ENZ wavelength of such nanoparticles can be easily controlled by suitably tuning the inner core of the nanoparticle. In our

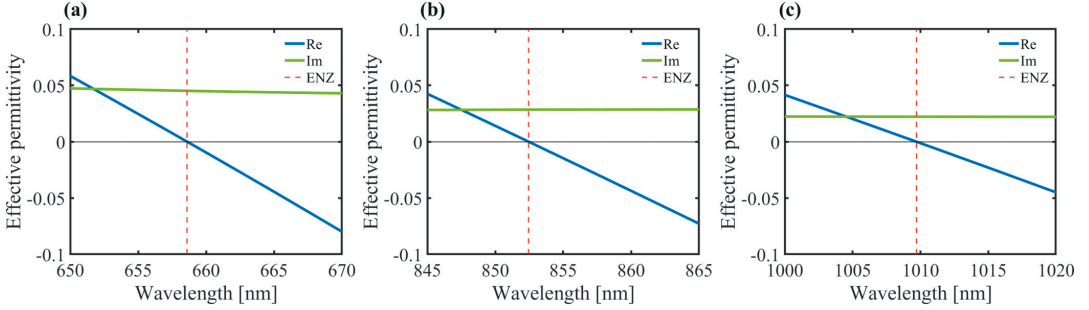


FIG. 2. Effective permittivities of different bilayer spheres near their characteristic ENZ wavelengths (a) $a_{2,1} = \{38, 40\}$, (b) $a_{2,1} = \{68, 70\}$, and (c) $a_{2,1} = \{98, 100\}$ nm. Here Re and Im represent the real and imaginary parts of effective permittivity, respectively. Their corresponding ENZ wavelengths are marked with red dashed lines.

simulations, it was found that the outer radius of the Ag-SiO₂ nanoparticle should fulfill $a_1 \leq \lambda_{\text{ENZ}}/10$. This is compatible with the implicit assumption, used to derive our effective model, that the wavelength of the electric field should be much larger than any length scale in the system, to guarantee that the effective-medium approach remains valid (i.e., it makes sense to use the Laplace equation for the electrostatic potential near a multilayered sphere to calculate the effective permittivity of such structures).

In addition, it was identified that one should consider the parametric variations of the inner core and outer shell of the nanoparticles, as huge thickness variations between the two layers could affect the bilayer nanoparticle from exhibiting ENZ properties. This is due to the bilayer nanoparticle exhibiting properties of the outer shell instead of the complex media. As such, it is relevant to choose the right fill fraction of the nanoparticle to attain the required ENZ properties.

To verify the reliability of the effective-medium approach described above, we compare the electromagnetic-field distribution of the proposed effective-medium theory and the bilayer structure. As can be seen from Fig. 3, the electric-field distributions outside the nanoparticle, calculated using STRATIFY, for both the case of a bilayer structure [Fig. 3(a)] and a bulk sphere with effective permittivity ϵ_{eff} [Fig. 3(b)]

at the ENZ wavelength, give relatively similar results, as can be seen from Fig. 3(c). The origin of this discrepancy can be traced back to the presence, in the actual bilayer structures, of surface waves, due to the external metallic coating, which locally modifies the electric field of the nanoparticle, making its near field different from the case of the effective medium. From this perspective, therefore, the fact that we observe, as reported in Fig. 3(c), the difference in the very vicinity of the surface of the nanoparticle is quite small, which is somehow expected, and does not jeopardize the validity of the effective-medium approach. This effect has been observed in similar situations, in planar metal-dielectric-based metamaterials [33]. Moreover, we also identified that a bilayer metal-dielectric structure is sufficient to obtain the desired ENZ properties. As a result, we focused on the particle with radii $a_{2,1} = \{98, 100\}$ nm, which can produce Rayleigh scattering since the particle size is smaller than the wavelength of the impinging electromagnetic field. Although a full numerical optimization could be performed, we only considered the ENZ nanoparticle with radii $a_{2,1} = \{98, 100\}$ nm, as it shows the capabilities of our approach shown in Fig. 3 and corresponds to experimentally plausible nanoparticles [34].

In addition, we numerically calculated the fundamental extinction cross sections and the ENZ-dependent parametric

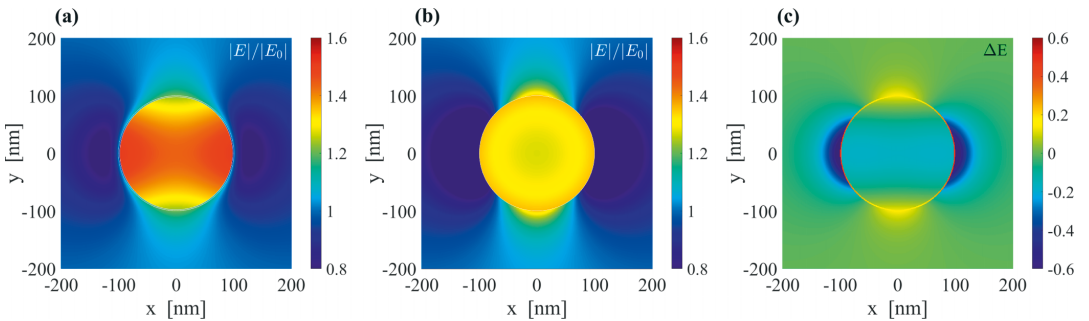


FIG. 3. Electric field for the bilayer structure, $a_{2,1} = \{98, 100\}$ nm at the ENZ wavelength. (a) Actual bilayer structure. (b) Bulk effective-medium structure. (c) Difference of the normalized near-field distribution between (b) and (a). As can be seen from (c), the two simulations are in good agreement with each other in general and they differ only in the vicinity of the surface.

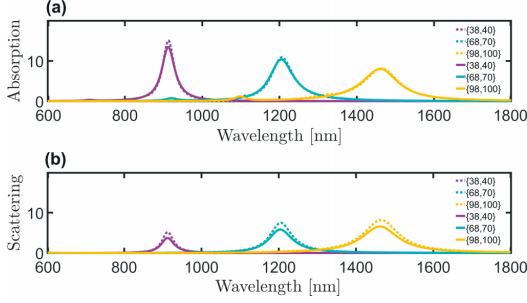


FIG. 4. (a) Absorption and (b) scattering cross sections for the bilayered spherical nanoparticles with full permittivity (solid lines) and effective permittivity (dashed lines) for radii $a_{2,1} = \{38, 40\}$ nm, $a_{2,1} = \{68, 70\}$ nm, and $a_{2,1} = \{98, 100\}$ nm. The values in the legend represent the radius values of the inner and outer spherical layers.

sweep for different layers of the ENZ nanoparticle in the case of a plane wave incident on it using full permittivity (without any effective-medium approximation) and the effective permittivity, coming from the effective-medium formulation. Figures 4(a) and 4(b) show the calculated absorption and scattering cross sections for three different ENZ nanoparticles using STRATIFY, i.e., $a_{2,1} = \{38, 40\}$ nm (purple), $a_{2,1} = \{68, 70\}$ nm (cyan), and $a_{2,1} = \{98, 100\}$ nm (orange), with absorption and scattering peak resonances at $\lambda \approx 913$, 1206, and 1466 nm, respectively. The maximum extinction resonance wavelengths for the proposed ENZ nanoparticles are redshifted compared to their characteristic ENZ wavelengths, which are presented in Table I. This is due to the resonant excitation of dipole surface plasmons on the ENZ nanoparticle. We note in fact that the obtained resonance enhancement for both scattering and absorption cross sections occurs when the condition $\epsilon_{\text{eff}} \approx -2$ (the so-called Fröhlich condition) for spherical nanoparticles is satisfied [35]. The absorption and scattering for the ENZ nanoparticle $a_{2,1} = \{98, 100\}$ nm have appreciably similar peak values. However, for the ENZ nanoparticle $a_{2,1} = \{38, 40\}$ nm and $a_{2,1} = \{68, 70\}$ nm, we obtain relatively low scattering peak values compared to its corresponding absorption cross-section peak values. It is also interesting to note that by changing the filling ratio of the ENZ nanoparticle, a passive tuning of the λ_{ENZ} can be observed, which corroborates the shift in the nanoparticle's peak absorbance and scattering cross sections. Intuitively, the redshift of the peak in the dipole resonance with increasing size could be linked to the weakening of their restoring force. Since the distance between charges on opposite sides of the ENZ

TABLE I. The ENZ nanoparticles with their characteristic ENZ wavelengths as well as their corresponding resonance wavelengths.

Nanoparticle size (nm)	λ_{ENZ} (nm)	$\lambda_{\text{resonance}}$ (nm)
{38, 40}	659	913
{68, 70}	852	1206
{98, 100}	1010	1466

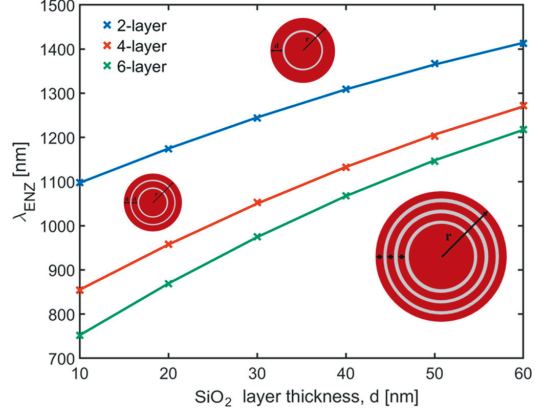


FIG. 5. The ENZ wavelengths calculated for three different structures of a set of SiO_2 layers, with varying thicknesses d . The SiO_2 inner core and the Ag layers in between are fixed with a radius of $a_2 = \{98\}$ nm and a thickness of 2 nm. The compositions of the multilayered nanospheres are schematically presented with red (SiO_2) and gray (Ag) circular layers, next to the relevant λ_{ENZ} plots, corresponding to two (blue), four (red), and six layers (green), with thickness d values ranging from 10 to 60 nm.

nanoparticle increases with size, in fact, their corresponding interaction decreases.

In addition to the absorption and scattering cross section of the ENZ nanoparticles, we numerically calculated the ENZ wavelengths for different layered nanoparticles by parametrically varying the thickness of SiO_2 overlaid on the outer Ag shell. The SiO_2 inner core and the Ag layers in between are fixed with a radius of $a_2 = \{98\}$ nm and a thickness of 2 nm. It is evident in Fig. 5 that by changing the thicknesses of the embedded SiO_2 layers, we attain different ENZ wavelengths for the other multilayered nanoparticles. For all the considered nanostructures, we see a linear trend that depicts that by varying the thicknesses of the SiO_2 layers, there is a corresponding shift in λ_{ENZ} for different layered structures. This signifies the possibility of extending the effective-medium formulation of the bilayered structure into multilayered nanoparticles.

V. CONCLUSION

Our work showed that effective-medium theory is potentially applicable to bilayer spherical nanoparticles to determine their unique spectral responses and ENZ properties. By changing the diameter of the ENZ nanoparticle, we identified a spectral shift in the spectral absorbance and scattering cross sections of the ENZ nanoparticle, which signifies a passive tuning of the proposed structure. As shown in subsequent discussion, the effective permittivity formulation works relatively well for bilayer structures and could be easily extended to multilayered structures. Although in this work we have only considered Ag- SiO_2 nanoparticles, as they are the most common and readily available commercially, our approach can in principle be applied to any combination of metal-dielectric material that follows the prescriptions we have given above.

However, the condition $a_1 \leq \lambda_{\text{ENZ}}/10$ is specific to Ag-SiO₂ and will take a different form, once the metal and/or dielectric is changed. Furthermore, as each metal's dispersion is different, this may change the spectrum as well as the ENZ wavelength. One can use different thicknesses and dielectric materials to adjust the wavelength and spectrum when the material is different. The electric-near-field response for both the bilayer and the effective-medium structures shows similar near-field optical responses. Our proposed ENZ nanoparticle can be obtained by low-cost chemical synthesis techniques to be utilized in applications that grasp the advantage of ENZ properties as well nanoparticle properties.

ACKNOWLEDGMENTS

The authors acknowledge financial support from the Academy of Finland Flagship Programme (PREIN, Decision No. 320165). H.C. acknowledges financial support from the European Research Council (Starting Grant project aQUARiUM, Agreement No. 802986). I.I. recognizes Optica for the Optica Foundation Amplify Scholarship and SPIE for the SPIE Optics and Photonics Education Scholarship.

I.I. and J.P. contributed equally to this work as well as H.C. and M.O.

- [1] A. Alù, M. G. Silveirinha, A. Salandrino, and N. Engheta, Epsilon-near-zero metamaterials and electromagnetic sources: Tailoring the radiation phase pattern, *Phys. Rev. B* **75**, 155410 (2007).
- [2] J. Zheng, H. A. Almossalami, K. Chen, X. Yu, and H. Ye, Permittivity acquisition of plasmonic materials at epsilon near zero wavelengths, *J. Appl. Phys.* **129**, 103101 (2021).
- [3] G. V. Naik, J. Kim, and A. Boltasseva, Oxides and nitrides as alternative plasmonic materials in the optical range [invited], *Opt. Mater. Express* **1**, 1090 (2011).
- [4] J. Gao, L. Sun, H. Deng, C. J. Mathai, S. Gangopadhyay, and X. Yang, Experimental realization of epsilon-near-zero metamaterial slabs with metal-dielectric multilayers, *Appl. Phys. Lett.* **103**, 051111 (2013).
- [5] R. Maas, J. Parsons, N. Engheta, and A. Polman, Experimental realization of an epsilon-near-zero metamaterial at visible wavelengths, *Nat. Photon.* **7**, 907 (2013).
- [6] M. Habib, I. Issah, E. Bermúdez-Ureña, and H. Caglayan, Self-rolling SiO₂/Au based epsilon-near-zero metamaterials, *Adv. Opt. Mater.* **10**, 2200081 (2022).
- [7] E. J. R. Vesseur, T. Coenen, H. Caglayan, N. Engheta, and A. Polman, Experimental Verification of $n = 0$ Structures for Visible Light, *Phys. Rev. Lett.* **110**, 013902 (2013).
- [8] U. Guler, V. M. Shalaev, and A. Boltasseva, Nanoparticle plasmonics: Going practical with transition metal nitrides, *Mater. Today* **18**, 227 (2015).
- [9] J. Yang, H. A. Almossalami, Z. Wang, K. Wu, C. Wang, K. Sun, Y. M. Yang, and H. Ye, Direct observations of surface plasmon polaritons in highly conductive organic thin film, *ACS Appl. Mater. Interfaces* **11**, 39132 (2019).
- [10] C. Graf and A. Van Blaaderen, Metalodielectric colloidal core-shell particles for photonic applications, *Langmuir* **18**, 524 (2002).
- [11] K. Hasegawa, C. Rohde, and M. Deutsch, Enhanced surface-plasmon resonance absorption in metal-dielectric-metal layered microspheres, *Opt. Lett.* **31**, 1136 (2006).
- [12] S. A. Scherbak and A. A. Lipovskii, Understanding the second-harmonic generation enhancement and behavior in metal core-dielectric shell nanoparticles, *J. Phys. Chem. C* **122**, 15635 (2018).
- [13] Y. Pu, R. Grange, C. L. Hsieh, and D. Psaltis, Nonlinear Optical Properties of Core-Shell Nanocavities for Enhanced Second-Harmonic Generation, *Phys. Rev. Lett.* **104**, 207402 (2010).
- [14] M. A. Ochsenkühn, P. R. Jess, H. Stoquert, K. Dholakia, and C. J. Campbell, Nanoshells for surface-enhanced Raman spectroscopy in eukaryotic cells: Cellular response and sensor development, *ACS Nano* **3**, 3613 (2009).
- [15] P. K. Jain and M. A. El-Sayed, Surface plasmon resonance sensitivity of metal nanostructures: Physical basis and universal scaling in metal nanoshells, *J. Phys. Chem. C* **111**, 17451 (2007).
- [16] C. Zhang, T. Zhang, Z. Zhang, and H. Zheng, Plasmon enhanced fluorescence and Raman scattering by [Au-Ag alloy NP cluster]@SiO₂ core-shell nanostructure, *Front. Chem.* **7**, 647 (2019).
- [17] C. K. Chan, R. C. Flagan, and J. H. Seinfeld, Resonance structures in elastic and Raman scattering from microspheres, *Appl. Opt.* **30**, 459 (1991).
- [18] F. Zhang, G. B. Braun, Y. Shi, Y. Zhang, X. Sun, N. O. Reich, D. Zhao, and G. Stucky, Fabrication of Ag@SiO₂@Y₂O₃:Er nanostructures for bioimaging: Tuning of the upconversion fluorescence with silver nanoparticles, *J. Am. Chem. Soc.* **132**, 2850 (2010).
- [19] V. S. Zuev, SPASER laser and Purcell factor, *Opt. Spectrosc.* **109**, 760 (2010).
- [20] M. A. Noginov, G. Zhu, A. M. Belgrave, R. Bakker, V. M. Shalaev, E. E. Narimanov, S. Stout, E. Herz, T. Suteewong, and U. Wiesner, Demonstration of a spaser-based nanolaser, *Nature (London)* **460**, 1110 (2009).
- [21] I. S. Curtis, R. J. Wills, and M. Dasog, Photocatalytic hydrogen generation using mesoporous silicon nanoparticles: Influence of magnesiothermic reduction conditions and nanoparticle aging on the catalytic activity, *Nanoscale* **13**, 2685 (2021).
- [22] D. Rativa and L. A. Gómez-Malagón, Colloidal plasmonic structures for harvesting solar radiation, *Renewable Energy* **118**, 947 (2018).
- [23] A. D. Phan, N. B. Le, N. T. Lien, and K. Wakabayashi, Multilayered plasmonic nanostructures for solar energy harvesting, *J. Phys. Chem. C* **122**, 19801 (2018).
- [24] M. G. Blaber, M. D. Arnold, and M. J. Ford, A review of the optical properties of alloys and intermetallics for plasmonics, *J. Phys.: Condens. Matter* **22**, 143201 (2010).
- [25] I. L. Rasskazov, P. S. Carney, and A. Moroz, STRATIFY: A comprehensive and versatile MATLAB code for a multilayered sphere, *OSA Continuum* **3**, 2290 (2020).
- [26] P. B. Johnson and R. W. Christy, Optical constants of the noble metals, *Phys. Rev. B* **6**, 4370 (1972).

- [27] L. F. Chen, C. K. Ong, and B. T. G. Tan, Effective permittivity of layered dielectric sphere composites, *J. Mater. Sci.* **33**, 5891 (1998).
- [28] C. T. Tai, *Dyadic Green's Function in Electromagnetic Theory* (The Book Service, Colchester, 1972).
- [29] W. C. Chew, *Waves and Fields in Inhomogeneous Media* (Kluwer, Amsterdam, 1990).
- [30] G. T. Papadakis, P. Yeh, and H. A. Atwater, Retrieval of material parameters for uniaxial metamaterials, *Phys. Rev. B* **91**, 155406 (2015).
- [31] P. Shekhar, J. Atkinson, and Z. Jacob, Hyperbolic metamaterials: fundamentals and applications, *Nano Convergence* **1**, 14 (2014).
- [32] J. D. Jackson, *Classical Electrodynamics*, 2nd ed. (Wiley, New York, 1975).
- [33] Y. Guo, C. L. Cortes, S. Molesky, and Z. Jacob, Broadband super-Planckian thermal emission from hyperbolic metamaterials, *Appl. Phys. Lett.* **101**, 131106 (2012).
- [34] X. Zhang, S. Ye, X. Zhang, and L. Wu, Optical properties of SiO₂@M (M = Au, Pd, Pt) core-shell nanoparticles: Material dependence and damping mechanisms, *J. Mater. Chem. C* **3**, 2282 (2015).
- [35] X. Fan, W. Zheng, and D. J. Singh, Light scattering and surface plasmons on small spherical particles, *Light Sci. Appl.* **3**, e179 (2014).

